

THE SYNTHESIS AND CHARACTERIZATION OF MIXED-ORGANIC-CATIONS TIN HALIDE PEROVSKITES FOR ENHANCED PHOTOVOLTAIC CELL APPLICATION



UNIVERSITY *of the*
WESTERN CAPE

Samkeliso Sanele Ndzimandze

BSc Honours Chemistry

A thesis submitted in fulfilment of the requirement for the degree of

Master of Science Chemistry

In the

Department of Chemistry, University of the Western Cape,
Cape Town, South Africa

Supervisor: Professor Emmanuel I. Iwuoha

Co-supervisor: Doctor Christopher E. Sunday

December 2018

Key words

Dimethylammonium tin iodide

Electrochemical

Energy band-gap

Ethylammonium tin iodide

Guanidinium dimethylammonium tin iodide

Guanidinium ethylammonium tin iodide

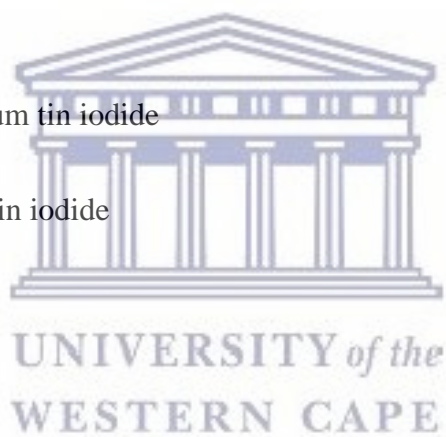
Guanidinium tin iodide

Optical

Photovoltaic

Power conversion efficiency

Tin halide perovskites



Abstract

In this research, novel hybrid perovskite materials were synthesized, characterized and applied in photovoltaic cells (PVCs) to enhance the performance of PVCs. Mixed-organic-cations tin halide perovskites (MOCTPs) were successfully synthesized using sol-gel method. These MOCTPs include guanidinium dimethylammonium tin iodide ([GA][$(\text{CH}_3)_2\text{NH}_2$] SnI_3) and guanidinium ethylammonium tin iodide ([GA][$\text{CH}_3\text{CH}_2\text{NH}_3$] SnI_3). The MOCTPs were studied in comparison to their single-organic-cation tin perovskites (SOCTPs), which include guanidinium tin iodide (GASnI_3), ethylammonium tin iodide ($[\text{CH}_3\text{CH}_2\text{NH}_3]\text{SnI}_3$) and dimethylammonium tin iodide $[(\text{CH}_3)_2\text{NH}_2]\text{SnI}_3$. High Resolution Scanning Electron Microscopy (HR SEM) of the five perovskite materials showed good crystallinity and tetragonal and hexagonal cubic shapes, characteristic of perovskites. These shapes were also confirmed from High Resolution Transmission Electron Microscopy (HR TEM), and the internal structure of the perovskites gave similar zone axes (ZAs) with those obtained from X-ray Diffraction (XRD). XRD showed tetragonal lattice shape for these perovskite materials. Fourier Transform Infrared (FTIR) demonstrated similar functional groups for both the SOCTPs and MOCTPs. FTIR bands that were observed are; N-H, C-H sp^3 , C-H aldehyde, N-H bend, C-N sp^3 and N-H wag. From the ^{13}C Nuclear Magnetic Resonance (NMR) results, the carbon atom of guanidinium iodide precursor shifts from downfield to upfield position, e.g. from 110.57 ppm to 38.49 ppm in GASnI_3 SOCTP. This confirms a shift upfield of the carbon atom in guanidinium iodide precursor as it bonded to Sn metal in the perovskite chemical structure. Similar behavior was also observed for the NMR spectra of $[\text{GA}][\text{CH}_3\text{CH}_2\text{NH}_3]\text{SnI}_3$ MOCTP, where C-2 and C-3 atoms of ethylammonium iodide precursor shifted upfield from 37.03 ppm to 15.69 ppm and 16.06 ppm to 14.39 ppm respectively.

Ultraviolet-Visible (UV-Vis) spectroscopy of the MOCTPs showed a red-shift in absorption relative to the SOCTPs. Correspondingly, the MOCTPs had narrow energy band gap (E_g) compared to the SOCTPs, e.g. $[GA][CH_3CH_2NH_3]SnI_3$ had a band gap of 1.44 eV while $[CH_3CH_2NH_3]SnI_3$ had a band gap of 2.89 eV. The MOCTPs had enhanced optical properties for photovoltaic application since materials with narrow band gap can harvest more solar energy from wider spectrum of light. Cyclic Voltammetry (CV) studies of the MOCTPs showed improved electrochemical properties relative to the SOCTPs. The CV showed increase in peak current (I_p), e.g. $GASnI_3$ perovskite recorded 28.78 μA while $[GA][CH_3CH_2NH_3]SnI_3$ perovskite recorded 62.60 μA for scan rate of 0.1 V/s and potential window between -1.0 and 1.0 V. The rate of diffusion of $[GA][CH_3CH_2NH_3]SnI_3$ perovskite from the bulk solution to the surface of the electrode is faster than the rate of diffusion of $GASnI_3$, hence the increase in current observed in the MOCTP. Electrochemical Impedance Spectroscopy (EIS) characterizations further confirmed that the electrochemical properties of the MOCTPs were improved compared to SOCTPs. The EIS showed reduced log impedance when MOCTPs are compared to SOCTPs, e.g. $[GA][CH_3CH_2NH_3]SnI_3$ recorded log impedance 4.37 while $GASnI_3$ recorded log impedance of 4.56. Phase angle of MOCTPs were higher than that of SOCTPs, e.g. $[GA][CH_3CH_2NH_3]SnI_3$ recorded a phase angle of 52.1° while $GASnI_3$ recorded a phase angle of 51.2° . Charge transfer resistance (R_{ct}) for MOCTPs reduced compared to that of SOCTPs, e.g. $[GA][CH_3CH_2NH_3]SnI_3$ showed R_{ct} of 12552 Ω while $GASnI_3$ recorded R_{ct} of 18201 Ω . All the observations from EIS results endorse that the SOCTPs impede flow of current more than the MOCTPs, hence the MOCTPs have improved conductive properties. The perovskites were further used in preparation of photovoltaic cells, and their power conversion efficiency (PCE) were quantified from the curve of current density-voltage (J-V). MOCTPs based photovoltaic cells recorded higher PCE

compared to their SOCTPs counterparts, e.g. [GA][(CH₃)₂NH₂]SnI₃ based cell achieved PCE of 2.79% while GASnI₃ based solar cell recorded PCE of 0.68% under non-optimized conditions. The MOCTPs had higher PCE than that of SOCTPs, confirming enhanced photovoltaic performance of MOCTPs. Steric hindrance that results from the surface structural modification of the mixed-organic-cations leads to improved perovskite film formation. In addition, mixing these organic-cations promoted passivation of perovskite surface defect sites, which helped hinder charge recombination and improved charge transfer efficiency.



Declaration

I declare that, “ *The synthesis and characterization of mixed-organic-cations tin halide perovskites for enhanced photovoltaic cell application* ” is my own work. That it has not been submitted before for any degree or examination in any other university, and that all sources used or quoted have been indicated or acknowledged as complete references.



Name: Samkeliso Sanele Ndzimandze

UNIVERSITY of the
WESTERN CAPE

Signature:

A handwritten signature in black ink, appearing to be 'SANELE'.

Date: December 2018

Acknowledgements

Firstly, I acknowledge my Lord and Savior Christ Jesus for giving me life and opportunity to study Master of Science degree at University of the Western Cape in His appointed season. Moreover, He graciously supplied resources, good health, and strength to accomplish this degree. I don't know where and what I would be if Jesus didn't love me. My heart and lips shall forever align in agreement, with praises and honor to the Most High God.

I express my deep gratitude and respect to my supervisor Professor Emmanuel I. Iwuoha for caringly giving me the proper guidance throughout the course of this research work. I am highly honored and blessed to have you as my supervisor, with no doubt I am great because I have worked with the great. May God richly bless you and your family. I am also grateful to my co-supervisor Doctor Christopher E. Sunday, I really can't imagine how this research project would be like without your patience and technical assistance. May favor always seek your name.

I appreciate members of the SensorLab for being team players in my research, Dr. Milua Masikini, Dr. Lindsay Wilson, Emmanuel Ramoroka, Kelechi Nwambaekwe, Kevin Tambwe, Samuel Mkehlane, Siyabonga Mdluli, Penny Mathumba, and many others. I also appreciate Professor Edith Beukes for selflessly assisting with NMR data in this research. Appreciated as well is Siphesihle Magubane from the Physics department.

I am saying a special thank you to my parents Albert Sikelela Ndzimandze and Bawinile Alexinah Ndzimandze for being the strongest support structure I know. I love them so much. I appreciate and love my brothers and sisters for their prayers and words of encouragement: Pastor Ndumiso Ndzimandze, Mancoba Ndzimandze, Pastor Ncamiso Ndzimandze, Lindokuhle Ndzimandze, May'bongwe Ndzimandze, Bhekiwe Ndzimandze and Phenduliwe Ndzimandze. I also appreciate my girlfriend Nomfundo Lukhele for the love and support she always gives to me. I love her so much.



UNIVERSITY *of the*
WESTERN CAPE

Dedication

I dedicate this project:

To my parents:

Albert Sikelela Ndzimandze and Bawinile Alexinah Ndzimandze

To my brothers and sisters:

Pastor Ndumiso Ndzimandze, Mancoba Ndzimandze, Pastor Ncamiso Ndzimandze, Lindokuhle Ndzimandze, May'bongwe Ndzimandze, Bhekiwe Ndzimandze and Phenduliwe Ndzimandze.

To my girlfriend:

Nomfundo Lukhele



UNIVERSITY *of the*
WESTERN CAPE

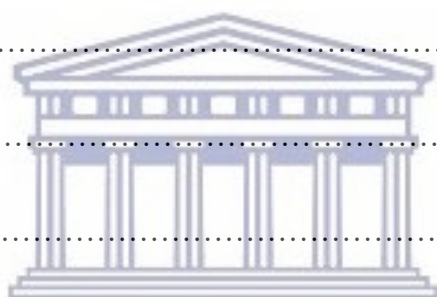
Table of contents

Title	page
Key words.....	(ii)
Abstract.....	(iii)
Declaration.....	(vi)
Acknowledgements.....	(vii)
Dedication.....	(ix)
Table of contents.....	(x)
List of figures.....	(xviii)
List of tables.....	(xxiv)
List of abbreviations.....	(xxvi)
Chapter 1.....	1
Introduction.....	1
1.1 Background information.....	1
1.2 Perovskites and its classification.....	2
1.3 Thin-film technology.....	8



UNIVERSITY of the
WESTERN CAPE

1.4 Problem statement.....	9
1.5 Aims and objectives.....	10
1.5.1 Aim.....	10
1.5.2 Objectives.....	10
1.6 Research framework.....	12
1.7 Thesis layout.....	13
1.8 References.....	14
Chapter 2.....	19
Literature review.....	19
2.1 Properties of perovskites.....	19
2.2 Morphology and crystallinity of perovskites.....	25
2.3 Historical and technological advancement of perovskites.....	28
2.4 Methods adopted in the synthesis of perovskites.....	37
2.5 Photovoltaic cell (PVC) device.....	39
2.6 Characterization techniques and working principles.....	44
2.6 Photophysical characterizations.....	44
2.6.1 High Resolution Scanning Electron Microscopy (HR SEM).....	44
2.6.2 High Resolution Transmission Electron Microscopy (HR TEM).....	46



UNIVERSITY of the
WESTERN CAPE

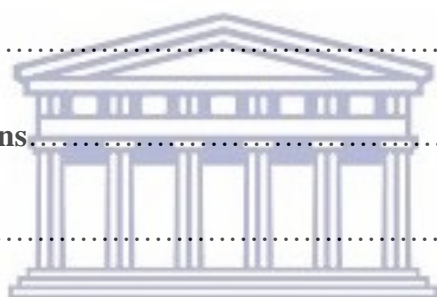
2.6.3 X-ray Diffraction (XRD).....	46
2.6.4 Brunauer-Emmett-Teller (BET).....	48
2.6.5 Ultraviolet-Visible (UV-Vis) spectroscopy.....	50
2.6.6 Photoluminescence (PL) spectroscopy.....	53
2.6.7 Fourier Transform Infrared (FTIR) spectroscopy.....	54
2.6.8 Raman spectroscopy.....	56
2.6.9 Thermogravimetric Analysis (TGA).....	57
2.6.10 Nuclear Magnetic Resonance (NMR) spectroscopy.....	58
Electrochemical characterizations	60
2.6.11 Cyclic Voltammetry (CV).....	60
2.6.12 Square Wave Voltammetry (SWV).....	61
2.6.13 Electrochemical Impedance Spectroscopy (EIS).....	62
2.6.14 J-V curve (current-voltage curve).....	63
2.7 References.....	65
Chapter 3	83
Experimental procedures	83
3.1 Chemical synthesis of ethylammonium tin iodide perovskite.....	83

3.1.1 Chemicals.....	83
3.1.2 Experimental procedure.....	84
3.2 Chemical synthesis of dimethylammonium tin iodide perovskite.....	85
3.2.1 Chemicals.....	85
3.2.2 Experimental procedure.....	85
3.3 Chemical synthesis of guanidinium tin iodide perovskite.....	86
3.3.1 Chemicals.....	86
3.3.2 Experimental procedure.....	86
3.4 Chemical synthesis of guanidinium ethylammonium tin iodide perovskite.....	87
3.4.1 Chemicals.....	87
3.4.2 Experimental procedure.....	87
3.5 Chemical synthesis of guanidinium dimethylammonium tin iodide perovskite.....	88
3.5.1 Chemicals.....	88
3.5.2 Experimental procedure.....	88
3.6 Characterization of the perovskites.....	89
3.7 Fabrication of photovoltaic cell devices.....	91
3.7.1 Chemicals.....	91
3.7.2 Procedure for synthesis of GASnI_3 precursor.....	91



UNIVERSITY of the
WESTERN CAPE

3.7.3 Procedure for synthesis of $[\text{CH}_3\text{CH}_2\text{NH}_3]\text{SnI}_3$ precursor.....	91
3.7.4 Procedure for synthesis of $[(\text{CH}_3)_2\text{NH}_2]\text{SnI}_3$ precursor.....	92
3.7.5 Procedure for synthesis of $[\text{GA}][(\text{CH}_3)_2\text{NH}_2]\text{SnI}_3$ precursor.....	92
3.7.6 Procedure for synthesis of $[\text{GA}][\text{CH}_3\text{CH}_2\text{NH}_3]\text{SnI}_3$ precursor.....	92
3.7.7 Assembly of photovoltaic cell (PVC) devices.....	93
3.8 References.....	95
Chapter 4.....	99
Results and discussion.....	99
Photophysical characterizations.....	99
4.1 HR SEM and EDS results.....	99
4.2 HR TEM results.....	104
4.2.1 HR TEM for ethylammonium tin iodide.....	104
4.2.2 HR TEM for dimethylammonium tin iodide.....	106
4.2.3 HR TEM for guanidinium tin iodide.....	107
4.2.4 HR TEM for guanidinium ethylammonium tin iodide.....	108
4.2.5 HR TEM for guanidinium dimethylammonium tin iodide.....	110
4.3 Small-Angle X-ray Scattering (SAXS) results.....	111
4.3.1 SAXS for ethylammonium tin iodide perovskite.....	111



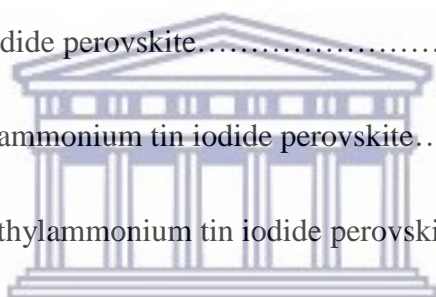
UNIVERSITY of the
WESTERN CAPE

4.3.2 SAXS for dimethylammonium tin iodide perovskite.....	114
4.3.3 SAXS for guanidinium tin iodide perovskite.....	116
4.3.4 SAXS for guanidinium dimethylammonium tin iodide perovskite.....	118
4.3.5 SAXS for guanidinium ethylammonium tin iodide perovskite.....	120
4.4 XRD results.....	122
4.5 FTIR results.....	127
4.6 NMR results.....	130
4.6.1 NMR for $[\text{CH}_3\text{CH}_2\text{NH}_3]\text{SnI}_3$	130
4.6.2 NMR for $[(\text{CH}_3)_2\text{NH}_2]\text{SnI}_3$	132
4.6.3 NMR for GASnI_3	133
4.6.4 NMR for $[\text{GA}][\text{CH}_3\text{CH}_2\text{NH}_3]\text{SnI}_3$	134
4.6.5 NMR for $[\text{GA}][(\text{CH}_3)_2\text{NH}_2]\text{SnI}_3$	135
4.7 UV-Vis results.....	137
Electrochemical characterizations.....	141
4.8 CV results.....	141
4.8.1 CV for perovskite precursor materials.....	141
4.8.2 CV for ethylammonium tin iodide.....	145
4.8.3 CV for dimethylammonium tin iodide perovskite.....	149



UNIVERSITY of the
WESTERN CAPE

4.8.4 CV for guanidinium tin iodide perovskite.....	152
4.8.5 CV for guanidinium ethylammonium tin iodide perovskite.....	155
4.8.6 CV for guanidinium dimethylammonium tin iodide perovskite.....	158
4.8.7 Electrochemical band gap (E_g).....	161
4.9 Electrochemical Impedance Spectroscopy results.....	163
4.9.1 EIS for ethylammonium tin iodide perovskite.....	164
4.9.2 EIS for dimethylammonium tin iodide perovskite.....	166
4.9.3 EIS for guanidinium tin iodide perovskite.....	169
4.9.4 EIS for guanidinium ethylammonium tin iodide perovskite.....	171
4.9.5 EIS for guanidinium dimethylammonium tin iodide perovskite.....	173
4.9.6 Combined EIS studies.....	176
Fabrication of SOCTP and MOCTP-based devices.....	178
4.10 Photovoltaic cells (PVCs) fabrication and characterization.....	178
4.11 References.....	184
Chapter 5.....	203
Conclusions and recommendations.....	203
5.1 Conclusions.....	206
5.2 Recommendations.....	208



UNIVERSITY of the
WESTERN CAPE

5.3 References.....189



UNIVERSITY *of the*
WESTERN CAPE

List of figures

Figure	Title	Page
Figure 1.1	The basic ABX ₃ perovskite structure	3
Figure 1.2	The family of perovskites	4
Figure 2.1	Colors of powder samples of Sn(phen)Cl _m I _n and Sn(phen)Br _m I _n series	24
Figure 2.2	Schematic diagram of the sol-gel method for the synthesis of ceramic perovskite	39
Figure 2.3	Solar cell schematic for planar device configuration	40
Figure 2.4	Structure of PEDOT:PSS	43
Figure 2.5	Structure of PCBM	44
Figure 2.6	Schematic diagram of HR SEM	45
Figure 2.7	Schematic diagram of XRD	47
Figure 2.8	(a) BET model of single layer adsorption, (b) BET model of a multilayer adsorption	49
Figure 2.9	A typical schematic diagram of UV-Vis instrument	52
Figure 2.10	Schematic diagram of the PL setup	54
Figure 2.11	Schematic diagram of FTIR	55
Figure 2.12	Schematic diagram of Raman spectrometer	57
Figure 2.13	Simplified schematic diagram for NMR	59
Figure 2.14	Schematic diagram of the experimental setup for EIS	62
Figure 2.15	Typical J-V curve of solar cells	63

Figure 3.1	Device architecture of the planar structure perovskite solar cell (glass/ITO/PEDOT:PSS/perovskite layer/PCBM/Al)	94
Figure 4.1	HR SEM images for the various perovskites taken at different resolutions	101
Figure 4.2	EDS spectra for the 5 perovskites	103
Figure 4.3	(a) and (b) HR TEM images for $[\text{CH}_3\text{CH}_2\text{NH}_3]\text{SnI}_3$ at different resolutions and (c) SAED of $[\text{CH}_3\text{CH}_2\text{NH}_3]\text{SnI}_3$	105
Figure 4.4	(a) and (b) HR TEM images for $[(\text{CH}_3)_2\text{NH}_2]\text{SnI}_3$ at different resolutions and (c) SAED of $[(\text{CH}_3)_2\text{NH}_2]\text{SnI}_3$	106
Figure 4.5	(a) and (b) HR TEM images for GASnI_3 at different resolutions and (c) SAED of GASnI_3	108
Figure 4.6	(a) and (b) HR TEM images for $[\text{GA}][\text{CH}_3\text{CH}_2\text{NH}_3]\text{SnI}_3$ at different resolutions and (c) SAED of $[\text{GA}][\text{CH}_3\text{CH}_2\text{NH}_3]\text{SnI}_3$	109
Figure 4.7	(a) and (b) HR TEM images for $[\text{GA}][(\text{CH}_3)_2\text{NH}_2]\text{SnI}_3$ at different resolutions and (c) SAED of $[\text{GA}][(\text{CH}_3)_2\text{NH}_2]\text{SnI}_3$	110
Figure 4.8	(a) PDDF for $[\text{CH}_3\text{CH}_2\text{NH}_3]\text{SnI}_3$ perovskite and (b) particle size distribution for the perovskite	112
Figure 4.9	Schematic presentation of proposed crystal growth	113
Figure 4.10	SAXS plots of (a) volume of the particle size and (b) intensity of the particle sizes for $[\text{CH}_3\text{CH}_2\text{NH}_3]\text{SnI}_3$ perovskite	114
Figure 4.11	(a) PDDF for $[(\text{CH}_3)_2\text{NH}_2]\text{SnI}_3$ perovskite and (b) particle size distribution for the perovskite	115
Figure 4.12	SAXS plots of (a) volume of the particle size and (b) intensity	116

	of the particle sizes for $[(\text{CH}_3)_2\text{NH}_2]\text{SnI}_3$ perovskite	
Figure 4.13	(a) PDDF for GASnI_3 perovskite and (b) particle size distribution for the perovskite	117
Figure 4.14	SAXS plot of (a) volume of the particle size and (b) intensity of the particle sizes for GASnI_3 perovskite	118
Figure 4.15	(a) PDDF for $[\text{GA}][(\text{CH}_3)_2\text{NH}_2]\text{SnI}_3$ perovskite and (b) particle size distribution for the perovskite	119
Figure 4.16	SAXS plots for (a) volume of the particle size and (b) intensity of the particle sizes for $[\text{GA}][(\text{CH}_3)_2\text{NH}_2]\text{SnI}_3$ perovskite	120
Figure 4.17	(a) PDDF for $[\text{GA}][\text{CH}_3\text{CH}_2\text{NH}_3]\text{SnI}_3$ and (b) particle size distribution for the perovskite	121
Figure 4.18	SAXS plots for (a) volume of the particle size and (b) intensity of the particle sizes of $[\text{GA}][\text{CH}_3\text{CH}_2\text{NH}_3]\text{SnI}_3$ perovskite	122
Figure 4.19	XRD pattern for the perovskites	124
Figure 4.20	Tetragonal structure of the perovskites	125
Figure 4.21	FTIR spectra for (a) $[(\text{CH}_3)_2\text{NH}_2]\text{SnI}_3$ (b) $[\text{CH}_3\text{CH}_2\text{NH}_3]\text{SnI}_3$ and (c) GASnI_3 , $[\text{GA}][\text{CH}_3\text{CH}_2\text{NH}_3]\text{SnI}_3$ and $[\text{GA}][(\text{CH}_3)_2\text{NH}_2]\text{SnI}_3$	128
Figure 4.22	^{13}C NMR spectra for EthI precursor and $[\text{CH}_3\text{CH}_2\text{NH}_3]\text{SnI}_3$ perovskite	132
Figure 4.23	^{13}C NMR spectra for DimI precursor and $[(\text{CH}_3)_2\text{NH}_2]\text{SnI}_3$ perovskite	133
Figure 4.24	^{13}C NMR spectra for GAI precursor and GASnI_3 perovskite	134

Figure 4.25	^{13}C NMR spectra for GAI precursor and $[\text{GA}][\text{CH}_3\text{CH}_2\text{NH}_3]\text{SnI}_3$ perovskite	135
Figure 4.26	^{13}C NMR spectra for GAI precursor and $[\text{GA}][(\text{CH}_3)_2\text{NH}_2]\text{SnI}_3$ perovskite	136
Figure 4.27	(a) UV-Vis spectra for $[\text{CH}_3\text{CH}_2\text{NH}_3]\text{SnI}_3$ and $[(\text{CH}_3)_2\text{NH}_2]\text{SnI}_3$, (b) UV-Vis for GASnI_3 , $[\text{GA}][\text{CH}_3\text{CH}_2\text{NH}_3]\text{SnI}_3$ and $[\text{GA}][(\text{CH}_3)_2\text{NH}_2]\text{SnI}_3$, inset shows peak c	138
Figure 4.28	Ligand to metal charge transfer (LMCT) involving an octahedral d^6 complex	139
Figure 4.29	CV for bare glassy carbon electrode (GCE) in supporting electrolyte and bare GCE in 0.05 M tin (II) iodide	142
Figure 4.30	CV for bare GCE in supporting electrolyte and bare GCE in 0.05 M tin powder	143
Figure 4.31	CV for bare GCE in supporting electrolyte and bare GCE in 0.05M $[\text{CH}_3\text{CH}_2\text{NH}_3]\text{SnI}_3$ perovskite	145
Figure 4.32	(a) CV at various scan rates and (b) Randles plot for $[\text{CH}_3\text{CH}_2\text{NH}_3]\text{SnI}_3$ perovskite	146
Figure 4.33	CV for bare GCE in supporting electrolyte and bare GCE in 0.05 M $[(\text{CH}_3)_2\text{NH}_2]\text{SnI}_3$ perovskite	150
Figure 4.34	(a) CV for bare GCE in 0.05 M $[(\text{CH}_3)_2\text{NH}_2]\text{SnI}_3$ at various scan rates and (b) Randles plot for the perovskite	151

Figure 4.35	CV for bare GCE in supporting electrolyte and bare GCE in 0.05 M GASnI_3 perovskite	153
Figure 4.36	(a) CV for bare GCE in 0.05 M GASnI_3 at various scan rates and (b) Randles plot for the perovskite	154
Figure 4.37	CV for bare GCE in supporting electrolyte and bare GCE in 0.05 M $[\text{GA}][\text{CH}_3\text{CH}_2\text{NH}_3]\text{SnI}_3$ perovskite	156
Figure 4.38	CV for bare GCE in 0.05 M $[\text{GA}][\text{CH}_3\text{CH}_2\text{NH}_3]\text{SnI}_3$ at various scan rates and (b) Randles plot for the perovskite	157
Figure 4.39	CV for bare GCE in supporting electrolyte and bare GCE in 0.05 M $[\text{GA}][(\text{CH}_3)_2\text{NH}_2]\text{SnI}_3$ perovskite	159
Figure 4.40	(a) CV for bare GCE in 0.05 M $[\text{GA}][(\text{CH}_3)_2\text{NH}_2]\text{SnI}_3$ at various scan rates and (b) Randles plot for the perovskite	160
Figure 4.41	(a) Nyquist and (b) Bode plots for $[\text{CH}_3\text{CH}_2\text{NH}_3]\text{SnI}_3$	164
Figure 4.42	Equivalence circuit used to analyze the EIS data for $[\text{CH}_3\text{CH}_2\text{NH}_3]\text{SnI}_3$	165
Figure 4.43	(a) Nyquist and (b) Bode plots for $[(\text{CH}_3)_2\text{NH}_2]\text{SnI}_3$	167
Figure 4.44	(a) Nyquist and (b) Bode plots for GASnI_3	169
Figure 4.45	(a) Nyquist and (b) Bode plot for $[\text{GA}][\text{CH}_3\text{CH}_2\text{NH}_3]\text{SnI}_3$ perovskite	171
Figure 4.46	(a) Nyquist and (b) Bode plots for $[\text{GA}][(\text{CH}_3)_2\text{NH}_2]\text{SnI}_3$ perovskite	174

Figure 4.47	The equivalence circuit that was used to fit [GA][(CH ₃) ₂ NH ₂]SnI ₃ EIS data	175
Figure 4.48	Nyquist plots for all the 5 perovskites	176
Figure 4.49	Bode plots: (a) log frequency vs log Z and (b) log frequency vs phase angle for all the 5 perovskites	177
Figure 4.50	J-V curves for (a) GAsnI ₃ , (b) [(CH ₃) ₂ NH ₂]SnI ₃ and (c) [CH ₃ CH ₂ NH ₃]SnI ₃ photovoltaic cell devices	180
Figure 4.51	J-V curves for (a) [GA][(CH ₃) ₂ NH ₂]SnI ₃ and (b) [GA][CH ₃ CH ₂ NH ₃]SnI ₃ photovoltaic cell devices	182



UNIVERSITY *of the*
WESTERN CAPE

List of tables

Table	Title	Page
Table 4.1	Averaged dimensions of crystallites (t) of the perovskites	127
Table 4.2	Calculated electrochemical band gaps relative to the respective perovskite materials	163
Table 4.3	Values of the elements of the circuit used to fit the [CH ₃ CH ₂ NH ₃] ₃ SnI ₃ EIS data	165
Table 4.4	Values of the elements of the circuit used to fit the [CH ₃ CH ₂ NH ₃] ₃ SnI ₃ EIS data	168
Table 4.5	Values of the elements of the circuit used to fit the GASnI ₃ EIS data	170
Table 4.6	Elements and their values of the plotted EIS data for [GA][CH ₃ CH ₂ NH ₃] ₃ SnI ₃ perovskite	172
Table 4.7	Elements and their values of the plotted EIS data of [GA][(CH ₃) ₂ NH ₂] ₃ SnI ₃ perovskite	175
Table 4.8	Device performance parameters of the SOCTPs photovoltaic cells	181
Table 4.9	Device performance parameters of the MOCTPs photovoltaic cells	183
Table 4.10	MAPbI ₃ device performance parameters with different Polystyrene concentrations	184
Table 5.1	Characteristic parameters and their percentage change	205

effected by mixing organic cations



UNIVERSITY *of the*
WESTERN CAPE

List of abbreviations

AC	Alternating current
BET	Brunauer - Emmett- Teller
CPE	Constant phase element
CV	Cyclic Voltammetry
DimI	Dimethylammonium iodide
DMF	N,N-dimethylformamide
DMSO	Dimethyl-sulfoxide
D_{ox}	Oxidation diffusion co-efficient
D_{red}	Reduction diffusion co-efficient
EDS	Energy-dispersive X-ray Spectroscopy
E_g	Energy band gap
EIS	Electrochemical Impedance Spectroscopy
E_{ox}	Oxidation potential
$E_{p,a}$	Anodic peak potential
$E_{p/2,c}$	Half cathodic peak potential
$E_{p,c}$	Cathodic peak potential

E_{red}	Reduction potential
EthI	Ethylammonium iodide
ETL	Electron transport layer
FET	Field effect transistor
FF	Fill factor
FTIR	Fourier Transform Infrared
GA	Guanidinium
GAI	Guanidinium iodide
GCE	Glassy carbon electrode
HOMO	Highest occupied molecular orbital
HR SEM	High Resolution Scanning Electron Microscopy
HR TEM	High Resolution Transmission Electron Microscopy
HTM	Hole transport material
I_p	Peak current
$I_{p,a}$	Anodic peak current
$I_{p,c}$	Cathodic peak current
IR	Infrared
J_{sc}	Short circuit current density

LMCT	Ligand to metal charge transfer
LUMO	Lowest unoccupied molecular orbital
MOCTP	Mixed-Organic-Cation Tin Halide Perovskites
NMR	Nuclear Magnetic Resonance
PCBM	6,6- phenyl- C61- butyric acid methyl ester
PCE	Power conversion efficiency
PDDF	Pair distance distribution function
PEC	Photoelectrochemical solar cell
PEDOT:PSS	Poly (3,4 ethylene dioxythiophene) polystyrene sulfonate
PFN	Poly [9,9-dioctylfluorene-9,9-bis (N,N-dimethyl-propyl) fluorene]
PL	Photoluminescence
PSC	Perovskite solar cell
PV	Photovoltaic
PVC	Photovoltaic cell
R_{ct}	Charge transfer resistance
R_s	Series resistance
SAED	Selected area electron diffraction
SAXS	Small-Angle X-ray Scattering

SOCTP	Single-Organic-Cation Tin Halide Perovskites
Spiro-OmeTAD	2,2',7,7'- Tetrakis [N,N- di(4- methoxyphenyl) amino] 9,9'- spirobifluorene
SWV	Square Wave Voltammetry
TGA	Thermogravimetric Analysis
UV-Vis	Ultraviolet-Visible spectroscopy
V_{oc}	Open current voltage
V	Scan rate
W_o	Warburg element (open)
W_s	Warburg element (short)
XRD	X-ray Diffraction
ZA	Zone axis



CHAPTER 1

INTRODUCTION

1.1 Background information

Energy is one of the most basic and primary needs for human life. Over the past years, most of the world's energy has been produced from fossil fuel-based sources, e.g. coal, gasoline, diesel fuel, heat oil, jet fuel, kerosene and natural gas [1]. Fossil fuel-based sources cause undesirable environmental effects such as acid rain and global warming [2, 3]. They are non-renewable and will run out in the future. There is a growing demand for high energy density which is due to increase in the world's population and industrial machineries. More energy is required to sustain domestic activities, electric vehicles and many emerging advanced technologies/ devices. Hence, there is need for an alternative, reliable and renewable energy source that will satisfy the huge energy demands with little or no adverse effects on the environment.

There are several known sources of clean and renewable energy namely; wind, solar, water, biomass and geothermal [4]. The energy source that stands out with sufficient capacity to supply global electricity needs is solar photovoltaic (PV) energy. Photovoltaic cells by function, collect solar energy through their light absorbing materials and change it directly into electrical energy. The word “photovoltaic” was named from the process of transforming photons of light energy into

voltage, which is electrical energy through a process called the photovoltaic (PV) effect [5]. From understanding this process, we can design simple photovoltaic devices that are easy to maintain. PV devices are most desirable for their advantage of being easy to construct as independent systems that give relatively good power outputs [6].

Photovoltaic cells require absorbing material such as methylammonium tin iodide perovskite film, that is incorporated within the cell structure. The primary function of the absorbing material is to absorb solar energy and transform it into free electrons via the photovoltaic effect [7]. When sunlight strikes a photovoltaic cell, energy is imparted to some electrons which are in turn promoted to higher energy level, a process called excitation. A semiconductor crystal has ability to produce significant free electrons upon illumination with light, hence generating electrical energy [8, 9]. PV cell exhibits a potential barrier that enables the excited electrons to produce voltage that can drive electricity through a circuit [10]. Current research in this area is mainly focusing on making perovskite cells that have high efficiency and are low cost to produce and maintain [11].

1.2 Perovskites and its classification

The term “perovskites” is used to describe a group of compounds characterized by the general formula ABX_3 . These compounds conform to the crystalline structure characteristic to that of calcium titanium oxide ($CaTiO_3$) [12]. Figure 1.1 shows the basic ABX_3 perovskite structure where component A can either be an inorganic or organic cation e.g. $(CH_3CH_2NH_3^+)$, B is a metal cation

e.g. Pb^{2+} , Sn^{2+} etc. while X is an anion either singly charged like I^- , Br^- , Cl^- or doubly charged like O^{2-} , S^{2-} etc. The unit cell is BX_6 octahedron where B is positioned at the center directly bonded to 6 surrounding X atoms. The unit cells form a network through corner-sharing as seen in figure 1.1, forming a very stable framework of many atoms. The A cations are placed in the 12 coordinated holes between the consecutive unit cells. These complexes exhibit various properties that make them useful in many applications such as solar cells, catalysis and light emitting diodes. The BX_6 has a key role in ferromagnetism and ferroelectricity.

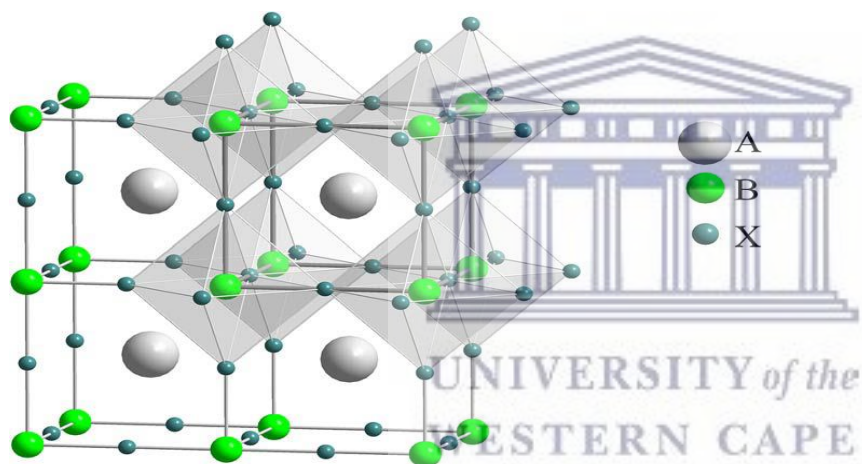


Figure 1.1: The basic ABX_3 perovskite structure. [13]

The major sub-divisions of the family of perovskites are inorganic oxides and halide perovskites. The most important class in this research is organometal halide perovskites (where mixed-organic-cation tin halide perovskites are classified), which is a sub-class of halide perovskites division. Perovskite material optimization and variation is made simple by composition control and phase

transition engineering [14]. This explains the diversity of perovskite compounds with varying optical and electrochemical properties. The figure below shows the classification of the crystalline systems of perovskites, see organometal halide perovskites.

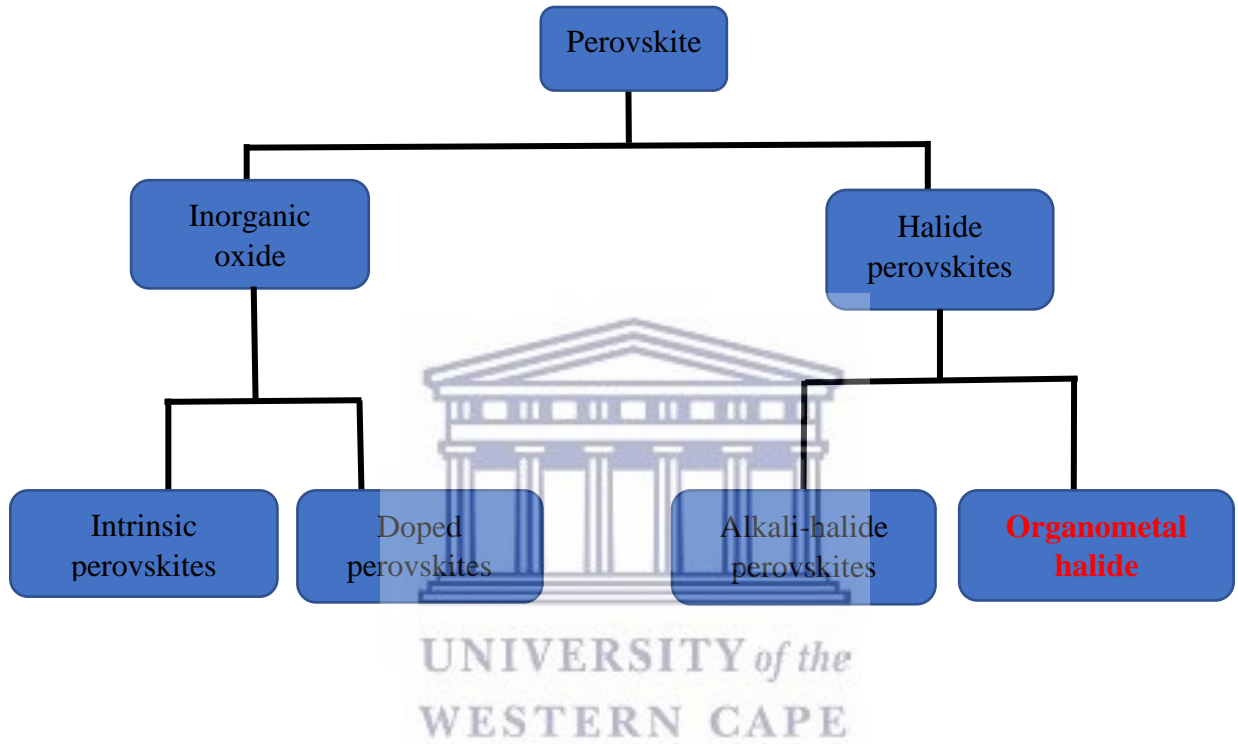
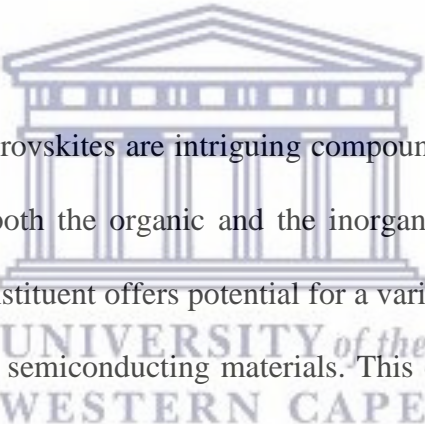


Figure 1.2: The family of perovskites.

Perovskite technology comes with some advantages over the silicon technology that is currently being used widely. The silicon technology is expensive and involves high-energy process generating high levels of waste material. On the other hand, the perovskite technology is simpler, low cost, lower embodied energy and reduces the environmental impact massively [15]. Perovskites possess desirable properties for use as photovoltaic absorbers which include sharp absorption edge relative to their composition, great light absorption coefficient, long hole and

electron diffusion distances, good hole and electron carrier mobility and manifest tolerance for defects. The most significant disorder amongst perovskite materials is the Schottky disorder which involves point defect in a crystal lattice. This phenomenon means lattice vacancy defect in non-ionic crystals. There are stoichiometric amounts of vacancies between cations and anions that are maintained within the crystal to keep an overall neutral charge. Furthermore, the perovskite structure is highly tunable because of the variety of organic and inorganic cations (A), central elements (B), usually Pb, and anions (X) that can be incorporated into a variety of “hybrid” structures, resulting in complete optical tunability over the entire visible spectrum [16]. Organic-inorganic perovskites are widely preferred due to their good tunability.



The organic-inorganic hybrid perovskites are intriguing compounds that enjoy a combination of physicochemical properties of both the organic and the inorganic constituent within the same complex [17]. The inorganic constituent offers potential for a variety of electronic properties that make possible the design of the semiconducting materials. This component further controls the magnetic and dielectric properties, mechanical properties such as hardness and thermal stability of the entire perovskite composite. Meanwhile, fluorescence, polarizability and mechanical properties as well as versatility of organic-inorganic perovskites are solely known to be contributed by the organic molecules in the perovskite structure [17]. Organic-inorganic hybrid perovskites that are halide-based show to be the most significant in this sub-class.

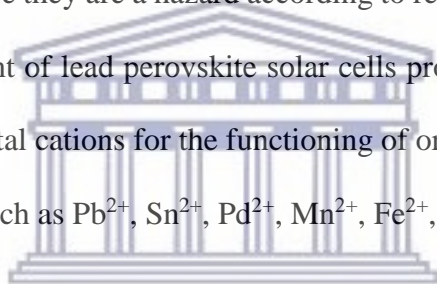
The first study of halide-based perovskites was done on cesium lead halides (CsPbX_3) by Moller, in 1958 [15]. The development of dye-sensitized photovoltaic cells that are constructed on liquid

electrolyte attracted a lot of interest amongst halide-based photovoltaic cells. Perovskite solar cell (PSC) devices have significantly increased the PCE of solar cells from 3.8% in 2009 to over 22% from latest reports [18]. The most extensively studied photovoltaic perovskites are methylammonium lead halide perovskites. This ABX_3 lead perovskite-type structure, is made of an extended arrangement of octahedra of corner-sharing PbI_6 framework, whereby methylammonium ion ($CH_3NH_3^+$) fills the A site and is surrounded by twelve close-neighboring iodide ions [19, 20]. Materials that exhibit the ABX_3 perovskite structure usually display vacancy-mediated diffusion process. Methylammonium lead iodide is a typical example where the vacancy-mediated diffusion is evident, which is largely due to ease of formation of Schottky disorder, with an intrinsic concentration of I^- , Pb^{2+} and $CH_3NH_3^+$ vacancies [21]. Inorganic perovskite oxides or halides have no interstitial migration since they lack interstitial space but depend solely on vacancy-mediated diffusion [21]. Over the years, halide-based perovskites have been synthesized, whereby the most explored organic cations for perovskite solar cells were incorporated, which include; methylammonium ($CH_3NH_3^+$), ethylammonium ($CH_3CH_2NH_3^+$) and formamidinium ($NH_2CH=NH_2^+$) cations [22].

The structure of the inorganic/organic perovskite is decisively determined by the size of the organic cation [23]. Small cations like methylammonium maintain a three-dimensional structure of the perovskite, larger cations, e.g. organic molecules containing phenyl-groups, will result in a layered structure with inorganic sheets alternating with organic layers hence producing lower dimensional materials [24]. Although lower dimensional compounds typically inhibit carrier mobility that is not expected for electronic materials, this disadvantage can be reduced by incorporating an organic component with desirable optical and electronic activities [25]. The use of planar aromatic organic

ligands that highly favor oriented p-stacking conformations was found to produce conjugated pathways that is suitable for electron and hole transport [26]. Hence, the choice of organic cation affects the perovskite sheet orientation.

The choice of organic cation in perovskite structure influences the structure of the composite material and in turn on the overall perovskite properties. This demonstrates the flexibility amongst the organic-inorganic perovskite materials, hence improving the ability for tailoring and understanding transport at lower dimensions of layered perovskites. Lead-based perovskites are environmentally toxic, and hence they are a hazard according to regulations of international waste disposal. The good advancement of lead perovskite solar cells prompted the search for lead-free halide perovskites. The best metal cations for the functioning of organic-inorganic framework are divalent transition metal ions such as Pb^{2+} , Sn^{2+} , Pd^{2+} , Mn^{2+} , Fe^{2+} , Ni^{2+} , Co^{2+} , Cu^{2+} etc. [27].



UNIVERSITY of the
WESTERN CAPE

Tin is a possible alternative to lead since it is in the same group as lead and share a lot of common features and characteristic properties in structure, and chemical reactivity. Such materials are a step towards reduced environmental toxicity of perovskite materials, more especially for disposable devices. Furthermore, bandgap tunability of some of lead-free halide perovskites improves optical properties of these materials by absorbing light energy in higher wavelength region. This narrowed band gap is a desirable feature for better performance in solar cells, light-sensors and optical communications [28]. One major challenge about tin is that it is an air sensitive metal that readily oxidizes from Sn^{2+} to Sn^{4+} . Most studies done on tin perovskites usually report stability problems of the perovskites due to tin. Dichloromethane (CH_2Cl_2) has been reported as a

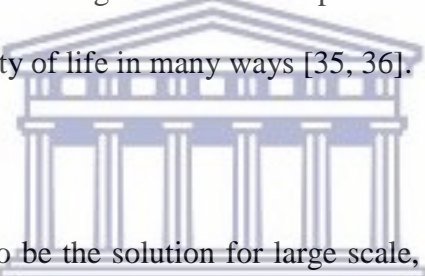
suitable electrolyte that is utilized in photoelectrochemical (PEC) solar cells that are liquid junction, giving relatively good stability of the perovskite because of its relatively higher dielectric constant [29]. The use of dichloromethane and the use of nitrogen glove box in all the synthetic steps have been proven to counter act the instability of Sn.

1.3 Thin-film technology

Thin-film technology involves the use of thin films in applications such as photovoltaic cells. Thin-films or solar cell application are thin layers (usually in nm range) of semiconductor materials applied to a solid substrate material. Studies have proven that thin-films considerably lower the cost of producing photovoltaic cells [30]. This is made possible since thin films cut down on the quantity of semiconductor material used for each unit of solar cell in comparison to silicon flakes, hence reduces the cost of manufacturing of photovoltaic cells [30]. Commonly used materials for thin film PV include cadmium telluride (CdTe), titanium dioxide (TiO_2), copper indium diselenide (CuInSe_2) and gallium arsenide (GaAs) [31]. Hybrid organometallic perovskites can have their properties studied on thin-film structures of the perovskite material. Thin-films of organometallic halide perovskite materials have diverse applications on a variety of thin-film devices, such as PSCs, thin-film transistors [32], and light-emitting diodes [33].

1.4 Problem Statement

There is an increasing demand for energy due to increasing populations and emerging advanced industrial machineries. This has brought new opportunities for renewable energy resources which do not harm the environment. The current sources of energy are harmful to the environment and they include; coal, oil, and gas in burning fossil fuels [34]. One of the major problems of fossil fuel energy source that have attracted public attention recently is the "greenhouse effect," which changes the earth's climate. Some parts of the earth experience acid rain, which destroys forests and disturbs sea-life. Over-use of burning fuels causes air pollution, making the populations of the world ill and degrading the quality of life in many ways [35, 36].



Solar cell photovoltaics seems to be the solution for large scale, renewable and clean source of energy for the world population [37]. The most promising organic-inorganic solar cell perovskites, $\text{CH}_3\text{NH}_3\text{PbX}$ are toxic due to the incorporation of lead in the crystal structure. Unfortunately, the desirable characteristics of solar cell perovskites are largely due to the conductive electrochemical properties of lead in the box-like perovskite structure. A maximum theoretical efficiency for optimum performance in a heterojunction device is over 30%, feasible by harvesting the ultraviolet light to near infrared photons up to 1.1 eV [38], and the current perovskite materials do not meet these standards, hence the search for better perovskite materials.

1.5 Aims and objectives

1.5.1 Aim:

Perovskites have demonstrated a great potential in being game-changers in photovoltaic cells through their flexible tunability and improved efficiency. This research aims to synthesize non-toxic, mixed-organic-cation tin halide perovskites with enhanced photo-electric properties and higher optical absorption coefficients for solar cell application.

1.5.2 Objectives:



Specific objectives adopted to achieve the aim of this research stated above include:

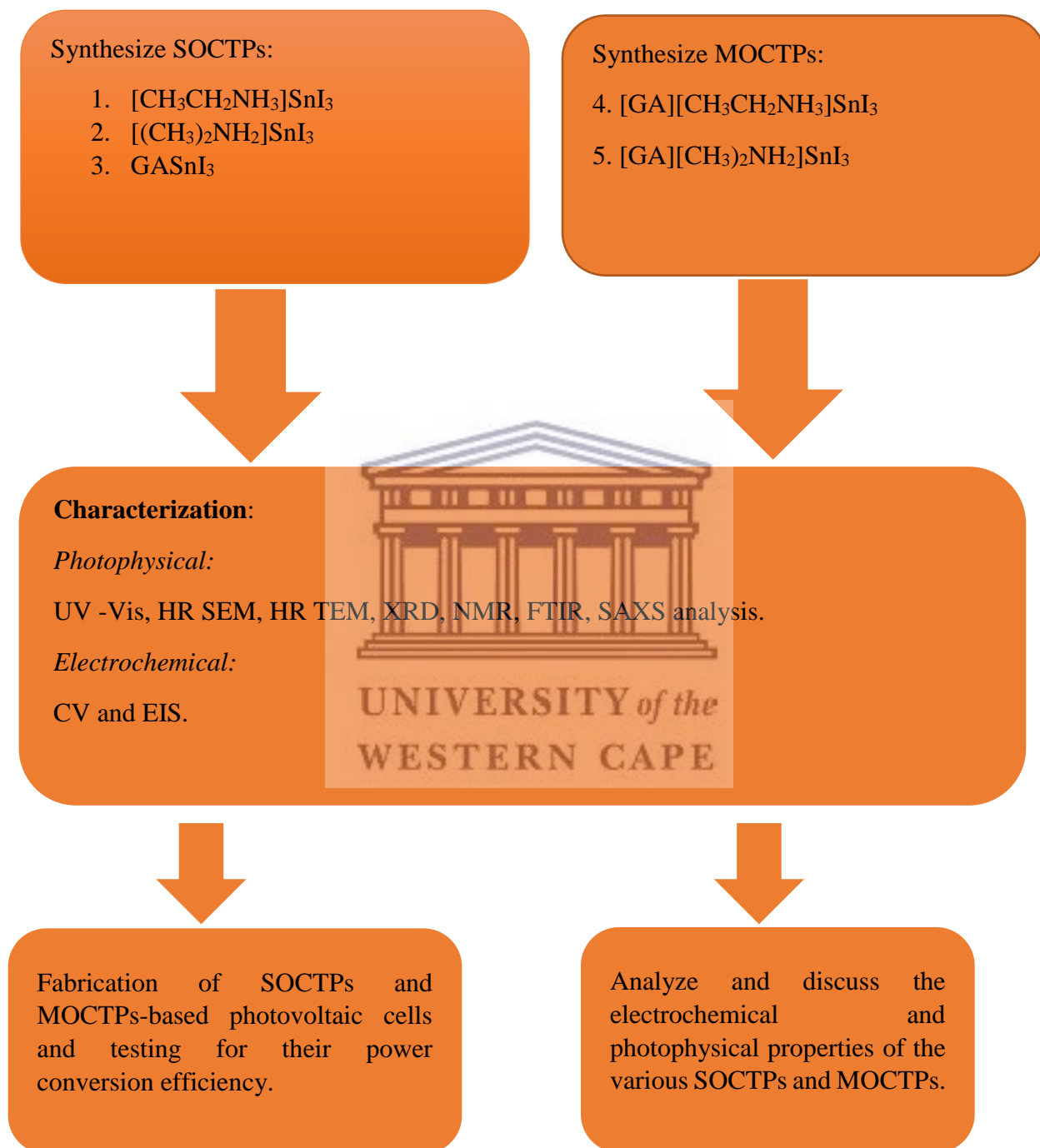
1. Synthesis of SOCTPs which include: ethylammonium tin iodide $[\text{CH}_3\text{CH}_2\text{NH}_3]\text{SnI}_3$, dimethylammonium tin iodide $[(\text{CH}_3)_2\text{NH}_2]\text{SnI}_3$ and guanidinium tin iodide (GASnI_3) perovskites, where GA is guanidinium.
2. Synthesis of MOCTPs, namely: guanidinium ethylammonium tin iodide $[\text{GA}][\text{CH}_3\text{CH}_2\text{NH}_3]\text{SnI}_3$ and guanidinium dimethylammonium tin iodide $[(\text{GA})(\text{CH}_3)_2\text{NH}_2]\text{SnI}_3$ perovskites.
3. Photophysical characterization of the various perovskites using HR SEM, HR TEM, SAXS, XRD, FTIR, NMR and UV-Vis.

4. Electrochemical characterization of the perovskites using CV and EIS.
5. Fabrication of photovoltaic cells: (a) photovoltaic cell devices based on GASnI_3 , $[(\text{CH}_3)_2\text{NH}_2]\text{SnI}_3$ and $[\text{CH}_3\text{CH}_2\text{NH}_3]\text{SnI}_3$ perovskites and (b) photovoltaic cell devices based on $[\text{GA}][(\text{CH}_3)_2\text{NH}_2]\text{SnI}_3$ and $[\text{GA}][\text{CH}_3\text{CH}_2\text{CH}_3]\text{SnI}_3$ perovskites.
6. Testing for power conversion efficiency of the photovoltaic cells.



UNIVERSITY *of the*
WESTERN CAPE

1.6 Research framework



1.7 Thesis layout

Chapter 1

This chapter introduces this research. Background information and classification of perovskites is given in this chapter. Perovskite thin-film technology is discussed here. The chapter also introduces the problem statement, aims and objectives as well as the research framework.

Chapter 2

Chapter 2 contains literature review as well as various characterization techniques and working principles. Literature review includes properties of perovskites, historical and technological advancements of perovskites, methods used to synthesize perovskites and information on photovoltaic cell devices.

Chapter 3

This chapter discusses experimental procedures adopted in this research. Chemical synthesis of perovskites, including chemicals used and experimental procedures are outlined in detail. Also included in this chapter are chemicals and procedures adopted to fabricate perovskite solar cells.

Chapter 4

Results and discussion. The results were discussed on various photophysical and electrochemical characterization techniques. Also discussed in this chapter is the power conversion efficiency of the fabricated perovskite solar cells.

Chapter 5

This chapter contains conclusions and recommendations.

1.8 References:

1. Tombe, S., Adam, G., Heilbrunner, H., Apaydin, D., Ulbricht, C., Sariciftci, N., Arendse, C., Iwuoha, E., Scharber, M. (2017). Optical and Electronic Properties of Mixed Halide (X=I, Cl, Br) Methylammonium Lead Perovskite Solar Cells. *Journal of Material Chemistry C*, 5, 1714-1723.
2. Barbir, F., Veziroglu, T., Plass, H. (1990). Environmental Damage Due to Fossil Fuels Use. *International Journal of Hydrogen Energy*, 15, 739-749.
3. Abas, N., Kalair, A., Khan, N. (2015). Review of Fossil Fuels and Future Energy Technologies. *Futures*, 69, 31-49.
4. Parida, B., Iniyar, S., Goic, R. (2011). A Review of Solar Photovoltaic Technologies. *Renewable and Sustainable Energy Reviews*, 15, 1625-1636.
5. Gratzel, M. (2007). Photovoltaic and Photoelectrochemical Conversion of Solar Energy. *Philosophical Transactions of the Royal Society A*, 365, 993-1005.
6. Pimentel, D., Herz, M., Glickstein, M., Zimmerman, M., Allen, R., Becker, K., Evans, J., Hussain, B., Sarsfeld, R., Grosfeld, A., Seidel, T. (2002). Renewable Energy: Current and Potential Issues. *American Institute of Biological Sciences*, 52, 1111-1120.
7. Razykov, T., Ferekides, C., Morel, D., Stefanakos, E., Ullal, H., Upadhyaya, H. (2011). Solar Photovoltaic Electricity: Current Status and Future Prospects. *Solar Energy*, 85, 1580-1608.

8. Gerischer, H. (1977). On the Stability of Semiconductor Electrons Against Photodecomposition. *Journal of Electroanalytical Chemistry and Interfacial Electrochemistry*, 82, 133-143.
9. Anaf, W., Schalm, O., Janssens, K., De Waal, K. (2011). Understanding the (In) Stability of Semiconductor Pigments by a Thermodynamic Approach. *Dyes and Pigments*, 113, 409-415.
10. Fthenakis, V., Kim, H. (2011). Life-cycle Analyses. *Solar Energy*, 85, 1609-1628.
11. Norton, B., Eames, P., Mallick, T., Huang, M., McCormack, S., Mondol, J., Yohanis, Y. (2011). Enhancing the Performance of Building Integrated Photovoltaics. *Solar Energy*, 85, 1629-1664.
12. Wang, D., Wright, M., Elumalai, N., Uddin, A. (2016). Stability of Perovskite Solar Cells. *Solar Energy Materials and Solar Cells*, 147, 255-275.
13. Borriello, I., Cantele, G., Ninno, D. (2008). Ab Initio Investigation of Hybrid Organic-Inorganic Perovskites Based on Tin Halides. *Physical Review B*, 77, article number 235214.
14. Chen, Y., He, M., Peng, J., Sun, Y., Liang, Z. (2016). Structure and Growth Control of Organic-inorganic Halide Perovskites for Optoelectronics: From Polycrystalline Films to Single Crystals. *Advanced Science*, 3, article number 1500392.
15. Moller, C. (1958). Crystal Structure and Photoconductivity of Caesium Plumbohalides. *Nature*, 182, 1436-1436.

16. Ma, J., Wang, L. (2017). The nature of Electron Mobility in Hybrid Perovskite $\text{CH}_3\text{NH}_3\text{PbI}_3$. *Nano Letters*, 17, 3646-3654.
17. Mitzi, D., Chondroudis, K., Kagan, C. (1999). Design, Structure and Optical Properties of Organic-inorganic Perovskites Containing an Oligothiophene Chromophore. *Inorganic Chemistry*, 38, 6246-6256.
18. Bi, Z., Liang, Z., Xu, X., Chai, Xu, D., Li, J., Li, M., Xu, G. (2017). Fast Preparation of Uniform Large Grain Size Perovskite Thin Film in Air Condition Via Spray Method for Highly Efficient Planar Solar Cells. *Solar Energy Materials & Solar Cells*, 162, 13-20.
19. Grätzel, M. (2014). The Light and Shade of Perovskite Solar Cells. *Nature Materials*, 13, 838-842.
20. Eames, C., Frost, J., Barnes, P., O'Regan, B., Walsh, A., Islam, M. (2015). Ionic Transport in Hybrid Lead Iodide Perovskite Solar Cells. *Nature Communications*, 6, article number 7497.
21. Ishihara, T. (1994). Optical Properties of Pbl-based Perovskite Structures. *Journal of Luminescence*, 60, 269-274.
22. Bretschneider, S., Weickert, J., Dorman, J., Schmidt-Mende, L. (2014). Physical and Electrical Characteristics of Lead for Solar Cell Applications. *Applied Physics Letters*, 2, article number 040701.
23. Stoumpos, C., Malliakas, C., Kanatzidis, M. (2013). Semiconducting Tin and Lead Iodide Perovskites with Organic Cations: Phase Transitions, High Mobilities, and Near-Infrared Photoluminescent Properties. *Inorganic Chemistry*, 52, 9019-9038.

24. Evans, H., Lehner, A., Labram, J., Fabini, D., Barreda, O., Smock, S., Wu, G., Chabinye, M., Seshadri, R., Wudl, F. (2016). (TTF) Pb₂I₅: A Radical Cation-Stabilized Hybrid Lead Iodide with Synergistic Optoelectronic Signatures. *Chemistry of Materials*, 28, 3607-3611.
25. Maughan, A., Kurzma, J., Neilson, J. (2015). Hybrid Inorganic-organic Materials with an Opto-electronically Active Aromatic Cation: (C₇H₇)₂SnI₆ and C₇H₇PbI₃. *Inorganic Chemistry*, 54, 370-378.
26. Travis, W., Knapp, C., Savory, C., Ganose, A., Kafourou, P., Song, X., Sharif, Z., Cockroft, J., Scanlon, D., Bronstein, H., Palgrave, R. (2016). Hybrid Organic-inorganic Coordination Complexes as Tunable Optical Response Materials. *Inorganic Chemistry*, 55, 3393-3400.
27. Gao, P., Grätzel, M., Nazeeruddin, M. (2014). Organohalide Lead Perovskites for Photovoltaic Applications. *Energy and Environmental Science*, 7, 2448-2463
28. Mitzi, D., Wang, S., Feild, C., Chess, C., Guloy, A. (1995). Conducting Layered Organic-inorganic Halides Containing (110) Oriented Perovskite Sheets. *Science*, 267, 1473-1476.
29. Lia, Y., Liu, H., Yang, D., Shang, Y., Shi, Z., Li, B., Jiang, X., Zhang, L., Quan, L., Quintero-Bermudez, R., Sutherland, B., Mi, Q., Sargent, E., Ning, Z. (2017). Highly Oriented Low-dimensional Tin Halide Perovskites with Enhanced Stability and Photovoltaic Performance. *Journal of American Chemical Society*, 139, 6693-6699.
30. Hsu, H., Ji, L., Zhao, H., Yu, E., Bard, A. (2015). A Liquid Junction Photoelectrochemical Solar Cell Based on p-Type MeNH₃PbI₃ Perovskite with 1.05 V Open-circuit Photovoltage. *Journal of the American Chemical Society*, 137, 14758-1464.

31. Mitzi, D. (2001). Templating and Structural Engineering in Organic-inorganic Perovskites. *Journal of the Chemical Society, Dalton Transactions*, 0, 1-12.
32. Mitzi, D., Chondroudis, K., Kagan, C. (2001). Organic-inorganic Electronics. *IBM Journal of Research and Development*, 45, 29-45.
33. Kojima, A., Teshima, K., Shirai, Y., Miyasaka, T. (2009). Organo-metal Halide Perovskites as Visible-light Sensitizers for Photovoltaic Cells. *Journal of the American Chemistry Society*, 131, 6050-6051.
34. Qin, P., Tanaka, S., Ito, S., Tetrault, N., Manabe, K., Nishino, H., Nazeeruddin, M., Gratzel, M. (2014). Inorganic Hole Conductor-based Lead Halide Perovskite Solar Cells with 12.4% Conversion Efficiency. *Nature Communications*, 5, article number 3834.
35. Najjar, Y. (2011). Gaseous Pollutants Formation and their Harmful Effects on Health and Environment. *Innovative Energy Policies*, 1, 1-9.
36. Zhang, J., Mauzerall, T., Liang, S., Ezzati, M., Remains, J. (2010). Environmental Health in China: Progress Towards Clean Air and Safe Water. *The Lancet*, 375, 1110-1119.
37. Bernal, C., Yang, K. (2014). First Principles Hybrid Functional Study of the Organic-inorganic Perovskites $\text{CH}_3\text{NH}_3\text{SnBr}_3$ and $\text{CH}_3\text{NH}_3\text{SnI}_3$. *Journal of Physical Chemistry*, 118, 24383-24383.
38. Shockley, W., Queisser, J. (1961). Detailed Balance Limit of Efficiency of p-n Junction Solar Cells. *Journal of Applied Physics*, 32, 510-519.

CHAPTER 2

LITERATURE REVIEW

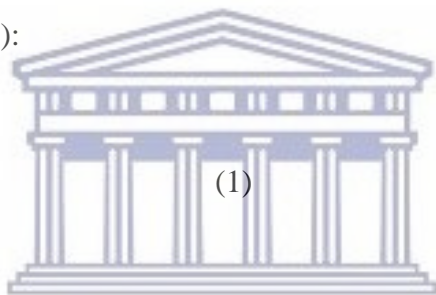
2.1 Properties of perovskites

The term “Perovskites” refers to a family of crystalline, chemical compounds that have their structure derived from (CaTiO_3) . These crystalline compounds are typically cubic in appearance. The characteristic chemical formula of a perovskites’ family is ABO_3 . The atoms of these materials are generally positioned so that twelve coordinated A atoms occupy the cube’s corners, octahedral O or X ions occupy the faces of the cubic structure, and tetrahedral B ions occupy the center of the crystal structure. Although perovskites are typically cubic, however they are not rigid but allow for changes that can occur in their structure. Their symmetry is technically orthorhombic since the structure is flexible to a slight distortion, making unit cells to be double the size of the cubic cell.

A typical example of such distortion amongst perovskites is observed in titanium cation of barium titanate (BaTiO_3), which may be prompted to move to an off-center position [1]. Compositions of orthorhombic perovskites conform to the basic Pbnm structure. Static atomic simulations were used on $\text{LaBaCo}_2\text{O}_{5.5}$ double perovskites to investigate orthorhombic intrinsic defects, based on the Born model [2]. $\text{LaBaCo}_2\text{O}_{5.5}$ orthorhombic perovskite exhibits $a_p \times 2a_p \times 2a_p$ supercell with Pmmm space group, in contrast the tetragonal structure exhibits $a_p \times a_p \times 2a_p$ with P4/mmm symmetry [2]. The results gave evidence that Ln/ Ba antisite disorder serves as the lowest energy

disorder reaction, where smaller antisite energies are given by the large Ln cations. This observation suggested that antisite energy in addition to Frenkel energy influences transport of oxygen vacancies. An electrostatic dipole results in which the positive and negative charges are made to align toward opposite directions in the structure, this change in symmetry distorts the cubic shape of the perovskite lattice. Generation of this dipole is a desirable feature in which it accounts for the ferroelectric attributes observed from barium titanate. Such compounds brought light in the expertise of energy since they are suitable for use in capacitors, which are electric components that temporarily store energy. Stability of the perovskite phases is largely controlled through consideration of geometric properties that are best represented by the Goldschmidt tolerance factor, t in equation (1):

$$t = (r_A + r_O) / \sqrt{2} (r_O + r_B)$$



(1)

where r_A , r_B , and r_O are the respective radii of A, B, and oxygen/ halogen ions. The Goldschmidt tolerance factor is engineered to fall between 0.75 and 1.00, to achieve perfect perovskite structure [3]. However, several perovskites that have tolerance factors falling outside this range have been reported [3]. All perovskites synthesized in this research have tolerance factors slightly above unity. Ionic radii for tin, guanidine, ethylammonium, dimethylammonium and iodine are 115 pm, 278 pm, 274 pm, 272 pm and 220 pm respectively. GASnI_3 has calculated theoretical tolerance factor of 1.05 while $[\text{CH}_3\text{CH}_2\text{NH}_3]\text{SnI}_3$ and $[(\text{CH}_3)_2\text{NH}_2]\text{SnI}_3$ both have tolerance factor of 1.04. $[\text{GA}][(\text{CH}_3\text{CH}_2\text{NH}_3)\text{SnI}_3$ and $[\text{GA}][(\text{CH}_3)_2\text{NH}_2]\text{SnI}_3$ mixed-organic-cation tin halides technically both have alternations of crystals with tolerance factors 1.05 and 1.04 within the same material.

Physical properties:

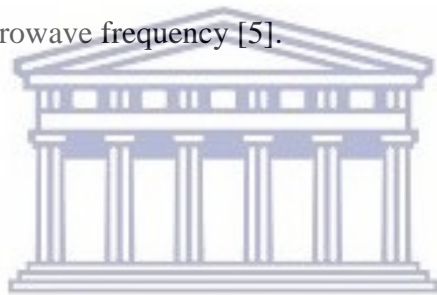
Perovskites are known to display various exciting physical properties such as ferroelectric, dielectric, pyroelectric, and piezoelectricity.

(i) Ferroelectricity

This phenomenon refers to the ability of certain materials to exhibit some spontaneous electric polarization. In this phenomenon, the positive and negative electric charges segregate, resulting in one side of the material positive and the other side negative. Electric polarization can be reversed in direction when an appropriate electric field is applied. Ferroelectricity is closely related to ferromagnetism, which is a phenomenon that occurs in materials such as iron. The most significant among the ferroelectrics are oxides with a perovskite structure [4]. The most common classical examples of ferroelectric perovskites are; BaTiO_3 and PbTiO_3 . The findings of Cohen [4] revealed that the ferroelectric phase of PbTiO_3 demonstrates a hybridization of the oxygen and lead states, which leads to a large strain that makes stable the perovskite tetragonal phase. On the other hand, the interaction between barium and oxygen atoms in BaTiO_3 is completely ionic, which favors formation of a rhombohedral structure [4].

(ii) Di-electricity

A Dielectric is an electrical insulator that gets polarized when aligned to an electric field. Electric charges shift slightly from their normal equilibrium positions resulting in a dielectric polarization, when an electric field is applied on a dielectric. Dielectric polarization causes positive charges in the crystal lattice to be positioned towards the direction of the field while the negative charges are forced to shift in the direction opposite to that of the positive charges. This phenomenon is useful since an internal electric field is created resulting in a reduced overall field in the entire dielectric. Examples of dielectric perovskites are the complex perovskite dielectric ceramics which are best for microwave frequency [5].



UNIVERSITY of the
WESTERN CAPE

(iii) Pyroelectricity

Pyroelectricity refers to the ability exhibited by certain materials to create an electrical potential when they are subjected to heat or cold. This change in temperature causes positive and negative charges in the material to migrate to opposite ends i.e. the material gets to be polarized causing an electrical potential to be established. The family of perovskites has predominant pyroelectric materials. Since perovskite solar cells are exposed to constant heating and cooling, it therefore means they will constantly generate an electrical potential in this process.

(iii) Piezoelectric

Piezoelectric is a feature exhibited by some materials to generate an electric charge when they are subjected to tensile stress. When piezoelectric material is exposed to conditions of tensile stress, the positive and negative charge centers within the material, which results in an external electrical field. When this shifting of negative and positive charges in the material is reversed, an outer electrical field stretches the material or either compresses the material. The piezoelectric effect is made useful in applications such as the sound production and detection, microbalances, generation of high voltages, ultra-fine focusing of light assemblies and generation of electronic frequency.



Optical properties:

Perovskites such as tin halide-based perovskites exhibit electronic properties, where they have high charge mobility and low charge trap density and spectral tunability. Such materials have a major flexibility making possible for the optical and electrochemical band gap to be finely tuned. In optoelectronic applications, fine tuning of these band gaps, enables engineering of the wavelengths of both emitted and absorbed light. For example, the bandgap of lead halide perovskites is tunable over wavelength range from ultraviolet to the near-infrared [6]. These optical properties of perovskites enable them to harvest light energy over wider wavelength ranges making them favorable for solar cell applications, they possibly are the future replacement to the current silicon technology which is infra-red transparent. Mo *et al.* [7] made use of the optical properties of perovskites and synthesized a series of perovskite materials represented as

$\text{Sn(phen)X}_m\text{Y}_n$. The materials made use of 1,10-phenanthroline as the organic component, Cl, Br, I halogens were used at varying concentrations as either X/Y and $m + n$ was designed to give the value of 4. The intention of the design of these perovskites was to investigate the behavior of main group metal halides when used as photosensitive dyes. It was found that the colors of the compounds are tunable as the mole ratio of the halides is made to change due to the mechanism involving ligand to ligand charge transfer (LLCT) [7]. This tunability is illustrated in figure 2.1 below.

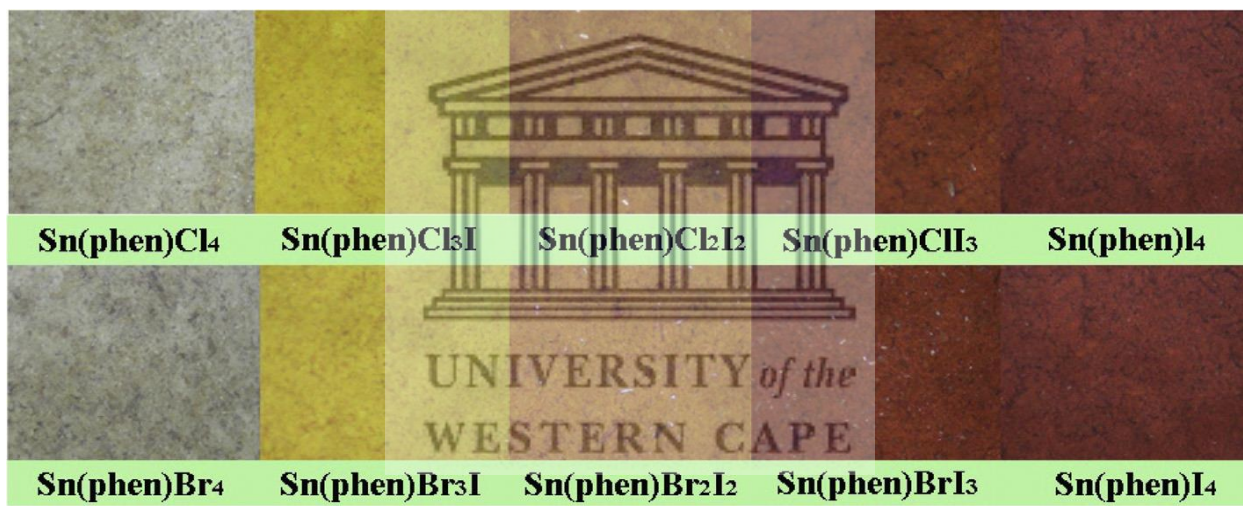


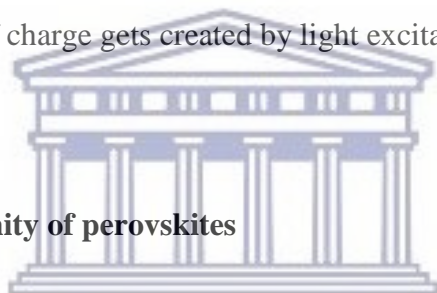
Figure 2.1: Colors of powder samples of $\text{Sn(phen)Cl}_m\text{I}_n$ and $\text{Sn(phen)Br}_m\text{I}_n$ series [7].

Electrical properties:

Perovskites exhibit electric properties which make them desirable for application in optoelectronics. Characteristic information of material's electrochemical properties, such as

charge diffusion lengths and ease of carrier mobilities is of paramount importance in the fabrication of optoelectronic devices. The electrical mobility, μ , refers to the ease of a charge carrier, which is either electrons (μ_e), or holes (μ_h) to move within a semiconductor when an electric field is applied. Electrical mobility is greatly considered for applications such as photodetectors and field effect transistors (FETs) [8]. This property is desirable since it causes a fast response time due to a drift in the electrical transport mechanism. The diffusion length is also an important parameter in charge transport. Diffusion length is used to describe the motion of electrons and holes by diffusion from areas with high carrier concentration regions in the semiconductor to areas with lower concentration. The diffusion lengths are major performance factors in the fabrication of optoelectronics where excess of charge gets created by light excitation.

2.2 Morphology and crystallinity of perovskites



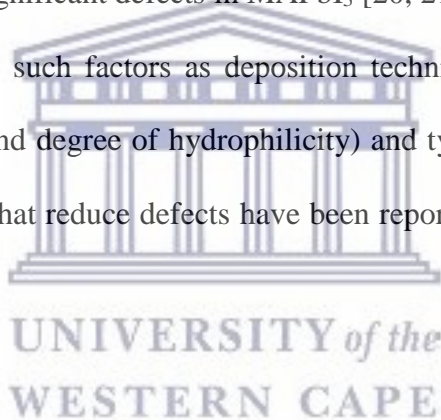
UNIVERSITY of the

WESTERN CAPE

Increase in PCE of inorganic-organic hybrid perovskite solar cells from 3.9% in 2008 to current certification record of more than 22% recently, has been largely due to constant improvement on the morphology and crystallinity of the materials [9-11]. The focus in fabrication of planar solar cells is on ensuring high quality films with controlled morphology and minimum pinholes in the film for high device performance. Good crystallinity of perovskite film is very important as this has an impact on factors such as charge dissociation efficiency, charge transport and diffusion length which play a vital role in improving PCE [12, 13]. Morphology of perovskite films is controlled by crystal defects [14, 15]. Increase in grain size of the films causes decrease in grain boundary and defects [16]. Consequently, the diffusion distance between hole and electron is

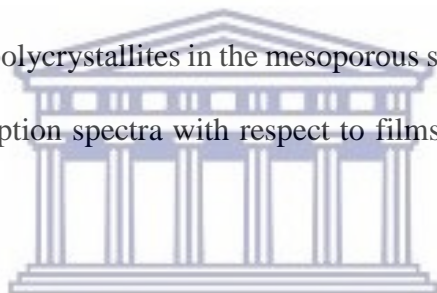
widened, while exciton diffusion rate is faster and composite resistance is larger [17]. Crystal defects form centers for non-radiation recombination and carrier trapping which in turn causes decrease in open circuit voltage (V_{oc}), short circuit current (J_{sc}) and fill factor (FF) of the solar cells [18]. Furthermore, defects cause significant hysteresis in photocurrent density-voltage (J-V) curves due to delayed charge injection and retarded photocurrent response [19].

Synthesis methods should aim at reducing number of defects. For example, excess methylammonium iodide (MAI) or PbI_2 and decomposition of MAI during annealing synthesis step will lead to formation of significant defects in $MAPbI_3$ [20, 21]. The crystallization behavior of perovskites is dependent on such factors as deposition technique, composition and surface factors (e.g. surface structure and degree of hydrophilicity) and type of solvents/ additives used [22]. Some synthesis methods that reduce defects have been reported, which include doping and solvent engineering [23-25].



HI additive is used to add I⁻ ions that will increase content of PbI_6^{4-} in $MAPbI_3$ perovskite [26], in which a smooth perovskite film is achieved through one-step deposition [27, 28]. When iodine is chosen as X-site halogen in perovskite structure, formation of polyiodides is usually a problem, which is well explained by coordination Chemistry [29, 30]. When I⁻ ions are in solution, they displace coordinated N,N-dimethylformamide (DMF) molecules to form metal iodide complexes e.g. PbI_3^- , PbI_4^{2-} , Pb_5^{3-} and PbI_6^{4-} [31]. Amongst these complexes, PbI_6^{4-} is the only fully coordinated and free octahedral complex, the lower coordination levels usually form crystal defects [32].

On the other hand, crystallinity problems are rarely an issue with mesoscopic solar cells since mesopores (TiO₂, NiO or Al₂O₃) provide physical constraint on crystal dimensions [33]. More extensive heterogeneous nucleation is promoted in mesoscopic cells which leads to smaller crystallites. Here good film quality with reasonably thick film necessary for excellent efficiency is achieved. It is often necessary to include an overlayer of the perovskite for good device performance in mesoscopic cells [34]. The crystals of the perovskite within the overlayer have larger grain size of ranges 100-1000 nm, which is necessary for enhanced charge transport and hence improved device performance. The polycrystalline films exhibit distinct absorption spectra whereby the spectra of smaller polycrystallites in the mesoporous scaffold show much broader and hypsochromically shifted absorption spectra with respect to films deposited on non-mesoporous substrates [35, 36].

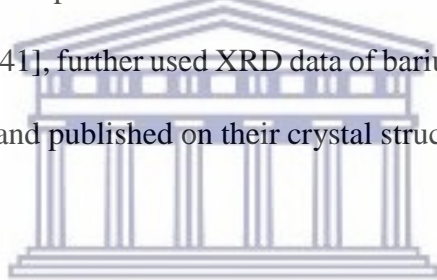


UNIVERSITY of the
WESTERN CAPE

Highly efficient devices fabricated from organic-inorganic halide perovskites have been observed with polycrystalline films that had various grain sizes, which suggests long charge-carrier diffusion lengths and harmless grain boundaries [37, 38]. This was substantially shown by Oga *et al.*, in which the minimum mobilities in CH₃NH₃PbI₃ films with various crystallite sizes (70-420 nm) had range between 10 and 20 cm² V⁻¹ s⁻¹ [39]. In addition to controlling crystallite size, crystallite quality should also be enhanced. This includes the presence of defects on the surface or within the perovskite crystals, and crystal orientation in which the crystals align in a certain direction for better charge transport.

2.3 Historical and technological advancement of perovskites

Perovskites were known as early as the nineteenth century. This was after the discovery of the perovskite mineral in the Urals which was first reported in 1839 by a well-known geophysicist (Gustav Rose) who named the mineral after Count Lev Aleksevich Von Perovski, a mineralogist [40]. The mineral exhibits a crystalline structure which was adopted to be characteristic to all chemical compounds under the family of perovskites. It took almost a century for the structure of perovskites to be described since the discovery of this ceramic. Goldschmidt, in 1926 [3] became the first to report on the structure of perovskites where he was focusing on the tolerance factors of perovskites. Megawin, in 1926 [41], further used XRD data of barium titanate (BaTiO_3) perovskite material to explore perovskites and published on their crystal structure.



Further work done on barium titanate revealed that the cubic crystalline lattice of this material may be altered. The Ti species in barium titanate (BaTiO_3) perovskite can be prompted to shift to a new position that is off-center. These changes introduce an orthorhombic symmetry, different from the symmetry of cubes, which is a result of the negative and positive charges aligning in opposite directions in the perovskite lattice, creating an electrostatic dipole [42]. The ferroelectric properties of barium titanate were found to be contributed by this electrostatic dipole, which makes it a favorable phenomenon. This perovskite compound as well as other familiar perovskites, were found that they could achieve impressive dielectric constants (ratio of the amount of stored electrical energy when a potential is applied, relative to the permittivity of a vacuum). Such compounds brought light in the expertise of energy and technology. They could be used to

temporarily store energy in electric components called capacitors and supercapacitors. More research on perovskites ensued, more specifically focusing on organic-inorganic halide perovskites.

Weber, in 1978 reported on the structure and physical properties of methylammonium lead halide $\text{CH}_3\text{NH}_3\text{PbX}_3$ (X represents Cl, Br, I) perovskites [43, 44], which attracted more research interests on the field of perovskites. Weber reported the $\text{CH}_3\text{NH}_3\text{PbX}_3$ to exhibit a cubic perovskite structure which has unit cell values of $a = 5,68 \text{ \AA}$ when chlorine was used in the site of halogen, $a = 5,92 \text{ \AA}$ when the site of halogen was occupied by bromine and $a = 6,27 \text{ \AA}$ when iodine occupied the halogen site [44]. The unit cell increased as the size of the halogen atom was increased. The compounds were reported to show intense color, however there was no significant conductivity under normal “p-resonance-bonding”. $\text{CH}_3\text{NH}_3\text{PbCl}_3$ perovskite is an option to the conclusions they got. Weber’s work had been motivated by the research that was done by Wells and collaborators in 1893 [45]. This group were the first to report on halide-based perovskites. Their investigations were done on (CsPbX_3) where X = Cl, Br or I, and Cs_4PbX_6 where X = Cl or Br. Wells found that CsPbCl_3 and CsPbBr_3 have the perovskite structure ABX_3 , and they are also tetragonally or mono-clinically distorted structure at room temperature [45]. Structural and optoelectronic characterization showed that both CsPbCl_3 and CsPbBr_3 are photoluminescence active. Moreover, composition of these compounds is strongly dependent on temperature and demonstrated a self-trapping behavior [46, 47].

Lead halide perovskites then became the object of focus in the field of perovskites, such that more interesting advancements were reported, and they became a promising candidate as an absorbing material in photovoltaic cells. Kojima *et al.* [48] studied two methylammonium-lead halide perovskite nano-materials, which are $\text{CH}_3\text{NH}_3\text{PbBr}_3$ and $\text{CH}_3\text{NH}_3\text{PbI}_3$. These perovskites were found to efficiently modify TiO_2 , by sensitizing it for converting visible-light when applied in photoelectrochemical cells [48]. The group assembled the nanocrystalline perovskites on TiO_2 films and found that the perovskite materials exhibit good band-gap absorptions relative to semiconductors. In addition, the $\text{CH}_3\text{NH}_3\text{PbI}_3$ -based photocell they fabricated recorded 3.8% PCE.

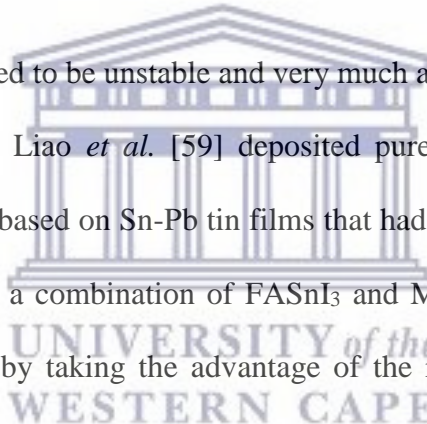
Kulkarni *et al.* [49] demonstrated tuning of energy band-gap of mixed-anion methylammonium lead halide perovskites. They varied concentration of iodine to bromine in the perovskite structure to obtain series of mixed halogen lead-based perovskites. The group successfully synthesized $\text{MAPb}(\text{I}_{1-x}\text{Br}_x)_2$ where the value of x was engineered to be between 0 and 1, by making use of sequential deposition synthesis method. They established that the optical properties of perovskite hybrids can be readily changed by altering or mixing the halogen precursor's concentration. They observed that the band gap of perovskites is largely influenced by the concentrations of precursor solutions and the conversion time of the precursor solutions. The absorption band edge shifted to longer wavelengths as the iodine concentration was increased in the perovskite film. Perovskite films with iodide to bromine ratio of greater than 0.7 were observed to adopt nanorod like morphological features.

Recent studies on mixed-halide hybrid perovskites have provided more insight into the effect of mixing halides in the crystal structure [50, 51]. Critical studies on the photo-induced halide segregation in mixed halide perovskites has contributed significantly in understanding these materials, which has brought great potential in the production of wide-band-gap light absorber materials for tandem solar cells [52, 53]. These materials display abilities of significantly high efficiency [54] and scalability [55] while production and running costs are kept low [56].

Tidhar *et al.* [57] investigated parameters that are significant for crystallization of $\text{CH}_3\text{NH}_3\text{PbI}_3$ and $\text{CH}_3\text{NH}_3\text{PbBr}_3$ perovskites when they are applied in solar cells. The investigation revealed that when PbCl_2 was added to the perovskite precursor solutions, the end-product is affected. The explanation to this comes from the presence of PbCl_2 nanocrystals during the fabrication process, which become heterogeneous nucleation sites when perovskite crystals form from the solution. This conclusion was drawn from SEM and cryo-TEM studies, which focused on synthesis of single perovskite crystals as well as the frozen perovskite precursor respectively. Also included in this study, was the effect of different temperatures and substrates on the process of perovskite nucleation. The power conversion efficiency of lead bromide perovskites was improved, resulting in 5.4% efficiency while open current voltage (V_{oc}) recorded 1.24 V [57].

Since lead is a toxic metal, Perovskite research started to move towards finding an alternative metal to lead. Borriello *et al.* [58] were the first researchers to investigate the photovoltaic properties of tin halide perovskites. They became the first to propose that tin halide perovskite could be used as photovoltaic. Calculations based on first-principles were performed on ASnX_3

perovskite crystals where A represents cesium, methylammonium and formamidinium cations and X represents chlorine and iodine. These calculations probed the perovskites' structural and electronic properties with different structural phases. The group reported that the structure of the inorganic cations plays a significant role in describing electronic properties of tin-halide perovskite. They showed that the stability against the distortion of the perovskite's cage strongly depends on the embedded A-site cation. The electronic properties of tin halide perovskites exhibit a band gap, that is tunable through a suitable choice of organic molecule with suitable ionic radius, as was established from their research on these materials.



Tin based materials were reported to be unstable and very much air sensitive which is an attribute associated with the use of tin. Liao *et al.* [59] deposited pure mixed tin-lead thin-films and fabricated photovoltaic cells of based on Sn-Pb tin films that had sufficiently low bandgap. For a change, the new precursor was a combination of FASnI_3 and MAPbI_3 precursors, as means to produce non-toxic perovskites by taking the advantage of the reported success on fabricating efficient Pb-free Sn photovoltaic solar cells and Pb-based photovoltaic cells. The molar ratio of the precursors of MAPbI_3 to FASnI_3 was carefully controlled through the molar ratio. The best-performing solar cell was fabricated from molar ratio 3:2 of formamidinium tin iodide precursor to methylammonium lead iodide precursor. This light absorber gave the lowest bandgap of approximately 1.2 eV [59].

To stabilize the air sensitive tin, Nagane *et al.* [60], fabricated and characterized non-toxic perovskites based on tin and germanium precursors, $\text{CH}_3\text{NH}_3\text{Sn}_{(1-x)}\text{Ge}_x\text{I}_3$ where x was restricted

to between 0 and 1. These compounds were found to possess band gaps that range from 1.3 to 2.0 eV, which makes them suitable contenders for optoelectronic applications, which include single junction solar cell devices and light-emitting diodes. They found that the thermodynamic stability and electronic properties of these materials calculated for all compositions and agree well with previously done experiments. These findings confirmed the possibility of a family of non-toxic perovskite semiconductors with suitable band-gaps for use in single-junction solar cells [60].

Chung *et al.* [61] became the first to dope CsSnI₃ with SnF₂ and used in dye photovoltaic cells as the hole transport material (HTM). The idea was further developed by adding the SnF₂ into the CsSnI₃ precursor solution in dimethyl sulfoxide (DMSO). The optimum concentration of SnF₂ was found to be 20% to form a good mixture with CsSnI₃ and produce a film with complete coverage on mesoporous TiO₂ (m-TiO₂). It is of significance to note that SnF₂ does not get integrated into the lattice to distort the local environment. XRD patterns indicated that the addition of SnF₂ eliminated the emergence of yellow non-perovskite multiform of CsSnI₃. The major role played by SnF₂ is to reduce the high carrier density of CsSnI₃, with holes, as the majority carriers [62]. However, some severe charge losses still take place when tin fluoride is used probably through monomolecular recombination with trapped charge due to high background carrier density.

Formamidinium (FA) became a common candidate at A site cation in organic-inorganic perovskites for solar cell application. Eperon *et al.* [63] conducted a research on formamidinium based perovskites. From this research, it was established that formamidinium based perovskites have an improved stability in air which makes them more favorable for solar cell application over

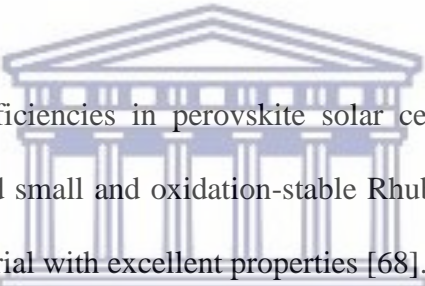
methylammonium based perovskites. Koh *et al.* [64] further demonstrated FASnI_3 perovskite solar cell with low bandgap of 1.41 eV and achieved a maximum photocurrent density of approximately 30 mA/cm^2 . The group indicated a PCE of 2.10% upon including SnF_2 in the synthetic steps of these tin halide perovskites.

Zhao *et al.* [65] synthesized mixed-organic-cation perovskites that are tin-based and subsequently characterized them. In their work, formamidinium and methylammonium organic cations were used at various molar ratios to formulate $(\text{FA})_x(\text{MA})_{1-x}\text{SnI}_3$ where FA represents formamidinium cation and MA represents methylammonium cation. The perovskites were investigated for use as perovskite solar cells (PSCs) that are lead-free. By optimizing the ratio of Formamidinium (FA) and Methylammonium (MA) cations, a maximum PCE of 8.12% was attained from solar cell device fabricated from 3:1 formamidinium to methylammonium cations mole ratio, which also recorded an impressive V_{oc} of 0.61 V, attributed to improved morphology of the perovskite film which helps inhibit the process of recombination in the solar device. The combination of these cations seems to be a better approach for efficiency enhancing of tin-based photovoltaic cells, since this approach produced a better efficiency than when single cations were used [65].

Yi *et al.* recently reported on optimal ratios of formamidinium (FA) and Cesium (Cs) ions as A-site cations while X-halogen site was also varied that led to a very good PCE in the fabricated solar cells [66]. The perovskite composed of $\text{Cs}_{0.2}\text{FA}_{0.8}\text{PbI}_{2.84}\text{Br}_{0.16}$ in which the fabricated hybrid perovskite solar cells were reported to yield average of over 17% PCE with negligible hysteresis and very good stability in ambient air. Stabilization of this perovskite was attributed to mixing of

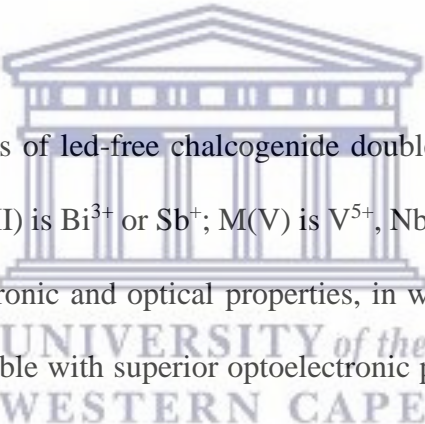
A-site cations, which stems from entropic gains and small internal energy input needed for formation of their solution in solid phase.

Lead perovskites that incorporate mixed cations and mixed halides have consistently improved the efficiency of perovskite solar cells, reaching efficiency of close to 30% in multijunction devices when used together with silicon cells at no surcharge [66, 67]. These perovskites were found to demonstrate efficient color tunability, which opened new avenues for high purity perovskite emitters in many applications including generation of light.



The approach of improving efficiencies in perovskite solar cells through mixing of cations motivated Saliba *et al.* to embed small and oxidation-stable Rb⁺ cation into cation cascade to form perovskite material with excellent properties [68]. This material has composition of rubidium, cesium, methylammonium and formamidinium cations respectively, RbCsMAFA. This novel perovskite achieved stabilized average efficiency of 20.2 % as well as an electroluminescence of 3.8% when device architecture of structure: glass/ fluorine-doped tin oxide/compact TiO₂/mesoporous TiO₂/perovskite/spiro-OMeTAD/Au was used [69]. For example, Cs/FA mixture suppresses halide segregation, which consequently favors band gaps for perovskite tandems [70, 71]. Moreover, open-circuit voltage of 1.24 V at a band gap of 1.63 eV was achieved that leads to a loss in potential of 0.39 volts, which shows better performance when compared to 0.4 V loss in potential exhibited by commercial silicon cells [68]. Cs/MA/FA-based photovoltaic cells are more thermally stable and more reproducible with respect to mixtures of MA/FA [72-74].

Billstrand *et al.* recently reported on a new solution-based method of synthesis of perovskites. This method produced colloidal Cs₄PbBr₆ perovskite particles that are stable in atmosphere, exhibit high luminescence properties and have high efficiency [75]. Zhang *et al.* introduced the use of ZnO materials as an alternative to TiO₂ electron transporting material. It was reported that ZnO share similar physical properties with TiO₂, but with much higher electron mobility, which makes it better electron transport material relative to commonly used TiO₂ [76]. Mahmood *et al.* further reported on a viable electrospinning route for the development of highly porous Indium-doped ZnO nanofibers as ETM in perovskite solar cells. This research produced highly efficient and hysteresis-free solar cells, which recorded 17.18% PCE [77].



Qingde *et al.* reported on a class of lead-free chalcogenide double perovskites A₂M(III)M(V)X₆ where A is Ca²⁺, Sr²⁺, Ba²⁺; M(III) is Bi³⁺ or Sb³⁺; M(V) is V⁵⁺, Nb⁵⁺, Ta⁵⁺; X is S²⁻, Se²⁻ [78]. The study focused on stability, electronic and optical properties, in which nine double chalcogenide perovskites were found to be stable with superior optoelectronic properties i.e. quasi-direct band gaps and balanced electron and hole effective masses. This is due to strong antibonding character at conduction band minimum and valence band maximum. However, these compounds were found to be thermodynamically unstable, indicating difficulty of formation of thin film phase [78].

Kim *et al.* synthesized polymer-stabilized CsPbBr₃ perovskite nanoparticles using ammonium bromide-functionalized polymers, which worked as both bromide precursors and stabilizing ligands [79]. This research found that the polymer-passivated perovskite nanoparticles have better

performance relative to conventional perovskite nanoparticles owing to enhanced optoelectronic stability as a result of their facile dispersion in polymer matrices [79].

Opaque paper with smooth surface has been developed and used as a conducting substrate for preparation of perovskite solar cells [80-84]. Gao *et al.* fabricated PSCs on Nanocellulose paper (NCP), which recorded PCE of 4.25%, V_{oc} of 0.69 V, J_{sc} of 17.46 mA cm⁻², and FF of 34.65% with no hysteresis [85]. NCP exhibits excellent features for optoelectronic devices such as mechanical strength, chemical and thermal stability [85]. Further work still needs to be done to improve performance of this wonderful invention.



Perovskites have already found their practical applications. In addition to capacitors, some perovskites have already been applied in piezoelectric devices, which are electrical components that produce a voltage when mechanical pressure is applied on them; conversely, when a magnetic field is applied on them, they change in dimension [86]. Piezoelectric perovskite ceramics have a wide application in optoelectronic products, which include devices for communication, timing devices that are crystal-controlled, pressure gauges, transducers, accelerometers and buzzers. Interestingly, environmental scientists are investigating the use of perovskites as materials that can encapsulate radioactive waste compounds safely.

2.4 Methods adopted in the synthesis of perovskites

The main methods that are used to synthesize perovskites are; solid state methods [87], gaseous phase preparations [88] and wet chemical methods (solution preparation) [89]. The adopted method to synthesize perovskites in this research is the sol-gel method which is a wet chemical method [90, 91]. Wet chemical methods have advantages over the other methods, which include lower temperature compared to the solid-state reactions, better homogeneity, greater flexibility in forming thin-films, improved reactivity and new compositions and better control of stoichiometry, particle size and purity.

Sol-gel method



UNIVERSITY of the
WESTERN CAPE

Sol-gel method of synthesis is a very common wet chemical technique employed in the fabrication of ceramic and glassy materials. The sol-gel is a process whereby nanoscale particles are made to settle from a colloidal suspension; resulting in ceramic or glassy materials. In this method, the solution (sol) gradually forms a network of both liquid and solid phase, which is followed by incomplete evaporation of the solvent, which could be through introduction of an initiator, resulting in the formation of the semi-solid, which is subsequently heated at elevated temperatures to yield the final product (solid) [92-94]. This is a cheap method that allows the fine control of the parameters of the product including size, composition and shape. Figure 2.2 shows a schematic diagram for process of sol-gel formation used to synthesize ceramic perovskite materials.

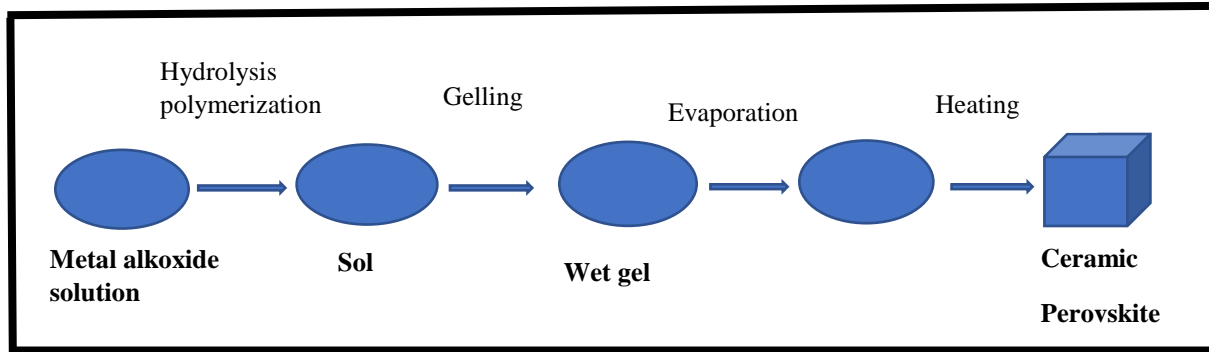


Figure 2.2: Schematic diagram of sol-gel method for the synthesis of ceramic perovskites.

2.5 Photovoltaic cell (PVC) device

These are solar cells that produce electric power through the conversion of solar energy into a stream of electrons through a process called photovoltaic effect. Current photovoltaic cell technology involves producing third generation devices that are less than $1\mu\text{m}$ thick [95]. Photovoltaic cells constructed on organic-inorganic hybrid perovskites, i.e. methylammonium lead halide perovskites have shown to be the most promising alternative. Perovskite photovoltaic cells have progressed rapidly in research over the past years. The general cell structure comprises a metal back contact, which is usually Al, Au or Ag, a hole transport material (organic or inorganic), perovskite layer as the light absorbing material, electron transport material (organic or inorganic) and a top contact layer (usually tin oxide doped with fluorine or indium oxide doped with tin). This device architecture is called planar heterojunction, and it is the most common in perovskite research. Correct engineering of the various device layers favors charge transport and collection

hence leading to good efficiencies. A schematic for planar device configuration is shown in figure 2.3.

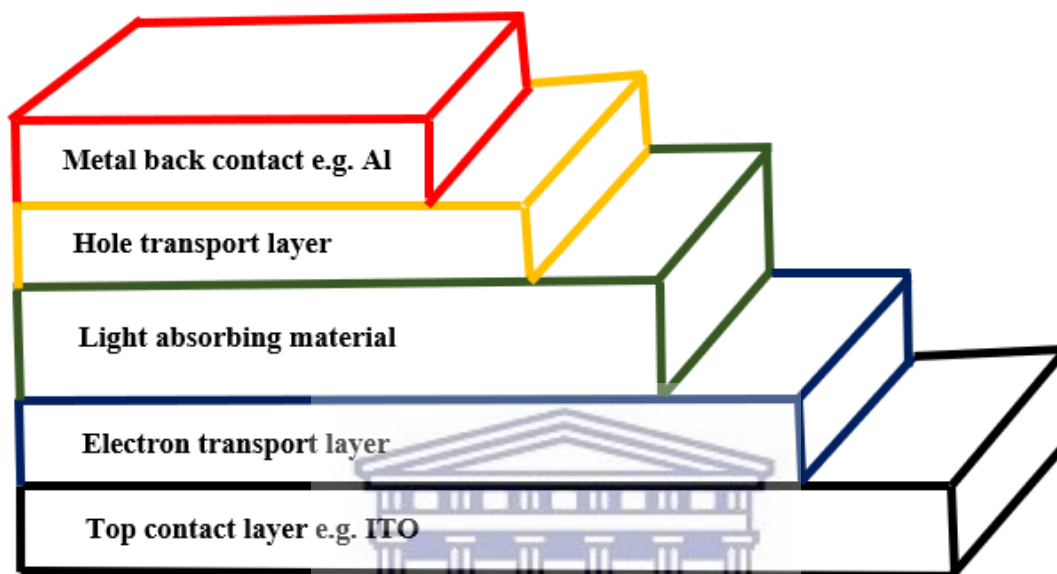


Figure 2.3: Solar cell schematic for planar device configuration.

UNIVERSITY of the
WESTERN CAPE

Performance of organic-inorganic metal halide perovskites seems not to be limited to any specific device architecture [96]. Salim *et al.* presented inevitable comparison between mesoscopic and planar solar cells whereby both architectures had comparable performances [96]. Film morphology is the main factor that influences device performance [97]. It is therefore of paramount importance to make good choice of deposition method, include additives to aid film treatment and minimize material composition. To obtain good-quality film morphology and hence good device performance, it is essential to lower the energy barrier for nucleation and to promote uniform growth of the perovskite crystals [98, 99].

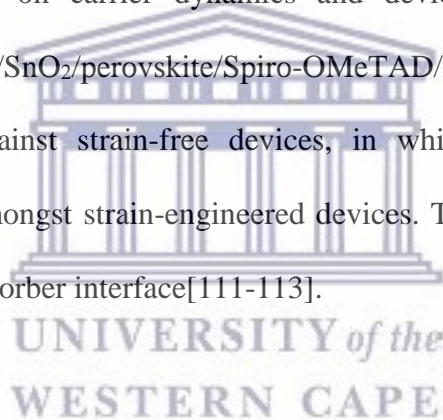
Leijtens *et al.* compared the electronic properties of both planar and mesoscopic cell architectures and found that perovskite films from the planar device exhibited superiority in terms of charge carrier mobility ($>20 \text{ cm}^2 \text{ V}^{-1} \text{ s}^{-1}$) [100]. However, solar cells prepared from planar architecture suffered from photovoltage loss, which was explained to be due to the high density of trap states in this configuration, resulting in high non-radiative electron-hole recombination [100]. Planar device architecture is very simple to construct, which makes it more technologically viable over mesoscopic architecture [101].

Snaith's group reported a perovskite cell device architecture that adopted planar heterojunction structure which included layers of FTO/TiO₂/MAPbI₂Cl/Spiro-OMeTAD/Ag. The device designed from this architecture managed to reach a power conversion efficiency of 1.8% [102]. Thereafter, the group optimized process conditions by preparing a succession of photovoltaic cells adopting the planar heterojunction structure, which recorded a maximum power conversion efficiency of 15.7%, open circuit voltage of 1.03V and fill factor of 0.749 [103, 104].

Shi *et al.* reported on inverted planar solar cell structure whereby the structure included indium tin oxide, poly-triarylamine, perovskite, phenyl-C61-butyric acid methyl ester, titanium and gold respectively, ITO/PTAA/MAPbI₃/PCBM/Ti/Au [105]. Previous work highlighted the importance in monitoring band alignments of the different layers to favor charge transport and collection in the device [106]. Efficiency of 18.21% was achieved when this device architecture was used.

More researchers on perovskite solar cells prefer to use planar device architecture that includes FTO glass, poly(3,4-ethylenedioxythiophene) polystyrene sulfonate (PEDOT:PSS), perovskite, PCBM and aluminium [107]. This architecture was chosen to fabricate solar cells from this research. This solar cell structure is favorable since it produces little cell-to-cell variability, shows hysteresis-free photovoltaic response [108]. Careful characterization coupled with modeling attribute the improved device performance to reduced defects from bulk and improved mobility of charge carrier in large-grain devices [109].

Studied the impact of strain on carrier dynamics and device performance using planar heterojunction solar cells ITO/SnO₂/perovskite/Spiro-OMeTAD/Ag [110]. They compared J-V curves of tensile strained against strain-free devices, in which they observed significant improvement in FF and V_{oc} amongst strain-engineered devices. This is due to improved carrier extraction dynamics around absorber interface [111-113].



Hole transport layer

In device architecture of photovoltaic cells, the role of the hole transport layer (HTL) is to assemble and transport electron holes from the perovskite light absorber which helps promote disunion of electron-hole pairs of the perovskite, in co-junction with the role played by the electron transport layer (ETL). Materials used as hole transporters can be divided into organic and inorganic materials. Organic materials, e.g. poly(3,4 ethylene dioxythiophene) polystyrene sulfonate, abbreviated as PEDOT:PSS and 2,2',7,7'-tetrakis[N,N-di(4-methoxyphenyl) amino]-9,9'-spirobifluorene abbreviated as spiro-OMeTAD are usually preferred because of their desirably

good penetration in nanoscale perovskites, making them good matches with the valence band of perovskites [114]. Figure 2.4 shows the structure of PEDOT:PSS.

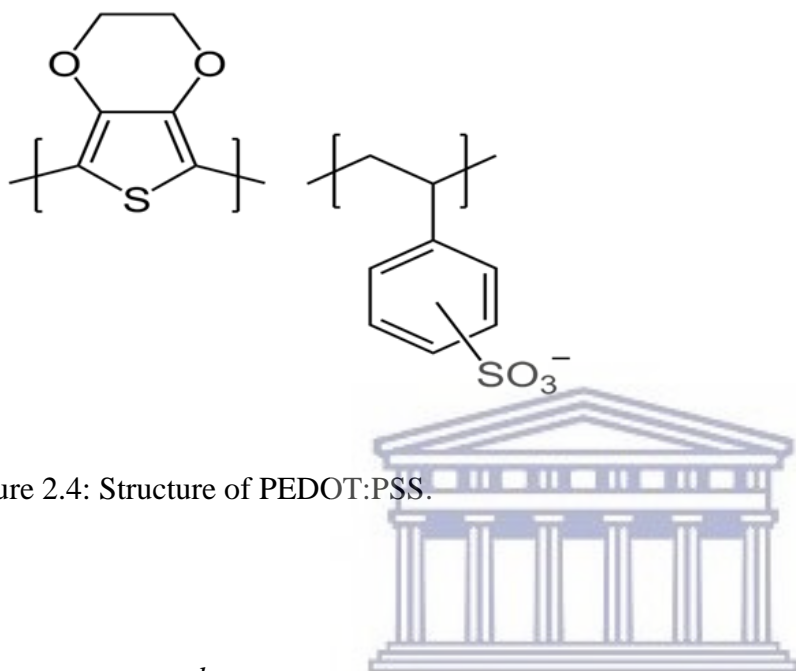


Figure 2.4: Structure of PEDOT:PSS.

Electron transport layer

The role of the electron transport layer in PVC is to establish an electron-selective barrier with the light absorber (perovskite), which helps promote photo generated electron extraction. Organic electron transport materials, i.e. poly[9,9-dioctylfluorene-9,9- bis(N,N-dimethyl-propyl)fluorene], abbreviated as PFN and is one of the fullerene derivatives and 6, 6-phenyl-C61-butyrac acid methyl ester abbreviated as PCBM were found to collect electrons better than the widely used TiO₂ [117]. Figure 2.5 shows the structure of PCBM.

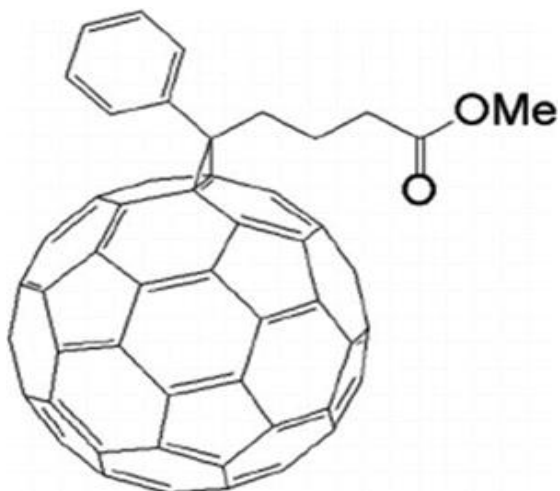
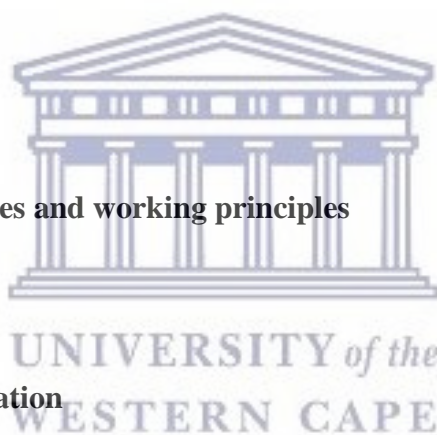


Figure 2.5: Structure of PCBM.

2.6 Characterization techniques and working principles



2.6 Photophysical characterization

2.6.1 High Resolution Scanning Electron Microscopy (HR SEM)

HR SEM is a characterization technique used to study the morphology and surface characteristics of nanomaterials. This technique focuses on the sample's surface and its composition, without providing the details about internal composition. This characterization technique provides a 3-dimensional image of the sample that is analyzed. HR SEM is a very useful technique; giving information to characterize perovskites and has one of the most common characterization techniques in the area of perovskites. Working principle is based on scattered electrons. The working principle involves a flow of primary electrons ejected from an electron gun that are

accelerated through the use of a grid and an anode. These accelerated electrons are directed and focused by condensing lenses and a scanning coil. The electron beam is made to be incident on the sample. Since the primary electrons have a high speed, they produce secondary electrons that bear low energy upon falling over the sample. The secondary electrons are collected and in turn produce some radiations on to photo multiplier tube which converts them into signals [93]. These signals are further intensified by the video amplifier and are fed to a screen for output. The final picture is created on the screen as the sample is scanned with the electron beam.

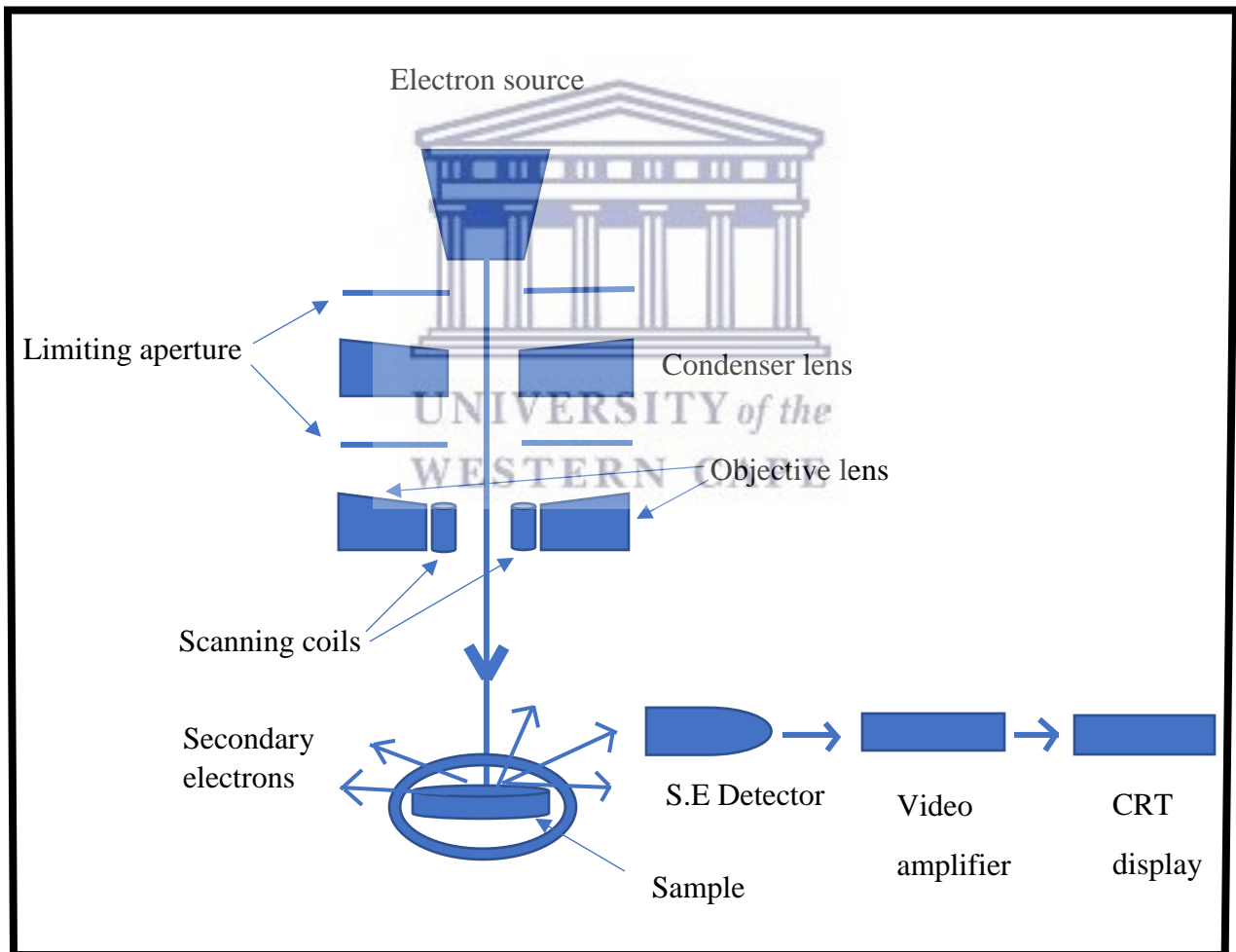
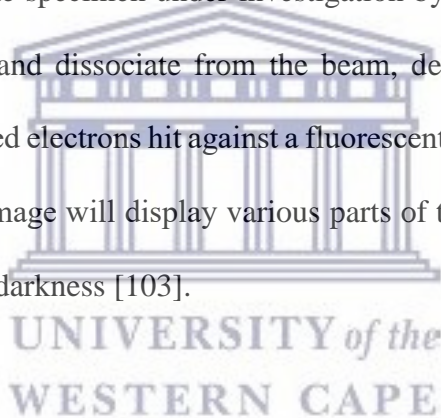


Figure 2.6: Schematic diagram of HR SEM.

2.6.2 High Resolution Transmission Electron Microscopy (HR TEM)

HR TEM is an analytical technique used to characterize nanoscale materials that operates on the same working principle as the light microscope. The difference however is that HR TEM uses electrons as the “light source” which makes it possible for this instrument to obtain a resolution gives a quality approximately one thousand times better than what a light microscope can give. This microscope has an electron source mounted at the top that emits electrons that are sent down the column of the microscope through vacuum [102]. The electrons are focused into a very thin beam that penetrates through the specimen under investigation by electromagnetic lenses. Some of the electrons are dispersed and dissociate from the beam, depending on the density of the material present. The un-scattered electrons hit against a fluorescent screen, which gives a “shadow image” of the specimen. This image will display various parts of the specimen, whereby varying density is showed according to darkness [103].



2.6.3 X-ray Diffraction (XRD)

XRD is a characterization technique that can be used for the phase identification and the relative percentages of different phases of the prepared materials. In addition, structural parameters like average spacing between rows or layers of atoms, orientation exhibited by a grain or single crystal, crystal structure a material has, shape and size a material has, and small crystalline regions’ internal stress can be calculated from the XRD data. Working principle of X-ray Diffraction is based on the interaction between crystalline sample and monochromatic X-rays, whereby constructive

interference forms. These high energy rays are then filtered to produce a monochromatic radiation which is concentrated and directed to fall on the sample.

When the incident rays interact with the sample, a constructive interference and a diffracted ray are produced if the conditions satisfy Bragg's law [104]. Bragg's law explains the relationship the electromagnetic radiation wavelength has with the lattice spacing and the diffraction angle in a crystalline sample. The major information is formed by the diffracted X-rays, which are then captured, processed and tallied. Scanning of the sample is done through a scale of 2θ angles. The random orientation of the powder material makes possible to attain all possible diffraction directions. The diffraction peaks are then converted to d-spacing, allowing the characterization of the material since all materials have a unique d-spacing [114]. Figure 2.7 shows a schematic diagram of XRD procedure.

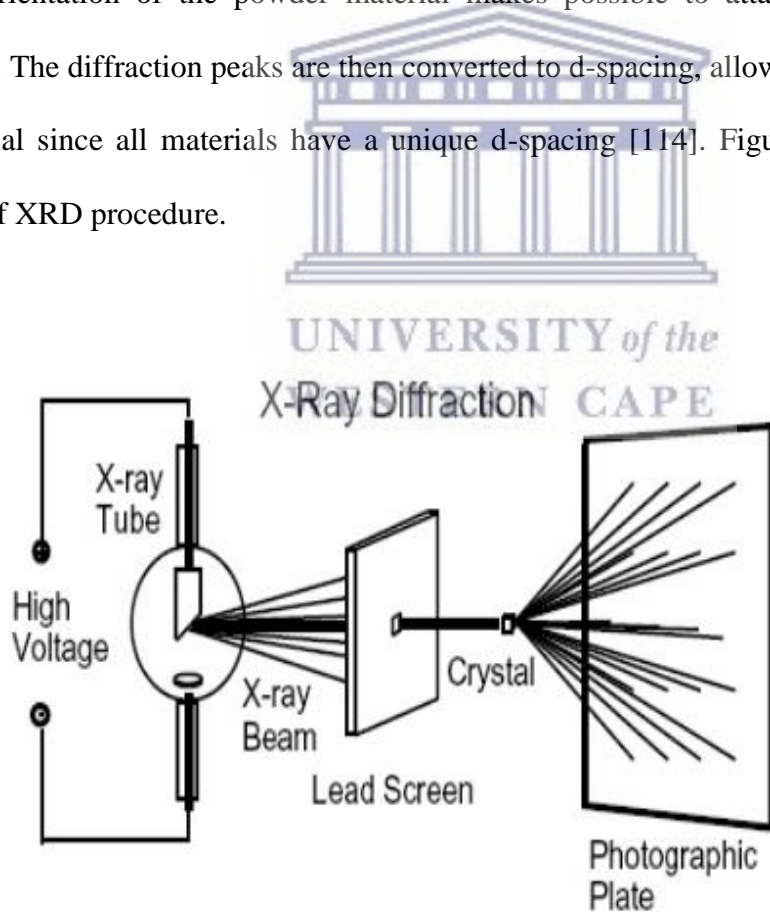


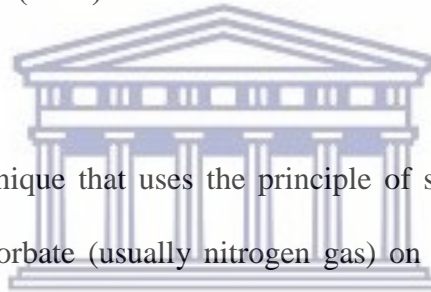
Figure 2.7: Schematic diagram of X-ray Diffraction [115].

The diffracted beam provides information about the d-spacing by applying Bragg's law given by:

$$n\lambda = 2d \sin\Theta \quad (2)$$

where n represents integer, λ represents the wavelength of incident wave, d represents the average distance between planes of the atomic lattice and Θ represents the angle between the scattering planes and incident ray.

2.6.4 Brunauer-Emmett-Teller (BET)



BET is a characterization technique that uses the principle of surface area values of different materials by adsorption of adsorbate (usually nitrogen gas) on an adsorbent. The BET theory explains the phenomenon of physical adsorption when molecules of gases interact with a solid substrate, hence measures the specific surface area of materials. The theory applies to systems that allow multilayer adsorption and usually employ probing gases that are unreactive with surfaces of the material as adsorbates to measure specific surface area [116, 117]. Figure 2.8 shows a BET model of a multilayer adsorption.

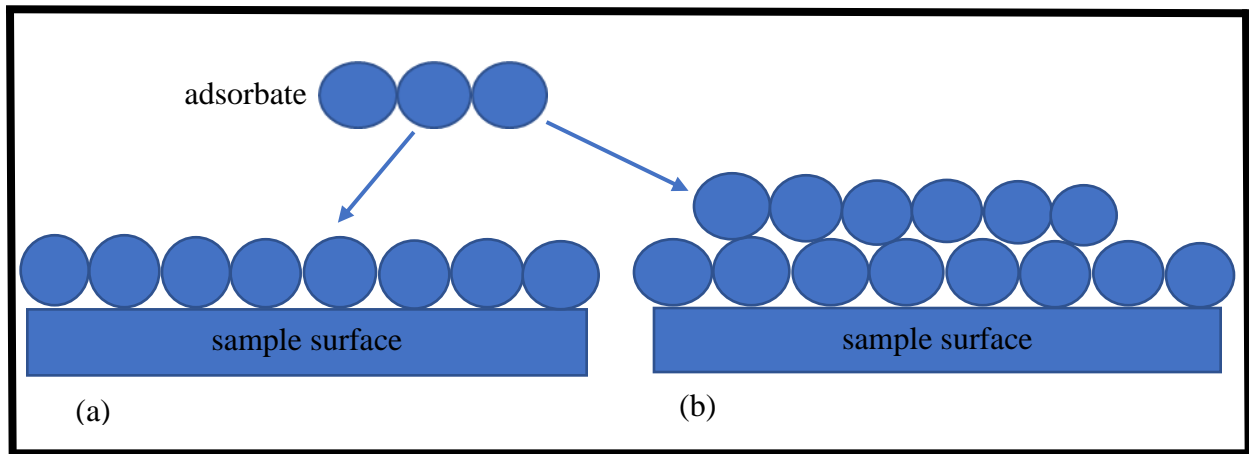
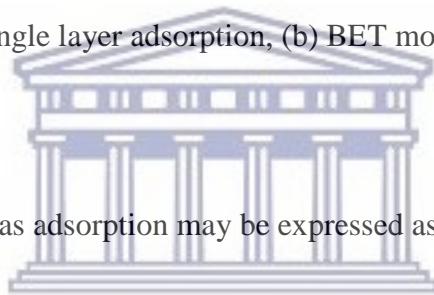


Figure 2.8: (a) BET model of single layer adsorption, (b) BET model of a multilayer adsorption.



The general BET equation for gas adsorption may be expressed as follows:

$$v = v_m c p / (p_0 - p) [1 + (c-1) (p / p_0)] \quad (3)$$

where v represents the adsorbed volume of gas, v_m is the volume of adsorbed monolayer, p represents the equilibrium gas pressure, p_0 represents saturation pressure and c is the BET constant.

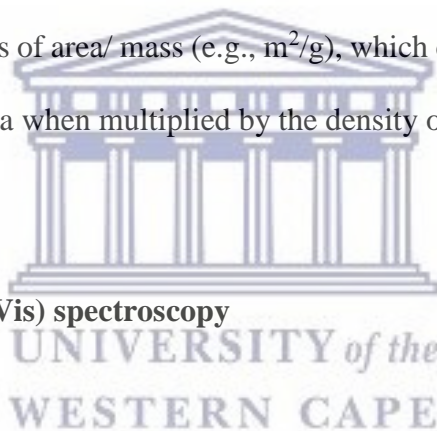
The same equation can be written as a linear function of p/p_0 as:

$$1/v [(p/p_0) - 1] = [c-1/v_m c] [p/p_0] + 1/v_m c \quad (4)$$

The y-intercept and slope of this function used to obtain values for the constants, where $c = (\text{slope}/\text{intercept} + 1)$ and $v_m = (1/(\text{slope} + \text{intercept}))$. To determine the specific surface area (S), the following equation is used:

$$S = v_m N_A / 22,400 \times m \quad (5)$$

where m is the mass of the sample and N_A is the Avogadro's number and 22,400 represents the value for volume of one mole of gaseous compound at standard temperature and pressure (STP). The surface area is given in units of area/ mass (e.g., m^2/g), which can further be simply converted to a volume-specific surface area when multiplied by the density of the material [118].



2.6.5 Ultraviolet-Visible (UV-Vis) spectroscopy

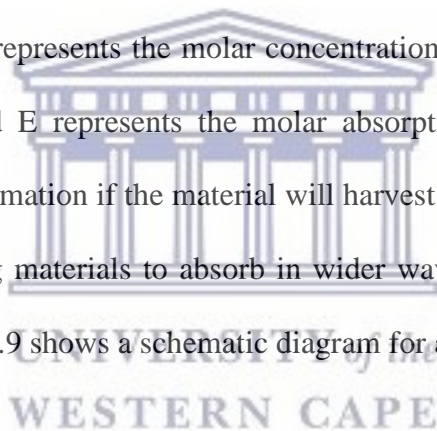
Ultraviolet-Visible spectroscopy is performed to analyze the light absorption of the perovskites. In perovskite solar cells, efficiency in light absorption by the absorber material is the major factor determining if the solar cell will work or not, UV-Vis is therefore of great importance. In this technique, light is illuminated onto the sample, which causes an electron to be excited corresponding to the difference in energy between an electronic transition happening inside the molecules, e.g. transition from bonding to anti-bonding orbital. As light is absorbed, a graph of the absorption of the sample is shown over range of wavelength selected. This principle adheres to Beer-Lambert law, whereby the rate of decrease of intensity of radiation and the incident radiation

of the sample solution are proportional when monochromatic light is made to pass through the solution [119].

Beer-Lambert law:

$$A = \log (I_0/ I) = ECL \quad (6)$$

where I_0 represents the intensity of light incident upon contact with sample cell, I is the intensity of light exiting sample cell, C represents the molar concentration of the solute, L represents the length of sample (in cm), and E represents the molar absorptivity. The wavelengths of the absorption peaks will give information if the material will harvest more light energy or not, i.e. it is more desirable for absorbing materials to absorb in wider wavelengths, from visible to near infrared for solar cells. Figure 2.9 shows a schematic diagram for a typical UV-Vis instrument.



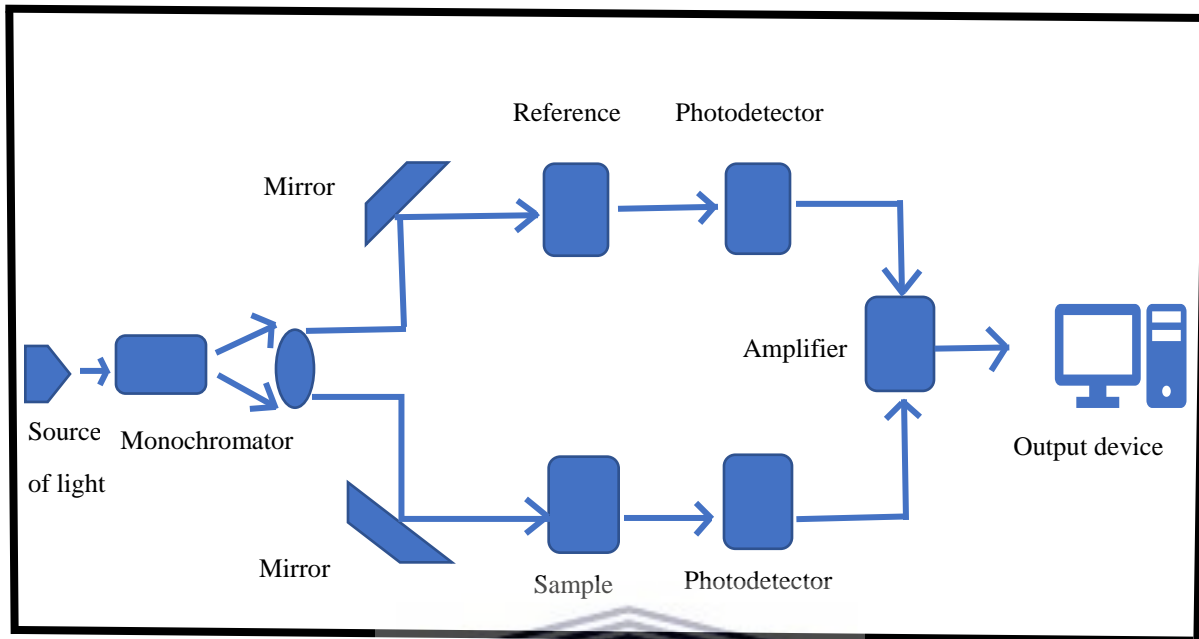


Figure 2.9: A typical schematic diagram of UV-Vis instrument.



Optical band-gap

Optical band-gap refers to the range in energy of a solid where no electron states can practically be found. Energy band gap is the energy difference in electron volts (eV) between the energy the valence band and that of the conduction band of insulating and semiconducting materials. Alternatively, the band-gap could also be described as the energy needed to promote a valence electron in an atom and cause it to jump to the conduction band, where it gains freedom to move within the crystal lattice and carry charge to conduct electrical energy. Information from the UV-Vis absorption peak of a material can be used to calculate the energy band gap as follows: [120]

[71]

$$E_g = hc / \lambda_{\text{cut off}} \quad (7)$$

where E_g is energy band gap, h is Planck's constant and $\lambda_{\text{cut off}}$ is the cut off wavelength obtained from the UV-Vis spectrum.

2.6.6 Photoluminescence (PL) spectroscopy

PL is a characterization technique that targets the emission of light from any form of matter that results from the absorption of light or electromagnetic radiation of suitable wavelength. Light emission is triggered by photoexcitation whereby photons cause electrons to be excited to an elevated energy level in an atom. After electron excitation, dissimilar relaxation processes generally occur in which photons are re-radiated as the electron returns to ground state. PL is hence an important technique for measuring the crystalline quality and purity of semiconductors and for measurement of the amount of disorder a system has [121, 122].

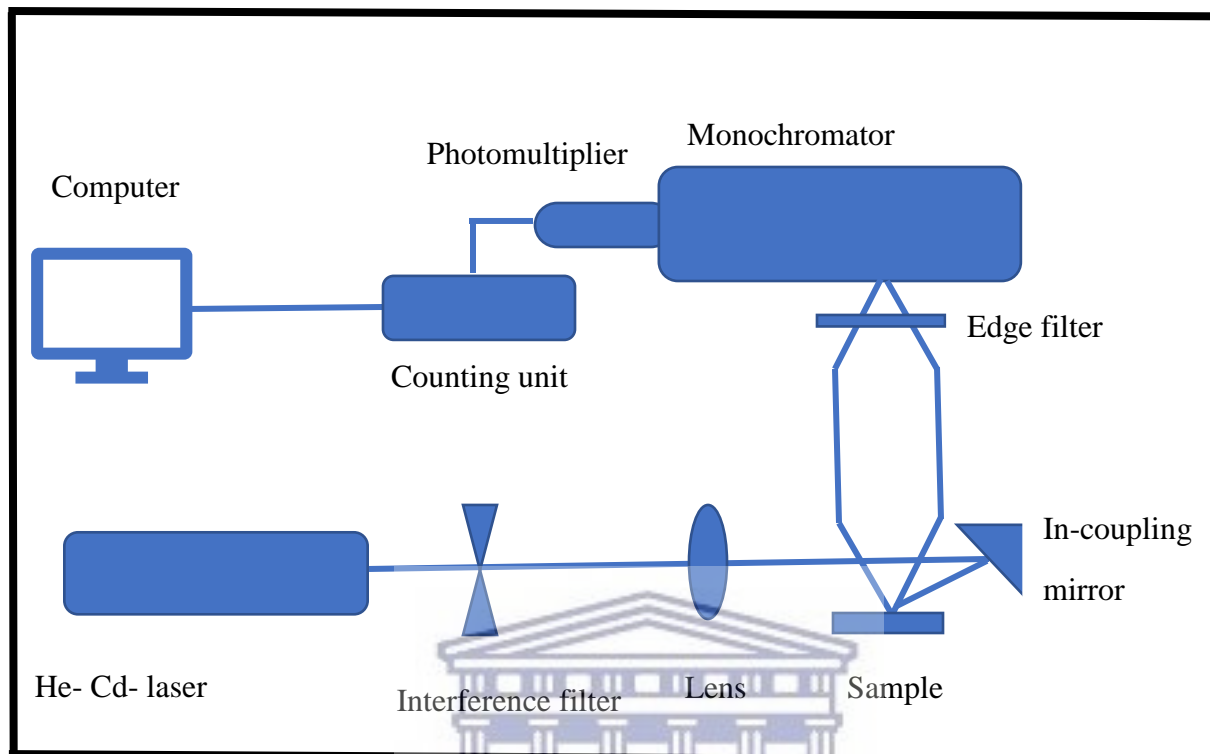


Figure 2.10: Schematic diagram of PL setup.

UNIVERSITY of the
WESTERN CAPE

2.6.7 Fourier Transform Infrared (FTIR) spectroscopy

FTIR is a technique used to identify organic molecules present in a sample, however in some cases it can also identify inorganic molecules. This analytical technique is used to measure Fourier transform infrared radiation absorbed by the sample against wavelength when infrared radiation is made to collide with the sample. The infrared absorption bands are characteristic to molecular components and structures of the sample; giving identification information of the sample. When a material is hit with infrared radiation, some of the infrared radiation is absorbed and will cause

molecules to be excited to an elevated vibrational state. In turn, the sample absorbs wavelengths that are characteristic of its molecular structure, thereby giving information about the molecular constituents and structure of the sample. FTIR instrumentation is composed of an interferometer that functions to regulate the wavelength from a source of broadband infrared. It also includes a detector which quantifies the intensity of transmitted light relative to its wavelength. The signal given by the detector is an interferogram, that is processed in a computer using Fourier transforms to acquire a single-beam infrared spectrum which shows absorption bands of functional groups present in the sample [117]. This information will then give identification of the sample. Figure 2.11 shows schematic diagram of FTIR.

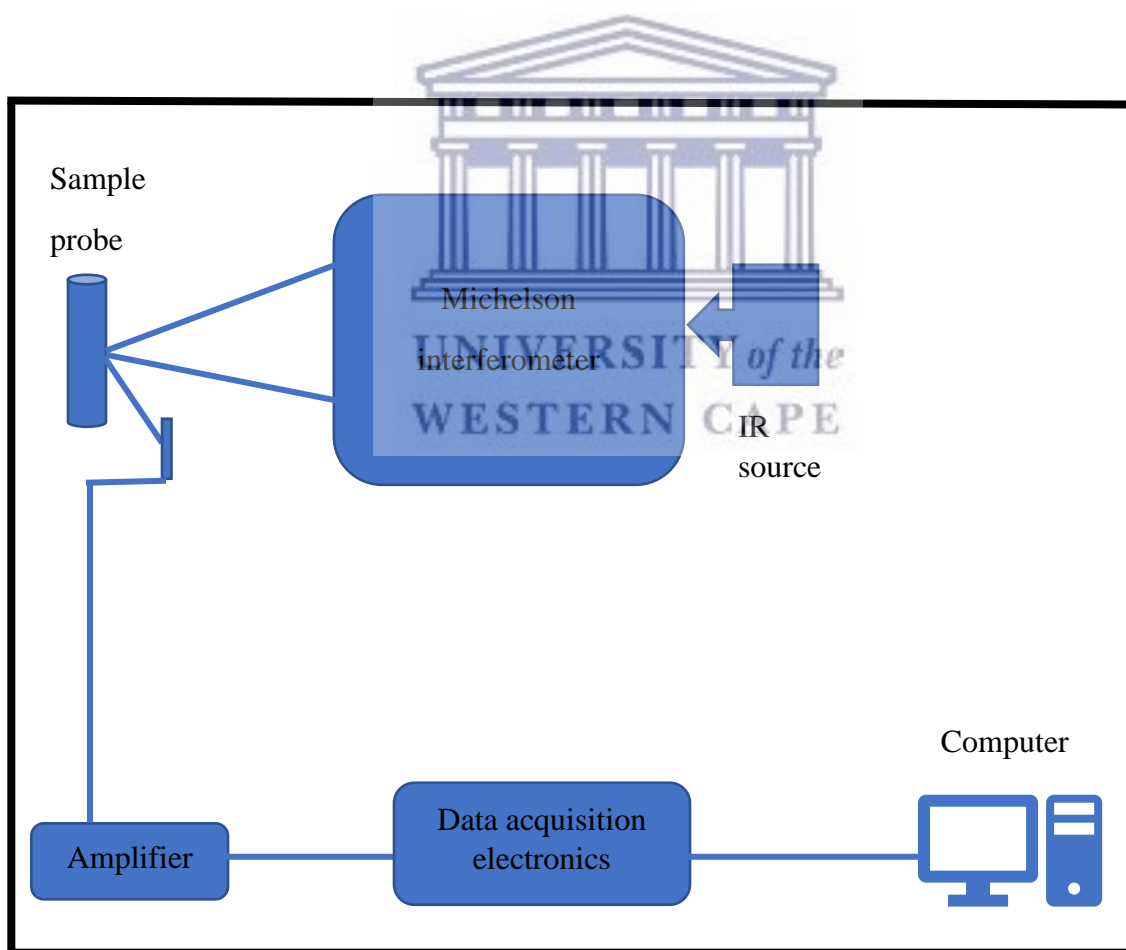


Figure 2.11: Schematic diagram of FTIR.

2.6.8 Raman spectroscopy

This is a characterization technique commonly used to get information on rotational and vibrational modes, as well as other low-frequency modes present in a system [123]. In Chemistry, Raman spectroscopy is useful by giving a structural fingerprint that helps in the identification of molecules. The principle of the spectrometer is based on interaction laser light has with molecular vibrations and other excitations that may be in the system, which results in a shift up or down of the energy of the laser photons. This shift in energy provides information about the vibrational modes that the system has [124]. A schematic diagram of the Raman spectrometer process is shown in figure 2.12.



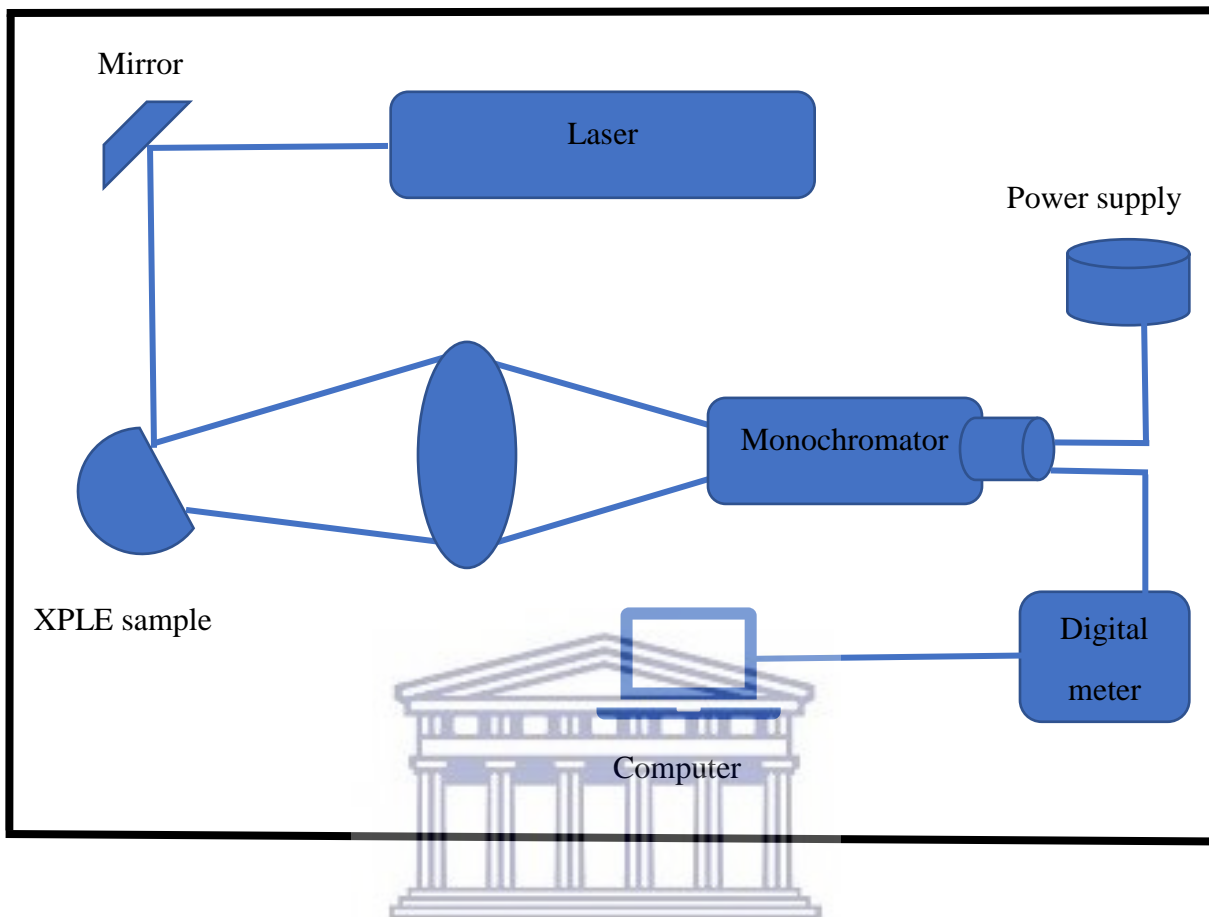


Figure 2.12: Schematic diagram of Raman spectrometer.

UNIVERSITY of the
WESTERN CAPE

2.6.9 Thermogravimetric Analysis (TGA)

TGA quantifies the amount of change in weight in a material, which is either a result of increase in temperature, or is a function of time, under nitrogen conditions or alternatively in helium or other gas atmosphere, or in vacuum. This technique gives information about physical phenomena, such as absorption, desorption and phase transitions. In addition, it also provides information about chemical phenomena such as chemisorption, solid-gas reactions most importantly reduction or

oxidation and thermal decomposition [125]. A thermogravimetric analyzer is composed of a precision balance fitted with a sample pan positioned inside a furnace where control temperature is programmed. In TGA experiment, temperature is raised gradually at constant rate, while in some applications the temperature is regulated against constant change in mass to experience a thermal reaction [126].

2.6.10 Nuclear Magnetic Resonance (NMR)

NMR is a spectroscopic technique used to study interaction between atomic nuclei and local magnetic fields. It is a very powerful and common technique scientists use to characterize organic samples. The organic sample is placed in a magnetic field region. This experiment makes use of radio waves which cause the nuclei of the sample to get excited into nuclear magnetic resonance (NMR) from which a signal is generated and is further detected by highly sensitive radio receivers. To characterize the sample; the knowledge that the resonance frequency is changed by intramolecular magnetic field surrounding an atom is exploited, whereby details of the electronic structure of a molecule are revealed and finally give the individual functional groups in the sample. The principle behind NMR is that all nuclei have an electrical charge while many nuclei have spin. Energy transfer takes place from the lower energy to elevated energy level as the sample is exposed to conditions of external magnetic field. Transfer in energy takes place at a wavelength corresponding to radio frequencies and when the spin comes back to its ground state level, energy is given off at the same frequency. The signal corresponding to this transfer is measured in many

steps and processed further to give an NMR spectrum for the nucleus concerned. Figure 2.13 represents a schematic diagram for NMR.

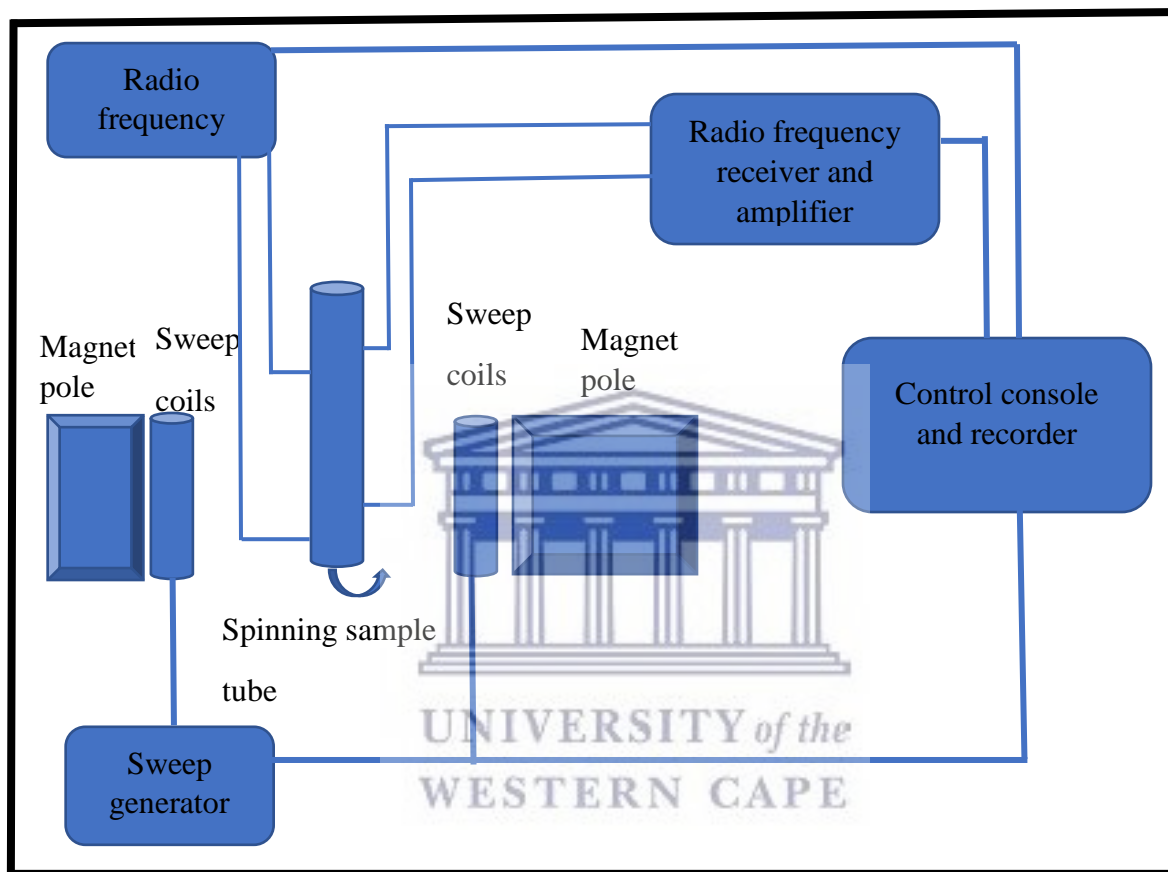
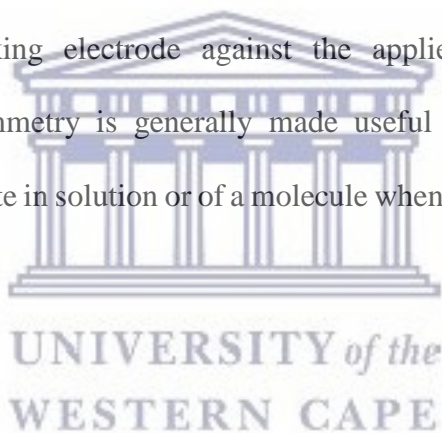


Figure 2.13: A simplified schematic diagram for NMR.

Electrochemical characterization

2.6.11 Cyclic Voltammetry (CV)

Cyclic Voltammetry experiment involves linear ramping of the working electrode potential against time. CV experiment, once the set potential is achieved, the working potential is ramped going the opposite direction until the initial potential is reached, unlike in linear sweep voltammetry experiment where the potential is ramped from lower limit to upper limit only. In CV, a plot of the current recorded at the working electrode against the applied voltage makes the cyclic voltammogram. Cyclic Voltammetry is generally made useful in studies of electrochemical properties exhibited by an analyte in solution or of a molecule when it is adsorbed onto the working electrode [127].



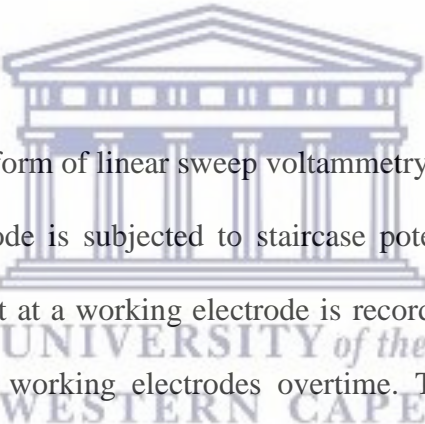
Electrochemical band gap

Cyclic Voltammetry helps us to determine the peak oxidation potential (V_{ox}), and the peak reduction potential (V_{red}), of the material under investigation [128]. Electrochemical band gap is based on the principle of the difference between the sample's highest occupied molecular orbital (HOMO) and its lowest unoccupied molecular orbital (LUMO). When a molecule or material is oxidized, the first electron is ejected from the HOMO (or valence band). When the molecule or material is reduced, an electron is injected into the conductance band which is assumed to be the

LUMO, thus, V_{ox} gives information about the energy at HOMO (valence band) while V_{red} gives information about the energy at LUMO (conductance band). The energy band-gap (in electron volts) is merely the difference between the oxidation and reduction potentials (in volts) when multiplied by the charge of an electron: $e = (-1 \text{ eV/ V})$ [129].

$$E_g (\text{eV}) = -e (V_{ox} - V_{red}) \quad (8)$$

2.6.12 Square Wave Voltammetry (SWV)



Square Wave Voltammetry is a form of linear sweep voltammetry which uses a combined square wave while the working electrode is subjected to staircase potential [130]. In a square wave voltammetry experiment, current at a working electrode is recorded while linearly scanning the voltage between reference and working electrodes overtime. Two pulses of the current are sampled; one pulse at the end of the forward scan and the other pulse at the end of the reverse scan. This current sampling at two points results in two different current waveforms collected. When the waveforms are viewed in segregation, the forward current waveform as well as the reverse current waveform imitate the emergence of a cyclic voltammogram, which represents both the cathodic and anodic halves.

2.6.13 Electrochemical Impedance Spectroscopy (EIS)

EIS can be used to separate processes occurring with different characteristic time scales in solar cells, which include capacitance, carrier conductivity and recombination resistance. Electrochemical impedance refers to the response shown by an electrochemical system when a potential is applied. Impedance spectroscopy's frequency dependence unveils underlying electrochemical processes. EIS characterizes a chemical process under electrical quantifications by exploiting Faraday's law. EIS response of a system is usually presented in Nyquist format, where the reactance is upturned since these systems have a capacitive behavior. A typical EIS setup is shown in figure 2.14.

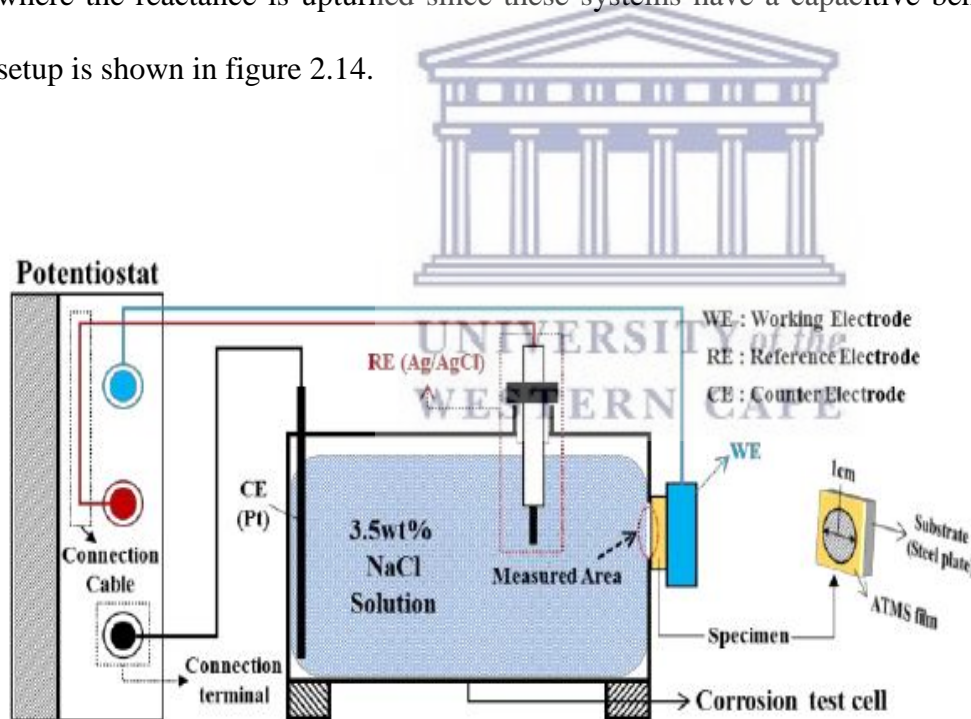


Figure 2.14: Schematic diagram of the experimental setup for EIS [131].

2.6.14 J-V curve

Device performance of a solar cell is determined from J-V curve, where J is current density (in A/cm²) and V is voltage (in Volts). Sometimes, Current (I)-Voltage (V) curve is used but the same conclusion of results is expected from both curves. In solar cells, the J-V curve is given by the superposition of the J-V curve of the photovoltaic cell diode in the dark with the current generated by light [132]. Under normal circumstances, exposure of the solar cell to light shifts down the J-V curve from the first to the fourth quadrant from where substantial power can be extracted from the diode. A typical J-V curve is shown in figure 2.15 below.

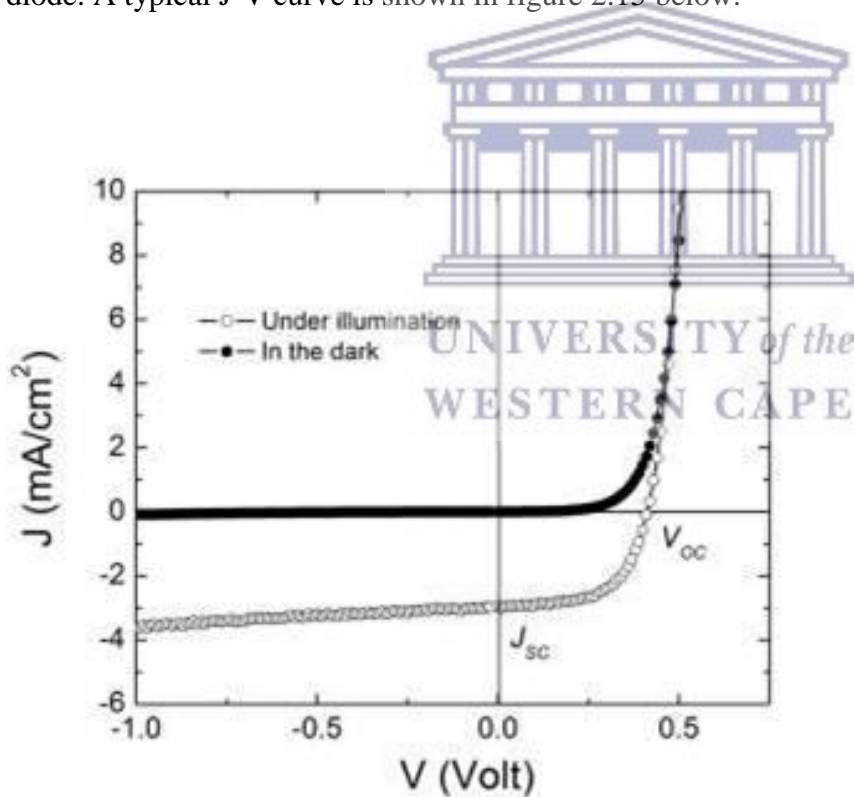


Figure 2.15: Typical J-V curve of solar cells [132].

Power conversion efficiency (PCE)

In photovoltaic cells, the PCE refers to the energy from sunlight that can be transfigured via photovoltaic effect into electricity. The PCE (η) is described as the ratio of the maximum output power (P_{\max}) to the irradiation intensity [133, 134]. Generally, the method that is followed to determine the PCE of a solar cell is to quantify the photocurrent by ramping the bias potential. The results obtained are plotted as current density versus voltage; represented as (J-V) curve [135]. A higher PCE is given by an increase in the V_{oc} , J_{sc} and FF with a decrease in P_{in} at the same time [136].

Equation (9) below is used to calculate the PCE:

$$\eta = P_{\max} / P_{in} = FF \times J_{sc} \times V_{oc} / P_{in}$$

(9)



where V_{oc} represents open circuit voltage, J_{sc} represents short circuit current density, FF represents fill factor (measure of squareness of the curve) and P_{in} represents the incident power.

2.7 References

1. Onnes, H. (1984). Discovery of Superconductivity. *Historical Studies in the Physical Sciences*, 15, 1-37.
2. Ruiz-Zepeda, F., Ma, C., Bahena, U., Cantu-Valle, J., Wang, H., Xu, X., Yacaman, M., Chen, L., Lorenz, B., Jacobson, A., Chu, P., Ponce, A. (2014). Nanodomain Induced Anomalous Magnetic and Electronic Transport Properties of $\text{LaBaCo}_2\text{O}_{5.5+\delta}$ Highly Epitaxial Thin Films. *Journal of Applied Physics*, 115, article number 024301.
3. Goldschmidt, V. (1926). Die Gesetze der Krystallochemie. *Die Naturwissenschaften*, 8, 477-485.
4. Cohen, E. (1992). Origin of Ferroelectricity in Perovskite Oxides. *Nature*, 358, 136-138.
5. Babout, M., Pramana, S., Hanlon, J., Dorcet, V., Smith, R., Paofai, S., Skinner, S. (2003). Stability of $\text{NdBaCo}_{2-x}\text{M}_{nx}\text{O}_{5+\delta}$ ($x=0,0.5$) Layered Perovskites in Humid Conditions Investigated by High-temperature *in situ* Neutron Powder Diffraction. *Journal of Material Chemistry A*, 33, 333-359.
6. Adinolfi, V., Peng, W., Walters, G., Bakr, O., Sargent, E. (2018). The Electrical and Optical Properties of Organometal Halide Perovskites Relevant to Optoelectronic Performance. *Advanced Materials*, 30, article number 1700764.
7. Mo, C., Li, Z., Que, C. (2017). Composition Dependent Structural, Optical and Photosensitive Properties of a Series of Charge-transfer Tin Halides. *Dyes and Pigments*, 141, 66-73.
8. Joannopoulos, J., Villeneuve, P., Fan, S. (1997). Photonic Crystals: Putting a New Twist on Light. *Nature*, 386, 143-149.

9. Saliba, M, Matsui, T., Domanski, K., Seo, J., Ummadisingu, A., Zakeeruddin, S., Correabena, J., Tress, W., Abate, A., Hagfeldt, A. (2016). Incorporation of Rubidium Cations into Perovskite Solar Cells Improves Photovoltaic Performance. *Science*, 354, 206-209.
10. Yang, W., Park, B., Jung, E., Jeon, N., Kim, Y., Lee, D., Shin, S., Seo, J., Kim, E., Noh, J. (2017). Iodide Management in Formamidinium-Lead-Halide-Based Perovskite Layers for Efficient Solar Cells. *Science*, 356, 1376-1379.
11. Tan, H., Jain, A., Voznyy, O., Lan, X., Fp, G., Fan, J., Quintero-Bermudez, R., Yuan, M., Zhang, B., Zhao, Y. (2017). Efficient and Stable Solution-Processed Planar Perovskite Solar Cells via Contact Passivation. *Science*, 355, 722-726.
12. Xing, G., Mathews, N., Sun, S., Lim, S., Lam, Y., Grätzel, M., Mhaisalkar, S., Sum. T. (2013). Long-Range Balanced Electron- and Hole-Transport Lengths in Organic-Inorganic $\text{CH}_3\text{NH}_3\text{PbI}_3$. *Science*, 342, 344-347.
13. Eperon, G., Burlakov, V., Docampo, P., Goriely, A., Snaith, H. (2014). Morphological Control for High Performance, Solution-Processed Heterojunction Perovskite Solar Cells. *Advanced Functional Materials*, 24, 151-157.
14. Ran, C., Xu, J., Gao, W., Huang, C., Dou, S. (2018). Defects in Metal Triiodide Perovskite Materials Towards High-Performance Solar Cells: Origin, Impact, Characterization, and Engineering. *Chemical Society Reviews*, 47, 4581-4610.
15. Wen, Y., Tang, Y., Yan, G. (2018). Large Grain Size $\text{CH}_3\text{NH}_3\text{PbI}_3$ Film for Perovskite Solar Cells with Hydroic Acid Additive. *AIP Advances*, 8, article number 095226.

16. Olyaeefar, B., Ahmadi-Kandjani, S., Asgari, A. (2018). Classical Modelling of Grain Size and Boundary Effects in Polycrystalline Perovskite Solar Cells. *Solar Energy Materials and Solar Cells*, 180, 76-82.
17. Chen, Y., Yi, H., Wu, X., Haroldson, R., Gartstein, Y., Rodionov, Y., Tikhonov, K., Zakhidov, A., Zhu, X., Podzorov, V. (2016). Extended Carrier Lifetimes and Diffusion in Hybrid Perovskites Revealed by Hall Effect and Photoconductivity Measurements. *Nature Communications*, 7, article number 12253.
18. Shi, T., Chen, J., Zheng, J., Li, X., Zhou, B., Cao, H., Wang, Y. (2016). Ti/Au Cathode for Electronic Transport Material-Free Organic-Inorganic Hybrid Perovskite Solar Cells. *Scientific Reports*, 6, article number 39132.
19. Huang, J., Yuan, Y., Shao, Y., Yan, Y. (2017). Understanding the Physical Properties of Hybrid Perovskites for Photovoltaic Applications. *Nature Review Materials*, 2, article number 17042.
20. Han, G., Koh, T., Lim, S., Goh, T., Guo, X., Leow, S., Begum, R., Sum, T., Mathews, N., Mhaisalka, S. (2017). Facile Method to Reduce Surface Defects and Trap Densities in Perovskite Photovoltaics. *ACS Applied Materials and Interfaces*, 9, 21292-21297.
21. Jacobsson, T., Correa-Baena, J., Anaraki, E., Philippe, B., Stranks, S., Bouduban, M., Tress, W., Schenk, K., Teuscher, J., Moser, J., Rensmo, H., Hagfeldt, A. (2016). Unreacted PbI₂ as a Double-Edged Sword for Enhancing the Performance of Perovskite Solar Cells. *Journal of The American Chemical Society*, 138, 10331-10343.
22. Huang, F., Dkhissi, Y., Huang, W., Xiao, M., Benesperi, I., Rubanov, S., Zhu, Y., Lin, X., Jiang, L., Zhou, Y., Gray-Weale, A., Etheridge, J., McNeill, C., Caruso, R., Bach, U., Spiccia, L., Cheng, Y. (2014). Gas-Assisted Preparation of Lead Iodide Perovskite Films

Consisting of a Monolayer of Single Crystalline Grains for High Efficiency Planar Solar Cells. *Nano Energy*, 10, 10-18.

23. Li, L., Chen, Y., Liu, Z., Chen, Q., Wang, X., Zhou, H. (2016). The Additive Coordination Effect on Hybrids Perovskite Crystallization and High-Performance Solar Cell. *Advanced Materials*, 28, 9862-9868.
24. Yuan, B., Zhao, S., Xu, Z., Song, D., Qiao, B., Li, Y., Qin, Z., Meng, J., Xu, X. (2018). Improving the Photovoltaic Performance of Planar Heterojunction Perovskite Solar Cells by Mixed Solvent Vapor Treatment. *RSC Advances*, 8, 11574-11579.
25. Fu, J., Sun, K., Yang, Ke., Hu, L., Leng, C., Kan, Z., Duan, T., Li, M., Shi, H., Xiao, Z., Lu, S., Ouyang, J. (2018). Improvement of Planar Perovskite Solar Cells Using a Phenol Additive. *Journal of Materials Chemistry C*, 6, 11519-11524.
26. B. Duan, Y. Ren, Y. Xu, W. Chen, Q. Ye, Y. Huang, J. Zhu and S. Dai. (2017). Identification and Characterization of a New Intermediate to Obtain High Quality Perovskite Films with Hydrogen Halides as Additives. *Inorganic Chemistry Frontiers*, 4, 473-480.
27. Kim, J., Yun, J., Wen, X., Soufiani, A., Lau, C., Wilkinson, B., Seidel, J., Green, M., Huang, S., Ho-Baillie, A. (2016). Nucleation and Growth Control of $\text{HC}(\text{NH}_2)_2\text{PbI}_3$ for Planar Perovskite Solar Cell. *Journal of Physical Chemistry C*, 120, 11262-11267.
28. Yang, Y., Feng, S., Li, M., Li, F., Zhang, C., Han, Y., Li, L., Yuan, J., Cao, L., Wang, Z., Sun, B., Gao, X. (2018). Nonfullerene Small-Molecule Acceptors with Perpendicular Side-Chains for Fullerene-Free Solar Cells. *Journal of Materials Chemistry A*, 6, 15433-15455 .

29. Huang, P., Wang, Y., Ke, J., Huang, C. (2017). The Effect of Solvents on the Performance of $\text{CH}_3\text{NH}_3\text{PbI}_3$ Perovskite Solar Cells. *Energies*, 10, article number 599.
30. Rahimnejad, S., Kovalenko, A., Forés, S., Aranda, C., Guerrero, A. (2016). Coordination Chemistry Dictates the Structural Defects in Lead Halide Perovskites. *Chemphyschem*, 17, 2795-2798.
31. Zhang, F., Bi, D., Pellet, N., Xiao, C., Li, Z., Berry, J., Zakeeruddin, M., Zhu, K., Grätzel, M. (2018). Suppressing Defects Through the Synergistic Effect of a Lewis Base and a Lewis Acid for Highly Efficient and Stable Perovskite Solar Cells. *Energy and Environmental Science*, 11, 3480-3490.
32. Sharenko, A., Mackeen, C., Jewell, L., Bridges, F., Toney, M. (2017). Evolution of Iodoplumbate Complexes in Methylammonium Lead Iodide Perovskite Precursor Solutions. *Chemistry of Materials*, 29, 1315-1320.
33. Jeon, N., Noh, J., Kim, Y., Yang, W., Ryu, S., Seok, S. (2014). Solvent Engineering for High-Performance Inorganic-Organic Hybrid Perovskite Solar cells. *Nature Materials*, 13, 897-903.
34. J. M. Ball, M. M. Lee, A. Hey and H. J. Snaith. (2013). Low-Temperature Processed Meso-Structured to Thin-Film Perovskite Solar Cells. *Energy and Environmental Science*, 2013, 6, 1739-1743.
35. D'Innocenzo, V., Grancini, G., Alcocer, M., Kandada, A., Stranks, S., Lee, M., Lanzani, G., Snaith, H., Petrozza, A. (2014). Excitons Versus Free Charges in Organo-lead Tri-halide Perovskites. *Nature Communications*, 2014, 5, article number 3586.
36. Wang, L., McCleese, C., Kovalsky, A., Zhao, Y., Burda, C. (2014). Femtosecond Time-Resolved Transient Absorption Spectroscopy of $\text{CH}_3\text{NH}_3\text{PbI}_3$ Perovskite Films: Evidence

- for Passivation Effect of PbI_2 . *Journal of The American Chemical Society*, 136, 12205-12208.
37. Burschka, J., Pellet, N., Moon, S., Humphry-Baker, R., Gao, P., Nazeeruddin, M., Grätzel, M. (2013). Sequential Deposition as a Route to High-Performance Perovskite- Sensitized Solar Cells. *Nature*, 499, 316-319.
38. Liu, M., Johnston, M., Snaith, H. (2013). Efficient Planar Heterojunction Perovskite Solar Cells by Vapor Deposition. *Nature*, 501, 395-398.
39. Oga, H., Saeki, A., Ogomi, Y., Hayase, S., Seki, S. (2014). Improved Understanding of the Electronic and Energetic Landscapes of Perovskite Solar Cells: High Local Charge Carrier Mobility, Reduced Recombination, and Extremely Shallow Traps. *Journal of The American Chemical Society*, 136, 13818-13825.
40. Golschmidt, V. (1926). The laws of Krystallochemie. *The Science*, 21, 477-485.
41. Megaw, H. (1945). Crystal Structure of Barium Titanate. *Nature*, 155, 484-485.
42. Von Hippel, A. (1950). Ferroelectricity, Domain Structure, and Phase Transitions of Barium Titanate. *Reviews of Modern Physics*, 22, 221-237.
43. Weber, D. (1978). $\text{CH}_3\text{NH}_3\text{PbX}_3$, a Pb(II)-System with Cubic Perovskite Structure. *Zeitschrift fur Naturforsch*, 33, 1443-1445.
44. Weber, D. (1978). $\text{CH}_3\text{NH}_3\text{SnBr}_x\text{I}_{3-x}$ ($x = 0-3$), A Sn(II)-System with the Cubic Perovskite Structure. *Zeitschrift fur Naturforsch*, 33, 862-865.
45. Wells, H. (1893). About the Cesium and Potassium lead halides. *Journal of Inorganic and General Chemistry*, 45, 1880-1910.
46. Stoumpos, C., Malliakas, C., Peters, J., Liu, Z., Sebastian, M., Im, J., Chasapis, T., Wibowo, A., Chung, D., Freeman, A., Wessels, B., Kanatzidis, M. (2013). Crystal Growth

of the Perovskite Semiconductor CsPbBr₃: A New Material for High-Energy Radiation Detection. *Crystal Growth and Design*, 13, 2722-2727.

47. Zhang, D., Eaton, S., Yu, Y., Dou, L., Yang, P. (2015). Solution-Phase Synthesis of Cesium Lead Halide Perovskite Nanowires. *Journal of The American Chemical Society*, 137, 9230-9233.
48. Kojima, A., Teshima, K., Shirai, Y., Miyasaka, T. (2009). Organometal Halide Perovskites as Visible-light Sensitizers for Photovoltaic Cells. *Journal of The American Chemical Society*, 13, 6050-6051.
49. Sneha, A., Kulkarni, T., Baikie, Yantara, N., Mathews. N., Mhaisalkar, S. (2014). Band-Gap Tuning of Lead Halide Perovskites Using a Sequential Deposition Process. *Journal of Material Chemistry A*, 2, 9221-9225.
50. Draguta, S., Sharia, O., Yoon, S., Brennan, M., Morozov, Y., Manser, J., Kamat, P., Schneider, W., Kuno, M. (2017). Rationalizing the Light-Induced Phase Separation of Mixed Halide Organic-Inorganic Perovskites. *Nature Communications*, 8, article number 200.
51. Hentz, O., Zhao, Z., Gradec ˇ ak, S. (2016). Impacts of Ion Segregation on Local Optical Properties in Mixed Halide Perovskite Films. *Nano Letters*, 16, 1485-1490.
52. Swarnkar, A., Marshall, A., Sanehira, E., Chernomordik, B., Moore, D., Christians, J., Chakrabarti, T., Luther, J. (2016). Quantum Dot-Induced Phase Stabilization of α -CsPbI₃ Perovskite for High-Efficiency Photovoltaics. *Science*, 354, 92-95.
53. Abdi-Jalebi, M., Andaji-Garmaroudi, Z., Cacovich, S., Stavrakas, C., Philippe, B., Richter, J., Alsari, M., Booker, E., Hutter, E., Pearson, A., Lilliu, S., Savenije, T., Rensmo

- H., Divitini G., Ducati, C., Friend, R., Stranks, S. (2018). Maximizing and Stabilizing Luminescence from Halide Perovskites with Potassium Passivation. *Nature*, 555, 497-501.
54. Yang, W., Park, B., Jung, E., Jeon, N., Kim Y., Lee, D., Shin, S., Seo, J., Kim, E., Noh, J., Seok, S. (2017). Iodide Management in Formamidinium-Lead-Halide-Based Perovskite Layers for Efficient Solar Cells. *Science*, 356, 1376-1379.
55. Li, Z., Klein, T., Kim, D., Yang, M., Berry, J., van Hest, M., Zhu, K. (2018). Scalable Fabrication of Perovskite Solar Cells. *Nature Review Materials*, 3, article number18017.
56. Song, Z., McElvany, C., Phillips, A., Celik, I., Krantz, P., Wathage, S., Liyanage, G., Apul, D., Heben, M. (2017). Technoeconomic Analysis of Perovskite Solar Module Manufacturing with Low-Cost Materials and Techniques. *Energy Environmental Science*, 10, 1297-1305.
57. Tidhar, Y., Edri, E., Weissman, H., Zahar, D., Hodes, G., Cahen, D., Boris, R., Kirmayer, S. (2014). Crystallization of Methyl Ammonium Lead Halide Perovskites: Implications for Photovoltaic Applications. *Journal of The American Chemical Society*, 136, 13249-13256.
58. Borriello, I., Cantele, G., Ninno, D. (2008). Ab Initio Investigation of Hybrid Organic-inorganic Perovskites Based on Tin Halides. *Physical Review B*, 77, article number 235214.
59. Liao, W., Zhao, D., Yu, Y., Shrestha, N., Ghimire, K., Grice, C., Wang, C., Xiao, Y., Cimaroli, A., Ellingson, R., Podraza, N., Zhu, K., Xiong, R., Yan, Y. (2016). Fabrication of Efficient Low-bandgap Perovskite Solar Cells by Combining Formamidinium Tin Iodide with Methylammonium Lead Iodide. *Journal of The American Chemical Society*, 138, 12360-12363.

60. Nagane, S., Ghosh, D., Hoyer, R., Zhao, B., Ahmad, S., Walker, A., Islam, M., Ogale, S., Sadhanala, A. (2018). Lead-Free Perovskite Semiconductors Based on Germanium-Tin Solid Solutions: Structural and Optoelectronic Properties. *Journal of Physical Chemistry C* 122, 11, 5940-5947.
61. Chung, I., Lee, B., He, J., Chang, R., Kanatzidis, M. (2012). All-solid-state Dye-sensitized Solar Cells with High Efficiency. *Nature*, 485, 486-489.
62. Ke, W., Zhao, D., Grice, C., Cimaroli, A., Fang, G., Yan, Y. (2015). Efficient Fully-vacuum-processed Perovskite Solar Cells Using Copper Phthalocyanine as Hole Selective Layers. *Journal of Material Chemistry A*, 3, 23888-23894.
63. Eperon, G., Stranks, S., Menelaou, C., Johnston, M., Herz, L., Snaith, H. (2014). Formamidinium Lead Trihalide: A Broadly Tunable Perovskite for Efficient Planar Heterojunction Solar Cells. *Energy and Environmental Science*, 7, 982-988.
64. Koh, T., Krishnamoorthy, T., Yantara, N. et al. (2015). Formamidinium Tin-based Perovskite with Low E_g for Photovoltaic Applications. *Journal of Material Chemistry A*, 3, 14996-15000.
65. Zhao, Z., Gu, F., Li, Y., Shi, C., Leong, W., Boix, P., Grimsdale, A., Mhaisalkar, S., Mathews, N. (2017). Mixed-organic-cation Tin Iodide for Lead-free Perovskite Solar Cells with an Efficiency of 8.12%. *Advanced Science*, 3, 14996-15000.
66. Yi, C., Luo, J., Meloni, S., Boziki, A., Ashari-Astani, N., Gratzel, C., Zakeerudin, S., Rothlisberger, U., Gratzel, M. (2016). Entropic Stabilization of Mixed A-Cation ABX_3 Metal Halide Perovskites for High Performance Perovskite Solar Cells. *Energy and Environmental Science*, 9, 656-662.

67. Lozano, G. (2018). The Role of Metal Halide Perovskites in Next-Generation Lighting Devices. *The Journal of Physical Chemistry Letters*, 9, 3987-3997.
68. Peedikakkandya, L., Bhargava, P. (2016). Composition Dependent Optical, Structural and Photoluminescence Characteristics of Cesium Tin Halide Perovskites. *The Royal Society of Chemistry Advanced*, 6, 19857-19860.
69. You, J., Meng L., Song T., Guo T., Yang Y., Chang W., Hong, Z., Chen, H., Zhou, H., Chen Q., Liu, Y., De Marco, N., Yang, Y. (2016). Improved Air Stability of Perovskite Solar Cells via Solution-Processed Metal Oxide Transport Layers. *Nature Nanotechnology*, 11, 75-81.
70. Li, Z., Yang, M., Park, J., Wei, S., Berry, J., Zhu, K. (2016). Stabilizing perovskite structures by tuning tolerance factor: Formation of Formamidinium and Cesium Lead Iodide Solid-State Alloys. *Chemistry Materials*, 28, 284-292.
71. McMeekin, D., Sadoughi, G., Rehman, W., Eperon, G., Saliba, M., Hörantner, M. (2016). A Mixed-Cation Lead Mixed-Halide Perovskite Absorber for Tandem Solar Cells. *Science* 351, 151-155.
72. Griffini, F., Correa-Baena, G., Saracco, G., Grätzel, M., Hagfeldt, Anders., Turri, S., Gerbaldi, C. (2016). Improving efficiency and stability of perovskite solar cells with photocurable fluoropolymers. *Advanced Functional Materials*, 26, 1127-1137.
73. Bi, D., Tress, W., Dar, M., Gao, P., Luo, J., Renevier, C., Schenk, K., Abate, A., Giordano, F., Baena, J., Decoppet, J., Zakeeruddin, S., Nazeeruddin, M., Grätzel, M., Hagfeldt, A. (2016). Efficient Luminescent Solar Cells Based on Tailored Mixed-Cation Perovskites. *Science Advances*, 2, article number 1501170.

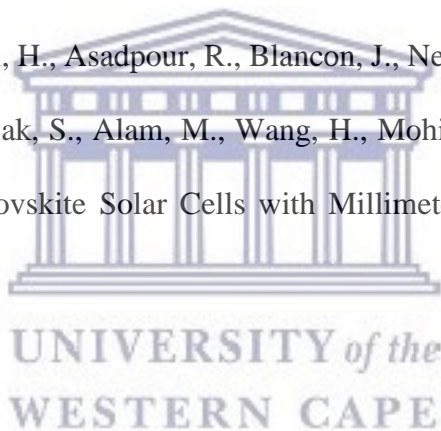
74. Giordano, F., Abate, A., Baena, J., Saliba, M., Matsui, T., Im, S., Zakeeruddin, S., Nazeeruddin, M., Hagfeldt, A., Graetzel, M. (2016). Enhanced Electronic Properties in Mesoporous TiO₂ via Lithium Doping for High-Efficiency Perovskite Solar Cells. *Nature Communications*, 7, article number 10379.
75. Billstrand, B., Bian, K., Karley, C., Ye, D. (2018). Solution-Based Synthesis of Cs₄PbBr₆ Perovskite Particles with High Luminescence and Stability. *Nanomaterials*, 3, 2825-2831.
76. Zhang, P., Wu, J., Zhang, T., Wang, Y., Liu, D., Chen, H., Ji, L., Liu, C., Ahmad, W., Chen, Z., Li, S. (2018). Perovskite Solar Cells with ZnO Electron-Transporting Materials. *Advanced Materials*, 30, article number 1703737.
77. Mahmood, K., Khalid, A., Ahmad, S., Mehran, M. (2018). Indium-Doped ZnO Mesoporous Nanofibres as Efficient Electron Transporting Materials for Perovskite Solar Cells. *Surface and Coatings Technology*, 352, 231-237.
78. Qingde, S., Hangyan, C., Wan-Jian, Y. (2019). Do Chalcogenide Double Perovskites Work as Solar Cell Absorbers: A First-Principles Study. *Chemistry of Materials*, 31, 244-250.
79. Kim, D., So, S., Ribbe, A., Liu, Y., Hu, W., Duzhko, V., Hayward, R., Emrick, T. (2019). Functional Polymers for Growth and Stabilization of CsPbBr₃ Perovskite Nanoparticles. *Chemical Communications*, 55, 1833-1836.
80. Lin, Y., Gritsenko, D., Liu, Q., Lu, X. & Xu, J. (2016). Recent advancements in functionalized paper-based electronics. *ACS Applied Material Interfaces*, 8, 20501-20515.
81. Zhang, Y., Zhang, L., Cui, K., Ge, S., Cheng, X., Yan, M., Yu, J., Liu, H. (2018). Flexible Electronics Based on Micro/Nanostructured Paper. *Advanced Materials*, 30, article number 1801588.

82. Hamed, M., Ainla, A., Güder, F., Christodouleas, D., Fernández-Abedul, M., Whitesides, G. (2016). Integrating Electronics and Microfluidics on Paper. *Advanced Materials*, 28, 5054-5063.
83. Ainla, A., Hamed, M., Güder, F., Whitesides, G. (2017). Electrical Textile Valves for Paper Microfluidics. *Advanced Materials*, 29, 1-10.
84. Güder, F., Ainla, A., Redston, J., Mosadegh, B., Glavan, A., Martin T., Whitesides, G. Paper-Based Electrical Respiration Sensor. (2016). *Angewandte Chemie (International ed. In English)*, 55, 5727-5732.
85. Gao, L., Chao, L., Hou, M., Liang, J., Chen, Y., Yu, H., Huang, W. (2019). Flexible, Transparent Nanocellulose Paper-Based Perovskite Solar Cells. *NPJ Flexible Electronics*, 3, 1-4.
86. Mason, T. (2011). Capacitor Dielectric and Piezoelectric Ceramics. Encyclopedia Britannica, Inc, 1970-1979.
87. Jeon, N, Lee, J., Noh, J., Nazeeruddin, M., Gratzel, M., Seok, S. (2013) . Efficient inorganic–organic hybrid perovskite solar cells based on pyrene arylamine derivatives as hole transporting materials. *Journal of The American Chemical Society*, 135, 19087-19090.
88. Chen, C., Kang, H., Hsiao, S., Yang, P., Chiang, K., Lin, H. (2014). Efficient and Uniform Planar-Type Perovskite Solar Cells by Simple Sequential Vacuum Deposition. *Advanced Materials*, 26, 6647-6652.
89. Wang, Q., Shao, Y., Dong, Q., Xiao, Z., Yuan, Y., Huang, J. (2014). Large Fill Factor Bilayer Iodine Perovskite Solar Cells Fabricated by a Low-Temperature Solution- Process. *Energy and Environmental Science*, 7, 2359-2365.

90. Dogan, F., Lin, H., Guilloix-Viry, M., Pena, O. (2015). Focus on Properties and Applications of Perovskites. *Science and Technology of Advanced Materials*, 16, article number 020301.
91. Lozano-Gorrín, A. (2012). Polycrystalline Materials. Theoretical and Practical Aspects. Universidad de La Laguna. Spain: In-Tech. 107-151.
92. Bian, Z., Zhu, J., Cao, F., Lu, Y., Li, H. (2009). *In situ* Encapsulation of Au Nanoparticles in Mesoporous Core-shell TiO₂ Microspheres with Enhanced Activity and Durability. *Chemical Communications*, 0, 3789-3791.
93. Hanaor, D., Chironi, I., Karatchevtseva, I., Triani, G., Sorrel, C. (2012). Single and Mixed Phase TiO₂ Powders Prepared by Excess Hydrolysis of Titanium Alkoxide. *Advances in Applied Ceramics*, 111, 149-158.
94. Hench, L., West, J. (1990). The Sol-gel Process. *Chemical Reviews*, 90, 33-72.
95. Brown, G., Wu, J. (2009). Third Generation Photovoltaics. *Laser and Photonics Reviews*, 3, 394-405.
96. Salim, T., Sun, S., Abe, Y., Krishna, A., Grimsdale, A., Ming Lam, Y. (2015). Perovskite-based Solar Cells: Impact of Morphology and Device Architecture on Device Performance. *Journal of Materials Chemistry A*, 3, 8943-8969.
97. H. Yu, F. Wang, F. Xie, W. Li, J. Chen and N. Zhao. (2014). The Role of Chlorine in the Formation Process of “CH₃NH₃PbI_{3-x}Cl_x” Perovskite. *Advanced Functional Materials*, 24, 7102-7108.
98. Zuo, C., Ding, L. (2014). An 80% FF Record Achieved for Perovskite Solar Cells by Using the NH₄Cl Additive. *Nanoscale*, 6, 9935-9938.

99. Liang, P., Liao, C., Chueh, C., Zuo, F., William, S., Xin, X., Lin, J., Jen, A. (2014). Additive Enhanced Crystallization of Solution-Processed Perovskite for Highly Efficient Planar-Heterojunction Solar Cells. *Advanced Materials*, 26, 3748-3754.
100. Leijtens, T., Stranks, S., Eperon, G., Lindblad, R., Johansson, E., McPherson, I., Rensmo, H., Ball, J., Lee, M., Snaith, H. (2014). Electronic Properties of Mesoporous Structured and Planar Organometal Halide Perovskite Films: Charge Trapping, Photodoping, and Carrier Mobility. *ACS Nano*, 8, 7147-7155.
101. Noel, N., Abate, A., Stranks, S., Parrott, E., Burlakov, V., Goriely, A., Snaith, H. (2014). Enhanced Photoluminescence and Solar Cell Performance Via Lewis Base Passivation of Organic-Inorganic Lead Halide Perovskites. *ACS Nano*, 8, 9815-9821.
102. Qiu, J., Qiu, Y., Yan, K., Zhong, M., Mu, C., Yan, H., Yang, S. (2013). All-solid-state Hybrid Solar Cells Based on a New Organometal Halide Perovskite Sensitizer and One-dimensional TiO₂ Nanowire Arrays. *Nanoscale*, 5, 3245-3248.
103. Liu, D., Kelly, T. (2014). Perovskite Solar Cells with a Planar Heterojunction Structure Prepared Using Room-temperature Solution Processing Techniques. *Nature Photonics*, 8, 133-138.
104. Liu, M., Johnston, M., Snaith, H. (2013). Efficient Planar Heterojunction Perovskite Solar Cells by Vapor Deposition. *Nature*, 501, 395-398.
105. Shi, T., Chen, J., Zheng, J., Li, X., Zhou, B., Cao, H., Wang, Y. (2016). Ti/Au Cathode for Electronic Transport Material-Free Organic-Inorganic Hybrid Perovskite Solar Cells. *Scientific Reports*, 6, article number 39132.

106. Huang, J., Yuan, Y., Shao, Y., Yan, Y. (2017). Understanding the Physical Properties of Hybrid Perovskites for Photovoltaic Applications. *Nature Review Materials*, 2, article number 17042.
107. Zhou, H., Chen, Q., Li, G., Luo, S., Song, T., Duan, H., Hong, Z., You, J., Liu, Y., Yang, Y. (2014). Interface Engineering of Highly Efficient Perovskite Solar Cells. *Science*, 345, 542-546.
108. Malinkiewicz, O., Yella, A., Lee, Y., Espallargus, G., Graetzel, M., Nazeeruddin, M., Bolink, H. (2014). Perovskite Solar Cells Employing Organic Charge-transport Layers. *Nature Photonics*, 8, 128-132.
109. Nie, W., Tsai, H., Asadpour, R., Blancon, J., Neukirch, A., Gupta, G., Crochet, J., Chhowalla, M., Tretiak, S., Alam, M., Wang, H., Mohite, A. (2015). High-Efficiency Solution-Processed Perovskite Solar Cells with Millimeter-Scale Grains. *Science*, 347, 522-525.
110. Zhu, C., Niu, X., Fu, Y., Li, N., Hu, C., Chen, Y., He, X., Na, G., Liu, P., Zai, H., Ge, Y., Lu, Y., Ke, X., Bai, Y., Yang, S., Chen, P., Li, Y., Sui, M., Zhang, L., Zhou, H., Chen, Q. (2016). Strain Engineering in Perovskite Solar Cells and its Impacts on Carrier Dynamics. *Nature Communications*, 10, article number 815.
111. Chen, H., Fu, W., Huang, C., Zhang, Z., Li, S., Ding, F., Shi, M., Li, C., Jen, A., Chen, H. (2017). Molecular Engineered Hole-Extraction Materials to Enable Dopant-Free, Efficient p-i-n Perovskite Solar Cells. *Advanced Energy Materials*, 7, article number 1700012.

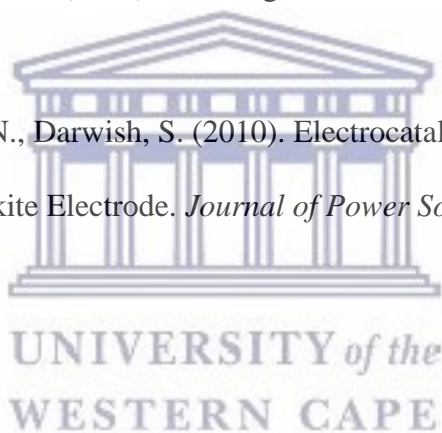


112. Rajagopal, A., Yang, Z., Jo, S., Braly, I., Liang, P., Hillhouse, H., Jen, A. (2017). Highly Efficient Perovskite-Perovskite Tandem Solar Cells Reaching 80% of the Theoretical Limit in Photovoltage. *Advanced Materials*, 29, article number 1702140.
113. Yadav, P., Dar, M., Arora, N., Alharbi, E., Giordano, F., Zakeeruddin, S., Gratzel, M. (2017). The Role of Rubidium in Multiple-Cation-Based High-Efficiency Perovskite Solar Cells. *Advanced Material*, 29, article number 1701077.
114. Zhou, D., Zhou, T., Tian, Y. (2018). Perovskite-based Solar Cells: Materials, Methods, and Future Perspectives. *Journal of Nanomaterials*, 2018, article number 8148072.
115. Docampo, P., Ball, J., Darwich, M., Eperon, G., Snaith, H. (2013). Efficient Organometal Trihalide Perovskite Planar Heterojunction Solar Cells on Flexible Polymer Substrates. *Nature Communications*, 4, article number 2761.
116. Liao, Y. (2007). Practical Electron Microscopy and Database.
117. Williams, D., Carter, C. (1996). Transmission Electron Microscopy. Springer-Verlag.
118. Wang, Z. (2000). Transmission Electron Microscopy of Shape-controlled Nanocrystals and their Assemblies. *Journal of Physical Chemistry*, 104, 1153-1175.
119. Kumar, A., Singh, N. (2015). Tribology Effect of Worn Out Surface of Aluminium Alloy Using Detonation Gun Spray Coating Process. *International Journal of Applied Sciences and Engineering Research*, 4, 152-165.
120. Bi, Z., Liang, Z., Xu, X., Chai, Z., Jin, H, Xu, D., Li, J., Li, M, Xu, G. (2017). Fast Preparation of Uniform Large Grain Size Perovskite Thin Film in Air Condition Via

Spray Deposition Method for Highly Efficient Planar Solar Cells. *Solar Energy Materials and Solar Cells*, 162, 13-20.

121. Klug, H., Alexander, L. (1974). X-ray Diffraction Procedures for Polycrystalline and Amorphous Materials. 2nd ed. Wiley, New York, 1- 892.
122. Brunauer, S., Emmett, P., Teller, E. (1938). Adsorption of Gases in Multimolecular Layers. *Journal of The American Chemical Society*, 60, 309-319.
123. Gosavi, P., Biniwale, R. (2010). Pure Phase LaFeO₃ Perovskite with Improved Surface Area Synthesized Using Different Routes and its Characterization. *Materials Chemistry and Physics*, 119, 324-329.
124. Stranks, S., Snaith, H. (2015). Metal-Halide Perovskites for Photovoltaic and Light-Emitting Devices. *Nature Nanotechnology*, 10, 391-402.
125. Monk, P. (2001). Fundamentals of Electroanalytical chemistry. Manchester Metropolitan University, Manchester, 1-384.
126. Jeng, J., Chiang, Y., Lee, M., Peng, S., Guo, T., Chen, P., Wen, T. (2013). CH₃NH₃PbI₃. Perovskite/Fullerene Planar-Heterojunction Hybrid Solar Cells. *Advanced Materials*, 25, 3727-3732.
127. Alfaraj, N., Mitra, S., Wu, F., Ajia I., Janjua, B., Prabaswara, A., Aljefri, R., Sun, H., Ng, T., Ooi, B., Roqan, I., Li, X. (2017). Photoinduced Entropy of InGaN/GaN p-i-n Double-heterostructure Nanowires. *Applied Physics Letters*, 110, article number 161110.
128. Elgrishi, N., Rountree, K., McCarthy, B., Rountree, E., Eisenhart, T., Dempsey, J. (2018). A Practical Beginner's Guide to Cyclic Voltammetry. *Journal of Chemical Education*, 95,197-206.

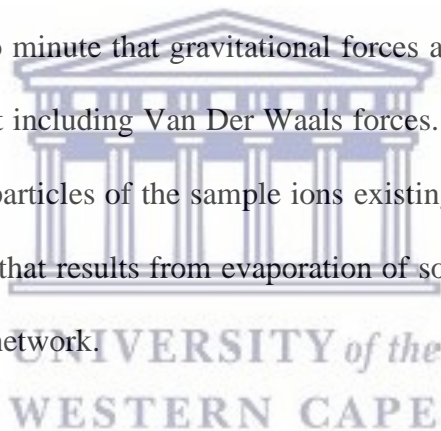
129. Hendel, S., Young, E. (2016). Introduction to Electrochemistry and the Use of Electrochemistry to Synthesize and Evaluate Catalysts for Water Oxidation and Reduction. *Journal of Chemical Education*, 93, 1951-1956.
130. Gardiner, D. (1989). Practical Raman Spectroscopy, Springer-Verlag.
131. Sfyri, G., Kumar, C., Sabapathi, G. 2015. Sub-Phthalocyanine as Hole Transporting Material for Perovskite Solar Cells. *Royal Society of Chemistry Advances*, 5, 69813-69818.
132. Lindholm, F., Fossum, J., Burgess, E. (1979). Application of the Superposition Principle to Solar-cell Analysis. *IEEE Transactions on Electron Devices*, 26, 165-171.
133. Coats, A., Redfern, J. (1963). Thermogravimetric Analysis: A Review. *Analyst*, 88, 906-924.
134. Galal, A., Atta, N., Darwish, S. (2010). Electrocatalytic Evolution of Hydrogen on a Novel SrPdO₃ Perovskite Electrode. *Journal of Power Sources*, 195, 3806-3809.



CHAPTER 3

EXPERIMENTAL PROCEDURES

Sol-gel method of nanoparticles synthesis has been used in all the perovskite materials synthesized in this research. The advantages of this technique include that it is cheap, uses lower temperatures and most importantly the product can be achieved as both bulk and thin (nano-scale) powders. The name “sol-gel” is derived from co-joining “sol” and “gel”. The name “sol” refers to a colloidal, in which the dispersed phase is so minute that gravitational forces are practically inapplicable, but only some surface charges exist including Van Der Waals forces. It can also be described as the molecular suspension of solid particles of the sample ions existing in a solvent. A “gel” may be described as a semi-rigid mass that results from evaporation of solvent from sol, leaving behind ions that unify in a continuous network.



(i) *SOCTPs*

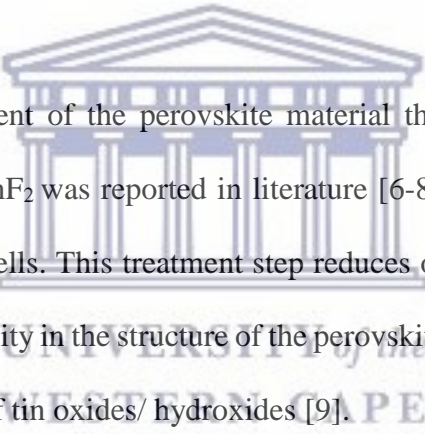
3.1 Chemical synthesis of $[\text{CH}_3\text{CH}_2\text{NH}_3]\text{SnI}_3$ perovskite

3.1.1 *Chemicals*

Ethylammonium iodide (98%, Sigma-Aldrich), tin (II) iodide (anhydrous, 99.99%, Sigma-Aldrich), tin (II) fluoride (99%, Sigma-Aldrich), N,N dimethylformamide (DMF, anhydrous, 99.5%, Sigma-Aldrich), ethanol (70%, Sigma-Aldrich).

3.1.2 Experimental procedure

The method used to synthesize this perovskite was modified from procedure used by Gruel *et al.* [1]. In a 25 mL round bottomed flask, 173 mg ethylammonium iodide perovskite precursor was reacted with 372 mg SnI₂ and 16 mg of SnF₂ in (1 mL, DMF, anhydrous, 99.8%, Sigma-Aldrich) at 125 °C with stirring for 1 h on a hot plate [1-5]. After the reaction, ethylammonium tin iodide perovskite (powder) was then collected, left at room temperature to cool and finally stored in 10 mL sample glass vial.



This procedure involves treatment of the perovskite material through addition of SnF₂ to the reaction mixture. Addition of SnF₂ was reported in literature [6-8] to help improve stability and PCE of tin-based photovoltaic cells. This treatment step reduces oxidation of Sn²⁺ to Sn⁴⁺. This oxidation impedes charge neutrality in the structure of the perovskite, which promotes degradation of the perovskite by formation of tin oxides/ hydroxides [9].

Chemical reaction:



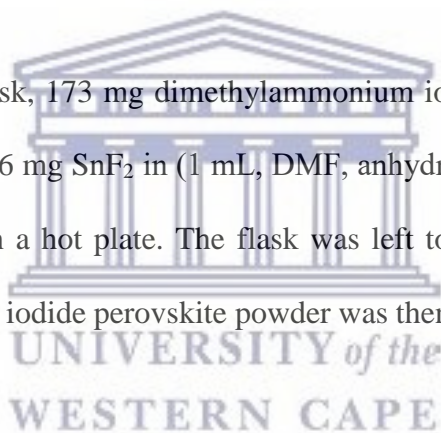
3.2 Chemical synthesis [(CH₃)₂NH₂]₃SnI₃ perovskite

3.2.1 Chemicals

Dimethylammonium iodide (Sigma-Aldrich), tin (II) iodide (anhydrous, 99.99%, Sigma-Aldrich), tin (II) fluoride (99%, Sigma-Aldrich), N,N dimethylformamide (DMF, anhydrous, 99.5%, Sigma-Aldrich), ethanol (70%, Sigma-Aldrich).

3.2.2 Experimental procedure

In a 25 mL round bottomed flask, 173 mg dimethylammonium iodide perovskite precursor was reacted with 372 mg SnI₂ and 16 mg SnF₂ in (1 mL, DMF, anhydrous, 99.8%, Sigma-Aldrich) at 125 °C with stirring for 1 h on a hot plate. The flask was left to cool at ambient temperature. Finally, dimethylammonium tin iodide perovskite powder was then collected and stored in 10 mL sample glass vial.



Chemical reaction:



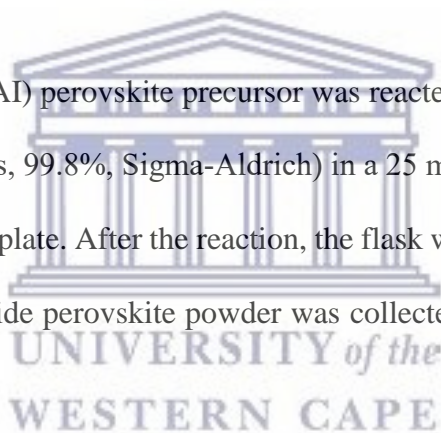
3.3 Chemical synthesis of GAsnI₃ perovskite

3.3.1 Chemicals

Guanidinium iodide (99%, Sigma-Aldrich), tin (II) iodide (anhydrous, 99.99%, Sigma-Aldrich), tin (II) fluoride (99%, Sigma-Aldrich), N,N dimethylformamide (DMF, anhydrous, 99.5%, Sigma-Aldrich), ethanol (70%, Sigma-Aldrich).

3.3.2 Experimental procedure

187 mg guanidinium iodide (GAI) perovskite precursor was reacted with 372 mg SnI₂ and 16 mg SnF₂ in (1 mL, DMF, anhydrous, 99.8%, Sigma-Aldrich) in a 25 mL round bottomed flask at 125 °C with stirring for 1 h on a hot plate. After the reaction, the flask was cooled at room temperature and finally guanidinium tin iodide perovskite powder was collected and stored in 10 mL sample glass vial.



Chemical reaction:



(ii) MOCTPs

3.4 Chemical synthesis of [GA][CH₃CH₂NH₃]SnI₃ perovskite

3.4.1 Chemicals

Guanidinium iodide (99%, Sigma-Aldrich), ethylammonium iodide (98%, Sigma-Aldrich), tin (II) iodide (anhydrous, 99.99%, Sigma-Aldrich), tin (II) fluoride (99%, Sigma-Aldrich), N,N dimethylformamide (DMF, anhydrous, 99.5 %, Sigma-Aldrich), ethanol (70%, Sigma-Aldrich).

3.4.2 Experimental procedure

Mixed-organic-cation mole ratio of 1:1 guanidinium ion to ethylammonium ion was used to synthesize the desired MOCTP. 93.5 mg guanidinium iodide (GAI) and 86.5 mg ethylammonium iodide perovskite precursors were reacted with 372 mg SnI₂ and 16 mg SnF₂ in (1 mL, DMF, anhydrous, 99.8 %, Sigma-Aldrich) in a 25 mL round bottomed flask at 125 °C with stirring for 1 h on a hot plate. After the reaction, the flask was cooled at room temperature and finally guanidinium ethylammonium tin iodide perovskite powder was collected and stored in 10 mL sample glass vial.

Chemical reaction:



3.5 Chemical synthesis of [GA][(CH₃)₂NH₂]SnI₃ perovskite

3.5.1 Chemicals

Guanidinium iodide (99%, Sigma-Aldrich), dimethylammonium iodide (Sigma-Aldrich), tin (II) iodide (anhydrous, 99.99%, Sigma-Aldrich), tin (II) fluoride (99%, Sigma-Aldrich), N,N dimethylformamide (DMF, anhydrous, 99.5% Sigma-Aldrich), ethanol (70%, Sigma-Aldrich).

3.5.2 Experimental procedure

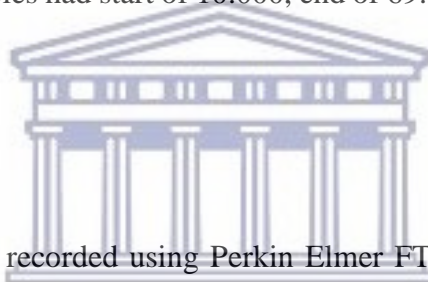
Mixed organic cation mole ratio of 1:1 guanidinium ion to dimethylammonium ion was used to synthesize this MOCTP. 93.5 mg guanidinium iodide (GAI) and 86.5 mg dimethylammonium iodide perovskite. After the reaction, the flask was cooled at room temperature and finally guanidinium ethylammonium precursors were reacted with 372 mg SnI₂ and 16 mg SnF₂ in (1 mL, DMF, anhydrous, 99.8%, Sigma-Aldrich) in a 25 mL round bottomed flask at 125 °C with stirring for 1 h on a hot plate. The perovskite powder was collected and stored in 10 mL sample glass vial.

Chemical reaction:



3.6 Characterization of the perovskites

HR SEM instrument (Auriga Zeiss) was used to study microscopic properties of $[\text{CH}_3\text{CH}_2\text{NH}_3]\text{SnI}_3$, $[(\text{CH}_3)_2\text{NH}_2]\text{SnI}_3$, $[\text{GA}][\text{CH}_3\text{CH}_2\text{NH}_3]\text{SnI}_3$ and $[\text{GA}][(\text{CH}_3)_2\text{NH}_2]\text{SnI}_3$ powder samples. Tecnai F20 instrument was used to capture HR TEM images of the 5 powder samples of perovskites. All SAXS results were recorded using Anton Paar SAXS space system. The SAXS analysis experiments were performed on liquid samples. Concentration of 0.005 M of all samples analyzed were prepared in N,N dimethylformamide (DMF, anhydrous, 99.5%, Sigma-Aldrich) solvent. All XRD samples had start of 10.000, end of 69.994, step of 0.034 and step-time of 96.8 recorded at 25 °C.



All FTIR results reported were recorded using Perkin Elmer FTIR spectrometer, spectrum two model. The samples were in powder form, grounded and pressed into a pellet before they were recorded. Potassium bromide (KBr) was used as the background for all the sample that were analyzed. The ^{13}C CPMAS spectra were recorded on a 11.4 Tesla Bruker Avance III HD NMR spectrometer, operating at frequencies of 500 MHz (^1H) and 125 MHz (^{13}C). Magic Angle Spinning (MAS) frequency was 5 kHz for all experiments. The samples were packed into standard zirconia 4mm rotors (Bruker). The standard CP sequence in the Bruker pulse program was used with ^1H 90° pulse length 2.5 μs , contact time 1.5 ms, for 1000 scans. A recycle delay of 7s was used for all CPMAS experiments and during acquisition, SPINAL64 decoupling at field strength 100 kHz was applied on ^1H channel. Chemical shifts were referenced to external adamant, using the downfield signal at 38.48 ppm relative to TMS (^{13}C).

All UV-Vis experiments were recorded using Epsilon 963 instrument. Samples of all materials analyzed were dissolved in DMF solvent before each experiment was done. All CV experiments were recorded using PalmSens electrochemical work station. Three electrode system was adopted, where the working electrode was glassy carbon electrode (GCE, surface area = 0.071 cm^2), counter electrode was platinum wire (diameter = 1.0 mm) and reference electrode was Ag/AgCl (saturated KCl solution) electrode [6, 7]. 5 mL of all electrolytes analyzed were measured into 10 mL electrochemical cell and de-aerated with nitrogen gas for at least 2 min. The working electrodes were polished before each experiment using alumina-micro polish slurries (1.0 mm, 0.3 mm and 0.05 mm) on polishing pads, sonicated for 10 min in ethanol and in de-ionized water respectively, and finally left to air-dry.



EIS experiments were recorded using CH electrochemical work station. Conventional three electrode system was adopted, where the working electrode was GCE (surface area = 0.071 cm^2), the counter electrode was platinum wire (diameter = 1.0 mm) and the reference electrode was Ag/AgCl (saturated KCl solution) electrode. 5 mL of electrolyte was measured into a 10 mL electrochemical cell and de-aerated with nitrogen gas for 2 min. The GCEs were polished pre-experiment using alumina-micro polish slurries (1.0 mm, 0.3 mm and 0.05 mm) on polishing pads, sonicated for 10 min in ethanol and in de-ionized water respectively, and finally left to air-dry. The experiments were all recorded over frequency range of 0 - 20 kHz [8, 9].

3.7 Fabrication of photovoltaic cell devices

3.7.1 Chemicals

Ethylammonium iodide (98%, Sigma-Aldrich), tin (II) iodide (anhydrous, 99.99%, Sigma-Aldrich), tin (II) fluoride (99%, Sigma-Aldrich), N,N dimethylformamide (DMF, anhydrous, 99.5%, Sigma-Aldrich), ethanol (70%, Sigma-Aldrich), dimethylammonium iodide (Sigma-Aldrich), guanidinium iodide (99%, Sigma-Aldrich), dichloromethane, PCBM, PEDOT:PSS.

Preparation of perovskite precursor solutions:

(i) SOCTPs

3.7.2 Procedure for synthesis of GASnI_3 precursor

Precursor solution for GASnI_3 perovskite was prepared by dissolving 372 mg SnI_2 , 16 mg SnF_2 and 93.5 mg guanidinium iodide in N,N-dimethylformamide (1 mL, DMF, anhydrous, 99.8%, Sigma-Aldrich). After mixing, the solution was placed on a hotplate at 100 °C until the tin precursor fully dissolved.

3.7.3 Procedure for synthesis of $[\text{CH}_3\text{CH}_2\text{NH}_3]\text{SnI}_3$ precursor

Preparation of $[\text{CH}_3\text{CH}_2\text{NH}_3]\text{SnI}_3$ precursor involved dissolving 372 mg SnI_2 , 16 mg SnF_2 and 174 mg ethylammonium iodide in N,N-dimethylformamide (1 mL, DMF, anhydrous, 99.8%, Sigma-Aldrich). The solution was placed on a hotplate at 100 °C until tin precursor was fully dissolved.

3.7.4 Procedure for synthesis of $[(CH_3)_2NH_2]SnI_3$ precursor

Precursor solution of $[(CH_3)_2NH_2]SnI_3$ was prepared by dissolving 372 mg SnI_2 , 16 mg SnF_2 and 174 mg dimethylammonium iodide in N,N-dimethylformamide (1 mL, DMF, anhydrous, 99.8%, Sigma-Aldrich). Undissolved tin from the solution was dissolved by placing the solution on hotplate at 100 °C.

(ii) MOCTPs

3.7.5 Procedure for synthesis of $[GA][(CH_3)_2NH_2]SnI_3$ precursor

$[GA][(CH_3)_2NH_2]SnI_3$ perovskite precursor solution was prepared by dissolving 372 mg SnI_2 , 16 mg SnF_2 and a mixture of 93.5 mg guanidinium iodide and 86.5 mg dimethylammonium iodide in N,N-dimethylformamide (1 mL, DMF, anhydrous, 99.8%, Sigma-Aldrich). The solution was placed on a hotplate at 100 °C until the tin precursor fully dissolved.

3.7.6 Procedure for synthesis of $[GA][CH_3CH_2NH_3]SnI_3$ precursor

Precursor solution of $[GA][CH_3CH_2NH_3]SnI_3$ was prepared by dissolving 372 mg SnI_2 , 16 mg SnF_2 , 93.5 mg guanidinium iodide and 86.5 mg ethylammonium iodide in N,N-dimethylformamide (1 mL, DMF, anhydrous, 99.8%, Sigma-Aldrich). The precursor solution was placed on hotplate at 100 °C to get tin fully dissolved.

3.7.7 Assembly of photovoltaic solar cell devices

ITO coated glass substrates were sonicated in hellmanex solution for 10 min. Thereafter, the substrates were rinsed twice in boiling water. The second sonication of the substrates was done in isopropanol for 10 min, which again was followed by rinsing them in boiling water twice. The cleaning process was completed by blowing the substrates with nitrogen gas.

Planar device architecture was adopted [10-14] to prepare devices that employed GASnI_3 , $[\text{CH}_3\text{CH}_2\text{NH}_3]\text{SnI}_3$, $[(\text{CH}_3)_2\text{NH}_2]\text{SnI}_3$, $[\text{GA}][\text{CH}_3\text{CH}_2\text{NH}_3]\text{SnI}_3$ and $[\text{GA}][(\text{CH}_3)_2\text{NH}_2]\text{SnI}_3$ perovskites as light absorbing materials. 30 μL PEDOT:PSS solution was deposited onto the pre-cleaned ITO coated glass substrates at 5000 rpm through spin coating for 30 s, which was followed by 10 min annealing on a hot plate at 140 °C [2, 15]. On top of PEDOT:PSS, 50 μL of the perovskite precursor solutions prepared in sections above were spin coated at 4000 rpm for 30 s with subsequent annealing for 10 min at 100 °C. 50 μL PCBM (2% wt. in dichlorobenzene) [16] was spin coated on top of the perovskite at 3000 rpm for 100 s, and subsequently annealed at 100 °C [17]. Finally, 75 nm layer of aluminium was deposited by thermal evaporation. Finally, the external quantum efficiency (EQE) of the solar cell devices were measured using fourier transform spectroscopy [18].

Adopted device architecture:

A planar device architecture was used to fabricate SOCTPs and MOCTPs-based photovoltaic cells, a method that was used by Chen *et al.* [2]. Figure 3.1 shows the planar architecture of the devices that were fabricated in this research.

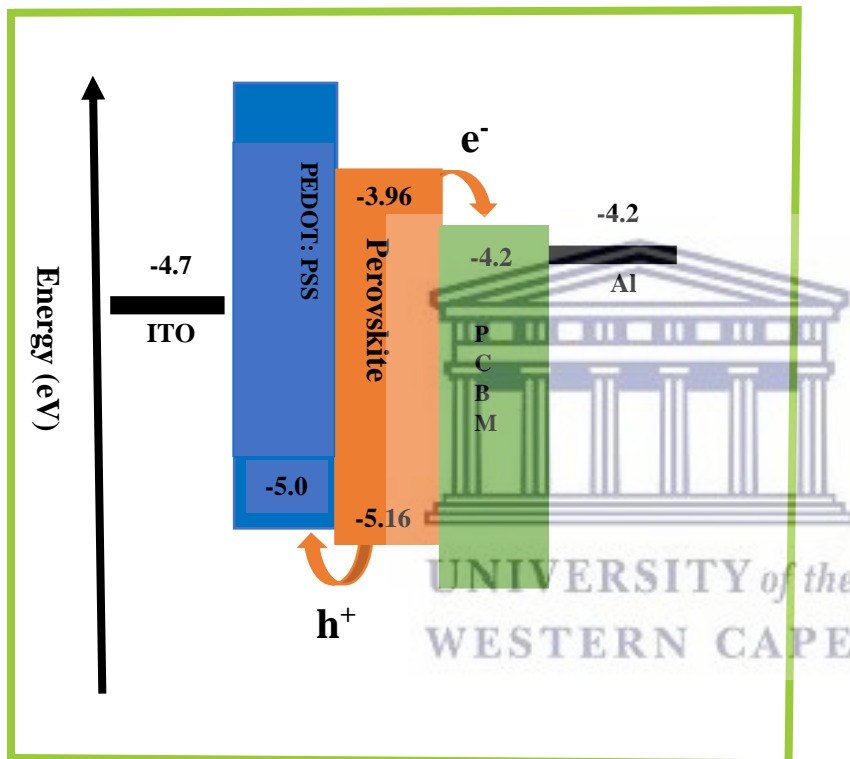


Figure 3.1: Planar structure device architecture adopted for perovskite solar cell (glass/ITO/PEDOT:PSS/perovskite layer/PCBM/Al).

3.8 References

1. Greul, E., Docampo, P., Bein, T. (2017). Synthesis of Hybrid Tin Halide Perovskite Solar Cells with Less Hazardous Solvents: Methanol and 1,4-Dioxane. *Z. Journal of General and Inorganic Chemistry*, 643, 1704-1711.
2. Chen, C., Bae, S., Chang, W, Hong, Z., Li, G., Chen, Q., Zhou, H., Yang, Y. (2015). Perovskite/Polymer Monolithic Hybrid Tandem Solar Cells Utilizing a Low-temperature, Full Solution Process. *Materials Horizons*, 2, 203-211.
3. Barwick, M., Ackzough, F., Freerer, R. (2006). Structure and Dielectric Properties of Perovskite Ceramics in the System $\text{Ba}(\text{Ni}_{1/3}\text{Nb}_{2/3})\text{O}_3$ - $\text{Ba}(\text{Zn}_{1/3}\text{Nb}_{2/3})\text{O}_3$. *Journal of the European Ceramic Society*, 26, 1767-1773.
4. Kim, H., Lee, C, Im, J., Lee, K., Moehl, T., Marchioro, A., Moon, S., Humphry-Baker, R., Yum, J., Moser, J., Gratzel, M., Park, N. (2012). Lead Iodide Perovskite Sensitized All-Solid-State Submicron Thin Film Mesoscopic Solar Cell with Efficiency Exceeding 9%. *Scientific Reports*, 2, article number 591.
5. Zhang, W., Saliba, M., Moore, D., Pathak, S., Horantner, M., Stergiopoulos, T., Stranks, S., Eperon, G., Alexander-Webber, J., Abate, A, Sadhanala, A., Yao, S., Chen, Y., Friend, R., Estroff, L., Wiesner, U., Snaith, H. (2015). Ultrasmooth Organic-Inorganic Perovskite Thin-Film Formation and Crystallization for Efficient Planar Heterojunction Solar cells. *Nature Communications*, 6, article number 6142.
6. Chung, I., Lee, B., He, J., Chang, R., Kanatzidis, M. (2012). All-solid-state Dye-sensitized Solar Cells with High Efficiency. *Nature*, 485, 486-489.

7. Ke, W., Zhao, D., Grice, C., Cimaroli, A., Fang, G., Yan, Y. (2015). Efficient Fully-vacuum-processed Perovskite Solar Cells Using Copper Phthalocyanine as Hole Selective Layers. *Journal of Material Chemistry A*, 3, 23888-23894.
8. Koh, T., Krishnamoorthy, T., Yantara, N. et al. (2015). Formamidinium Tin-based Perovskite with Low E_g for Photovoltaic Applications. *Journal of Material Chemistry A*, 3, 14996-15000.
9. Noel, N., Stranks, S., Abate, A., Wehrenfennig, C., Guarnera, S., Haghighirad, A., Sadhanala, A., Eperon, G., Pathak S., Johnston, M., Petrozza, A., Herz, L., Snaith, H. (2014). Lead- Free Organic-Inorganic Tin Halide Perovskites for Solar Cell Applications. *Energy and Environmental Science*, 7, 3060-3068.
10. Cho, H., Jeong, S., Park, M., Kim, Y., Wolf, C., Lee, C., Heo, J., Sadhanala, A., Myoung, N., Yoo, S., Im, S., Friend, R., Lee, T. (2015). Overcoming the Electroluminescence Efficiency Limitations of Perovskite Light-Emitting Diodes. *Science*, 2015, 350, 1222-1225.
11. Su A Rez, I., Ju A Rez-P E Rez, E., Bisquert, J., Mora-Ser O, I., Mart I Nez-Pastor, J. (2015). Electrochemical Impedance Analysis of Perovskite-Electrolyte Interfaces. *Advanced Materials*, 27, article number 6157.
12. Ball, J., Stranks, S., Horantner, M., Huttner, S., Zhang, W., Crossland, E., Ramirez, I., Riede, M., Johnston, M., Friend, R., Snaith, H. (2015). Optical Properties and Limiting Photocurrent of Thin-Film Perovskite Solar Cells. *Energy and Environmental Science*, 2015, 8, 602-609.
13. Pazos-Outon, L., Szumilo, M., Lamboll, R., Richter, J., Crespo-Quesada, M., Abdi-Jalebi, M., Beeson, H., Vrucinic, M., Alsari, M., Snaith, H., Ehrler, B., Friend, R., Deschler, F.

- (2016). Photon Reabsorption Masks Intrinsic Bimolecular Charge-Carrier Recombination in $\text{CH}_3\text{NH}_3\text{PbI}_3$ Perovskite. *Science*, *351*, 1430-1433.
14. Chen, C., Kang, H., Hsiao, S., Yang, P., Chiang, K., Lin, H. (2014). Efficient and Uniform Planar-Type Perovskite Solar Cells by Simple Sequential Vacuum Deposition. *Advanced Materials*, *26*, 6647-6652.
15. Eperon, G., Burlakov, V., Docampo, P., Goriely, A., Snaith, H. (2014). Morphological Control for High Performance, Solution-Processed Planar Heterojunction Perovskite Solar Cells. *Advanced Functional Materials*, *24*, 151-157.
16. Liu, D., Kelly, T. (2014). Perovskite Solar Cells with a Planar Heterojunction Structure Prepared Using Room-Temperature Solution Processing Techniques. *Nature Photonics*, *8*, 133-138.
17. You, J., Hong, Z., Yang, Y., Chen, Q., Cai, M., Song, T., Chen, C., Lu, S., Liu, Y., Zhou, H., Yang, Y. (2014). Low-Temperature Solution-Processed Perovskite Solar Cells with High Efficiency and Flexibility. *ACS Nano*, *8*, 1674-1680.
18. Barrows, A., Pearson, A., Kwak, C., Dunbar, A., Buckley, A., Lidzey, D. (2014). Efficient Planar Heterojunction Mixed-Halide Perovskite Solar Cells Deposited via Spray Deposition. *Energy Environmental Science*, *7*, 2944.
19. Zhou, H., Shi, Y., Dong, Q., Zhang, H., Ying, Y., Wang, K., Du, Y., Ma, T. (2014). Hole-Conductor-Free, Metal-Electrode-Free $\text{TiO}_2/\text{CH}_3\text{NH}_3\text{PbI}_3$ Heterojunction Solar Cells Based on a Low Temperature Carbon Electrode. *Journal of Physical Chemistry Letters*, *5*, 3241-3246.
20. Zuo, C., Ding, L. (2014). An 80.11% FF Record Achieved for Perovskite Solar Cells by Using the NH_4Cl Additive. *Nanoscale*, *6*, 9935-9938.

21. Xiao, M., Huang, F., Huang, W., Dkhissi, Y., Zhu, Y., Etheridge, J., Gray-Weale, A., Bach, U., Cheng, Y., Spiccia, L. (2014). A Fast Deposition-Crystallization Procedure for Highly Efficient Lead Iodide Perovskite Thin-Film Solar Cells. *Angew Chem Int Ed*, 126, 10056-10061.
22. Vanecek, M., Poruba, A. (2002). Fourier-Transform Photocurrent Spectroscopy of Perovskite Solar Cells. *Applied Physical Chemistry Letters*, 80, 719-721.



UNIVERSITY *of the*
WESTERN CAPE

CHAPTER 4

RESULTS AND DISCUSSION

Photophysical characterization

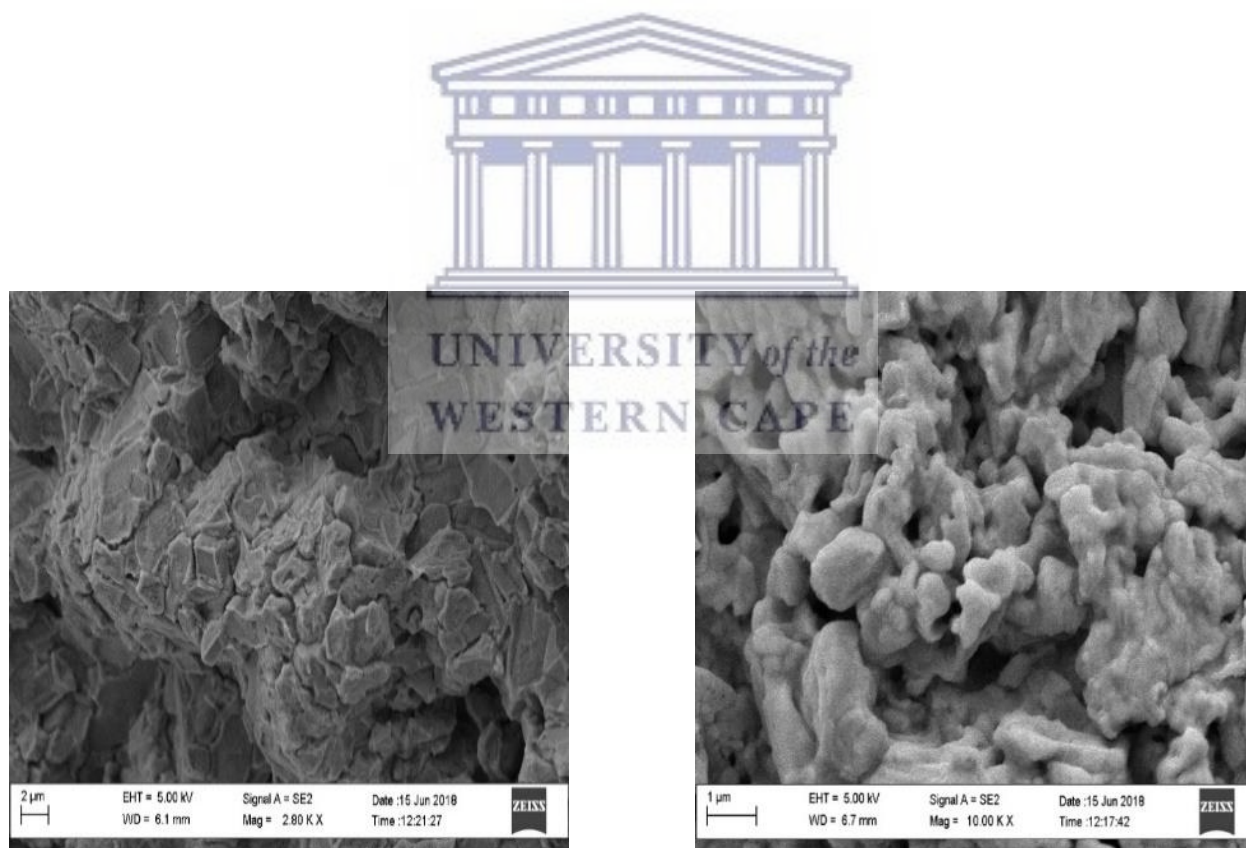
4.1 High Resolution Scanning Electron Microscopy (HR SEM) and Energy-dispersive X-ray Spectroscopy (EDS) results.

The 5 perovskite materials show good crystallinity and cubic shapes, well characteristic of perovskites reported in literature which exhibit tetragonal and hexagonal cubic structures [1, 2]. Variations in morphology of perovskites gives rise to different performances in the solar cell devices fabricated [3]. The surface morphology of (a) $[(\text{CH}_3)_2\text{NH}_2]\text{SnI}_3$ and (c) GASnI_3 shows good homogeneity as there are no pinholes in between the single crystals, however (b) $[\text{CH}_3\text{CH}_2\text{NH}_3]\text{SnI}_3$, (d) $[\text{GA}][(\text{CH}_3)_2\text{NH}_2]\text{SnI}_3$ and (e) $[\text{GA}][\text{CH}_3\text{CH}_2\text{NH}_3]\text{SnI}_3$ exhibit some pinholes between their crystals. Pinholes influence the efficiency of solar cells, they specifically affect the short circuit current and open circuit voltage in contrasting ways [4].

Zhang *et al.* reported on MAPbI_3 perovskites that exhibit no pinholes in their morphology, achieved by dropping ethyl acetate antisolvent onto the precursor films during spin coating [5]. Addition of ethyl acetate was reported to play a role in regulating the nucleation, hence improving compactness of the thin-film, improving grain size, while defect density reduced which realized high power conversion efficiency, owing to reduced electron recombination[5]. Mixing organic

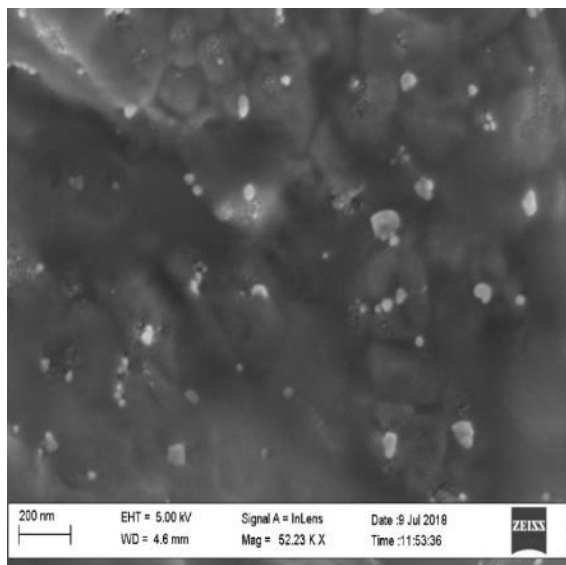
cations improved the quality of the perovskite grain size [6-7] as seen in HR SEM images of the various single and mixed-organic-cation tin halide perovskites (figure 4.1).

Mixed hybrid perovskites usually suffer from inhomogeneity of thin film due to composition separation and/or thermal stress [8]. Substantial chemical mismatch among components, and non-equilibrium growth may occur during film formation. Inhomogeneity correlates to residual strains, which result in lattice distortion of microscopic crystal structure, and further affect optoelectronic properties of the perovskite [8-13].

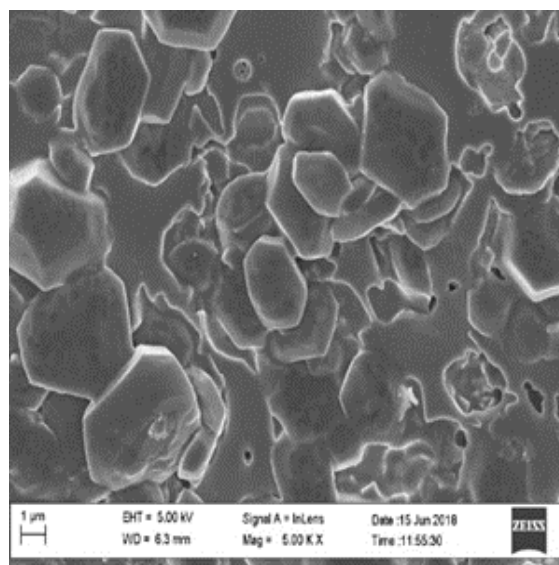


(a) $[(\text{CH}_3)_2\text{NH}_2]\text{SnI}_3$

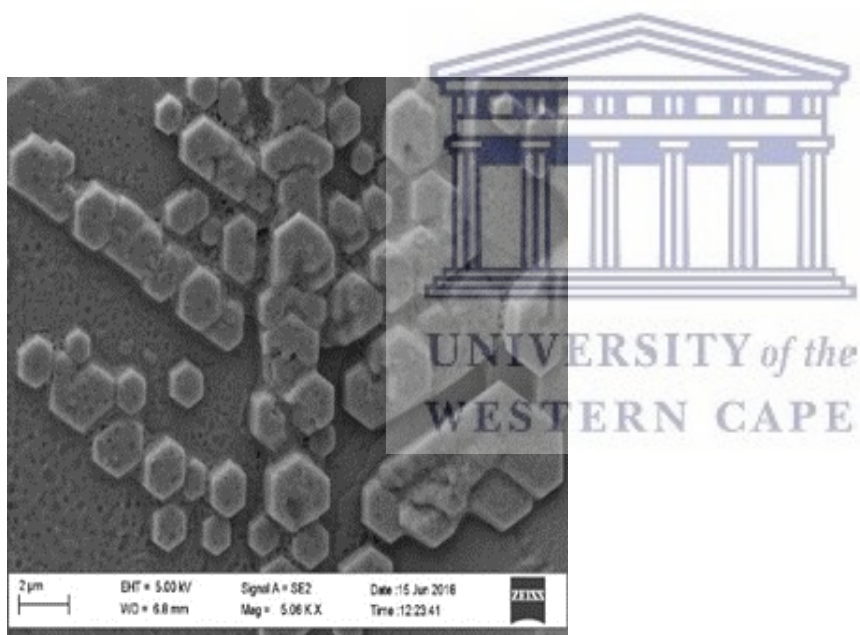
(b) $[\text{CH}_3\text{CH}_2\text{NH}_3]\text{SnI}_3$



(c) GASnI₃



(d) [GA][(CH₃)₂NH₂]SnI₃

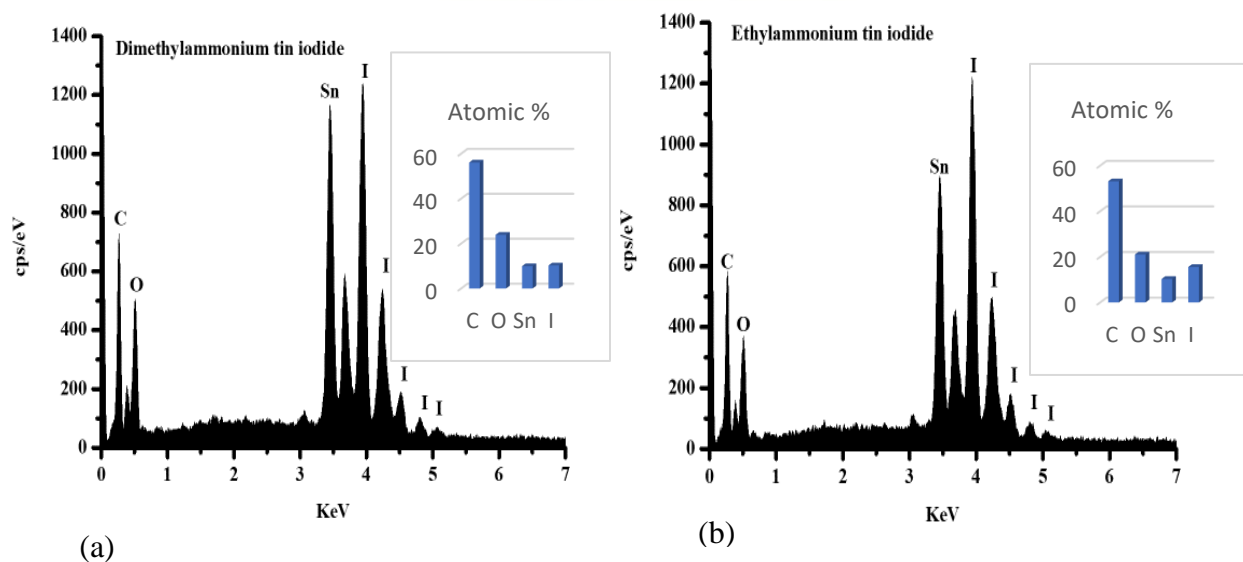
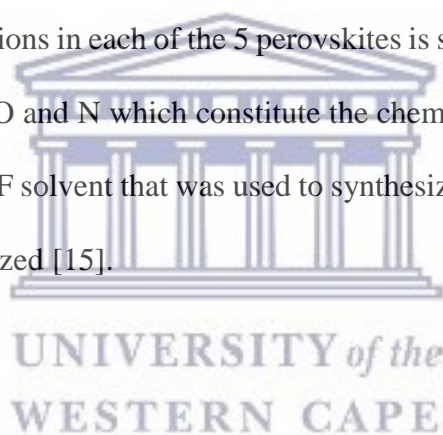


(e) [GA][CH₃CH₂NH₃]SnI₃

Figure 4.1: HR SEM images for the various perovskites taken at different resolutions.

EDS

EDS, in co-junction with HR SEM is used to give the elemental composition of a sample. When the sample is struck with a beam of electrons, some electrons are ejected from the atoms of the sample's surface. The electron vacancies left behind are in turn filled by electrons from a higher energy state, subsequently, an X-ray is emitted to make a balance between the energy in the two electron states. The energy that is emitted is dependent on the characteristics of the element from which it was emitted [14]. The EDS detects the X-rays that the sample emits during this process. The elemental composition in a sample volume is given by spectrum of X-ray energy versus counts. The elemental compositions in each of the 5 perovskites is shown in is shown in figure 4.2. The elements include Sn, I, C, O and N which constitute the chemical formula of the compounds except O which is from the DMF solvent that was used to synthesize them. Insets show the atomic percentage in the samples analyzed [15].



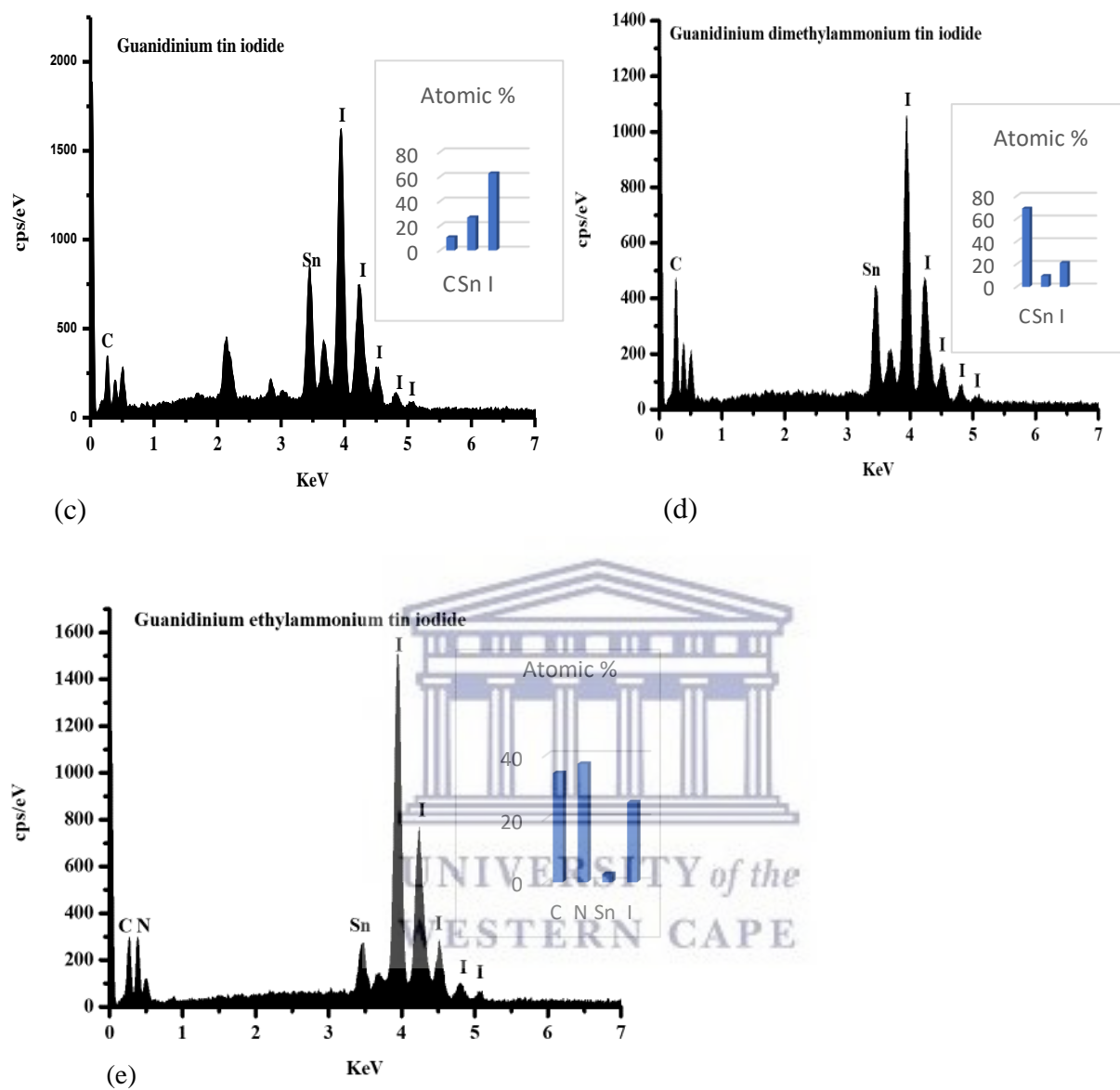
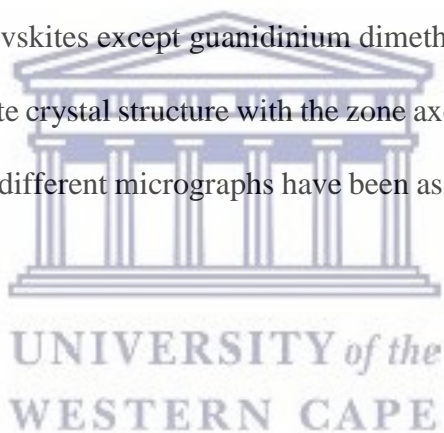


Figure 4.2: EDS spectra for the 5 perovskites.

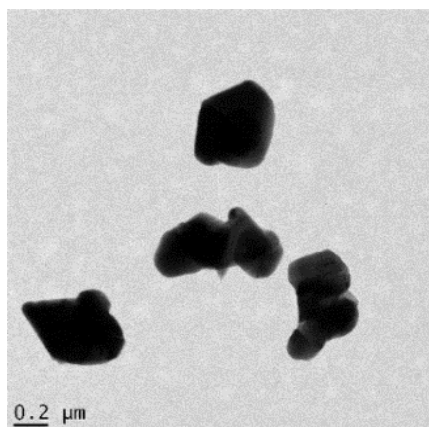
4.2 High Resolution Transmission Electron Microscopy (HR TEM) results

The polycrystallinity, grain sizes and grain boundaries of perovskite films have a strong influence on charge generation and transport, carrier dynamics and overall power conversion efficiency of the photovoltaic solar cell [16]. The images of all the perovskites showed that the materials are polycrystalline. Selected area electron diffraction (SAED) gives some useful structural information of the sample that is used to complement XRD technique. The SAED obtained for the 5 perovskites show that the perovskite materials are highly crystalline, which is shown by the electron diffraction rings in the micrograph [17]. Sharp diffraction spots seen in the (SAED) patterns observed in all the perovskites except guanidinium dimethylammonium tin iodide can be indexed to a tetragonal perovskite crystal structure with the zone axes (ZAs) of (110) or (001) [18]. Electron diffraction rings in the different micrographs have been assigned to specific lattice planes of the perovskites [18].

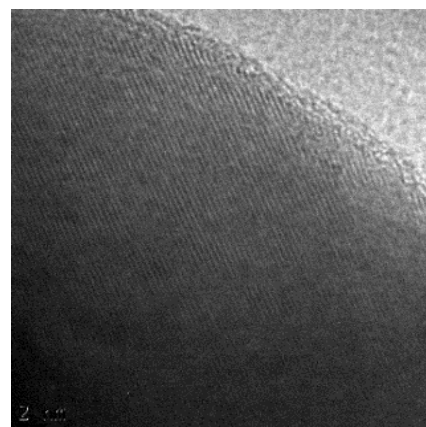


4.2.1 HR TEM for ethylammonium tin iodide

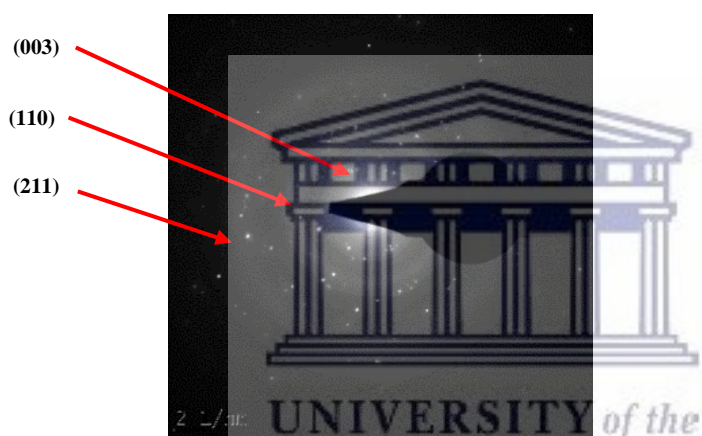
Average particle size of the perovskite was found to be 109.0 nm, d spacing of lattice plane was calculated to be 0.23 nm which corresponds to (310) lattice plane. The SAED electron diffraction rings corresponding to (003), (110) and (211) lattice planes were observed. Figure 4.3 shows the HR TEM images of the perovskite at different resolutions.



(a)



(b)



(c)

Figure.4.3: (a) and (b) HR TEM images for $[\text{CH}_3\text{CH}_2\text{NH}_3]\text{SnI}_3$ at different resolutions and (c) SAED for $[\text{CH}_3\text{CH}_2\text{NH}_3]\text{SnI}_3$.

4.2.2 HR TEM for dimethylammonium tin iodide

87.8 nm average perovskite particle size was obtained, and 0.29 nm d spacing of lattice plane which corresponds to (220) lattice plane. HR TEM micrographs taken at different resolutions of the perovskite are shown in figure 4.4 below.

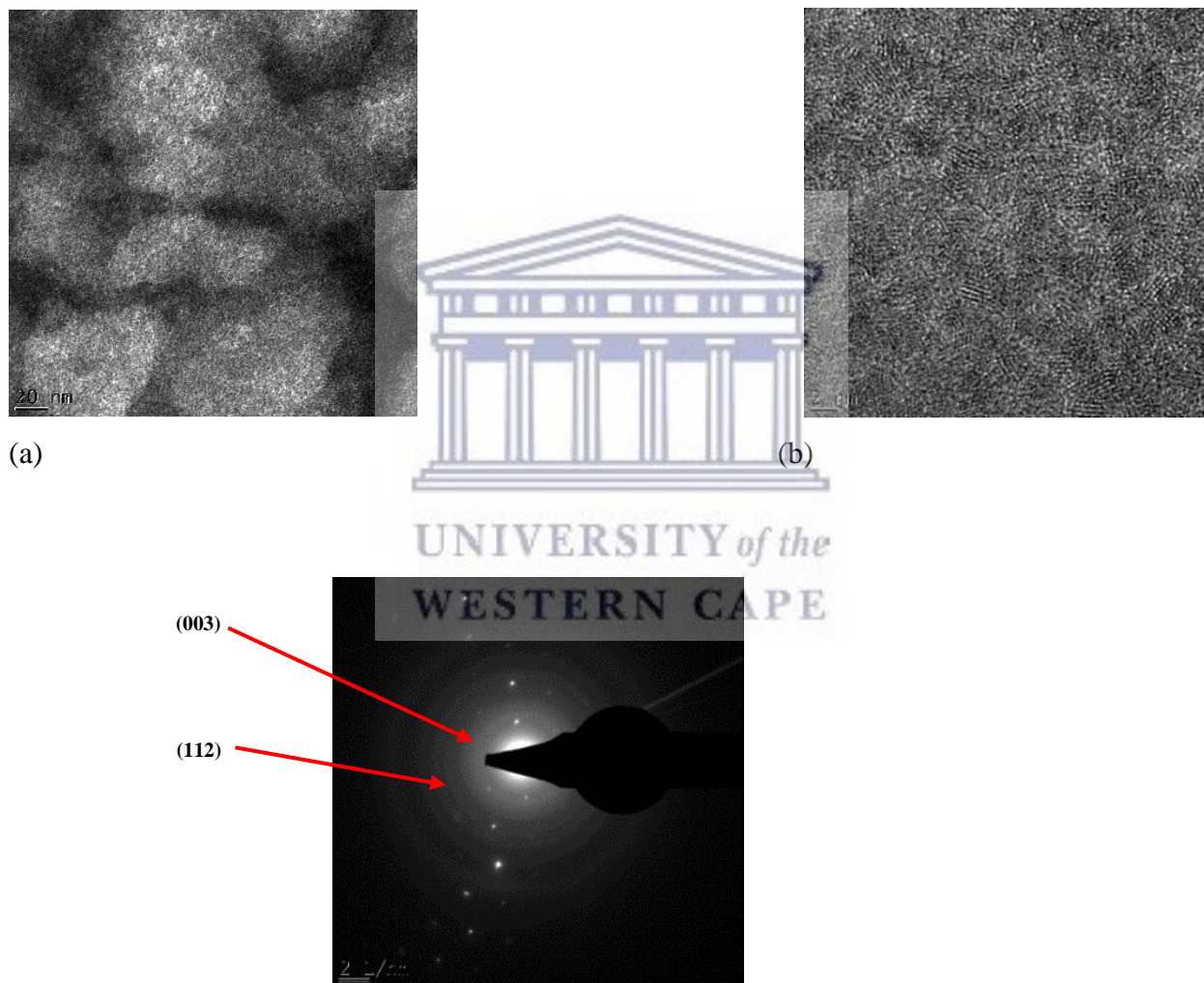
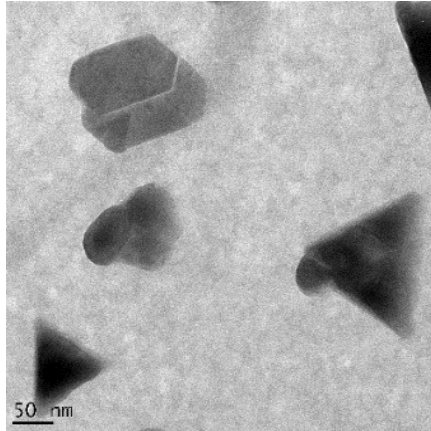


Figure 4.4: (a) and (b) HR TEM images for $[(\text{CH}_3)_2\text{NH}_2]\text{SnI}_3$ at different resolutions and (c) SAED for $[(\text{CH}_3)_2\text{NH}_2]\text{SnI}_3$.

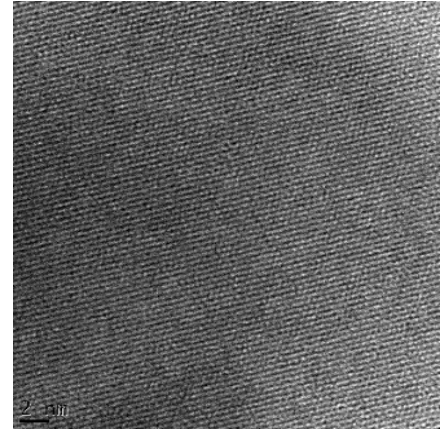
4.2.3 HR TEM for guanidinium tin iodide

Two particle shapes were observed, trigonal and hexagonal. The same observation was reported by Darriet *et al.* whereby hexagonal perovskite-type materials present more than one particle shape, owing to the stacking of mixed layers [19]. This is observed in materials that exhibit 2-D crystals derived from (ABX₃) structure. This phenomenon is not strange since guanidinium tin iodide is derived from this basic perovskite structure. Various phases of perovskite crystal structures may occur from mixed stacking of the layers. Perovskite hexagonal polytypes may form compounds that adopt new types of structures derived from mixed stacking of the layers [20]. A new structure is formed, which is explained to be due to re-ordering of the stacking sequence in the perovskite cubic shape. Formation and decomposition of the perovskite is reversible where the oxidation of tin is the driving force for these processes at intermediate temperatures [21].

The diffraction intensity of the perovskite tetragonal phase was correlated with a direct increase in the SnI₂ trigonal phase intensity. This correlation indicates that the structure is a stacked architecture, with SnI₂ formed on top of the underlying perovskite layers [22]. The average particle sizes were found to be 94.0 nm and 102.4 nm respectively. The d spacing of lattice plane was 0.23 nm which was assigned to (310) lattice plane. Figure 4.5 shows HR TEM micrographs of the perovskite at different resolutions.



(a)



(b)

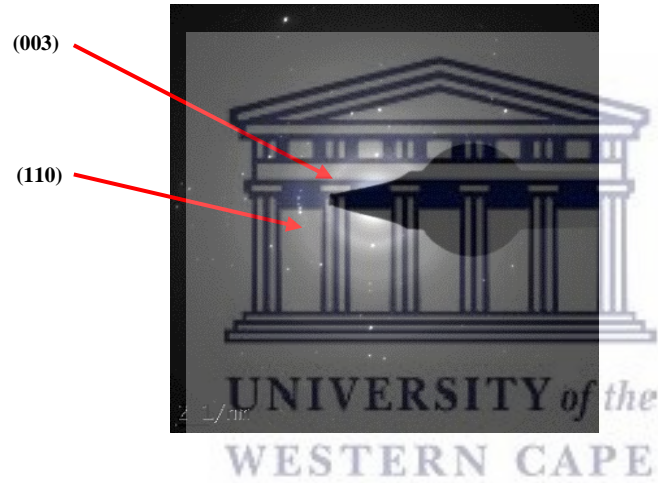
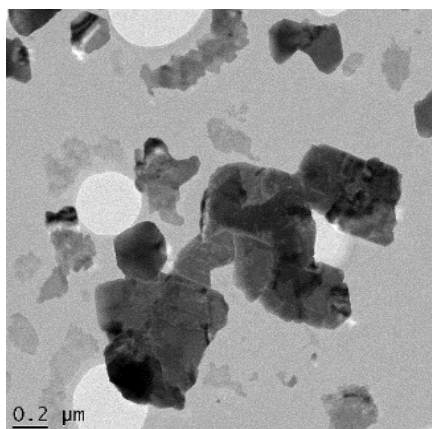


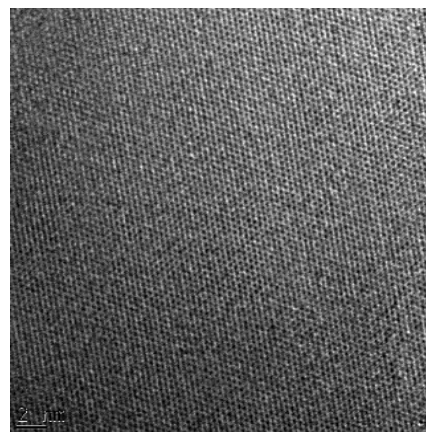
Figure 4.5: (a) and (b) HR TEM images for GASnI_3 at different resolutions and (c) SAED for GASnI_3 .

4.2.4 HR TEM for guanidinium ethylammonium tin iodide

Average particle size of 115 nm and lattice plane d spacing of 0.23 nm was achieved, corresponding to film growth along (310) lattice plane. HR TEM micrographs of the perovskite at different resolutions are shown in figure 4.6 below.



(a)



(b)



(c)

Figure 4.6: (a) and (b) HR TEM images for $[GA][CH_3CH_2NH_3]SnI_3$ at different resolutions and (c) SAED for $[GA][CH_3CH_2NH_3]SnI_3$.

4.2.5 HR TEM for guanidinium dimethylammonium tin iodide

Average particle size of 93 nm was attained. Lattice plane d spacing was found to be 0.27 nm, which corresponds to (310) lattice plane. Figure 4.7 shows HR TEM micrographs of the perovskite at different resolutions.

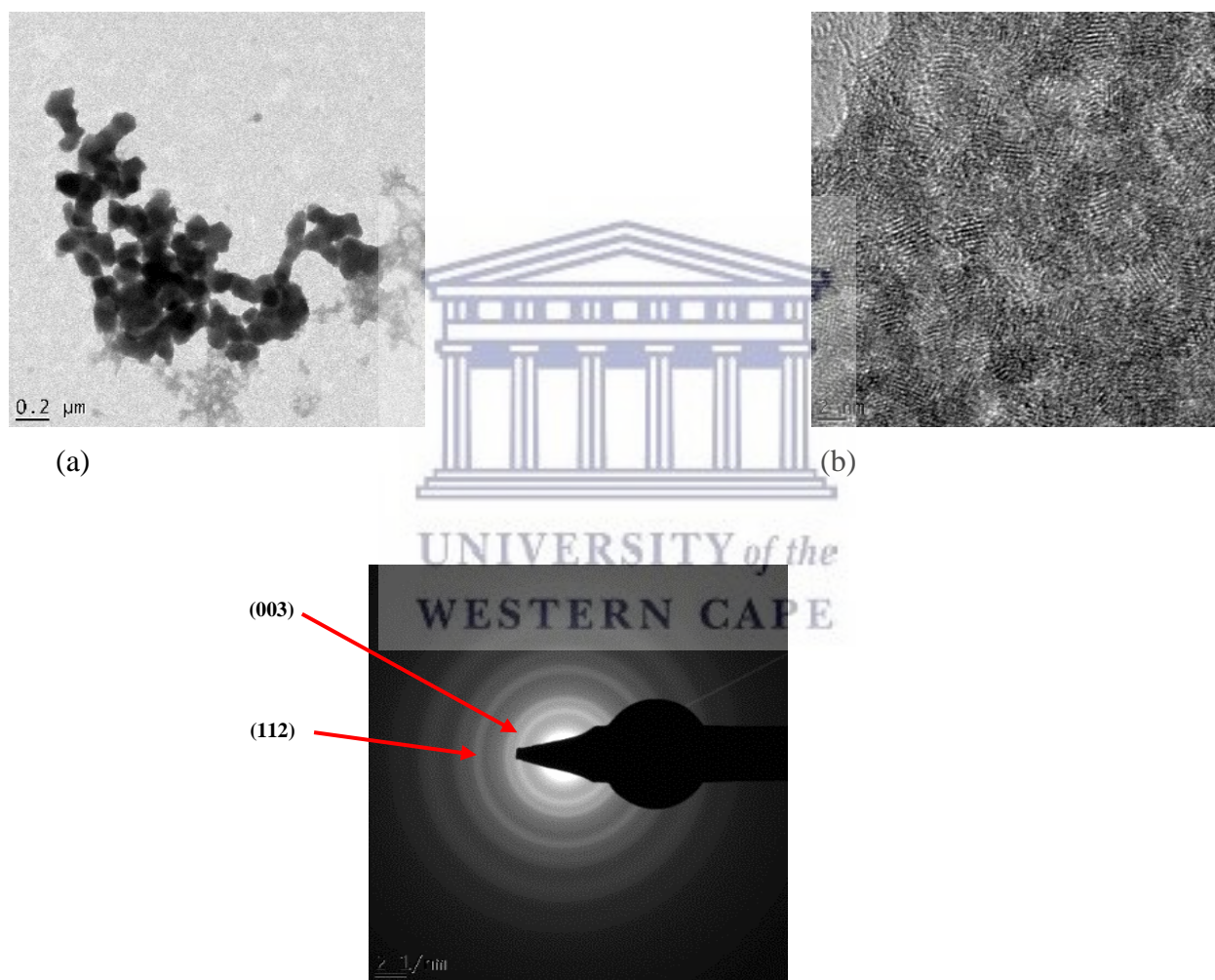


Figure 4.7: (a) and (b) HR TEM images for $[GA]((CH_3)_2NH_2)SnI_3$ at different resolutions and (c) SAED for $[GA]((CH_3)_2NH_2)SnI_3$.

4.3 Small-Angle X-ray Scattering (SAXS) results

4.3.1 SAXS for $[\text{CH}_3\text{CH}_2\text{NH}_3]\text{SnI}_3$ perovskite

Figure 4.8 (a) below shows the pair distance distribution function (PDDF) for the $[\text{CH}_3\text{CH}_2\text{NH}_3]\text{SnI}_3$ perovskite. This PDDF shows a dip around 30 nm which stretches down to the negative. PDDF is a histogram of distances which is determined by contrast values ($\Delta\rho$) that are in turn connected by each distance. In this case, all distances that happen to cross the border from positive to negative ($\Delta\rho$) values count negative [23], hence the histogram shows a dip that stretches to the negative ($\Delta\rho$). This PDDF suggests that the shape of this perovskite particles is a core shell hollow sphere.

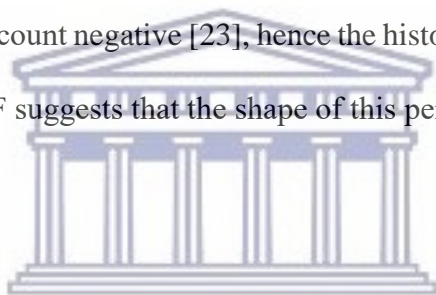


Figure 4.8 (b) is particle size distribution of the perovskite sample, it shows that the sample has two particle sizes, $r = 8.0$ nm and 67.6 nm. This technique compliments TEM by showing more information especially on smaller particle sizes. These two sizes are smaller than the average particle size (109.0 nm) that was obtained through HR TEM for the same perovskite. Because of lateral confinement, crystals grow mainly in the vertical direction during nucleation. This results into a strain inside the film that leads to cracking into smaller units, while smaller crystals on the surface of film grow together [24.] Proposed mechanism for perovskite conversion is shown in figure 4.9.

GISAXS has been shown to be a powerful tool to probe the nanometer scale morphology of thin organic and inorganic films and to explain morphological implications for their behavior in organic and dye-sensitized solar cells [25, 26]. Thus, GISAXS is complementary to imaging techniques like atomic force microscopy (AFM) or scanning electron microscopy (SEM), which only probe the sample surface [27, 28]. There is a large amount of smaller crystals inside the bulk of SnI₂ perovskite precursor film than closer to the film surface. This depletion of smaller crystals relative to larger ones on the film surface is further supported by SEM images. This disparity increases upon conversion of SnI₂ to perovskite, as crystals inside the bulk probably split due to the strain. Smaller crystals on the surface, however, are partially dissolved and get united with the larger crystals by Ostwald-type ripening, which explains why ripening of the crystals usually forms poly-dispersed particles [29, 30].

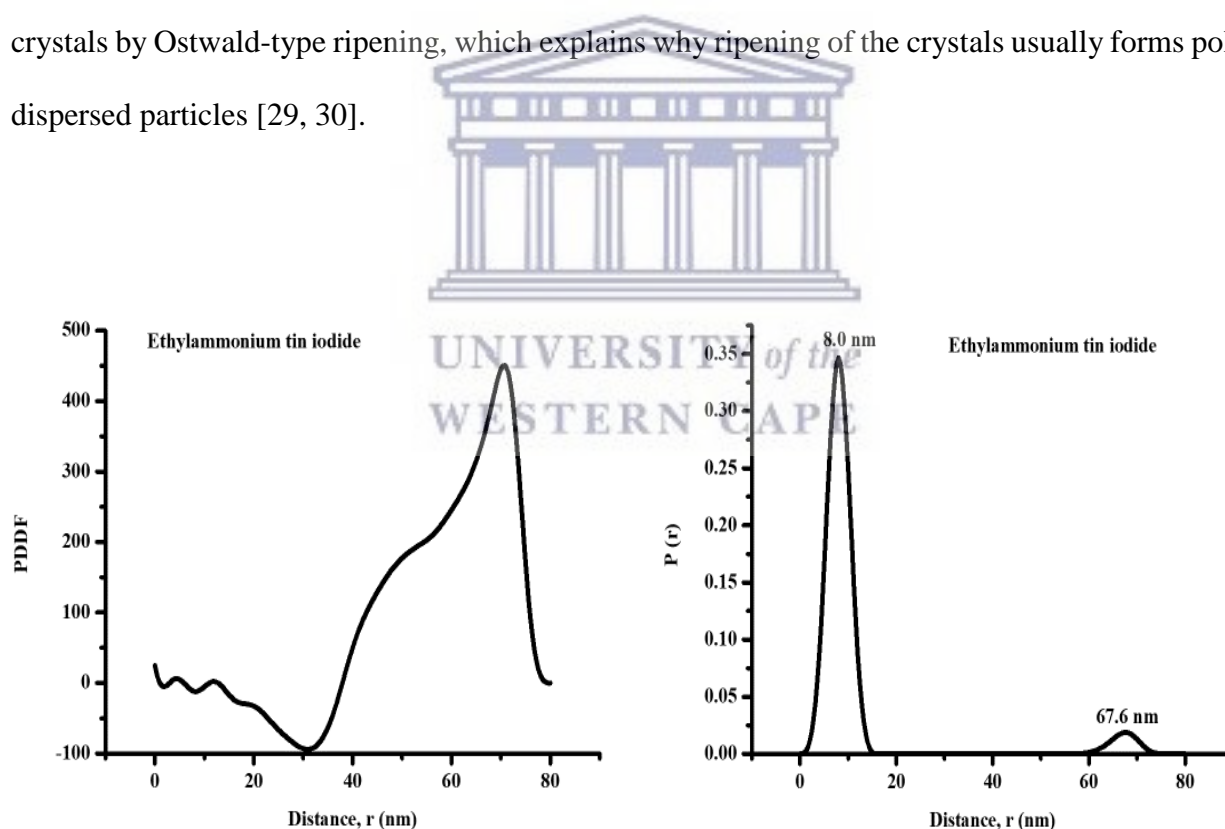


Figure 4.8: (a) PDDF for [CH₃CH₂NH₃]₃SnI₃ perovskite, (b) particle size distribution of the perovskite.

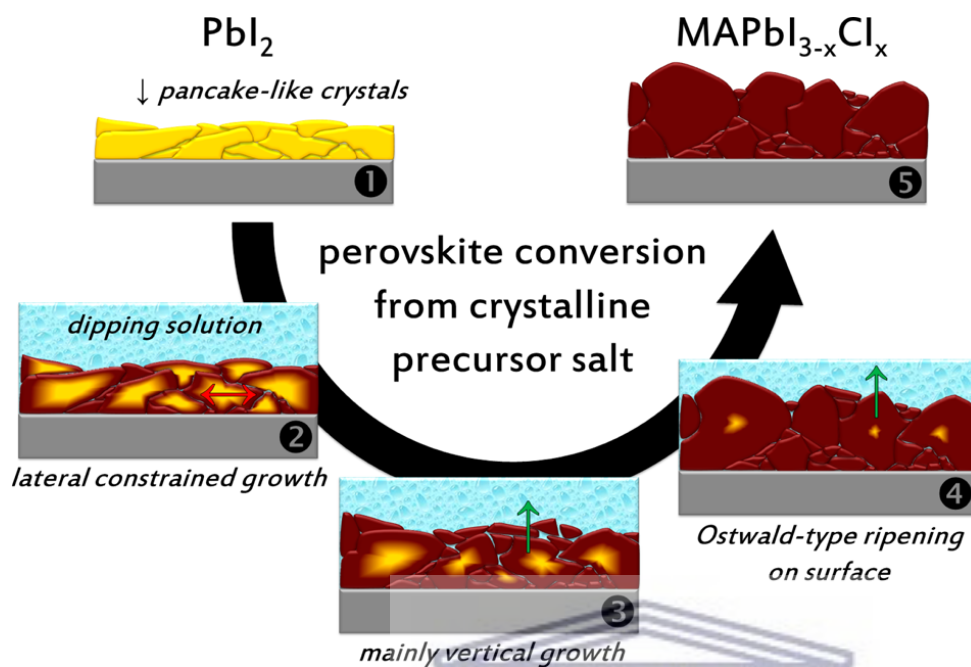


Figure 4.9: Schematic presentation of proposed crystal growth [24].

Figure 4.10 (a) below shows SAXS plot of volume fraction of particle sizes. The plot shows only the volume fraction of particle size $r = 8.0$ nm, which means that the population of particle size $r = 67.6$ nm was way smaller. The plot of intensity X-ray scatter of the particle sizes, figure 4.10 (b) confirms the presence of $r = 8.0$ nm and $r = 68.0$ nm particles, with higher intensity of $r = 68.0$ nm since the bigger the particle size, the more intense the X-rays will be scattered.

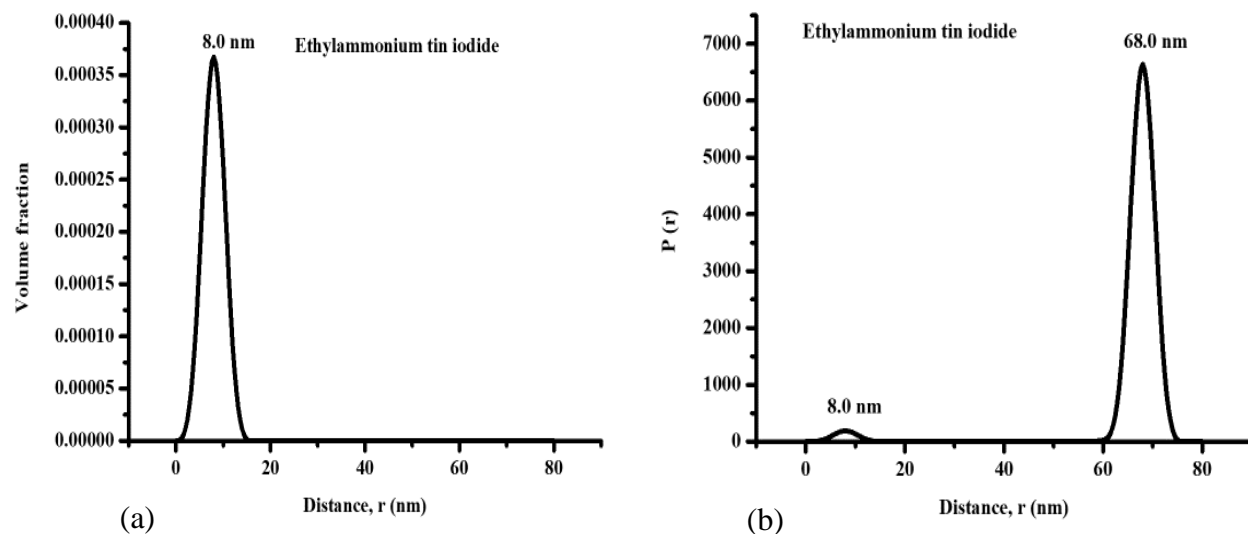


Figure 4.10: SAXS plots of (a) volume of the particle size and (b) intensity of the particle sizes of $[\text{CH}_3\text{CH}_2\text{NH}_3]\text{SnI}_3$ perovskite.



UNIVERSITY of the
WESTERN CAPE

4.3.2 SAXS for $[(\text{CH}_3)_2\text{NH}_2]\text{SnI}_3$ perovskite

PDDF of $[(\text{CH}_3)_2\text{NH}_2]\text{SnI}_3$ is shown in figure 4.11 (a) below. This plot shows that the perovskite has particles of arbitrary shape. The shape cannot be deduced from this information without additional information. HR TEM may be used to complement this information about the shape of the particles [23]. Figure 4.11 (b) shows particle size distribution of the perovskite sample, two particle sizes, $r = 2.0$ nm and 18.0 nm were recognized. Similar to $[\text{CH}_3\text{CH}_2\text{NH}_3]\text{SnI}_3$, these two particle sizes are way too smaller than 87.8 nm average particle size obtained from HR TEM for $[(\text{CH}_3)_2\text{NH}_2]\text{SnI}_3$. Average particle size may not reveal a true resemblance of the sample particle size.

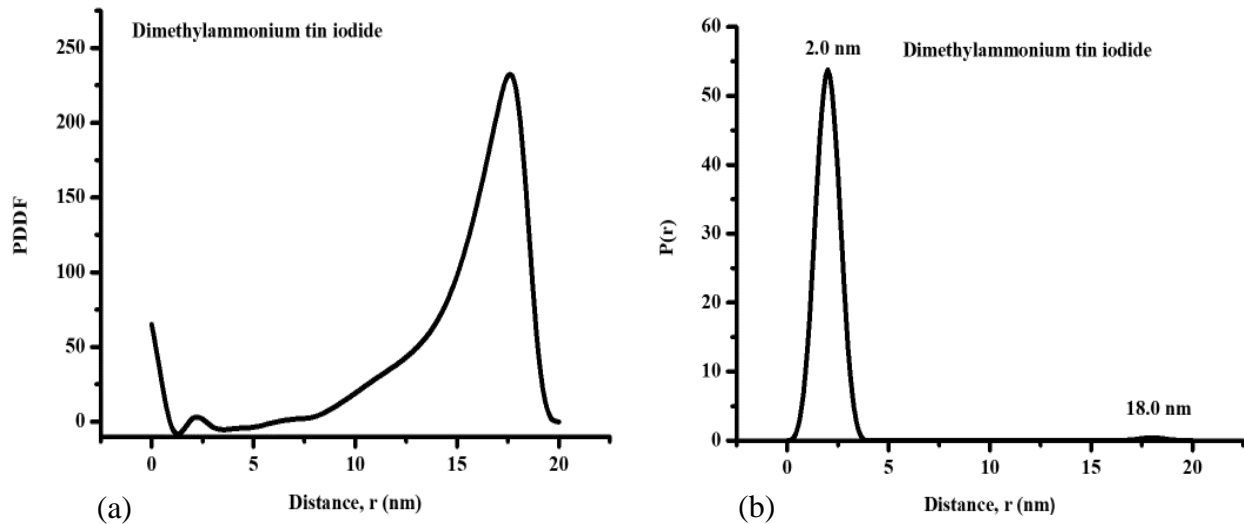


Figure 4.11: (a) PDDF for $[(\text{CH}_3)_2\text{NH}_2]\text{SnI}_3$ perovskite, (b) particle size distribution of the perovskite.

Figure 4.12 (a) below shows SAXS plots of $[(\text{CH}_3)_2\text{NH}_2]\text{SnI}_3$. Plot (a) shows only the volume fraction of particle size $r = 2.0$ nm. The population of particle size $r = 18.0$ nm was insignificant in volume fraction. The plot of intensity X-ray scatter of the particle sizes, figure 4.12(b) confirms the presence of $r = 2.0$ nm and $r = 18.0$ nm particles. As expected, the larger particle ($r = 18.0$ nm) has X-ray scattering of higher intensity.

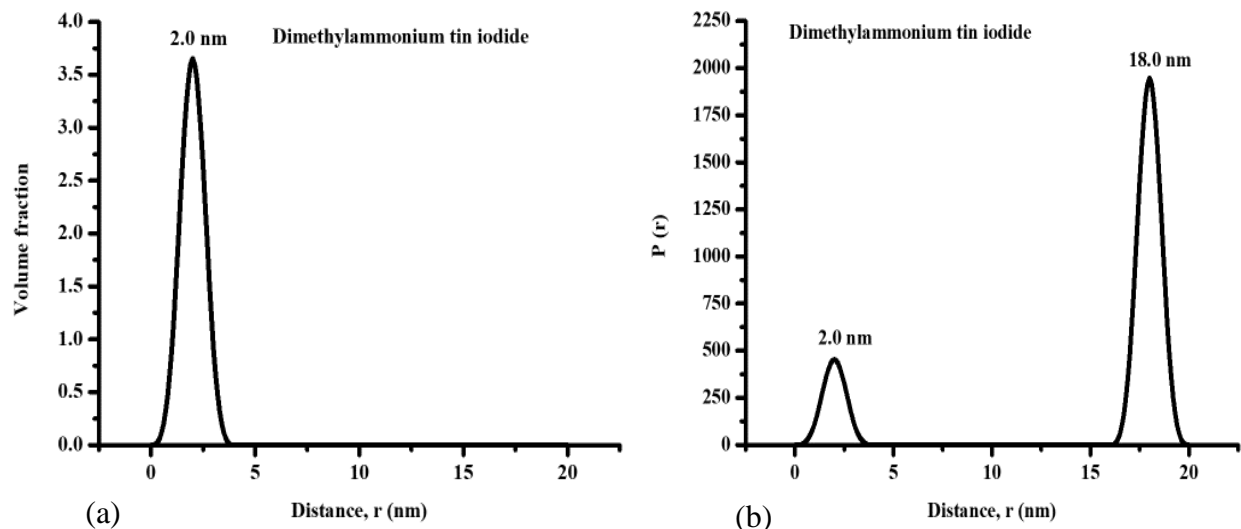


Figure 4.12: SAXS plots of (a) volume of the particle size and (b) intensity of the particle sizes for $[(\text{CH}_3)_2\text{NH}_2]\text{SnI}_3$ perovskite.



UNIVERSITY of the
WESTERN CAPE

4.3.3 SAXS for GASnI_3 perovskite

Figure 4.13 (a) shows PDDF of GASnI_3 perovskite. Observed in this plot is a pronounced peak at 66.3 nm and a smaller peak at 115.7 nm as seen below. This PDDF shows aggregates (i.e. particles that join and stick together) of two subunits [27]. Figure 4.13 (b) is a plot of particle size distribution of the perovskite. The sample has two particle sizes, $r = 65.0$ nm and 97.5 nm as seen below. The 97.5 nm particle size is comparable to the average particle size of 102.4 nm that was obtained from HR TEM experiment on the same material [25]. Both SAXS and HR TEM gave results with comparable particle size [26].

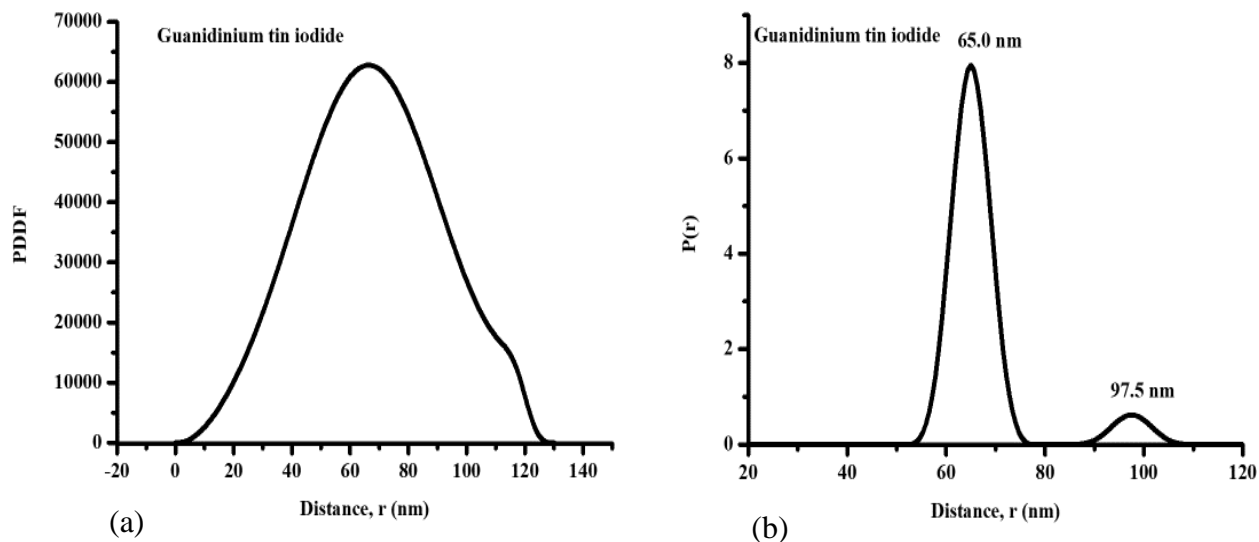


Figure 4.13: (a) PDDF for GASnI_3 perovskite and (b) particle size distribution of the perovskite.

Figure 4.14 (a) shows the volume fraction of particle size $r = 65.0$ nm and 97.5 nm. Particles $r = 65.0$ are more than particles $r = 97.5$ nm in the sample. The plot of intensity of the X-ray scatter of the particle sizes in figure 4.14 (b) confirms the presence of $r = 67.6$ nm and $r = 98.2$ nm particles. The smaller particles ($r = 67.6$ nm) had X-ray scattering of higher intensity than the bigger particles ($r = 98.2$ nm) because of the aggregation of the two subunits [27].

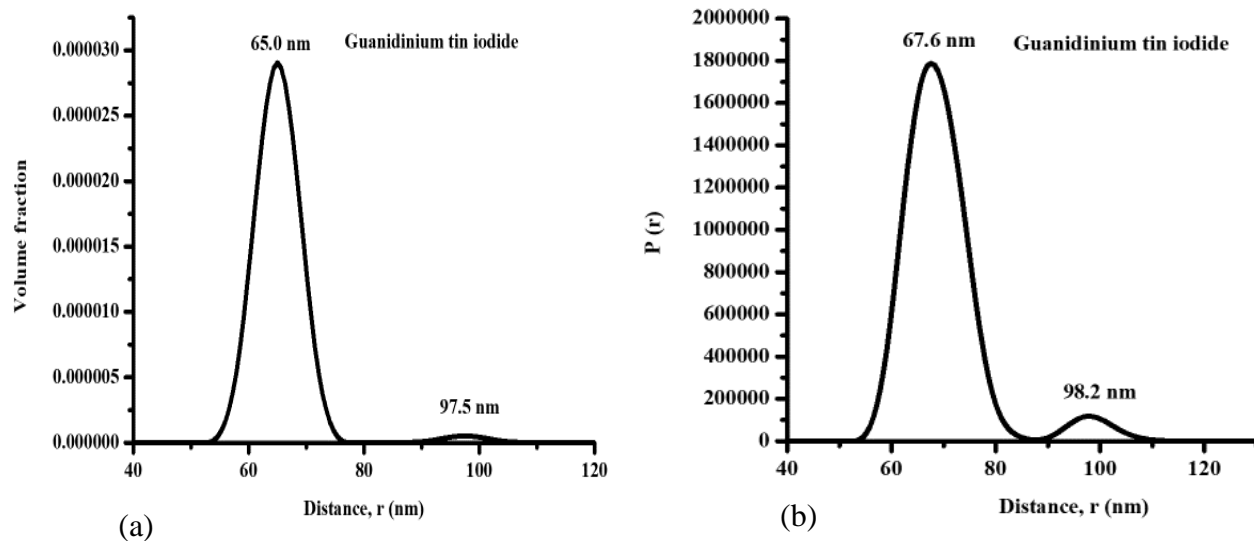


Figure 4.14: SAXS plots of (a) volume of the particle size and (b) intensity of the particle sizes for GASnI_3 perovskite.



UNIVERSITY of the
WESTERN CAPE

4.3.4 SAXS for $[\text{GA}][(\text{CH}_3)_2\text{NH}_2]\text{SnI}_3$ perovskite

PDDF of $[\text{GA}][(\text{CH}_3)_2\text{NH}_2]\text{SnI}_3$ perovskite is shown in figure 4.15 (a) below. This plot shows a dip around 30 nm which stretches down to the negative. In this PDDF, all distances that went past the border from positive to negative ($\Delta\rho$) values count negative [30], hence the histogram shows a dip that stretches to the negative ($\Delta\rho$). This information tells us that the shape of this perovskite particles is a core shell hollow sphere. Plot for particle size distribution, figure 4.15 (b) shows that the perovskite sample has two particle sizes, $r = 8.0$ nm and 68.4 nm. The biggest size (68.4 nm) is smaller than 93.0 nm particle size that was shown by HR TEM for this perovskite.

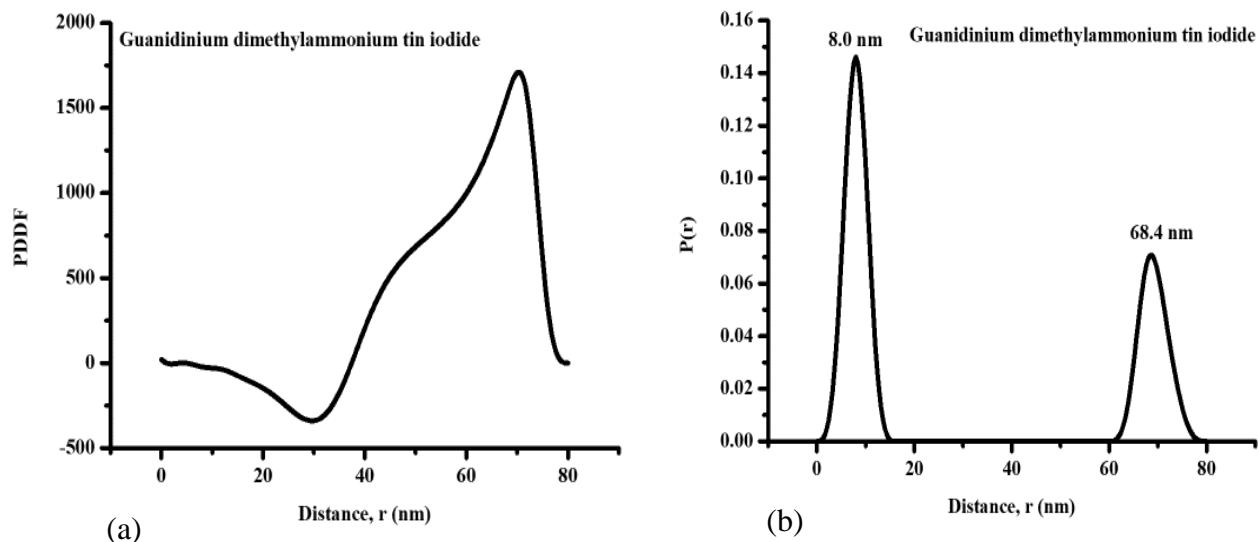


Figure 4.15: (a) PDDF for $[\text{GA}][(\text{CH}_3)_2\text{NH}_2]\text{SnI}_3$ perovskite and (b) particle size distribution of the perovskite.

Figure 4.16 (a) shows volume fraction of particle size $r = 8.0$ nm and 68.4 nm. Particles $r = 8.0$ nm are way more than particles $r = 68.4$ nm in the sample hence only $r = 8.0$ nm is seen in this plot. The plot of intensity of the X-ray scatter of the particle sizes, figure 4.16 (b) confirms the presence of $r = 8.0$ nm and $r = 70.8$ nm particles. The larger particle ($r = 70.8$ nm) has X-ray scattering of higher intensity.

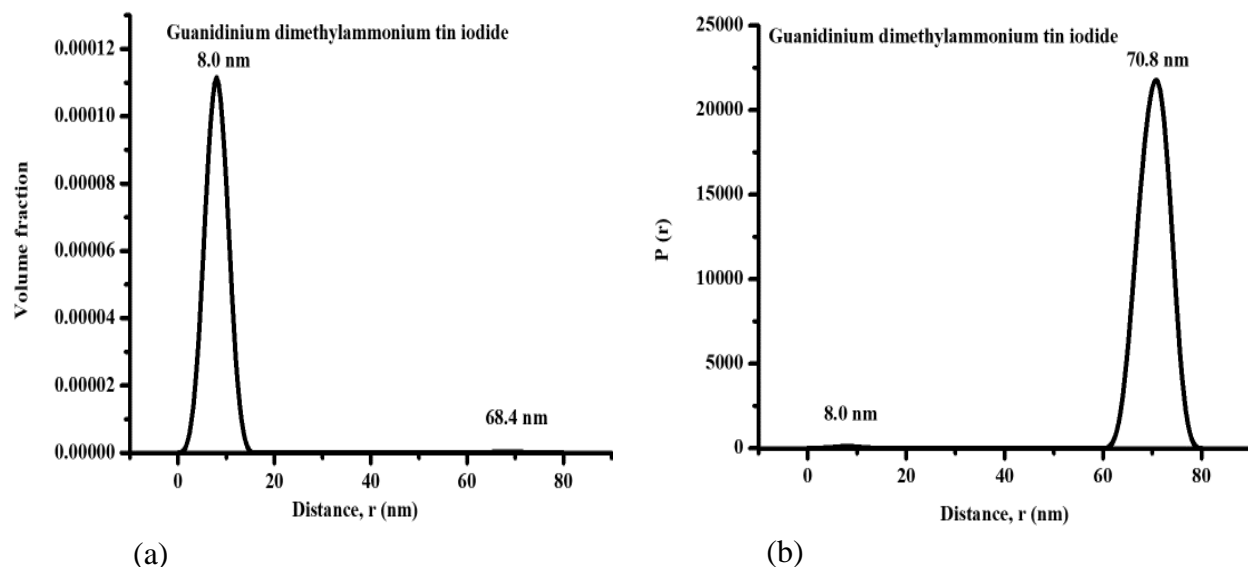
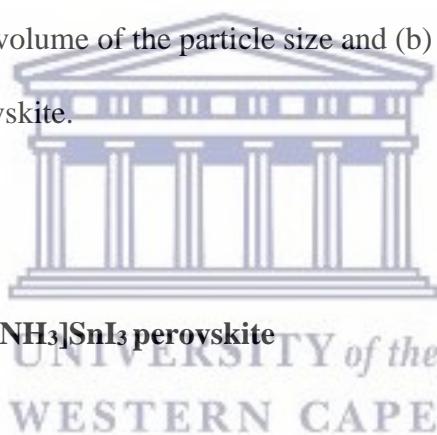


Figure 4.16: SAXS plots of (a) volume of the particle size and (b) intensity of the particle sizes for [GA] $[(\text{CH}_3)_2\text{NH}_2]\text{SnI}_3$ perovskite.



4.3.5 SAXS for [GA] $[\text{CH}_3\text{CH}_2\text{NH}_3]\text{SnI}_3$ perovskite

PDDF of [GA] $[\text{CH}_3\text{CH}_2\text{NH}_3]\text{SnI}_3$ perovskite is shown in figure 4.17 (a) below. The PDDF shows a dip around 40 nm which stretches down to the negative. This PDDF gives information that the shape of this perovskite particles is a core shell hollow sphere [23]. Plot (a) shows that the sample is poly-dispersed [30], with three particle sizes, $r = 12.0, 72.0$ and 108.0 nm as seen in figure 4.17 (b). The biggest particle size (108.0 nm) is comparable to 115 nm average size that was obtained from HR TEM experiment. Both techniques were complimentary, in which SAXS revealed even sizes of smaller particles [29].

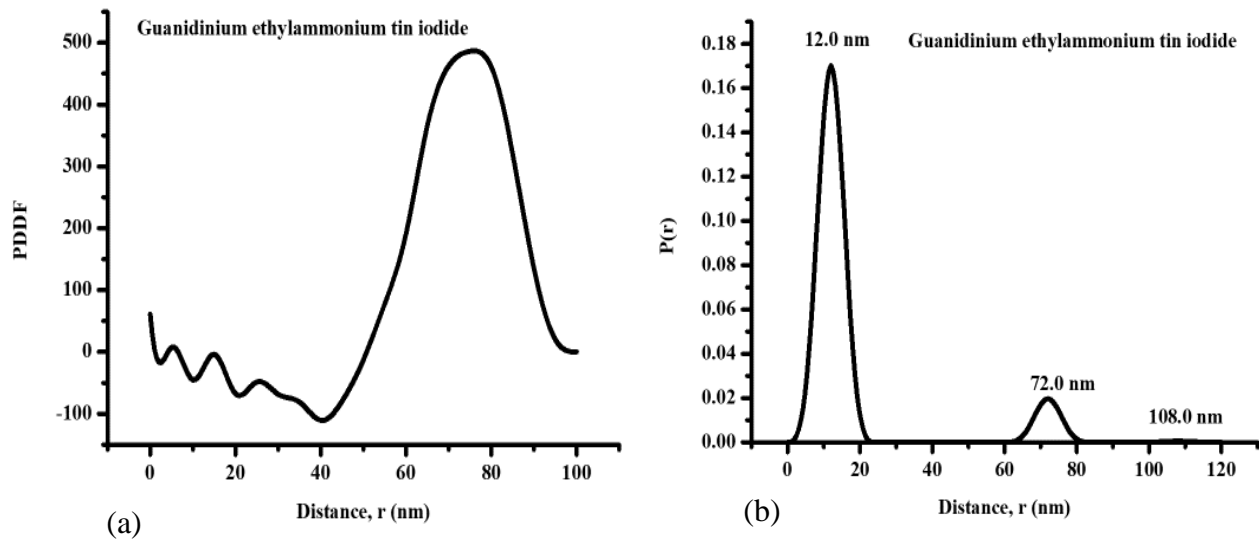


Figure 4.17: (a) PDDF for $[\text{GA}][\text{CH}_3\text{CH}_2\text{NH}_3]\text{SnI}_3$ and (b) particle size distribution of the perovskite.

Figure 4.18 (a) below shows the volume fraction of particle size $r = 12.0$ nm only, which shows that it is by far more than the rest in the sample. The plot of intensity of the X-ray scatter of the particle sizes in figure 4.18 (b) confirms the presence of all the three particle sizes. Particle size $r = 77.5$ nm has X-ray scattering of highest intensity as seen in the figure below.

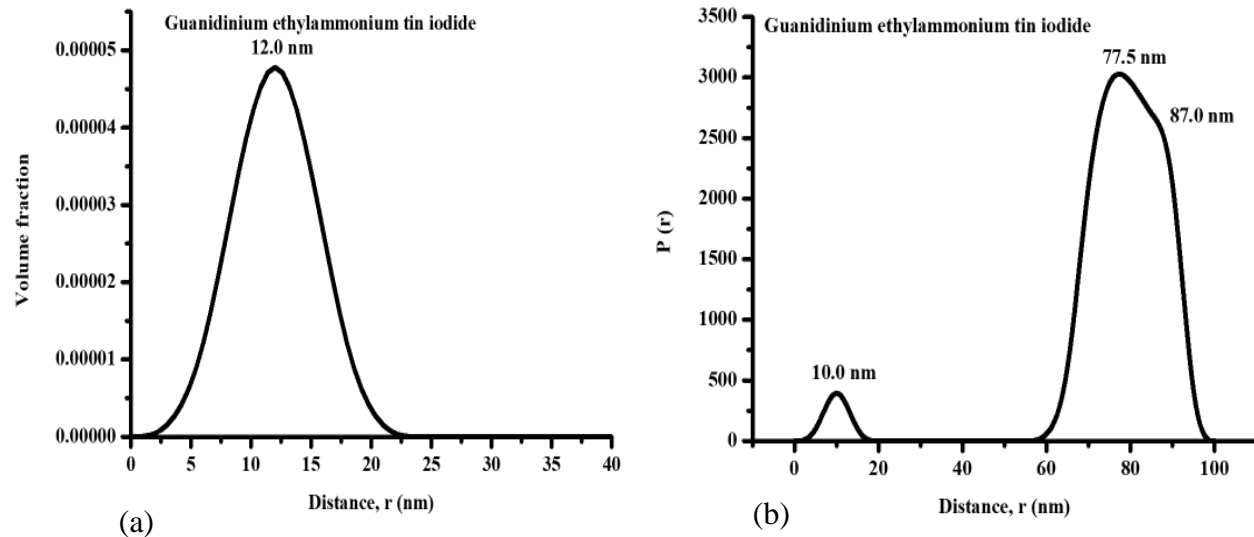
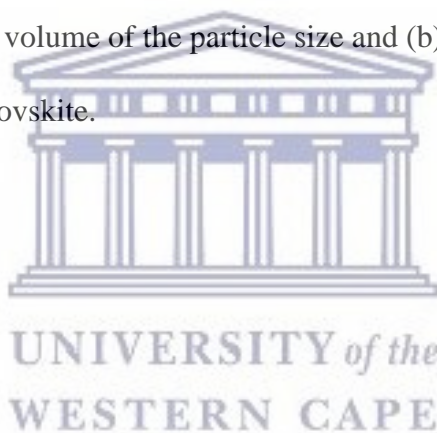


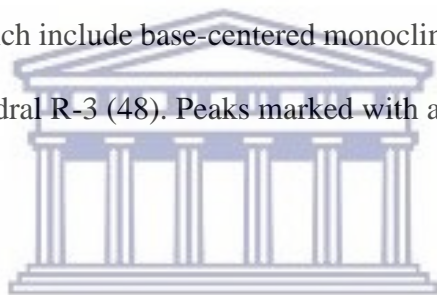
Figure 4.18: SAXS plots for (a) volume of the particle size and (b) intensity of the particle sizes for [GA][CH₃CH₂NH₃]SnI₃ perovskite.



4.4 XRD results

XRD analysis of the perovskites was done since understanding the crystal growth of these materials affects their electronic, optoelectronic, and photovoltaic properties [31]. This technique was used to give information about the crystalline properties of the perovskites. Figure 4.19 below shows the XRD patterns of the 5 perovskites. Diffraction peaks are observed at approximately 13.0, 17.0, 22.6, 25.1, 26.5, 31.9, 34.5, 39.6, and 43.2 two-theta degrees, respectively corresponding to the reflections from (110), (112), (211), (202), (220), (310), (312), and (314) crystal planes characteristic to the tetragonal (14/mcm) perovskite structure [32, 33]. These diffraction peaks agree with literature for perovskite thin films. It was observed that some of the

perovskites showed fewer diffraction peaks, noteworthy however is that these peaks still were in positions corresponding to tetragonal structure, e.g. guanidinium tin iodide diffraction peaks. This result could be caused by strong texture in the sample. It is also noted that the diffraction peak intensities vary from one perovskite to the next, which indicates that the compounds have varying degree of ordering. XRD line broadening is caused by dislocations in non-cubic materials like the perovskites that were synthesized in this research, which do not conform to perfectly cubic shape [34]. Non-cubic materials allow orientation factors that relate to diffraction profile parameters (line widths, fourier coefficients) in a way that favors elastic behavior and lattice geometry of the scattering perovskite crystals [35]. XRD pattern of SnI₂ precursor was also done. This starting material exhibited 3 phases, which include base-centered monoclinic with space group C2/m (12), cubic Pa3 (205), and rhombohedral R-3 (48). Peaks marked with asterisks belong to the pure SnI₂ phases.



Tsai *et al.* found that their layered perovskite exhibited diffraction peaks at 14.20°, 28.48° and 43.28°, which match the diffraction peak positions of (111), (202) and (313) crystallographic planes from layered perovskite (BA)₂(MA)₃Pb₄I₁₃, respectively [36] However, diffraction peaks of (110), (220) and (314) crystallographic planes from 3D MAPbI₃ perovskite located at 14.05°, 28.45° and 43.13° crystallographic planes and layered perovskite (BA)₂(MA)_{n-1}Pb_nI_{3n+1} (n = 2, 3) also agreed with the XRD pattern quite well. In comparison, diffraction peaks obtained from all perovskites studied in this research support 3D structure [37-43].

Note-worthy is that, indexing of peaks from both layered perovskites (n = 4) and 3D-like perovskite phases suggest possibility that both layered and 3D-like perovskites could be present in

same sample at various orientations [44]. Weak diffraction peaks at low-angle (less than 14°) can be observed in XRD spectrum; like in the case of $[\text{CH}_3\text{CH}_2\text{NH}_3]\text{SnI}_3$ and $[\text{GA}][(\text{CH}_3)_2\text{NH}_2]\text{SnI}_3$, the absence of such peaks in layered perovskite thin film samples might be explained by the small amount of randomly oriented layered perovskite phases present [45, 46].

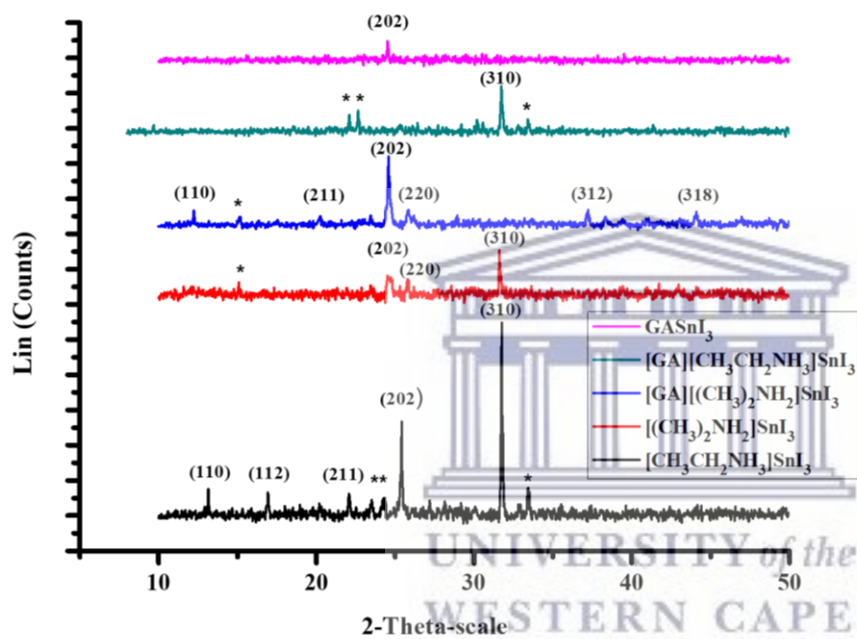


Figure 4.19: XRD pattern for the perovskites.

All perovskite compounds studied in this research conform to tetragonal perovskite basic structure. The various organic cations used occupy the corners of the cubic structure, which is the A site of the compounds. Iodine occupies each of the faces of the cube as it directly bonds to the central atom, forming octahedral complex, this is the X site of the structure. Lastly, the B site which is the central atom in this structure is occupied by Sn and is smaller. This structure is shown in figure 4.20.

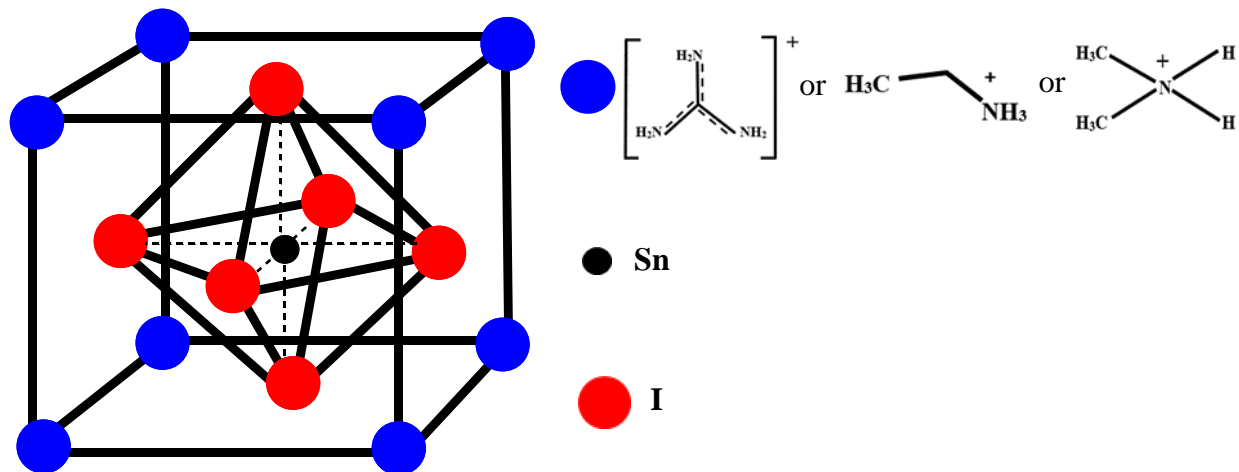
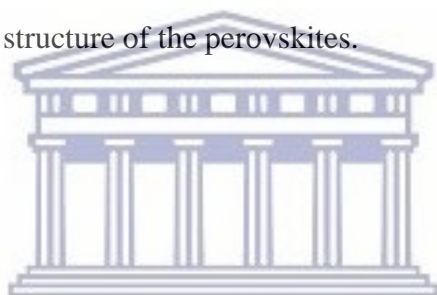


Figure 4.20: Tetragonal crystal structure of the perovskites.



UNIVERSITY of the
WESTERN CAPE

Scherrer equation:

The Scherrer equation relates crystallite size to the peak width in XRD. Crystallite size may not be equal to particle size due to the occurrence of aggregates from polycrystalline diffracting domain. The Scherrer equation (stated below) has been used to calculate the crystallite size of the various perovskites.

$$t = K\lambda / (B \cos\theta) \quad (15)$$

where t represents the averaged dimension of crystallites, K represents the Scherrer constant close to unity (0.9 has been used), λ represents the wavelength of X-ray, B represents the integral width

of a reflection in radians, at 2θ scale. The optical and electrical properties of light absorbing materials for photovoltaic cells strongly influenced by their crystalline structure [47, 48]. The crystals of organic metal halides exhibit various structural transitions which are dependent on the temperatures used during heating. These transitions involve cubic, tetragonal and orthorhombic phases. When the temperature is decreased, the cubic phase is transformed into tetragonal phase which is the most common amongst perovskites. The tetragonal phase has symmetry lower than that of cubic phase, which is due to ordering of the halide ions.

When temperature is further decreased, the tetragonal phase transforms into orthorhombic phase due to ordering of cations in the unit cells [50]. Senanayak *et al.* observed that lead iodide perovskite films with smaller grain size have crystallites that prefer orientation out of plane along (110) direction [51]. In contrast, ethylammonium tin iodide, dimethylammonium tin iodide and guanidinium ethylammonium tin iodide prefer orientation along (310) direction while guanidinium tin iodide and guanidinium dimethylammonium tin iodide prefer orientation along (202) direction. Senanayak *et al.* further observed that lead iodide thin films with larger grain size have sharper diffraction spots while thin films with smaller grain size have broader peaks [51]. Increased grain sizes of hybrid halide perovskite materials enhance charge transport and collection efficiency which subsequently improves PCE of the fabricated solar cell devices [52]. It is therefore favorable to control particle growth such that optimal grain size is achieved. Crystallinity is greatly improved at higher temperatures. A temperature (125 °C) higher than the traditional perovskite annealing temperature (100 °C) was adopted. The Ostwald recrystallization model is used to explain enlarged grain size. This process involves two steps and is driven by surface energy. In the first step, small-sized crystals dissolve due to higher equilibrium vapor pressure. The second step involves

formation of large-sized crystals to cause a decrease in the surface energy leading to improved grains. Table 4.1 below shows the calculated averaged dimensions of the various perovskite crystallite.

Table 4.1: Averaged dimensions of crystallites (t) of the perovskites.

Perovskite	t (nm)
$[\text{CH}_3\text{CH}_2\text{NH}_3]\text{SnI}_3$	196.0
$[(\text{CH}_3)_2\text{NH}_2]\text{SnI}_3$	124.3
GASnI_3	180.0
$[\text{GA}][\text{CH}_3\text{CH}_2\text{NH}_3]\text{SnI}_3$	104.5
$[\text{GA}][(\text{CH}_3)_2\text{NH}_2]\text{SnI}_3$	177.9

UNIVERSITY of the
WESTERN CAPE

4.5 FTIR results

Figure 4.21 below shows the FTIR spectra of all the 5 perovskites.

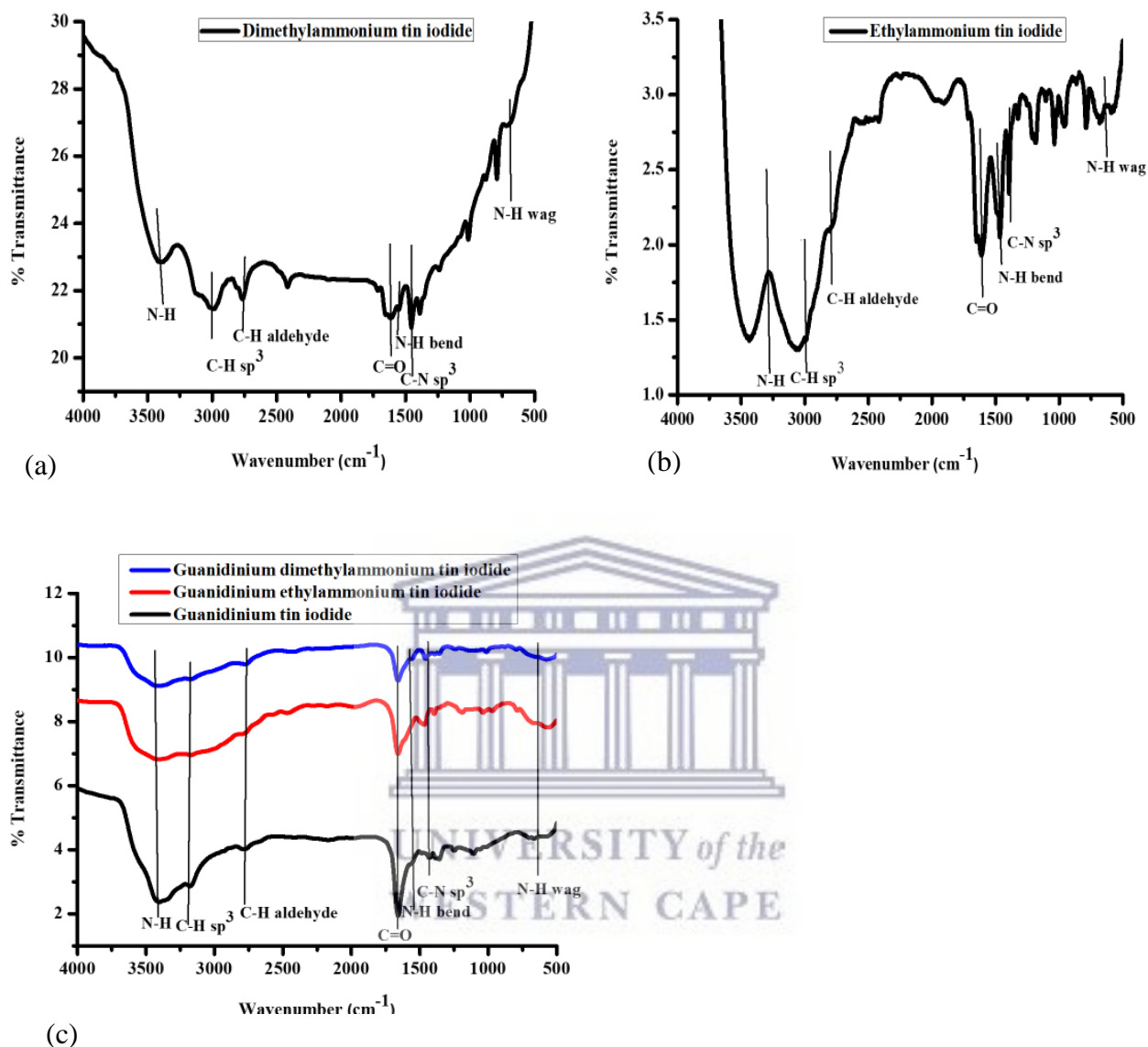


Figure 4.21: FTIR spectra for (a) $[(\text{CH}_3)_2\text{NH}_2]\text{SnI}_3$, (b) $[\text{CH}_3\text{CH}_2\text{NH}_3]\text{SnI}_3$ and (c) GASnI_3 , $[\text{GA}][\text{CH}_3\text{CH}_2\text{NH}_3]\text{SnI}_3$ and $[\text{GA}][(\text{CH}_3)_2\text{NH}_2]\text{SnI}_3$.

All the perovskites showed the expected IR bands characteristic to the structure of these materials complexed in DMF solvent which was used in their synthesis. Absorption bands observed in all perovskites are consistent with literature [53]. The N-H stretch which absorbs between 3400 and

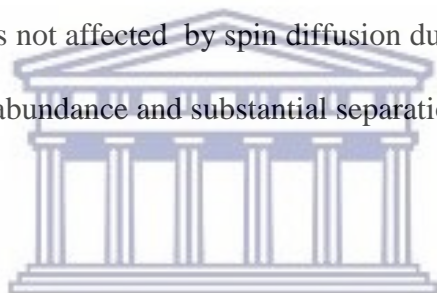
3250 cm^{-1} was observed in all 5 perovskites. This band is usually medium and appears as a double band, which confirms the presence of primary or secondary amines or amides in the perovskite [54]. The C-H sp^3 band (3000-2850 cm^{-1}) is also observed in all 5 perovskites. This C-H stretch is usually medium and confirms alkanes in the chemical structure of the compound.

The C-H stretch aldehyde (2830-2695 cm^{-1}) was observed in all the 5 perovskites. This is a medium band that originates from the C-H bond in an aldehyde group [55]. The aldehyde group confirmed is from the DMF solvent that was used in the synthesis steps of these materials. The aldehyde group from DMF solvent also contributed a strong C=O stretch (1740-1665 cm^{-1}) in all the perovskites. Also observed in all the perovskites is the N-H bend (1650-1580 cm^{-1}) which is a medium band confirming primary amines in the structure of the analyzed material. The C-N sp^3 (1450-1250 cm^{-1}) band was also observed in all the perovskites and lastly is the broad N-H wag (910-665 cm^{-1}) confirming primary and secondary amines [56]. Similar bands were observed for SOCTPs and MOCTPs, hence it can be deduced that mixing the organic cations did not cause bonding amongst these cations.

Glaser *et al.* analyzed the shifts of methylammonium lead halide perovskite vibrational peak positions between various halides to infer the extent of interaction between organic moiety and the surrounding inorganic cage. They found the same vibration bands observed with these perovskites, and further established that the positions of the NH_3^+ stretching vibrations point to significant hydrogen bonding between the methylammonium and the halides for all three perovskites [57].

4.6 Nuclear Magnetic Resonance (NMR) spectroscopy results

Solid state ^{13}C NMR spectroscopy of the perovskite precursors used to synthesize the perovskites were recorded as well as for the perovskites. These precursors include guanidinium iodide (GAI), ethylammonium iodide (EthI) and dimethylammonium iodide (DimI) while the various perovskites are GASnI_3 , $[\text{CH}_3\text{CH}_2\text{NH}_3]\text{SnI}_3$, $[(\text{CH}_3)_2\text{NH}_2]\text{SnI}_3$, $[\text{GA}][\text{CH}_3\text{CH}_2\text{NH}_3]\text{SnI}_3$ and $[\text{GA}][\text{CH}_3\text{CH}_2\text{NH}_3]\text{SnI}_3$. Solid state ^{13}C magic angle spinning (MAS) NMR, is a very powerful tool for studying the difference of the C–H vectors at different sites. The ^{13}C spin-lattice relaxation time in the rotating frame $T1\rho$ is not affected by spin diffusion due to the weak dipolar coupling, which results from low natural abundance and substantial separation of the nuclei [58, 59].



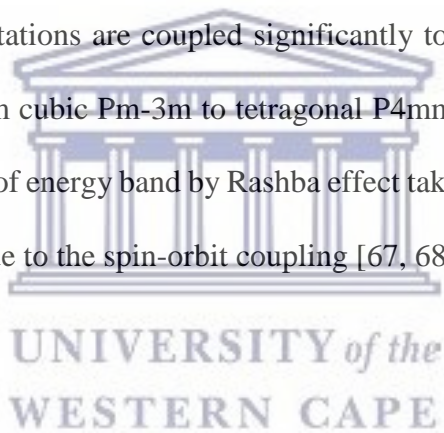
UNIVERSITY of the
WESTERN CAPE

(i) SOCTPs

4.6.1 NMR for $[\text{CH}_3\text{CH}_2\text{NH}_3]\text{SnI}_3$

Figure 4.22 shows ^{13}C spectra of EthI precursor plotted on the same axis with $[\text{CH}_3\text{CH}_2\text{NH}_3]\text{SnI}_3$ perovskite. Commercially synthesized EthI precursor shows two peaks labelled C-1 and C-2, which are due to two carbon atoms in the chemical structure of EthI [60]. Based on the chemical shift, C-1 is a carbon peak from methyl carbon which was observed to have a peak split at 14.3 and 16.0 ppm [61]. C-2 is a carbon peak from CH_2 in the EthI structure, which occurred at chemical shift 37.5 ppm. This peak is downfield due to bonding with iodine which is more electronegative in the chemical structure of EthI. This result is consistent with what was already established, where

the ^{13}C chemical shifts for alkyl carbons was found in smaller chemical shifts while those for aryl carbons shifted to higher chemical shifts due to increase in electronegativity of the substituents [62-64]. The ^{13}C of $[\text{CH}_3\text{CH}_2\text{NH}_3]\text{SnI}_3$ perovskite shows peaks around the same chemical shifts relative to its EthI commercially synthesized precursor except that the C-2 shows some splitting in its peaks. This carbon is the carbon bonded to nitrogen atom that forms a bond with tin in the reaction of EthI with SnI_2 to form $[\text{CH}_3\text{CH}_2\text{NH}_3]\text{SnI}_3$ perovskite. C-2 peak in the perovskite splits into three peaks at 37.0, 38.8 and 39.6 ppm. The splitting of this peak is due to coupling between tin and carbon confirming bonding of tin in the structure. [65, 66]. Similar studies involving MAPbI_3 perovskite showed that MA units easily rotate in PbI_6 cuboctahedral, which was supported by experimental data. These rotations are coupled significantly to the PbI_3 lattice causing some structural changes to occur from cubic Pm-3m to tetragonal P4mm and vice versa. As a result, a momentum dependent splitting of energy band by Rashba effect takes place, which induces a multi band gap electronic structure due to the spin-orbit coupling [67, 68].



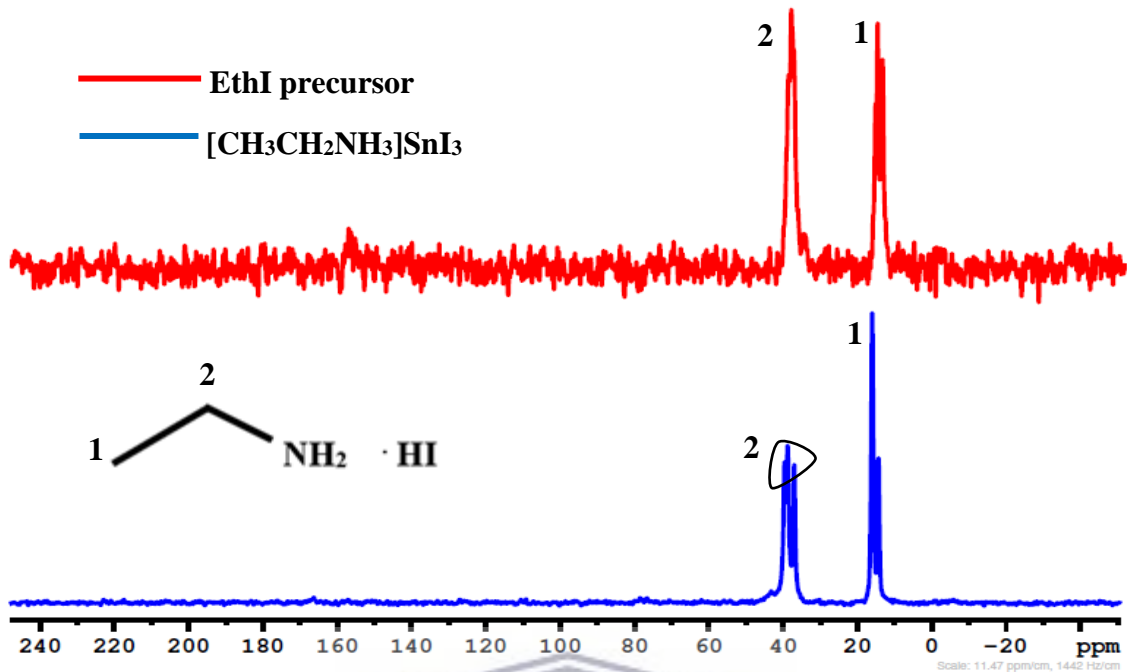


Figure 4.22: ^{13}C NMR spectra for EthI precursor and $[\text{CH}_3\text{CH}_2\text{NH}_3]\text{SnI}_3$ perovskite.

4.6.2 NMR for $[(\text{CH}_3)_2\text{NH}_2]\text{SnI}_3$

Spectra of ^{13}C NMR for DimI and $[(\text{CH}_3)_2\text{NH}_2]\text{SnI}_3$ are shown in figure 4.23. Commercially produced DimI precursor shows one very prominent peak at chemical shift at 38.8 ppm as seen in figure 4.23 below. This peak is attributed to the CH_3 carbon atoms in the chemical structure of the precursor, the two carbons have the same chemical environments and will show as one signal. This is consistent with similar studies to elucidate structure of $\text{Cs}/\text{FA}/\text{MA}/\text{PbI}_3$ perovskite whereby ^{13}C spectrum showed MA at 30 ppm while FA was at 155 ppm [69]. The same peak is observed from ^{13}C spectrum of $[(\text{CH}_3)_2\text{NH}_2]\text{SnI}_3$, except that the peak now shows splitting which occurs at 37.4 and 39.2 ppm. This splitting is due to coupling of tin and carbon, confirming the presence of tin in the structure.

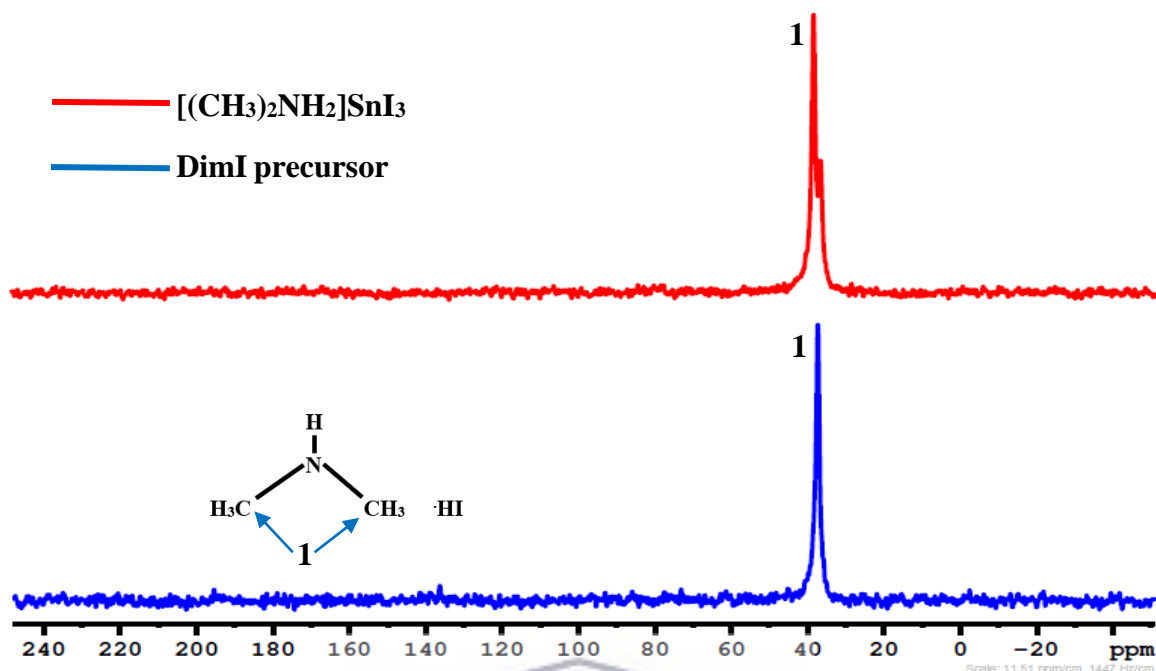


Figure 4.23: ^{13}C NMR spectra for DimI precursor and $[(\text{CH}_3)_2\text{NH}_2]\text{SnI}_3$ perovskite.

4.6.3 NMR for GASnI_3

Figure 4.24 shows ^{13}C NMR spectra of guanidinium iodide (GAI) precursor plotted together with GASnI_3 . It is observed that C-1 in the precursor is shielded in GASnI_3 since iodine atom (more electronegative) bonded to C-1 is replaced by tin atom (less electronegative). However, the tin atom still has high density of electrons since it is surrounded by iodine atoms. Observed is also a peak at 29.45 ppm from carbon atoms of DMF which was used as the solvent. C-1 is shielded from 110.57 ppm to 38.49 ppm.

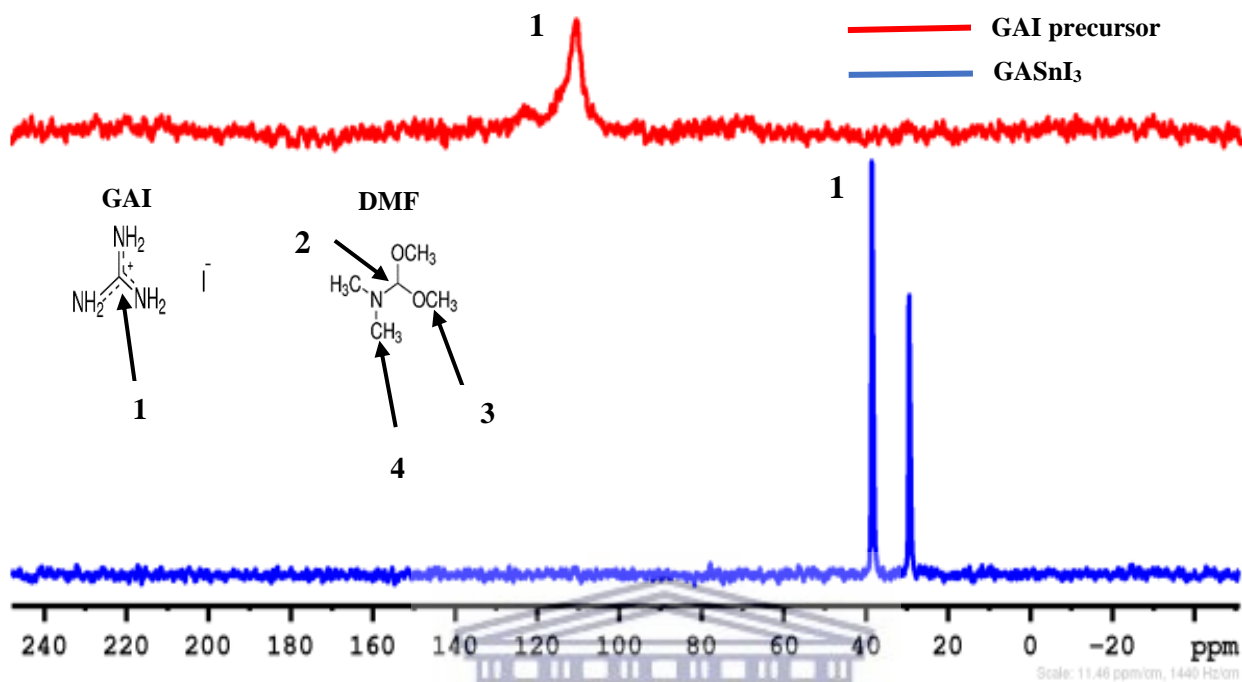


Figure 4.24: ^{13}C NMR spectra for GAI precursor and GAsnI_3 perovskite.

(ii) *MOCTPs*

4.6.4 NMR for $[\text{GA}][\text{CH}_3\text{CH}_2\text{NH}_3]\text{SnI}_3$

A ^{13}C NMR spectrum of GAI precursor was plotted together with $[\text{GA}][\text{CH}_3\text{CH}_2\text{NH}_3]\text{SnI}_3$ spectrum in figure 4.25 below. The same behavior whereby carbon atom of the precursor shifts upfield due to bonding to tin which is less electronegative relative to iodine atom that gets displaced. C-1 shifts from 110.57 ppm to 38.17 ppm, C-2 and C-3 are observed at 15.69 ppm and 14.38 ppm respectively.

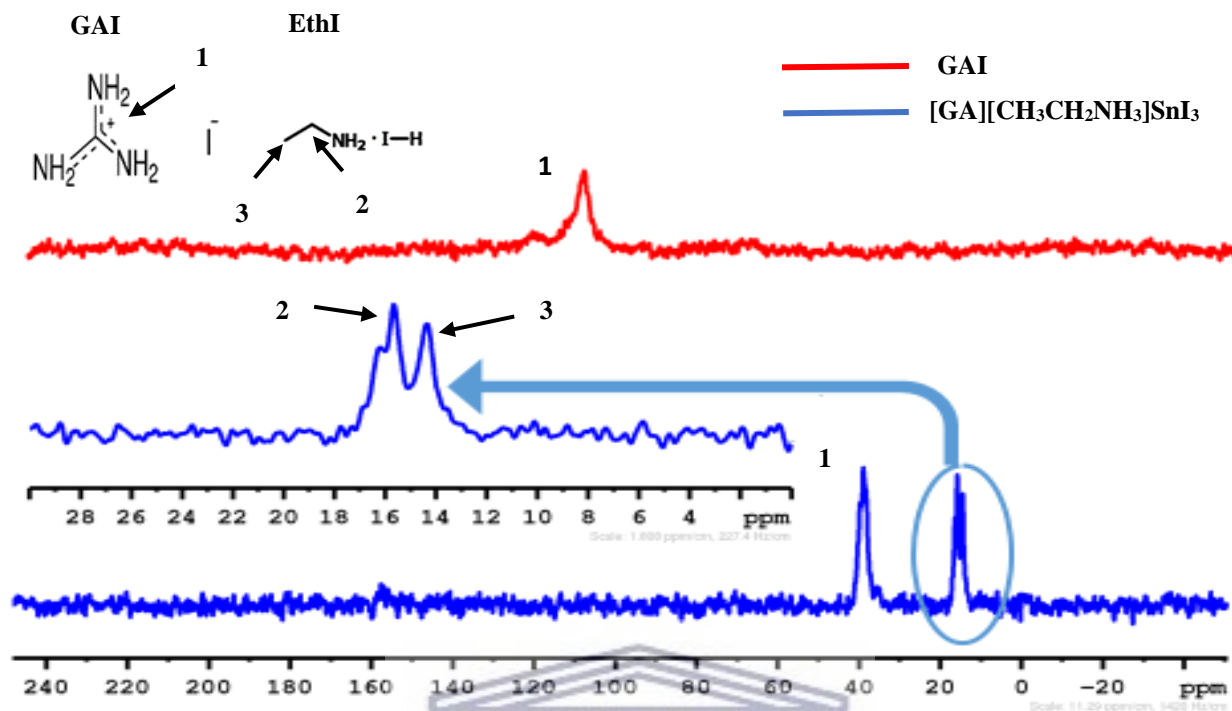


Figure 4.25: ^{13}C NMR spectra for GAI precursor and $[\text{GA}][\text{CH}_3\text{CH}_2\text{NH}_3]\text{SnI}_3$.

4.6.5 NMR for $[\text{GA}][(\text{CH}_3)_2\text{NH}_2]\text{SnI}_3$

Figure 4.26 shows ^{13}C NMR spectra of GAI precursor and $[\text{GA}][(\text{CH}_3)_2\text{NH}_2]\text{SnI}_3$. The precursor shows a prominent peak due its carbon atom at chemical shift 110.57 ppm. This peak is not present in the MOCTP $[\text{GA}][(\text{CH}_3)_2\text{NH}_2]\text{SnI}_3$. One intense peak at 39.2 ppm is observed from the ^{13}C NMR of $[\text{GA}][(\text{CH}_3)_2\text{NH}_2]\text{SnI}_3$ which is attributed to the two carbon atoms from DimI precursor that have the same chemical environment and hence present as a single signal in the spectrum. The structure of these perovskites evidenced by NMR data allow for amine-cavity interactions to introduce some mechanical properties on the hybrid perovskites [70, 71]. Here, the framework is strengthened by interactions between protonated amine and metal-halide cavity, greatly improving

the mechanical properties. Kieslich *et al.* studied the role of amine-cavity interactions in determining mechanical properties of ferroelectric hybrid perovskites [72]. They found that interactions between protonated amine and the metal-formate cavity can be described as salt bridges like those in proteins and artificially synthesized helical polymers. Hydrogen bonds and ionic interactions come to play at the same time. Other transitions that influence mechanical properties of hybrid perovskites include orientational order-disorder phenomena [73]. Order-disorder transitions are temperature driven e.g. $(\text{CH}_3)_2\text{NH}_2\text{Zn}(\text{HCOO})_3$ hybrid perovskite undergoes significant order-disorder phase transition at 156 K. The organic cationic moieties from the synthesized perovskites are bound by hydrogen bonds to the halide (Iodide) in the fashion (N-H...I), and essentially are trapped inside the cage of the perovskite. The state of motion of the organic cationic moiety is temperature dependent [74].

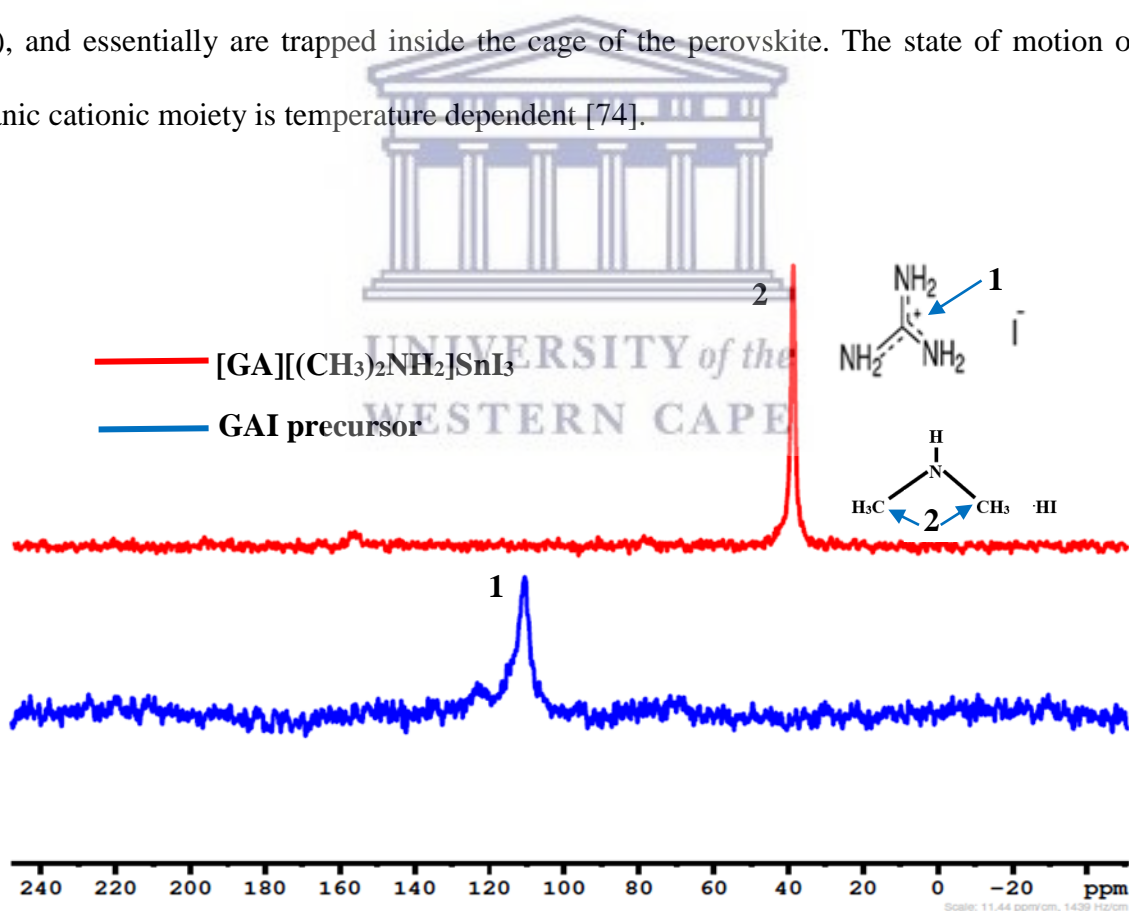
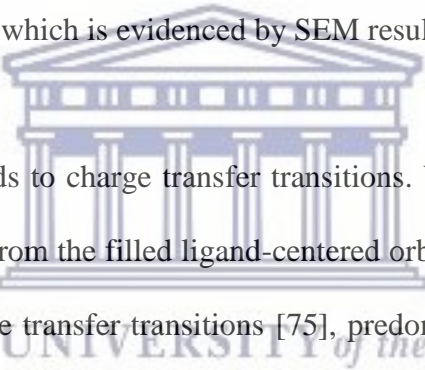


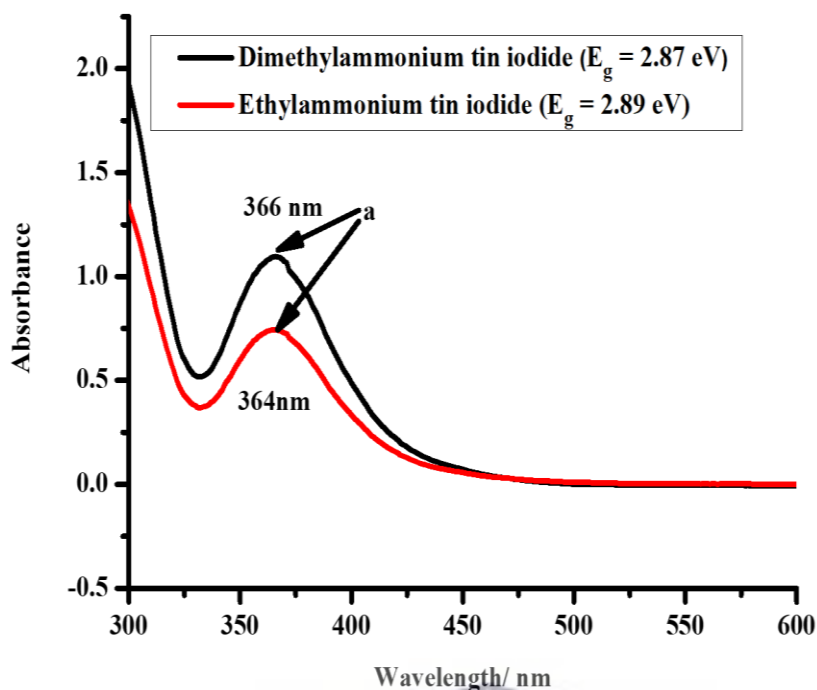
Figure 4.26: ^{13}C NMR spectra for GAI precursor and $[\text{GA}][(\text{CH}_3)_2\text{NH}_2]\text{SnI}_3$.

4.7 UV-Vis results

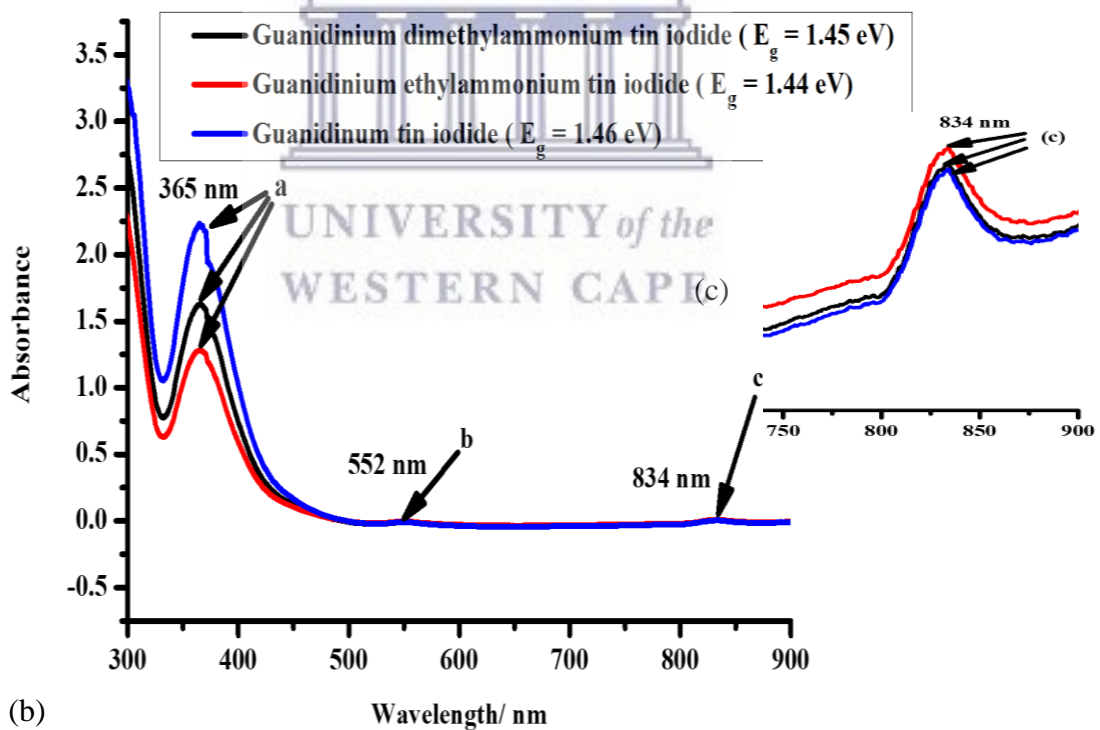
The absorption spectrum of the perovskites is consistent with literature [32, 75]. All the spectra show a very prominent peak (364, 365 and 366 nm), labelled (a) with different intensities of absorption. This broad peak is commonly reported in literature [76] and this region makes these materials suitable for photovoltaic cell application [77]. Guanidinium tin iodide recorded the highest intensity of this peak, and it was observed that mixing either ethylammonium tin iodide or dimethylammonium tin iodide with guanidinium ion improved the intensity of peak (a). The reason for increased peak intensity is attributed to improved grain-size which in turn improved light absorption and surface coverage which is evidenced by SEM results.



This absorption peak corresponds to charge transfer transitions. When electrons are exposed to higher energy, they get excited from the filled ligand-centered orbitals to the half-filled d orbital, producing ligand to metal charge transfer transitions [75], predominant in such complexes with ligands that have high energy lone pairs. In UV-visible spectra, absorption peaks in the range of 100 nm to 300 nm are normally attributed to $n \rightarrow \sigma^*$ or $\pi \rightarrow \pi^*$, and peaks observed in the region higher than 300 nm usually arise due to the transition of $n \rightarrow \pi^*$ [78]. Using this knowledge, all peaks observed in these perovskites are attributed to be due to transition of $n \rightarrow \pi^*$. Figure 4.27 below shows UV-Vis spectra of the various perovskites.



(a)



(b)

Figure 4.27: (a) UV-Vis spectra for $[\text{CH}_3\text{CH}_2\text{NH}_3]\text{SnI}_3$ and $[(\text{CH}_3)_2\text{NH}_2]\text{SnI}_3$, (b) UV-Vis of GASnI_3 , $[\text{GA}][\text{CH}_3\text{CH}_2\text{NH}_3]\text{SnI}_3$ and $[\text{GA}][(\text{CH}_3)_2\text{NH}_2]\text{SnI}_3$, inset shows peak c.

Ligand to metal charge transfer gives rise to intense bands, which result in the reduction of the metal. Ligand to metal charge transfer in organic-inorganic perovskites originates from hydrogen bonds (N-H...X), where X is a halogen [79]. This hydrogen bonding attracts the organic and inorganic groups. Here hydrogen bonding reduces the electron density around the iodide ion and causes the charge transfer metal to ligand Sn---I. High covalency of ligand-metal is associated with low energy. The overlap of the donor and acceptor orbitals involved in the process of charge transfer is proportional to the intensities of these transitions[79]. It is observed in figure 4.27 (a) above that the overlap of both the donor and acceptor orbitals involved in charge transfer is greater in $[(\text{CH}_3)_2\text{NH}_2]\text{SnI}_3$ than in $[\text{CH}_3\text{CH}_2\text{NH}_3]\text{SnI}_3$ perovskite and as expected the overlap is greater in $[\text{GA}][(\text{CH}_3)_2\text{NH}_2]\text{SnI}_3$ than $[\text{GA}][\text{CH}_3\text{CH}_2\text{NH}_3]\text{SnI}_3$ MOCTPs. Laporte forbidden transitions (intra-atomic d-d transitions), whereby parity remains the same may also be seen, giving rise to weak absorptions. Figure 4.27 (b) above shows two weak absorptions at 552 and 834 nm, labelled (b) and (c) respectively which correspond to d-d forbidden transitions. Figure 4.28 below shows ligand to metal charge transfer:

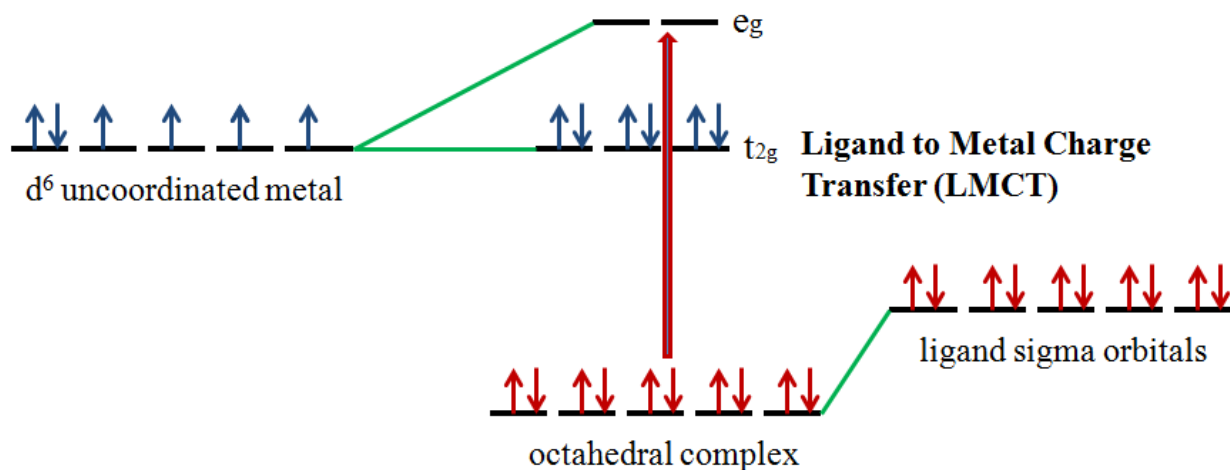


Figure 4.28: Ligand to metal charge transfer (LMCT) for an octahedral d^6 complex [79].

It was observed that mixing guanidinium ion with either dimethylammonium or ethylammonium caused a redshift (shifting to higher wavelength) of peak c, as seen in the inset above. As a result, [GA][CH₃CH₂NH₃]₂SnI₃ showed the narrowest optical band gap of 1.44 eV. [GA][CH₃CH₂NH₃]₂SnI₃ perovskite also had an improved optical band gap of 1.45 eV and GAsnI₃ showed a band gap of 1.46 eV. [(CH₃)₂NH₂]₂SnI₃ and [CH₃CH₂NH₃]₂SnI₃ exhibit the widest optical band gap of 2.87 and 2.89 eV respectively. The MOCTPs recorded the highest peak intensities as observed in inset (figure 4.27 (b)).

Interestingly, mixed-organic-cations perovskites show superior light absorption characteristics to single-organic-cation perovskites. These compounds outperform most studied perovskite (CH₃NH₃PbI₃), which has absorption characteristics of range 500-790 nm [80] relative to range of 365 to 834 nm recorded in the synthesized MOCTPs. Mixing organic cations caused reduction in electrochemical and optical band gaps of these 3D compounds. Stoumpos *et al.* synthesized long chain 2D perovskite compounds (CH₃(CH₂)₃NH₃)₂(CH₃NH₃)_{n-1}Pb_nI_{3n+1} where (n = 1, 2, 3, 4, ∞) perovskites. The optical band gaps of the series were 2.43 eV, 2.17 eV, 2.03 eV, 1.91 eV and 1.50 eV for the n = 1, 2, 3, 4, ∞ respectively, which none could achieve band gap narrower than that of the MOCTPs [81].

The optical energy band gap was calculated using equation (7):

$$E_g = hc / \lambda_{\text{cut off}} \quad (7)$$

Where h is Planck's constant (J.s), c is the speed of light (m/s) and $\lambda_{\text{cut off}}$ (nm) is the cut off wavelength obtained from the spectrum.

Electrochemical characterizations

4.8 Cyclic Voltammetry

4.8.1 CV for the perovskite precursor materials



UNIVERSITY of the
WESTERN CAPE

Figure 4.28 shows the CV of bare (GCE) in supporting electrolyte (comprising of dichloromethane (CH_2Cl_2 , anhydrous, 99.8%), 2mM benzoquinone and 0.1 M tetrabutylammonium hexafluoro phosphate) and bare GCE in 0.05 M tin (II) iodide precursor. The CV were recorded over the potential range of -1.0 V to 1.0 V at a scan rate of 0.05 V/s. For the supporting electrolyte peaks were observed at ($I_{p,a} = 45.14 \mu\text{A}$, $E_{p,a} = -0.50 \text{ V}$) and ($I_{p,c} = -81.31 \mu\text{A}$, $E_{p,c} = -0.70 \text{ V}$). While in the CV of tin (II) iodide, additional peaks were observed at ($I_{p,a} = 11.19 \mu\text{A}$, $E_{p,a} = -0.50 \text{ V}$), ($I_{p,a} = 15.00 \mu\text{A}$, $E_{p,a} = 0.33 \text{ V}$), ($I_{p,a} = 20.57 \mu\text{A}$, $E_{p,a} = 0.62 \text{ V}$), ($I_{p,a} = 57.48 \mu\text{A}$, $E_{p,a} = 0.83 \text{ V}$), ($I_{p,c} = -22.78 \mu\text{A}$, $E_{p,c} = 0.59 \text{ V}$), ($I_{p,c} = -17.49 \mu\text{A}$, $E_{p,c} = 0.41 \text{ V}$) and ($I_{p,c} = -52.58 \mu\text{A}$, $E_{p,c} = -0.09 \text{ V}$)

labelled (a) to (g) respectively. This indicates that tin (II) iodide is electrochemically active at these mentioned peaks, shown in figure 4.29.

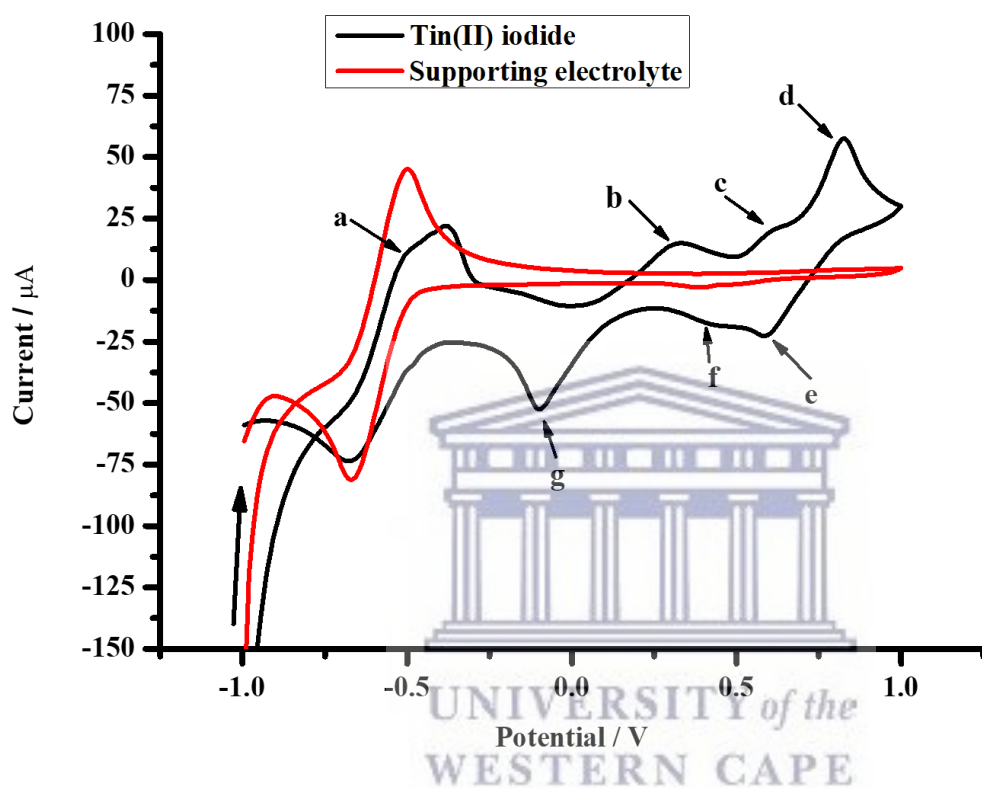


Figure 4.29: Cyclic voltammogram for bare GCE in supporting electrolyte and bare GCE in 0.05 M tin (II) iodide.

Figure 4.30 shows the CV of bare GCE in the supporting electrolyte described in section 4.8.1 above, and bare GCE in 0.05 M tin powder dissolved in the same electrolyte. CV measurements were made over potential range of -1.0 V to 1.0 V at a scan rate of 0.05 V/s. Additional peaks were not observed in the voltammogram of tin powder compared to that of bare GCE in supporting

electrolyte, indicating that tin powder is not electrochemically active in this supporting electrolyte within the potential window established in this experiment.

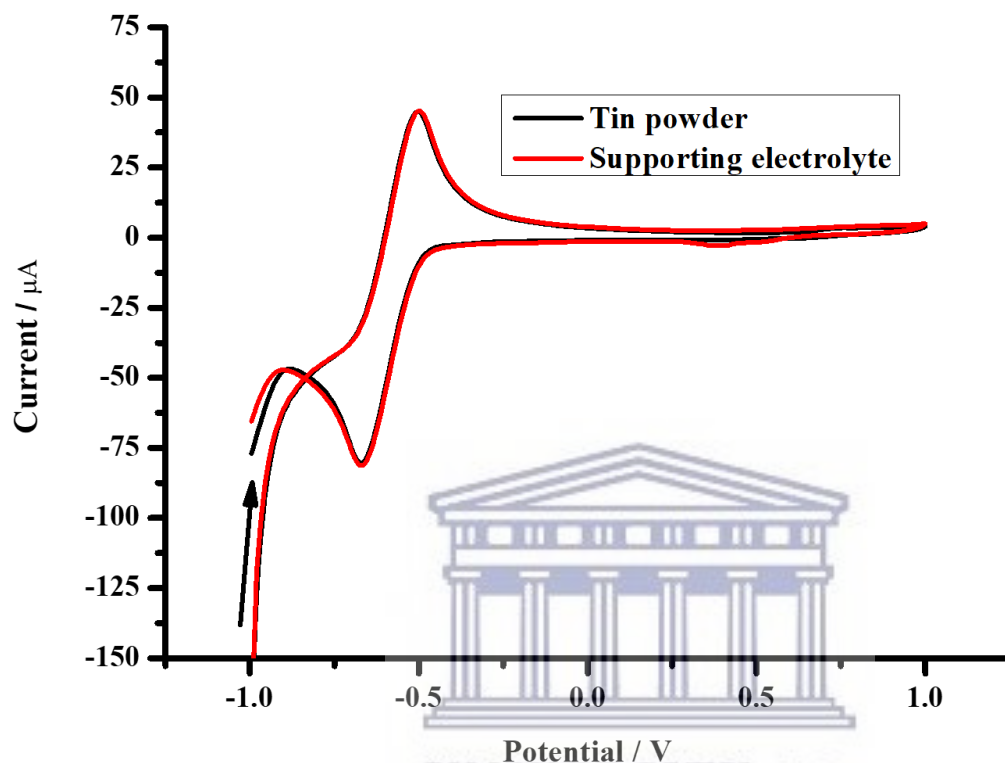


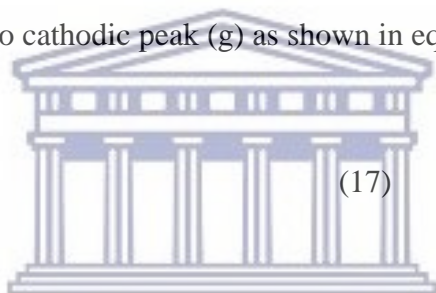
Figure 4.30: Cyclic voltammogram for bare GCE in supporting electrolyte and bare GCE in 0.05 M tin powder.

With the above information established, peaks (a) to (g) in figure 4.29 above can be attributed to iodine/iodide redox reaction. Peak (a) is the anodic peak of the supporting electrolyte that became visible. The most important half redox reaction of iodine/iodide is explained by reaction (16) below [82, 83]. The oxidation reaction is attributed to anodic peak (d) and the reduction reaction is attributed to cathodic peak (e). This reaction is represented by the most prominent peaks in the CV of the perovskites in this work. The reaction was established to be responsible for the reduction of

the perovskites, giving rise to the most important peaks in this work with regards to conversion of light to electricity [83].



In solution, iodine is known to form a tri-iodide ion (I_3^{-}), which establishes an equilibrium with free iodine and iodide ion [82, 84]. The oxidation reaction is attributed to anodic peak (b) and the reduction reaction is attributed to cathodic peak (g) as shown in equation (17) below:



Iodine electrochemistry attributes peak (c) to be due to forward reaction as shown in equation (18) below [84, 85]. Peak (c) is attributed to the oxidation reaction, while cathodic peak (f) is attributed to the reduction reaction as seen below.



Before studying the electrochemistry of the novel MOCTPs, it was found necessary to first study the electrochemistry of their SOCTPs.

(i) SOCTPs

4.8.2 CV for $[\text{CH}_3\text{CH}_2\text{NH}_3]\text{SnI}_3$ perovskite

CV of $[\text{CH}_3\text{CH}_2\text{NH}_3]\text{SnI}_3$ perovskite was recorded over a potential range of -1.0 to 1.0 V at a scan rate of 0.05 V/s. Five peaks were observed: peak a ($I_{p,a} = 4.746 \mu\text{A}$, $E_{p,a} = 0.160 \text{ V}$), peak b ($I_{p,a} = 9.929 \mu\text{A}$, $E_{p,a} = 0.380 \text{ V}$), peak c ($I_{p,a} = 18.278 \mu\text{A}$, $E_{p,a} = 0.665 \text{ V}$), peak d ($I_{p,c} = -2.968 \mu\text{A}$, $E_{p,c} = 0.370 \text{ V}$) and peak e ($I_{p,c} = -17.497 \mu\text{A}$, $E_{p,c} = -0.140 \text{ V}$) as shown in figure 4.31.

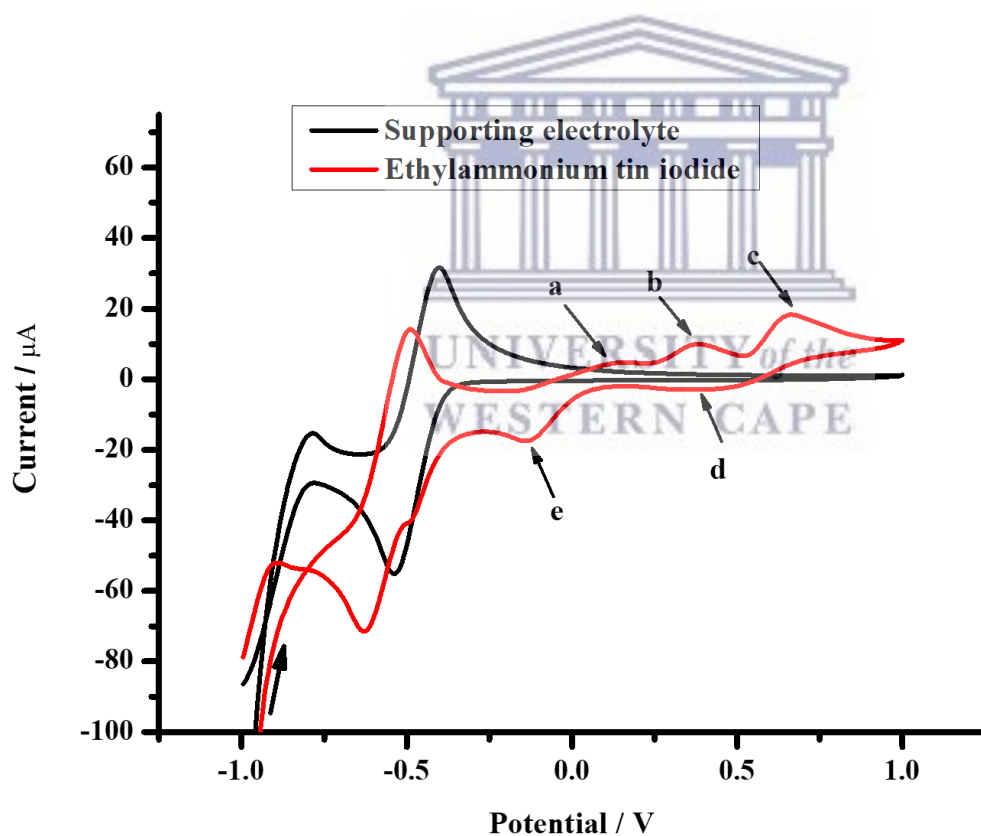


Figure 4.31: CV for bare GCE in supporting electrolyte and bare GCE in 0.05M $[\text{CH}_3\text{CH}_2\text{NH}_3]\text{SnI}_3$ perovskite.

To study only the CV behavior of $[\text{CH}_3\text{CH}_2\text{NH}_3]\text{SnI}_3$ perovskite, the potential window was narrowed to the range -0.3 V to 1.0 V and measured at different scan rates, see Figure 4.32 (a). Figure 4.32 (b) shows the Randles plot of the CV that was obtained from plotting peaks (c) and (e) for oxidation and reduction reactions respectively. Peak current increases with increase in scan rate. Surface bound electro-active $[\text{CH}_3\text{CH}_2\text{NH}_3]\text{SnI}_3$ was successfully and firmly immobilized onto the surface of glassy carbon electrode. The anodic current ($I_{p,a}$) and cathodic peak current ($I_{p,c}$), increase linearly with increase in scan rate. The electron transfer at the electrode-perovskite film interface is rapid, adsorption and diffusion controlled [86].

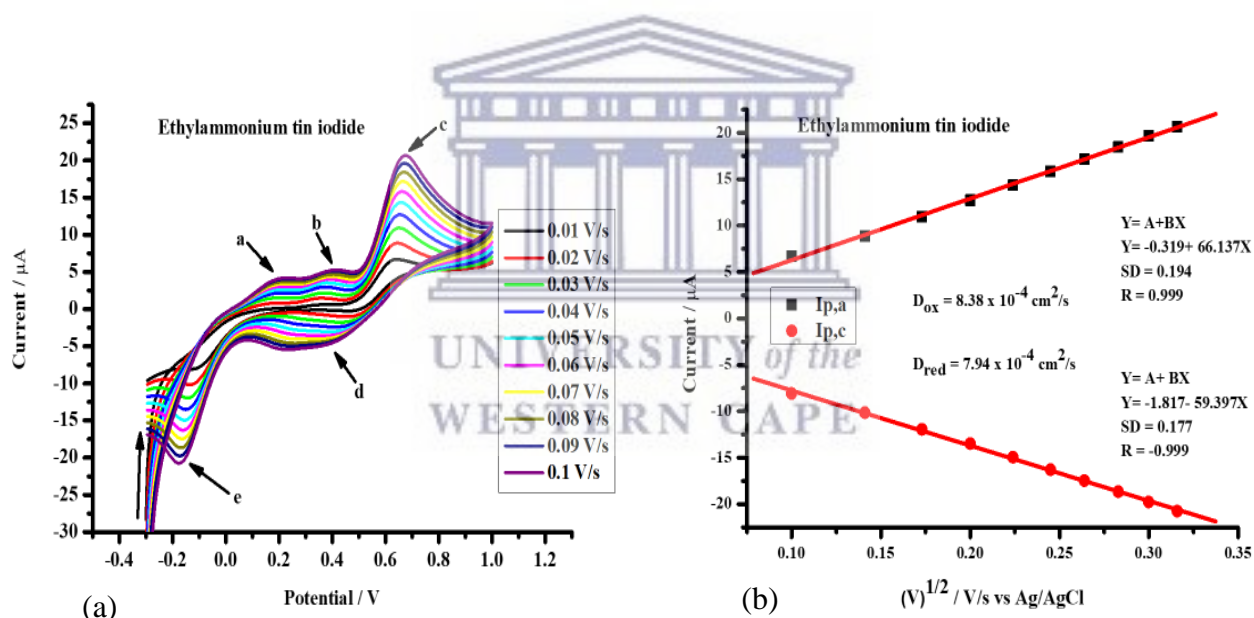


Figure 4.32: (a) CV for $[\text{CH}_3\text{CH}_2\text{NH}_3]\text{SnI}_3$ at various scan rates and (b) Randles plot for $[\text{CH}_3\text{CH}_2\text{NH}_3]\text{SnI}_3$ perovskite.

Careful examination of a voltammogram helps diagnose which reaction step mechanism is occurring as well as the kinetics of the reaction [87, 88].

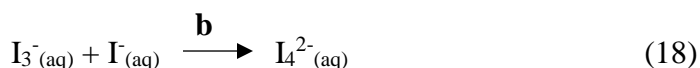
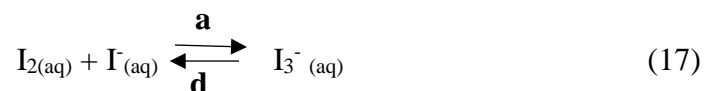
Reaction mechanism:

Sequential electron transfer process electron-transfer reversible process (E_rE_r):

where E indicates electron transfer step while r indicates reversibility [87, 88].



The system has three electron transfer steps. The appearance of the voltammogram depends upon difference in formal potential of the three electrochemical steps. In principle, as separation between more than one reduction peaks ($\Delta E_{1/2}$) decreases, the peaks are expected to merge to become a single two-electron peak [89]. Sampson *et al.*, reported on typical E_rE_r process that involved two electron transfer steps [90]. The iodine/iodide redox reactions already discussed in this chapter explain the oxidation and reduction peaks of the electro-active perovskite that were observed as follows:



Redox reaction (18) does not show a reduction peak in the CV of this perovskite which is because the product, $I_4^{2-}_{(aq)}$, is an insoluble precipitate that does not react further [82]. The Randles-Sevcik equation (11) was used to investigate dependence of peak current (I_p) on scan rate (ν). Plots of I_p against $(\nu)^{1/2}$ are linear as seen in figure 4.32 (b). Examination of peak-peak separation (in figure 4.32 (a)) shows shift with scan rate. The process of electron transfer is therefore electrochemically quasi-reversible [91]. Diffusion co-efficient (D_{ox} and D_{red}) gives the rate at which the electro-active ions and the surface atoms of the electrode exchange in the electrolyte. The D_{ox} and D_{red} were calculated to be $8.38 \times 10^{-4} \text{ cm}^2/\text{s}$ and $7.94 \times 10^{-4} \text{ cm}^2/\text{s}$ respectively, which indicates that the rate of electron transfer does not differ substantially during both reduction and oxidation processes. The electrochemical system is a multi-step electron transfer, where one electron transferred in every step [92]. The number of electrons was calculated using equation (22):

Randles-Sevcik equation:

$$I_p = 0.4463 nFA C (nF\nu D / RT)^{1/2} \quad (21)$$

where I_p represents current maximum in amps, n represents number of electrons transferred in the redox event (usually 1), A represents electrode area in cm^2 , F represents Faraday constant in C mol^{-1} , D represents diffusion coefficient in cm^2/s , C represents concentration in mol/cm^3 , ν represents scan rate in V/s , R represents gas constant in $\text{J K}^{-1} \text{ mol}^{-1}$, T represents temperature in K .

$$E_{p/2,c} - E_{p,c} = (56.5/n) \text{ mV} \quad (22)$$

where $E_{p/2,c}$ is the half cathodic peak potential, $E_{p,c}$ is the cathodic peak potential and n is the number of electrons.

It is necessary to establish whether currents measured during the CV experiments are related to charge carrier injection into the perovskite material or real Faradaic events for the perovskite [93]. First oxidation peak occurs at less positive potential than valence band, which implies that $[\text{CH}_3\text{CH}_2\text{NH}_3]\text{SnI}_3$ is irreversibly oxidized before hole injection can take place [94]. The second reduction peak matches the potential of the conduction band which means that an irreversible transformation of the electroactive species occurs before conduction band gets flooded with electrons. The photogenerated holes and the electrons do not corrode the electrode materials as they get transferred to electron transport layer (ETL) and hole transport layer (HTL) [95].

4.8.3 CV for $[(\text{CH}_3)_2\text{NH}_2]\text{SnI}_3$ perovskite

The approach of studying the CV of $[(\text{CH}_3)_2\text{NH}_2]\text{SnI}_3$ perovskite adopted was the same as that used in $[\text{CH}_3\text{CH}_2\text{NH}_3]\text{SnI}_3$ above. The CV was first recorded over a potential range of -1.0 V to 1.0 V at a scan rate of 0.05 V/s. Similarly, five peaks emerged which did not show when bare GCE in supporting electrolyte was recorded, labelled as peak a ($I_{p,a} = 3.535 \mu\text{A}$, $E_{p,a} = 0.050 \text{ V}$), peak b ($I_{p,a} = 7.620 \mu\text{A}$, $E_{p,a} = 0.375 \text{ V}$), peak c ($I_{p,a} = 17.391 \mu\text{A}$, $E_{p,a} = 0.650 \text{ V}$), peak d ($I_{p,c} = -2.737 \mu\text{A}$, $E_{p,c} = 0.365 \text{ V}$) and peak e ($I_{p,c} = -18.003 \mu\text{A}$, $E_{p,c} = -0.220 \text{ V}$) as shown in figure 4.33 below.

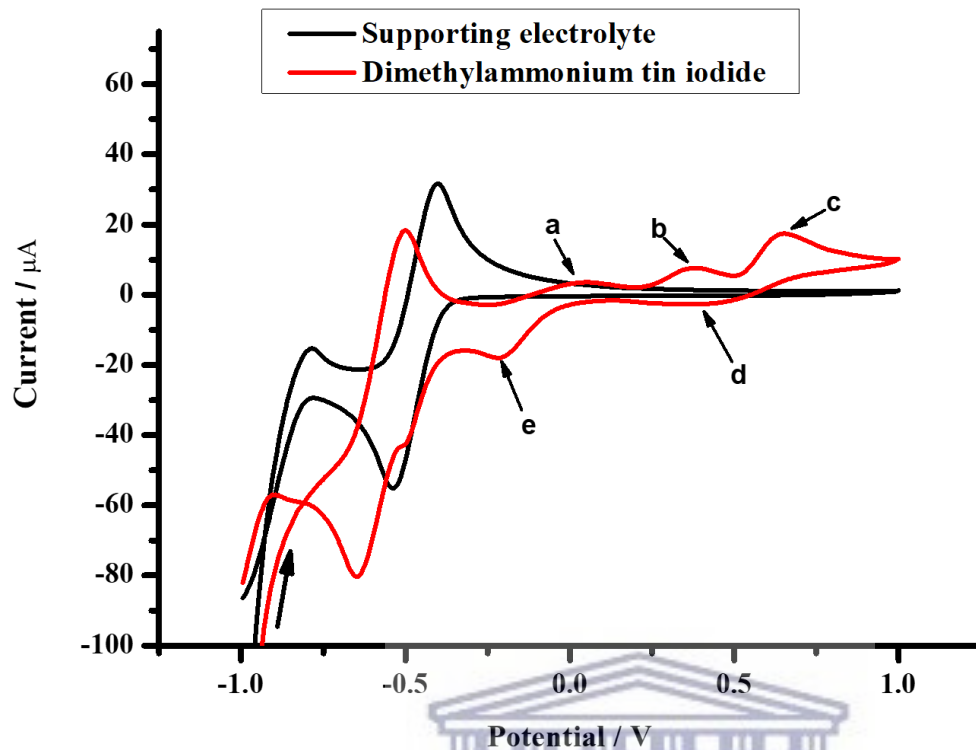


Figure 4.33: CV for bare GCE in supporting electrolyte and bare GCE in 0.05 M $[(\text{CH}_3)_2\text{NH}_2]\text{SnI}_3$ perovskite.

Figure 4.34 (a) shows the CV studies of the perovskite in a narrowed potential window (-0.3V to 1.0 V) at various scan rates and (b) shows the Randles plot of the perovskite established through plotting of peaks (c) and (e).

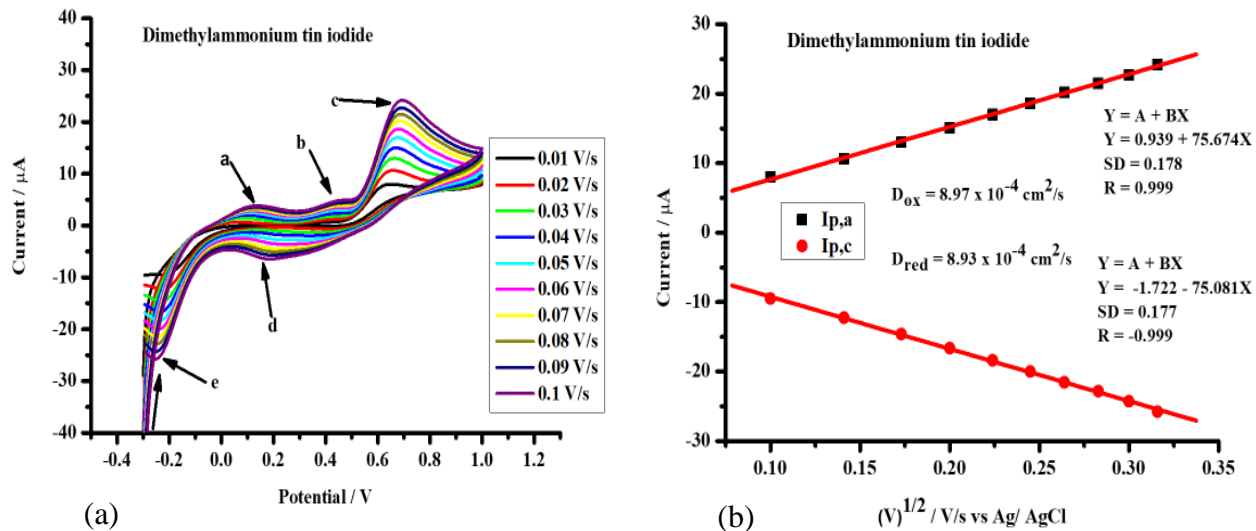


Figure 4.34: (a) CV for bare GCE in 0.05 M $[(\text{CH}_3)_2\text{NH}_2]\text{SnI}_3$ at various scan rates and (b) Randles plot for the perovskite.

Reaction mechanism:

The mechanism already explained in section 4.8.2 is used to explain electron transfer in $[(\text{CH}_3)_2\text{NH}_2]\text{SnI}_3$ perovskite. The mechanism is sequential electron transfer process electron-transfer reversible process (E_rE_r) [96] The oxidation and reduction peaks, (a) to (e), recorded in this potential window are attributed to the iodine/iodide redox reactions (1), (2) and (3) which have been explained in ethylammonium tin iodide perovskite in section 4.8.2.

Randles plots of I_p against $(v)^{1/2}$ show linear dependence of peak current with scan rate as seen in figure 4.34 (b), which indicates that the electron transfer at the electrode-perovskite film interface is rapid, adsorption and diffusion controlled. Peak-peak separation (in figure 4.34 (a)) shifts with scan rate [89], hence the process of electron transfer is electrochemically quasi-reversible. Diffusion co-efficient (D_{ox} and D_{red}) gives the rate at which the electro-active ions and the surface

atoms of the electrode exchange in the electrolyte. The D_{ox} and D_{red} were calculated to be $8.97 \times 10^{-4} \text{ cm}^2/\text{s}$ and $8.93 \times 10^{-4} \text{ cm}^2/\text{s}$ respectively, which implies that the rate of electron transfer is similar during oxidation and reduction processes. The system is a multi-step electron transfer that involves one electron [90].

4.8.4 CV for GASnI_3 perovskite

Figure 4.35 below shows the CV studies of GASnI_3 perovskite recorded at wider potential range of -1.0 V to 1.0 V and 0.05 V/s scan rate. When the CV of bare GCE in the perovskite was investigated, 5 new peaks (excluding the supporting electrolyte's peaks) showed, labelled (b) to (f). Peak a ($I_{p,a} = 11.71 \mu\text{A}$, $E_{p,a} = -0.26 \text{ V}$) is oxidation peak of the supporting electrolyte and peak b ($I_{p,b} = 26.129 \mu\text{A}$, $E_{p,b} = 0.345 \text{ V}$), peak c ($I_{p,c} = 67.854 \mu\text{A}$, $E_{p,c} = 0.780 \text{ V}$), peak d ($I_{p,d} = -16.449 \mu\text{A}$, $E_{p,d} = 0.385 \text{ V}$), peak e ($I_{p,e} = -24.710 \mu\text{A}$, $E_{p,e} = -0.220 \text{ V}$) and peak f ($I_{p,f} = -42.154 \mu\text{A}$, $E_{p,f} = -0.380 \text{ V}$) originate from the electro-activity of the perovskite material.

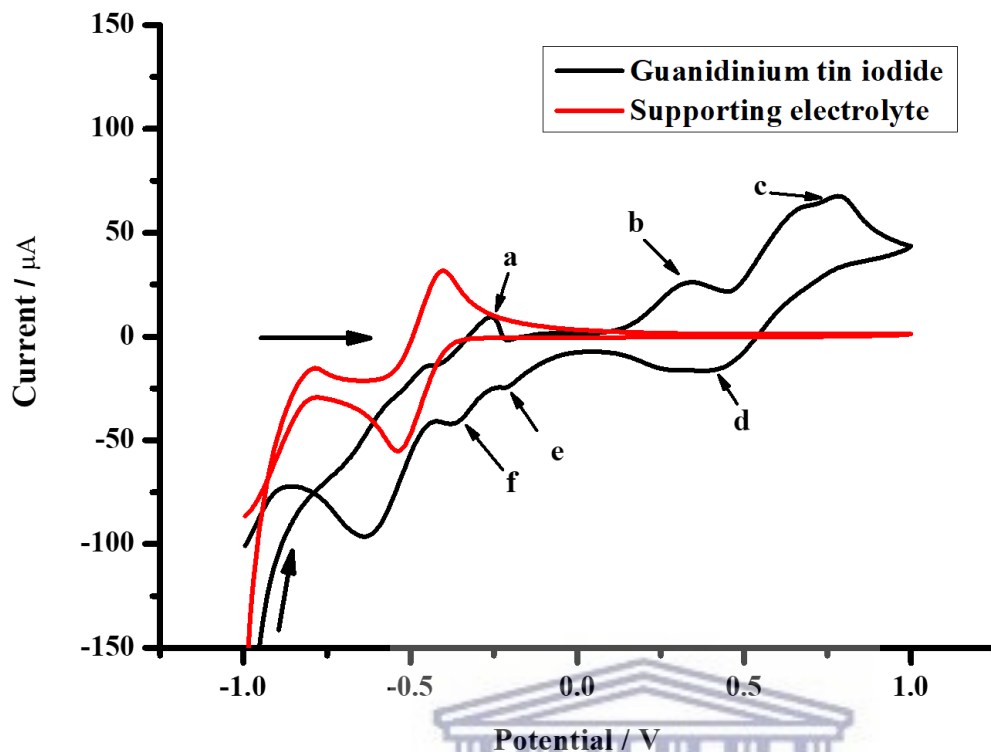


Figure 4.35: CV for bare GCE in supporting electrolyte and bare GCE in 0.05 M GASnI_3 perovskite.

CV studies of only GASnI_3 perovskite, recorded at various scan rates, was established in the range of -0.5 V to 1.0 V. This window unfortunately does not exclude peak (a) which is an oxidation peak from the supporting electrolyte. Like the perovskites discussed in earlier sections, the anodic peaks shift slightly to the right and the cathodic peaks shift slightly to the left as the scan rate. Figure 4.36 (a) shows CV studies of the perovskite at various scan rates and (b) shows the Randles plot of the perovskite obtained through plotting peaks (c) and (d).

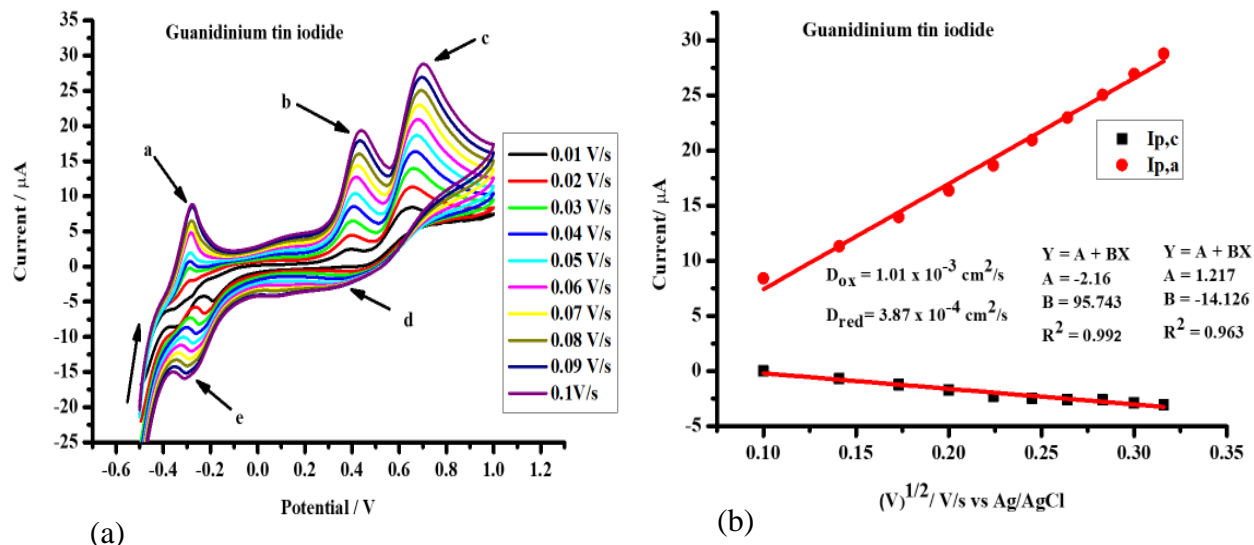
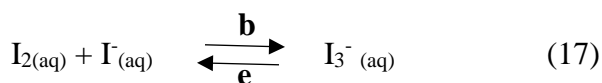
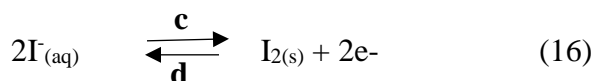


Figure 4.36: (a) CV for bare GCE in 0.05 M GASnI₃ at various scan rates and (b) Randles plot for the perovskite.

Reaction mechanism:

Similar to the previously discussed perovskites, the electrochemical reaction steps for GASnI₃ follow the sequential electron transfer process electron-transfer reversible process (E_rE_r) [87, 88]. When the potential window was narrowed, four peaks were observed that are attributed to the oxidation and reduction of the perovskite, namely peak b, c, d and e. Reduction and oxidation reactions (16) and (17) explain the four peaks:



Randles plots of I_p against $(\nu)^{1/2}$ show linear dependence of peak current with scan rate (see figure 4.36 (b)). which indicates that the electron transfer at the electrode-perovskite film interface is rapid, adsorption and diffusion controlled. Peak-peak separation (in figure 4.36 (a)) shifts with scan rate, hence the process of electron transfer is electrochemically quasi-reversible [89]. D_{ox} and D_{red} differ substantially, with values of $1.10 \times 10^{-3} \text{ cm}^2/\text{s}$ and $3.87 \times 10^{-4} \text{ cm}^2/\text{s}$ respectively, indicating faster electron transfer during oxidation compared to reduction. The reaction involves transfer of one electron in multi-steps.

(ii) *MOCTPs*



4.8.5 CV for [GA][CH₃CH₂NH₃]₃SnI₃ perovskite

The CV studies of [GA][CH₃CH₂NH₃]₃SnI₃ perovskite was recorded over a potential range of -1.0 V to 1.0 V at 0.05 V/s scan rate. Seven new peaks appeared that did not show when GCE in supporting electrolyte was recorded under the same parameters, labelled (a) to (g). Peak a ($I_{p,a} = 16.81 \mu\text{A}$, $E_{p,a} = -0.26 \text{ V}$) is an oxidation peak of the supporting electrolyte. Peak b ($I_{p,a} = 7.769 \mu\text{A}$, $E_{p,a} = -0.130 \text{ V}$), peak c ($I_{p,a} = 34.079 \mu\text{A}$, $E_{p,a} = 0.360 \text{ V}$), peak d ($I_{p,c} = 47.485 \mu\text{A}$, $E_{p,c} = 0.610 \text{ V}$), peak e ($I_{p,c} = -5.641 \mu\text{A}$, $E_{p,c} = 0.385 \text{ V}$), peak f ($I_{p,c} = -46.916 \mu\text{A}$, $E_{p,c} = -0.270 \text{ V}$) and peak g ($I_{p,c} = -51.654 \mu\text{A}$, $E_{p,c} = -0.400 \text{ V}$) indicate that the perovskite is electro-active, see figure 4.37.

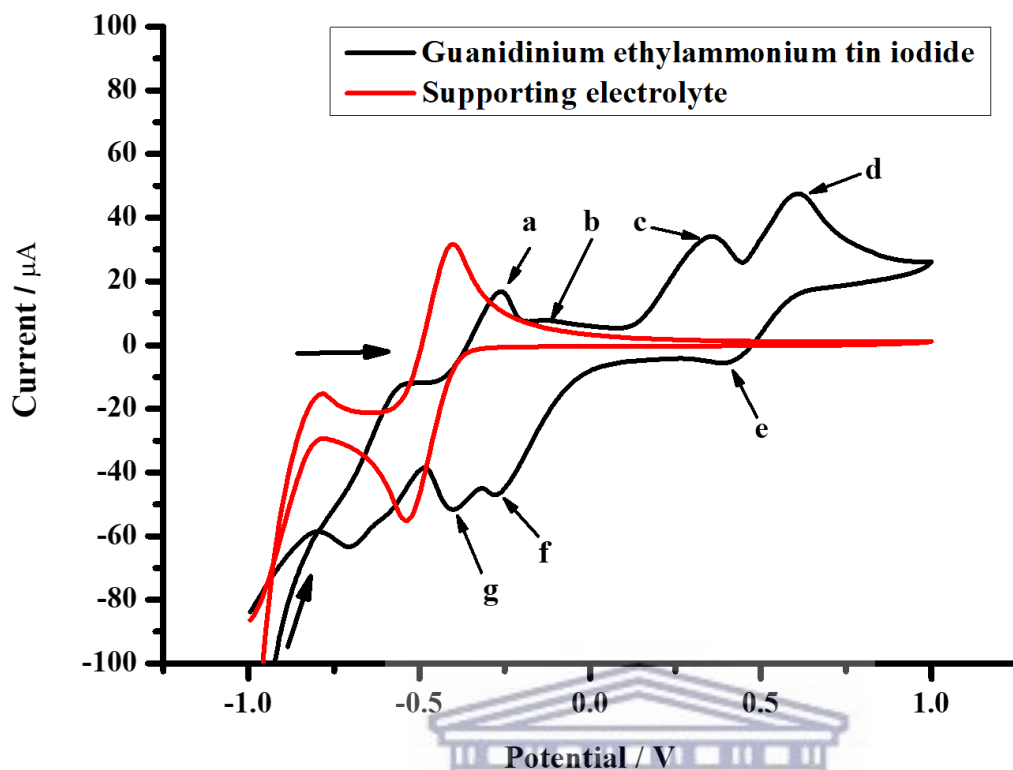


Figure 4.37: CV for bare GCE in supporting electrolyte and bare GCE in 0.05 M [GA][CH₃CH₂NH₃]₃SnI₃ perovskite.

A narrowed potential window of the range -0.5 to 1.0 V and scan rate of 0.05 V/s was established to focus the CV studies only to [GA][CH₃CH₂NH₃]₃SnI₃ electro-activity. Peak (a) could not be excluded in this established working potential window, but it was established to be the supporting electrolyte's oxidation peak. Figure 4.38 (a) below shows the CV studies of the perovskite at various scan rates, (b) shows the Randles plot of the perovskite obtained through plotting peaks (d) and (e) for oxidation and reduction reactions respectively. The anodic peaks shift slightly to the right and the cathodic peaks shift slightly to the left as the scan rate increases.

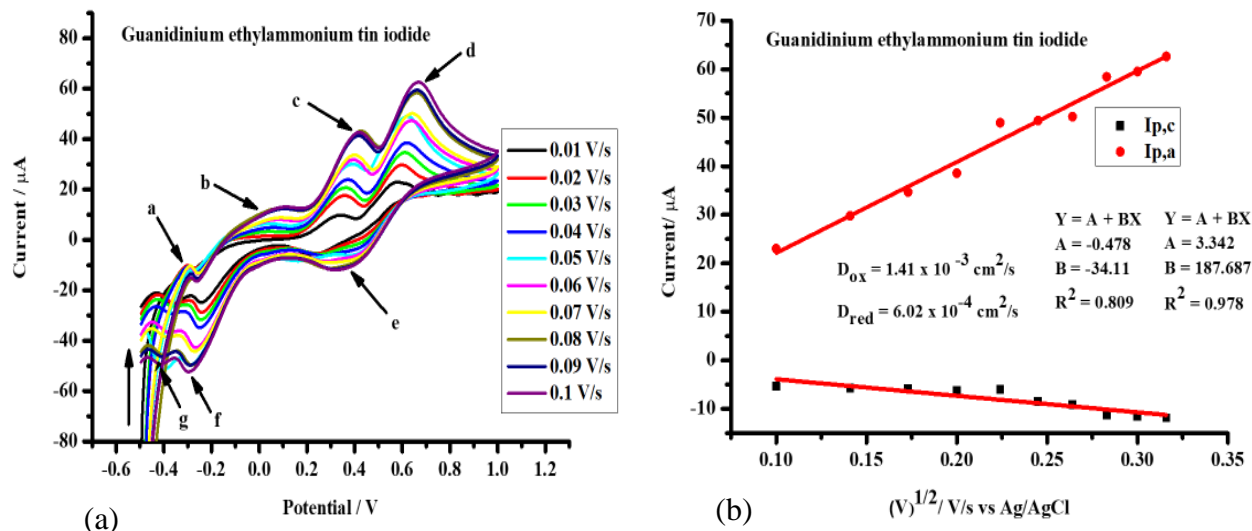
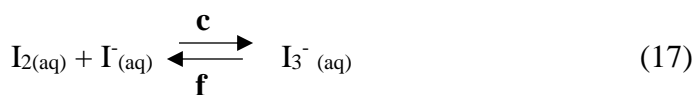
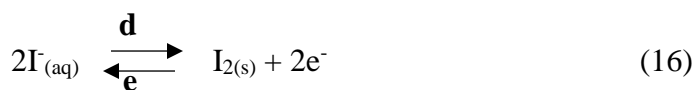


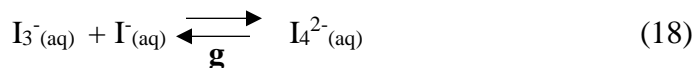
Figure 4.38: CV for bare GCE in 0.05 M [GA][CH₃CH₂NH₃]SnI₃ at various scan rates and (b) Randles plot for the perovskite.

Reaction mechanism:

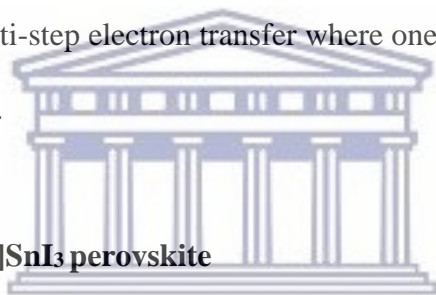
Similar to the SOCTPs, the electrochemical reaction steps for GASnI₃ follow the sequential electron transfer process electron-transfer reversible process (E_rE_r) [87, 88]. The system has three reaction steps, in which all peaks are more pronounced relative to SOCTPs, which is due to improved electrochemical properties of MOCTPs. The following reduction and oxidation reactions explain the six peaks observed in this potential window of the CV of this MOCTP.



b



Randles plots of I_p against $(\nu)^{1/2}$ show linear dependence of peak current with scan rate as seen in figure 4.38 (b), which indicates that the electron transfer at the electrode-perovskite film interface is rapid, adsorption and diffusion controlled. Peak-peak separation (in figure 4.38 (a)) shifts with scan rate, hence the process of electron transfer is electrochemically quasi-reversible [89]. The electro-active ions and the surface atoms of the electrode exchange in the electrolyte (D_{ox} and D_{red}) were $1.41 \times 10^{-3} \text{ cm}^2/\text{s}$ and $6.02 \times 10^{-4} \text{ cm}^2/\text{s}$ respectively. The process of oxidation of the perovskite had faster rate of electron transfer when compared to reduction process. The electrochemical system is a multi-step electron transfer where one electron is transferred in every reduction or oxidation step [86].



UNIVERSITY of the
WESTERN CAPE

4.8.6 CV for [GA][(CH₃)₂NH₂]₃SnI₃ perovskite

Figure 4.39 below shows CV studies of [GA][(CH₃)₂NH₂]₃SnI₃ perovskite recorded over a potential range of -1.0 V to 1.0 V at scan rate of 0.05 V/s. Like [GA][CH₃CH₂NH₃]₃SnI₃ perovskite in section 4.8.5, seven new peaks that did not show with bare GCE in supporting electrolyte were recorded. Anodic peak (a) is an oxidation peak from the supporting electrolyte. Peak b ($I_{p,a} = 4.885 \mu\text{A}$, $E_{p,a} = 0.040 \text{ V}$), peak c ($I_{p,a} = 33.904 \mu\text{A}$, $E_{p,a} = 0.330 \text{ V}$), peak d ($I_{p,c} = 51.460 \mu\text{A}$, $E_{p,c} = 0.640 \text{ V}$), peak e ($I_{p,c} = -21.053 \mu\text{A}$, $E_{p,c} = 0.235 \text{ V}$), peak f ($I_{p,c} = -52.629 \mu\text{A}$, $E_{p,c} = -0.280 \text{ V}$) and peak g ($I_{p,c} = -59.379 \mu\text{A}$, $E_{p,c} = -0.400 \text{ V}$), indicate electro-activity of the perovskite.

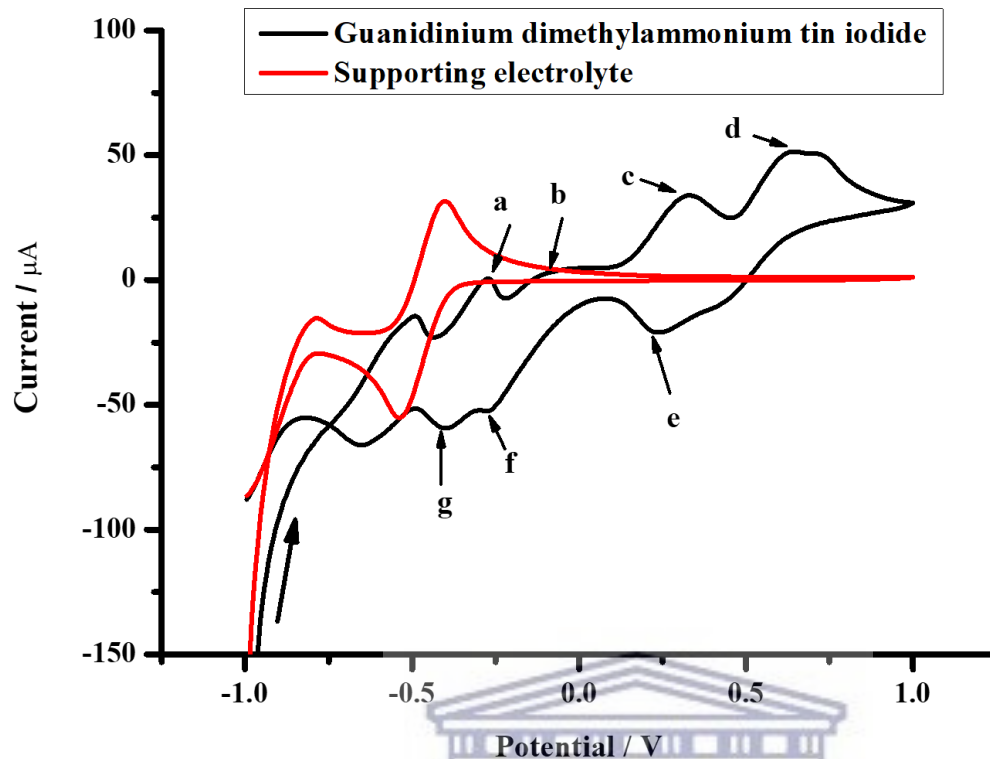


Figure 4.39: CV for bare GCE in supporting electrolyte and bare GCE in 0.05 M [GA][(CH₃)₂NH₂]SnI₃ perovskite.

A new working potential window was established in the range -0.5 V to 1.0 V at 0.05 V/s scan rate. Just like with guanidinium ethylammonium tin iodide, supporting electrolytes' peak (a) could not be cut outside this established working potential window. Figure 4.40 (a) below shows the CV studies of the perovskite at this narrow potential window at various scan rates, (b) shows the Randles plot of the perovskite when peaks (d) and (e) were plotted for oxidation and reduction reactions respectively. Surface bound electro-active species was successfully and firmly immobilized onto the surface of glassy carbon electrode. This is based on the observation that anodic peaks shift slightly to the right and the cathodic peaks shift slightly to the left as the scan rate increases.

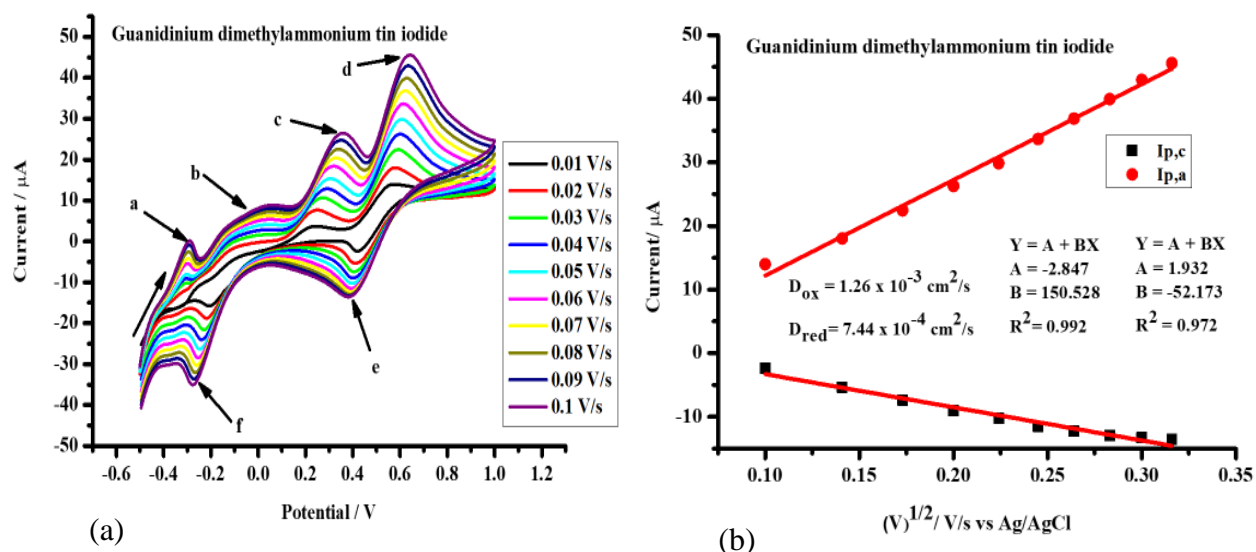
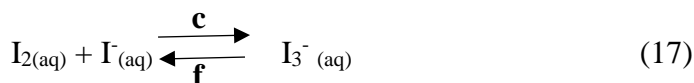
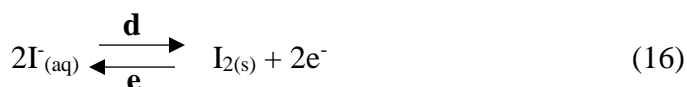
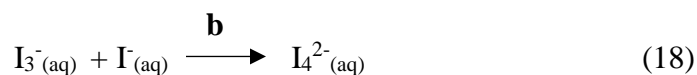


Figure 4.40: (a) CV for bare GCE in 0.05 M [GA][(CH₃)₂NH₂]SnI₃ at various scan rates and (b) Randles plot for the perovskite.

Reaction mechanism:

This electrochemical system follows the sequential electron transfer process electron-transfer reversible process (E_rE_r) as well [87, 88]. All peaks are more pronounced relative to SOCTPs, confirming improved electrochemical properties of MOCTPs relative to SOCTPs. The following reduction and oxidation reactions explain the peaks observed in this potential window of the CV of [GA][(CH₃)₂NH₂]SnI₃.





The $\text{I}_{4^{2-}(\text{aq})}$ species in reaction (18) was not reduced probably because it is an insoluble precipitate as mentioned before. Randles plots of I_p against $(\nu)^{1/2}$ show linear dependence of peak current with scan rate as seen in figure 4.40 (b), which indicates that the electron transfer at the electrode-perovskite film interface is rapid, adsorption and diffusion controlled. Peak-peak separation (in figure 4.40 (a)) shifts with scan rate, hence the process of electron transfer is electrochemically quasi-reversible [87, 89]. The Diffusion coefficient (D_{ox} and D_{red}) were calculated to be $1.21 \times 10^{-3} \text{ cm}^2/\text{s}$ and $7.44 \times 10^{-4} \text{ cm}^2/\text{s}$ respectively. The rate of electron transfer was faster when the perovskite was oxidized compared to when it was reduced. The system is a multi-step electron transfer that involves one electron in every reduction or oxidation step [86, 89].

4.8.7 Electrochemical band gap

Table 1 shows the electrochemical band gaps of the 5 perovskites, which were calculated using equations (23) and (24):

$$E_{\text{HOMO}} = -eV [E_{\text{ox onset}} + 4.41] \text{ and } E_{\text{LUMO}} = -eV [E_{\text{red onset}} + 4.41] \quad (23)$$

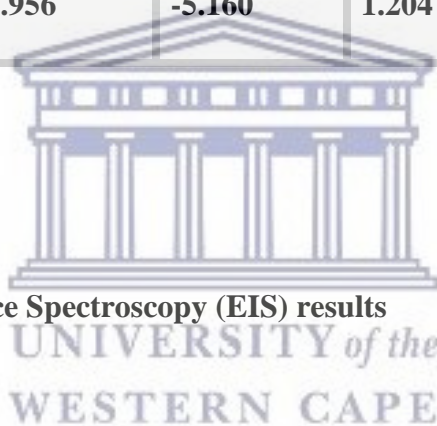
$$\text{Energy band gap } (E_g) = E_{\text{HOMO}} - E_{\text{LUMO}} \quad (24)$$

where $E_{\text{ox onset}}$ and $E_{\text{red onset}}$ are the potentials for the first oxidation peak and first reduction peak respectively. The value 4.41 is obtained from addition of half potential of ferrocene standard (0.41 V) - ferrocene value (-4.8 V).

The band gaps followed the order; $\text{GASnI}_3 > [\text{GA}][(\text{CH}_3)_2\text{NH}_2]\text{SnI}_3 > [\text{GA}][\text{CH}_3\text{CH}_2\text{NH}_3]\text{SnI}_3 > [(\text{CH}_3)_2\text{NH}_2]\text{SnI}_3 > [\text{CH}_3\text{CH}_2\text{NH}_3]\text{SnI}_3$. This order is similar to that obtained from optical band gap studies. Mixing guanidinium ion (ionic radius 278 pm) with organic cation of smaller ionic radius narrowed the band gap in the resulting mixed organic cation perovskite [97]. Ethylammonium and dimethylammonium have ionic radii of 274 pm and 272 pm respectively. The values obtained for electrochemical band gaps of GASnI_3 , $[\text{GA}][(\text{CH}_3)_2\text{NH}_2]\text{SnI}_3$ and $[\text{GA}][\text{CH}_3\text{CH}_2\text{NH}_3]\text{SnI}_3$ are closer to the optical band gaps of the respective material. $[\text{CH}_3\text{CH}_2\text{NH}_3]\text{SnI}_3$ and $[(\text{CH}_3)_2\text{NH}_2]\text{SnI}_3$, however, shows significant difference between electrochemical and optical band gaps as seen in table 4.2 below.

Table 4.2: Calculated electrochemical band gaps relative to the respective perovskite materials.

Perovskite	E_{HOMO} (eV)	E_{LUMO} (eV)	Electrochemical band gap (eV)	Optical band gap (eV)
$[\text{CH}_3\text{CH}_2\text{NH}_3]\text{SnI}_3$	-4.175	-5.225	1.050	2.89
$[(\text{CH}_3)_2\text{NH}_2]\text{SnI}_3$	-4.160	-5.225	1.060	2.87
GASnI_3	-3.945	-5.205	1.260	1.46
$[\text{GA}][\text{CH}_3\text{CH}_2\text{NH}_3]\text{SnI}_3$	-3.960	-5.160	1.200	1.44
$[\text{GA}][(\text{CH}_3)_2\text{NH}_2]\text{SnI}_3$	-3.956	-5.160	1.204	1.45



4.9 Electrochemical Impedance Spectroscopy (EIS) results

The AC potential was biased at 0 mV in all recorded EIS experiments as this leads to low induced diffusion current and simplified electrical circuit [30]. The real (Z') part is plotted on the x-axis against the imaginary part (Z'') on the y-axis to obtain the Nyquist plot over a frequency range in Ohm (Ω). This plot gives a relation to the electrical model [98], however the Nyquist plot does not give information about the frequency used to record any chosen point [99, 100]. In contrast, the Bode plot shows information about frequency hence is usually preferred over Nyquist plot [86]. In the Bode plot, the log frequency is plotted on the x-axis against the log of modulus of impedance and the absolute values of phase-shift on the y-axis.

4.9.1 EIS for [CH₃CH₂NH₃]₃SnI₃ perovskite

Presented in figure 4.41 below are the Nyquist and Bode fitted plots of a bare GCE in 0.05 M [CH₃CH₂NH₃]₃SnI₃, where supporting electrolyte comprised of dichloromethane (CH₂Cl₂, anhydrous, 99.8%), 2mM benzoquinone and 0.1 M tetrabutylammonium hexafluoro phosphate. This electrochemical system was adopted from Li *et al.* [101].

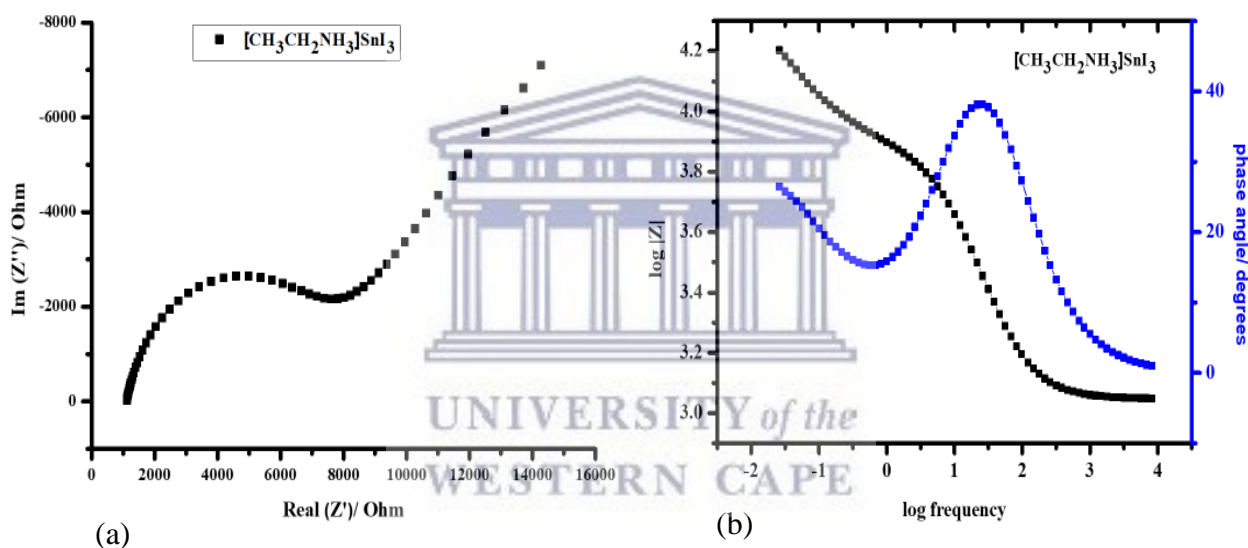


Figure 4.41: (a) Nyquist and (b) Bode plots for [CH₃CH₂NH₃]₃SnI₃.

The equivalence circuit that was used to fit the impedance data is shown in figure 4.42 below, while the values obtained for elements of the circuit are shown in table 4.3. The series resistance (R_s) represents resistance of substrate, which recorded $R_s = 1113 \Omega$ for this perovskite. The parallel resistor charge transfer resistance (R_{ct}) recorded $R_{ct} = 6325 \Omega$ while capacitor (CPE) constant phase element recorded $CPE = 0.836 \text{ nF}$. Both parallel resistor and capacitor represent the band

bending at the interface, resulting in an imperfect capacitor [102]. The diffusion component adheres to Warburg-type of diffusion of ions in solution. This is given by the recorded value of $W_o = 0.517 \Omega s^{1/2}$, Warburg element (open) W_o .

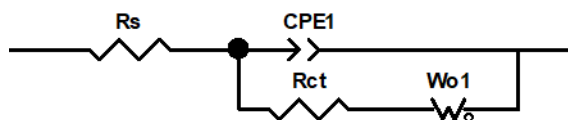


Figure 4.42: Equivalence circuit used to analyze the EIS data for $[\text{CH}_3\text{CH}_2\text{NH}_3]\text{SnI}_3$.

Table 4.3: Values of the elements of the circuit used to fit $[\text{CH}_3\text{CH}_2\text{NH}_3]\text{SnI}_3$ EIS data.

Element	Value	% Error
$R_s (\Omega)$	1113	0.306
$R_{ct} (\Omega)$	6325	1.301
CPE1- P (nF)	0.836	0.489
$W_o1\text{-P} (\Omega s^{1/2})$	0.517	1.735

When a semiconductor electrode is immersed in an electrolyte, a space charge layer/ Helmholtz layer interface is formed. The motion of charge carrier (electrons or holes) through this interface can be explained through modelling from macroscopic impedance as parallel and series resistors and capacitors [103]. From the EIS studies of $[\text{CH}_3\text{CH}_2\text{NH}_3]\text{SnI}_3$, it was observed that the

perovskite film shows 2 time-constants in complex plane plot. The EIS spectrum can be fitted to an ideal parallel resistor and capacitor circuit in the high frequency range. This region corresponds to the space charge layer of the perovskite film [103]. A transition in to a linear region is observed in the Nyquist plot for this perovskite, which indicates an additional diffusion component to the recorded overall capacitance [104]. This electrochemical system has the smallest charge transfer resistance amongst the perovskites studied in this research, $R_{ct} = 6325 \Omega$ while R_s was high, $R_s = 1113 \Omega$, indicating a high electron transfer rate at the electrode-electrolyte interface [105]. This faster rate of electron transfer was also corroborated by CV studies whereby the diffusion coefficients were very high, making this SOCTP ideal for solar cell and other applications.

4.9.2 EIS for $[(CH_3)_2NH_2]SnI_3$ perovskite



Figure 4.43 below shows the Nyquist and Bode plots of bare GCE in 0.05 M $[(CH_3)_2NH_2]SnI_3$ perovskite, where the supporting electrolyte comprised of dichloromethane (CH_2Cl_2 , anhydrous, 99.8%), 2mM benzoquinone and 0.1 M tetrabutylammonium hexafluoro phosphate. Same electrochemical system setup adopted is same as in section 4.9.1 above.

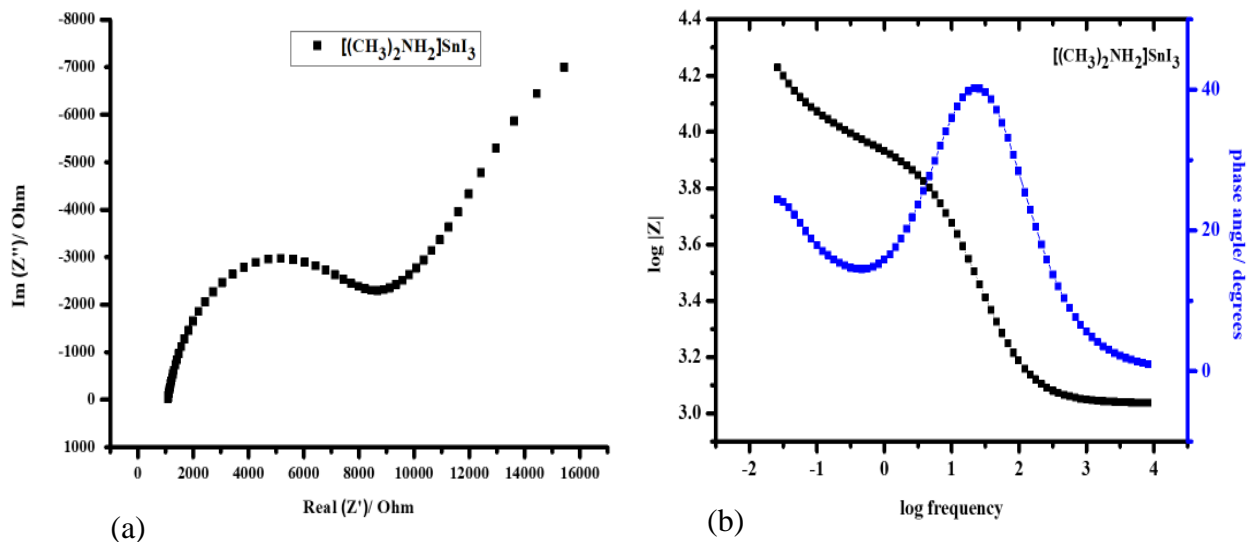


Figure 4.43: (a) Nyquist and (b) Bode plots for $[(\text{CH}_3)_2\text{NH}_2]\text{SnI}_3$.

The equivalence circuit that was used to fit the EIS data for the $[(\text{CH}_3)_2\text{NH}_2]\text{SnI}_3$ perovskite is shown in figure 4.42 above while the elements of the circuit and their fitted values are shown in table 4.4 below. This perovskite recorded series resistance $R_s = 1084 \Omega$ which is lower than that recorded for $[\text{CH}_3\text{CH}_2\text{NH}_3]\text{SnI}_3$ in section 4.9.1 above. This system recorded parallel resistor $R_{ct} = 7212 \Omega$ which is higher than that recorded for $[\text{CH}_3\text{CH}_2\text{NH}_3]\text{SnI}_3$ perovskite while capacitor (CPE) constant phase element recorded same value of $\text{CPE} = 0.517 \text{ nF}$. Both the parallel resistor and capacitor conform to imperfect capacitor behavior [103]. The diffusion component in this system adheres to Warburg-type of diffusion of ions in solution as well, which recorded a value of $W_o = 0.517 \Omega\text{s}^{1/2}$.

Table 4.4: Values of the elements of the circuit used to fit $[(\text{CH}_3)_2\text{NH}_2]\text{SnI}_3$ EIS data

Element	Value	% Error
$R_s (\Omega)$	1084	0.323
$R_{ct} (\Omega)$	7212	1.333
CPE1-P (nF)	0.837	0.479
Wo1-P ($\Omega s^{1/2}$)	0.517	2.139

It was observed that the EIS spectrum for $[(\text{CH}_3)_2\text{NH}_2]\text{SnI}_3$ perovskite film shows same behavior as $[\text{CH}_3\text{CH}_2\text{NH}_3]\text{SnI}_3$, showing 2 time-constants in complex plane plot. The high frequency region corresponds to the space charge of the $[(\text{CH}_3)_2\text{NH}_2]\text{SnI}_3$ perovskite since the spectrum can be fitted to an ideal parallel resistor and capacitor circuit in the high frequency range [106, 107]. Linear region is also observed in the Nyquist plot for this perovskite, which indicates an additional diffusion component to the recorded overall capacitance. This electrochemical system has the small charge transfer resistance $R_{ct} = 7212 \Omega$ while series resistance recorded $R_s = 1084 \Omega$, which is comparable to the values obtained in the perovskite discussed in section 4.9.1 above. Both EIS and CV studies show similar observations whereby $[\text{CH}_3\text{CH}_2\text{NH}_3]\text{SnI}_3$ and $[(\text{CH}_3)_2\text{NH}_2]\text{SnI}_3$ SOCTP have similar electrochemical behavior, showing the best electron transfer reactions.

4.9.3 EIS for GASnI₃ perovskite

Figure 4.44 below shows the Nyquist and Bode plots of a bare GCE in 0.05 M GASnI₃ perovskite, where the supporting electrolyte comprised of dichloromethane (CH₂Cl₂, anhydrous, 99.8%), 2mM benzoquinone and 0.1 M tetrabutylammonium hexafluoro phosphate.

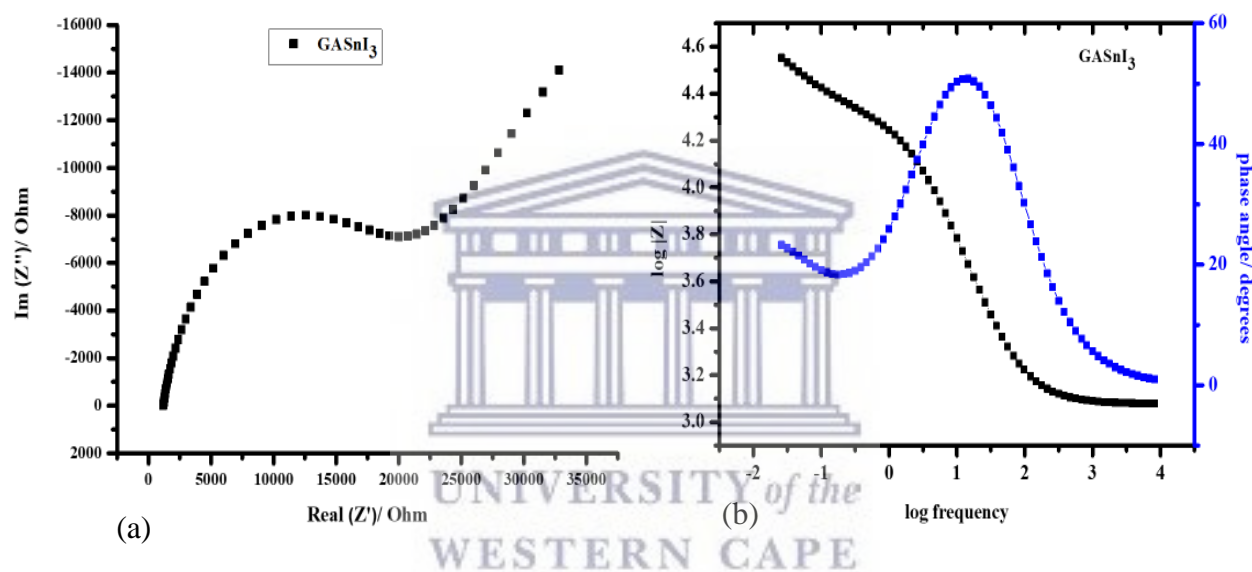


Figure 4.44: (a) Nyquist and (b) Bode plots for GASnI₃.

The same equivalence circuit (figure 4.42) was used to fit the impedance data of GASnI₃ perovskite, while the values obtained for the various elements of the circuit are shown in table 4.5 below. GASnI₃ recorded series resistance $R_s = 1194 \Omega$, parallel resistor $R_{ct} = 18201 \Omega$ while constant phase element recorded $CPE = 0.843 \text{ nF}$. The R_{ct} recorded for this SOCTP is way too larger than that of perovskites discussed in sections 4.91 and 4.92 above. This means that electron transfer for GASnI₃ perovskite is poor compared to the other discussed SOCTP materials [105,

106]. Guanidinium ion has the largest ionic radius of 278 pm, in which its cationic species (GASnI_3)⁺ is large and diffuses slower at the electrode/ solution interface. This observation agrees with CV studies whereby GASnI_3 had lower diffusion co-efficient compared to the other 2 SOCTPs. However, both the parallel resistor and capacitor for this perovskite still conform to imperfect capacitor behavior [103]. The diffusion component in this system adheres to Warburg-type of diffusion of ions in solution as well, which recorded a value of $W_0 = 0.488 \Omega\text{s}^{1/2}$.

Table 4.5: Values of the elements of the circuit used to fit GASnI_3 EIS data.

Element	Value	% Error
$R_s (\Omega)$	1194	0.346
$R_{ct} (\Omega)$	18201	1.997
CPE1-P (nF)	0.843	0.410
W_0 1-P ($\Omega\text{s}^{1/2}$)	0.488	3.379

The EIS spectrum for GASnI_3 perovskite film shows same behavior as the perovskites discussed in sections above, showing 2 time-constants in complex plane plot. The high frequency region is attributed to correspond to the space charge of this perovskite whereby its spectrum can be fitted to an ideal parallel resistor and capacitor circuit in the high frequency range. Linear region is also observed in the Nyquist plot for this perovskite, which indicates an additional diffusion component to the recorded overall capacitance [103]. This electrochemical system has the small charge transfer resistance $R_{ct} = 7212 \Omega$ while series resistance recorded $R_s = 1084 \Omega$, which is comparable

to the values obtained in the perovskite discussed in section 4.9.1 above. Both EIS and CV studies show similar observations whereby $[\text{CH}_3\text{CH}_2\text{NH}_3]\text{SnI}_3$ and $[(\text{CH}_3)_2\text{NH}_2]\text{SnI}_3$ SOCTP have similar electrochemical behavior, showing the best electron transfer reactions.

4.9.4 EIS for $[\text{GA}][\text{CH}_3\text{CH}_2\text{NH}_3]\text{SnI}_3$ perovskite

Nyquist and Bode plots of a bare GCE in 0.05 M $[\text{GA}][\text{CH}_3\text{CH}_2\text{NH}_3]\text{SnI}_3$ are shown in figure 4.45 below, where the supporting electrolyte comprised of dichloromethane (CH_2Cl_2 , anhydrous, 99.8%), 2mM benzoquinone and 0.1 M tetrabutylammonium hexafluoro phosphate.

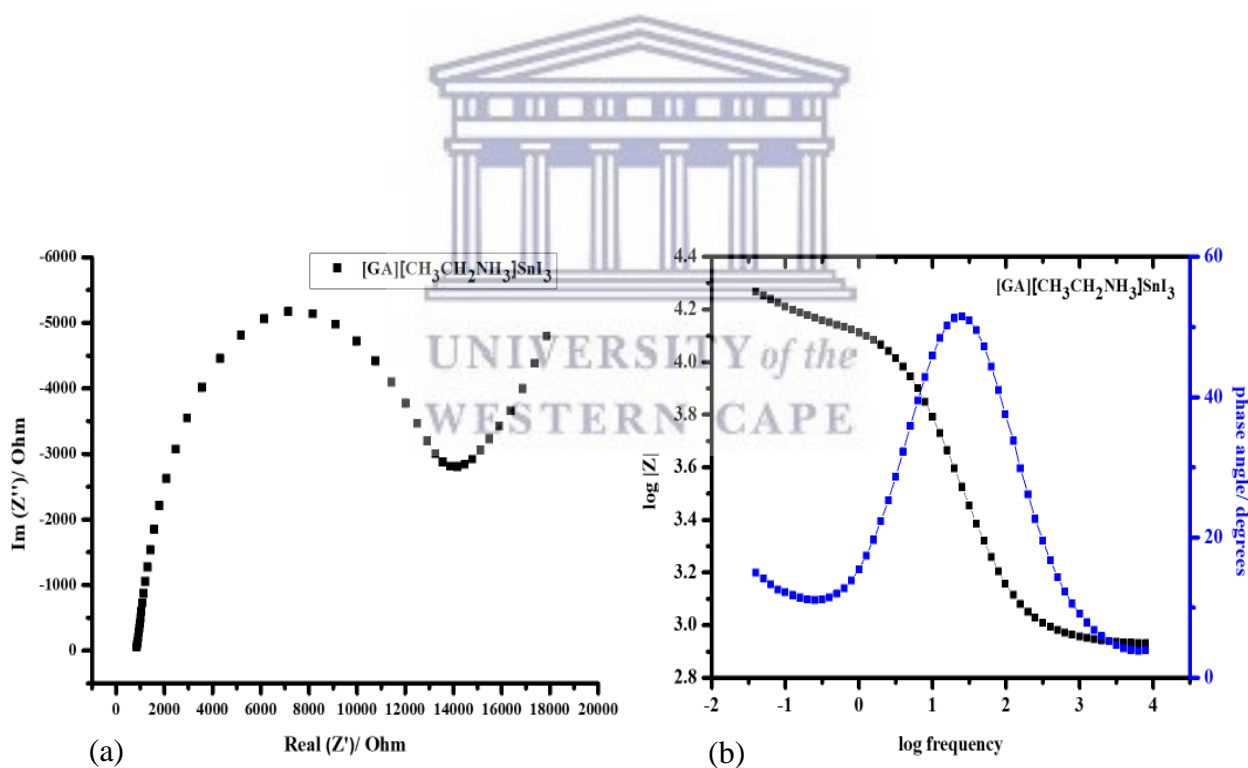


Figure 4.45: (a) Nyquist and (b) Bode plots for $[\text{GA}][\text{CH}_3\text{CH}_2\text{NH}_3]\text{SnI}_3$ perovskite.

The equivalence circuit that was adopted to fit the EIS data for [GA][CH₃CH₂NH₃]SnI₃ MOCTP is shown in (figure 4.42) above. The various elements and their values are shown in table 4.6 below. This MOCTP recorded series resistance $R_s = 862.2 \Omega$, resistance to charge transfer $R_{ct} = 12552 \Omega$ while constant phase element recorded $CPE = 0.861 \text{ nF}$. The R_{ct} recorded for this MOCTP shows a significant reduction compared to GASnI₃ SOCTP. This means that electron transfer was greatly improved when guanidinium and ethylammonium ions were mixed [105]. The resulting mixture of organic cations has reduced ionic radius since ethylammonium has ionic radius of 274 pm. The cationic species ([GA][CH₃CH₂NH₃]SnI₃)⁺ diffuses faster at the electrode/ solution interface, resulting to faster electron transfer in the kinetics of the system [105]. The EIS studies corroborate with CV studies, in which [GA][CH₃CH₂NH₃]SnI₃ showed higher diffusion coefficient compared to GASnI₃. Both the parallel resistor and capacitor for this perovskite follow imperfect capacitor behavior [106, 107]. The diffusion component in the system adheres to Warburg-type of diffusion of ions in solution, which recorded a value of $W_o = 0.519 \Omega s^{1/2}$.

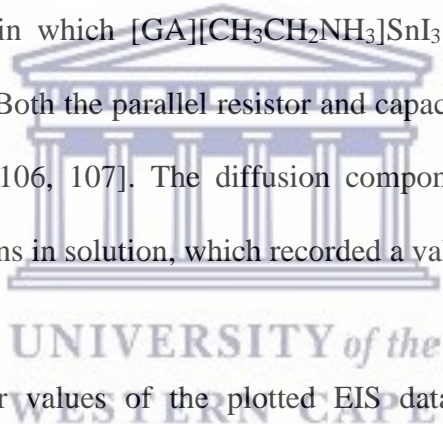


Table 4.6: Elements and their values of the plotted EIS data for [GA][CH₃CH₂NH₃]SnI₃ perovskite.

Element	Values	% Error
R_s (Ω)	862.2	0.349
R_{ct} (Ω)	12552	1.289
CPE1-P (nF)	0.861	0.355
W_o1-P (Ωs^{1/2})	0.519	4.886

The same electrochemical behavior is shown by $[\text{GA}][\text{CH}_3\text{CH}_2\text{NH}_3]\text{SnI}_3$ film EIS spectrum as with the perovskites discussed in sections above, showing 2 time-constants in complex plane plot. The high frequency region here is also attributed to space charge of this perovskite, whereby its spectrum can be fitted to an ideal parallel resistor and capacitor circuit in this frequency range. Linear region is also observed in the Nyquist plot, indicating that there is an additional diffusion component to the recorded overall capacitance. Both EIS and CV studies show that this species of mixed organic cations has improved electrochemical properties in comparison to GASnI_3 SOCTP, making it better suited for solar cell application [106].

4.9.5 EIS for $[\text{GA}][(\text{CH}_3)_2\text{NH}_2]\text{SnI}_3$ perovskite

Fitted EIS data is shown in the Nyquist and Bode plots of a bare GCE in 0.05 M $[\text{GA}][(\text{CH}_3)_2\text{NH}_2]\text{SnI}_3$, where the supporting electrolyte comprised of dichloromethane (CH_2Cl_2 , anhydrous, 99.8%), 2mM benzoquinone and 0.1 M tetrabutylammonium hexafluoro phosphate.

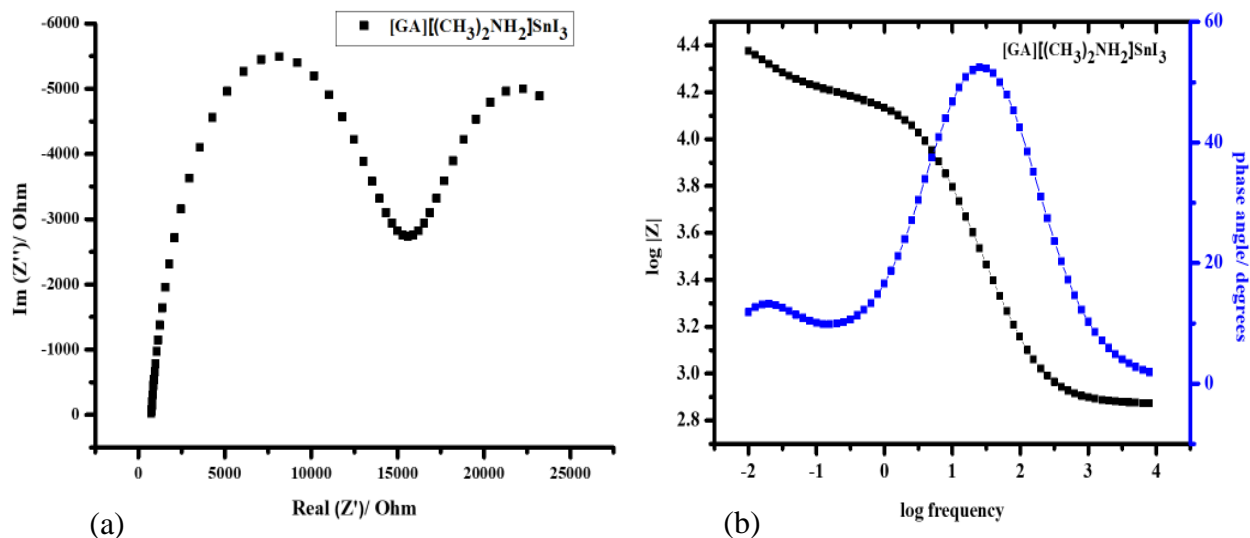


Figure 4.46: (a) Nyquist and (b) Bode plots for $[\text{GA}][(\text{CH}_3)_2\text{NH}_2]\text{SnI}_3$ perovskite.

The adopted equivalence circuit to fit the EIS data for $[\text{GA}][(\text{CH}_3)_2\text{NH}_2]\text{SnI}_3$ perovskite is shown in Figure 4.47 while the elements of the circuit and their fitted values are shown in table 4.7. This MOCTP $R_s = 742.1 \Omega$, $R_{ct} = 13357 \Omega$ and $\text{CPE} = 0.845 \text{ nF}$. The R_{ct} recorded for this MOCTP shows a significant reduction compared to GASnI_3 -SOCTP but slightly higher than that of $[\text{GA}][(\text{CH}_3\text{CH}_2\text{NH}_3)\text{SnI}_3$ MOCTP. This means that electron transfer was greatly improved when guanidinium and dimethylammonium ions were mixed [103, 105]. This result was expected since the resulting mixture of organic cations has reduced ionic radius owing to smaller ionic radius of dimethylammonium ionic radius (272 pm). The EIS studies corroborate with CV studies for this perovskite, in which $[\text{GA}][(\text{CH}_3)_2\text{NH}_3]\text{SnI}_3$ showed higher diffusion co-efficient compared to GASnI_3 . Both the parallel resistor and capacitor for this perovskite conform to imperfect capacitor behavior. The diffusion component in the system adheres to Warburg-type of diffusion of ions in solution, which recorded a value of $W_o = 0.433 \Omega\text{s}^{1/2}$.

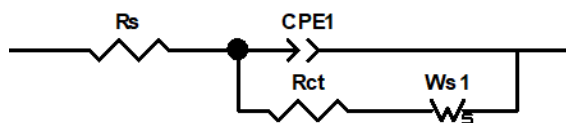


Figure 4.47: The equivalence circuit that was used to fit [GA][(CH₃)₂NH₂]₃SnI₃ EIS data.

Table 4.7: Elements and their values of the plotted EIS data of [GA][(CH₃)₂NH₂]₃SnI₃ perovskite.

Element	Values	% Error
R_s (Ω)	742.1	0.304
R_{ct} (Ω)	13357	0.905
CPE1-P (nF)	0.845	0.263
W_{s1}-P (Ωs^{1/2})	0.433	2.493

UNIVERSITY of the
WESTERN CAPE

The lower the value for R_{ct} , the more desirable is the perovskite for a more effective and rapid transporting ability for the electron and hole, which would further improve the performance of the PSC especially the fill factor [108]. Additionally, the value of CPE is closely related to the surface area of the material. The larger the CPE, the larger the surface area [109, 110]. The material with larger surface area is likely to promote the power conversion efficiency of the photovoltaic solar cell. Amongst these perovskites, the CPE values are comparable, but the two MOCTPs have the highest CPE values, which suggests that they are likely to improve the PCE.

4.9.6 Combined EIS studies

The EIS data of all 5 perovskites were plotted together in the Nyquist and Bode plots to compare their electrochemical behavior. Figure 4.48 shows the Nyquist plots while figure 4.49 shows the Bode plots.

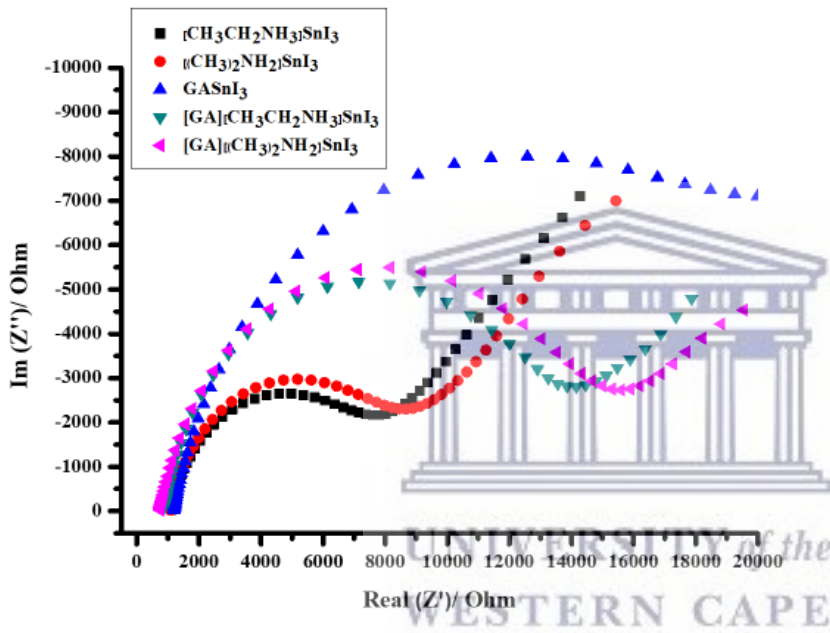


Figure 4.48: Nyquist plots for all the 5 perovskites.

From the plot of log frequency vs log $|z|$ (figure 4.49 (a)), it is observed that the total impedance of the electrodes decreased, which is caused by Ohmic resistance from the solution resistance. The total impedance increased at lower frequencies due to additional resistance in the system contributed by charge transfer resistance [111]. At lower frequencies, the impedance follows the order; $[\text{CH}_3\text{CH}_2\text{NH}_3]\text{SnI}_3 < [(\text{CH}_3)_2\text{NH}_2]\text{SnI}_3 < [\text{GA}][(\text{CH}_3)_2\text{NH}_2]\text{SnI}_3 < [\text{GA}][\text{CH}_3\text{CH}_2\text{NH}_3]\text{SnI}_3 < \text{GAsnI}_3$. The lower the total impedance at lower frequency, the more conductive the material is.

The mixed organic cation perovskites show better conductive properties based on the log frequency vs log phase angle studies, figure 4.49 (b). GASnI_3 has phase angle at lower frequency while the rest of the perovskites have phase angle almost at same frequency, which is an indication that GASnI_3 is more resistive to current and is a poor conductor. Guanidinium has the largest ionic radius amongst these organic cations, hence the larger the cation, the less conductive is the semiconductor material. $[\text{GA}][(\text{CH}_3)_2\text{NH}_2]\text{SnI}_3$ and $[\text{GA}][\text{CH}_3\text{CH}_2\text{NH}_3]\text{SnI}_3$ have higher phase angles compared to the single organic cations and they are shifted to higher frequencies. These two perovskites also showed higher currents in CV studies after GASnI_3 .

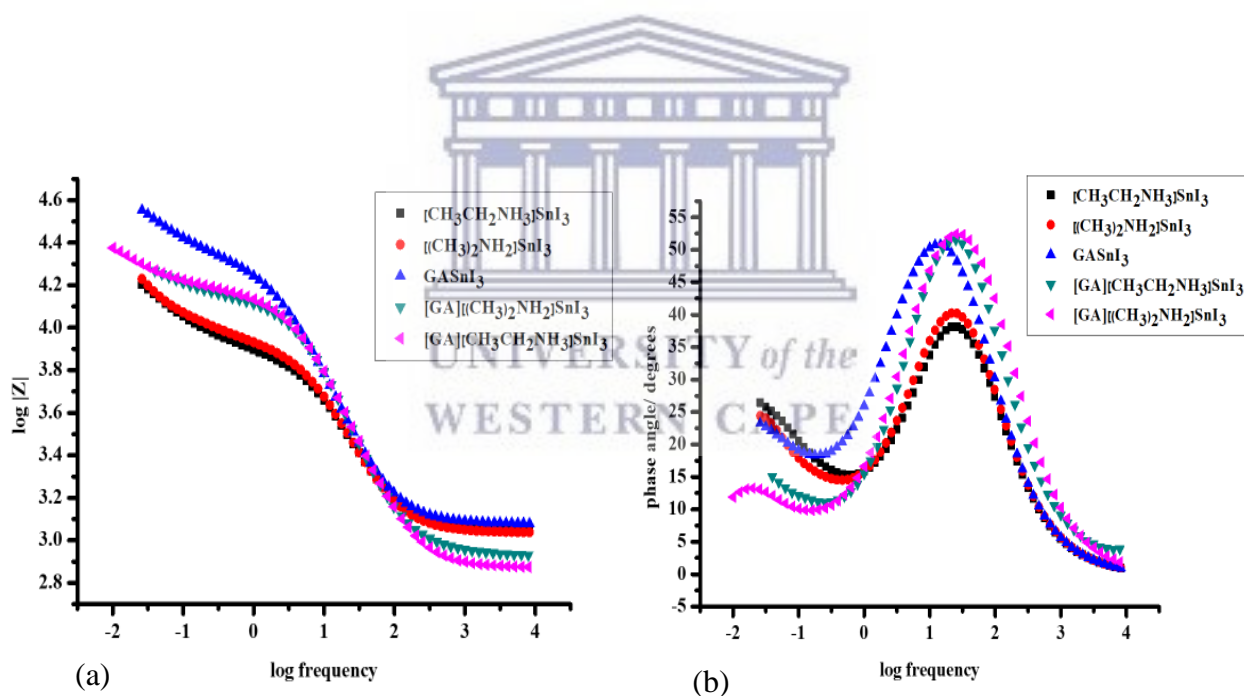


Figure 4.49: Bode plots: (a) \log frequency vs $\log |Z|$ (b) \log frequency vs phase angle for all the 5 perovskites.

Fabrication of SOCTP and MOCTP-based photovoltaic devices

4.10 Photovoltaic cells (PVC) fabrication and characterization

Planar device architecture was adopted to prepare SOCTP and MOCTP-based photovoltaic cells, a method that was used by Chen *et al.* [112]. Details of the methodology are found in chapter 3. A thickness of 75 nm aluminium layer was achieved during its thermal deposition. Figure 3.1 below shows the architecture of the perovskite solar cell device showing separation and transport of photogenerated charges. The expected band alignments in the structure of the device favors charge transport and collection [113-115].

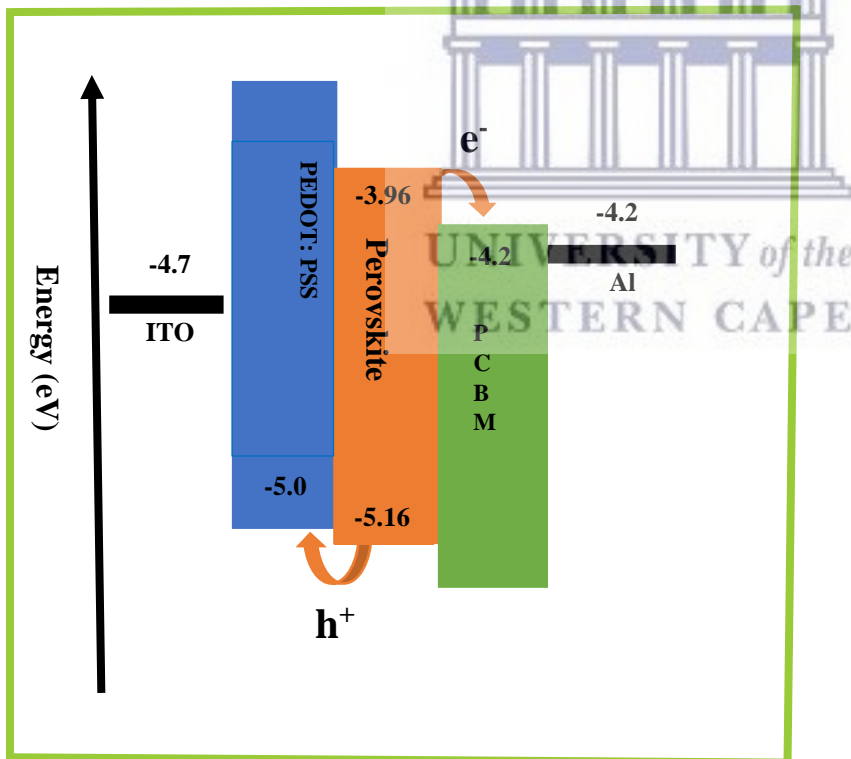
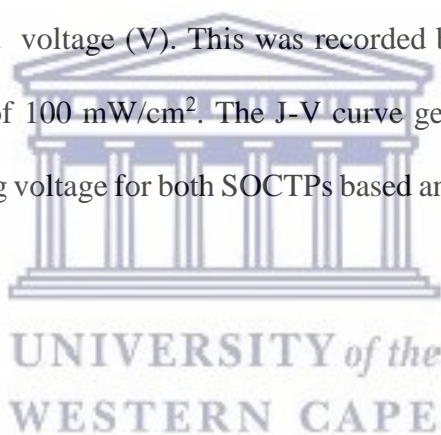


Figure 3.1: Planar structure device architecture adopted for perovskite solar cell (glass/ITO/PEDOT:PSS/perovskite layer/PCBM/Al).

When light energy strikes the perovskite (light absorber), charge separation of electron-hole pairs takes place, electrons jump from valence to conduction band and holes remain in the valence band of the perovskite. Since PEDOT:PSS has valence band at -5.0 eV, a value higher than the valence band of the perovskites, it can extract the generated hole pairs and transports them [112]. On the other hand, PCBM has a conduction band at -4.2 eV, which is lower energy compared to the conduction band of the perovskite. This is ideal for PCBM to extract the excited electrons in the conduction band of the perovskite. This process generates electricity which is measured from the aluminium and ITO contacts. The devices were further characterized by measuring the current density (J) in (mA/cm^2) against voltage (V). This was recorded between -0.2 V to 1.0 V in the dark and in with illumination of $100 \text{ mW}/\text{cm}^2$. The J-V curve generated shows that the current density increases with increasing voltage for both SOCTPs based and MOCTPs based photovoltaic cells (see figure 4.50 and 4.51).



(i) *SOCTPs*

Figure 4.49 below shows J-V curves of the various photovoltaic cells for SOCTPs both in dark and under 1 sun illumination. All these photovoltaic cells do not show pronounced shift between recordings in dark and under light, probably due to short circuit.

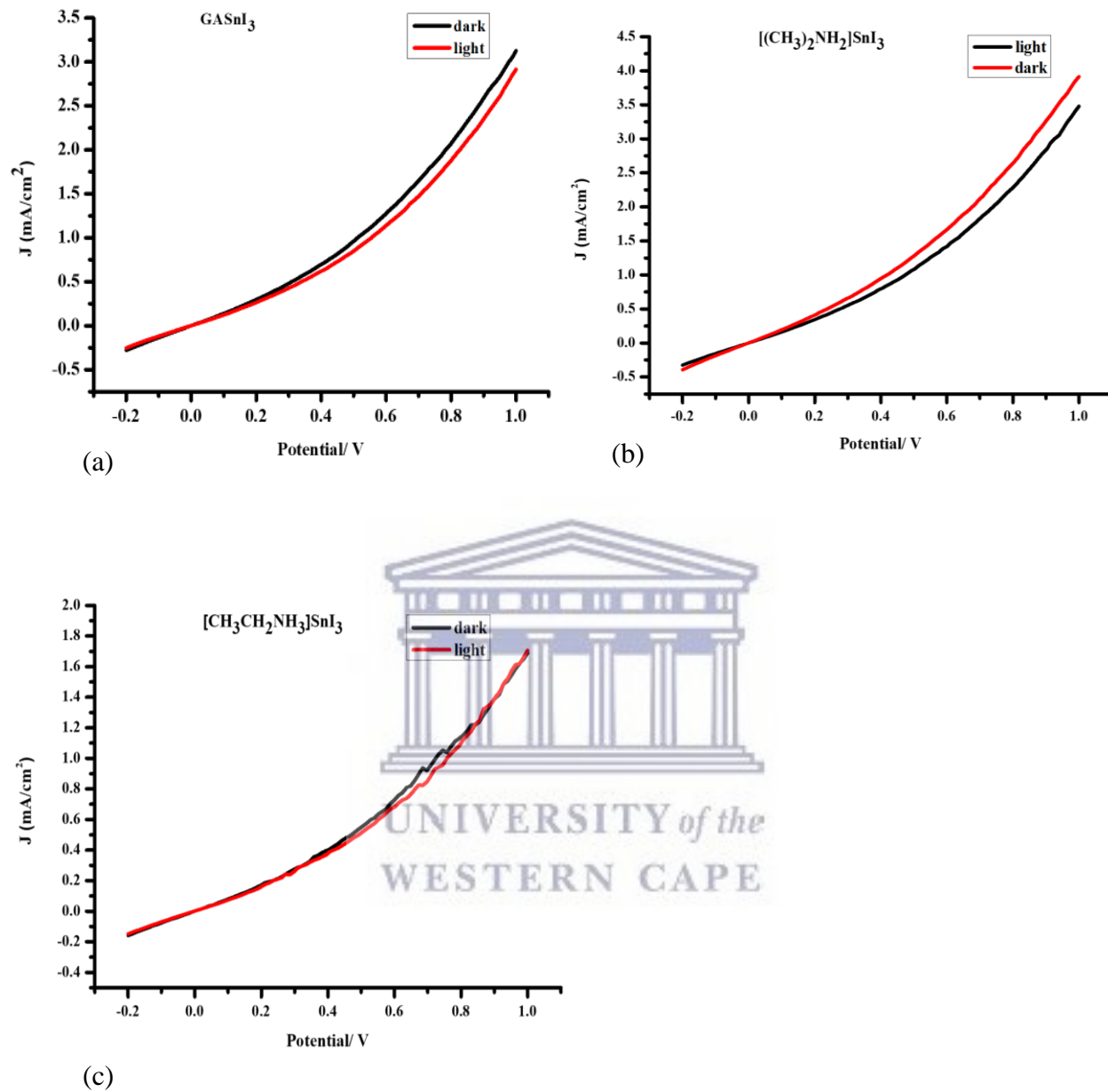


Figure 4.50: J-V curves for (a) GAsnI₃, (b) [(CH₃)₂NH₂]SnI₃ and (c) [CH₃CH₂NH₃]SnI₃ photovoltaic cell devices.

The Power conversion efficiency (PCE) of the devices were calculated using equation (9) below.

$$\eta = P_{\max} / P_{\text{in}} = FF \times J_{\text{sc}} \times V_{\text{oc}} / P_{\text{in}} \quad (9)$$

where V_{oc} represents open circuit voltage, J_{sc} represents short circuit current density, FF represents fill factor and P_{in} represents incident power (100 mW/cm^2).

Table 4.5 below shows the device performance parameters of the photovoltaic cells (PVC). The power conversion efficiencies of GASnI_3 , $[(\text{CH}_3)_2\text{NH}_2]\text{SnI}_3$ and $[\text{CH}_3\text{CH}_2\text{NH}_3]\text{SnI}_3$ perovskite devices were calculated to be 0.68, 0.12 and 0.11% respectively. The values of V_{oc} and J_{sc} are too small to give good PCE, which suggest poorly formed thin films that were used to fabricate these devices.



Table 4.8: Device performance parameters for the SOCTPs photovoltaic cells.

Perovskite device	V_{oc} (V)	J_{sc} (mA/cm^2)	FF (%)	PCE (%)
GASnI_3	0.00614	0.00547	20.36	0.68
$[(\text{CH}_3)_2\text{NH}_2]\text{SnI}_3$	0.00955	0.00632	20.10	0.12
$[\text{CH}_3\text{CH}_2\text{NH}_3]\text{SnI}_3$	0.00611	0.00508	35.00	0.11

(ii) MOCTPs

J-V curves of the MOCTPs are shown in figure 4.51 below. Just like with the SOCTPs, it is observed that the shift from curve obtained under dark to curve obtained under illumination with light is not much under non-optimized conditions. The V_{oc} and J_{sc} values recorded are also close to zero value which lowers the PCE of the devices [116]. Device performance parameters for the MOCTPs solar cells are presented in table 4.9.

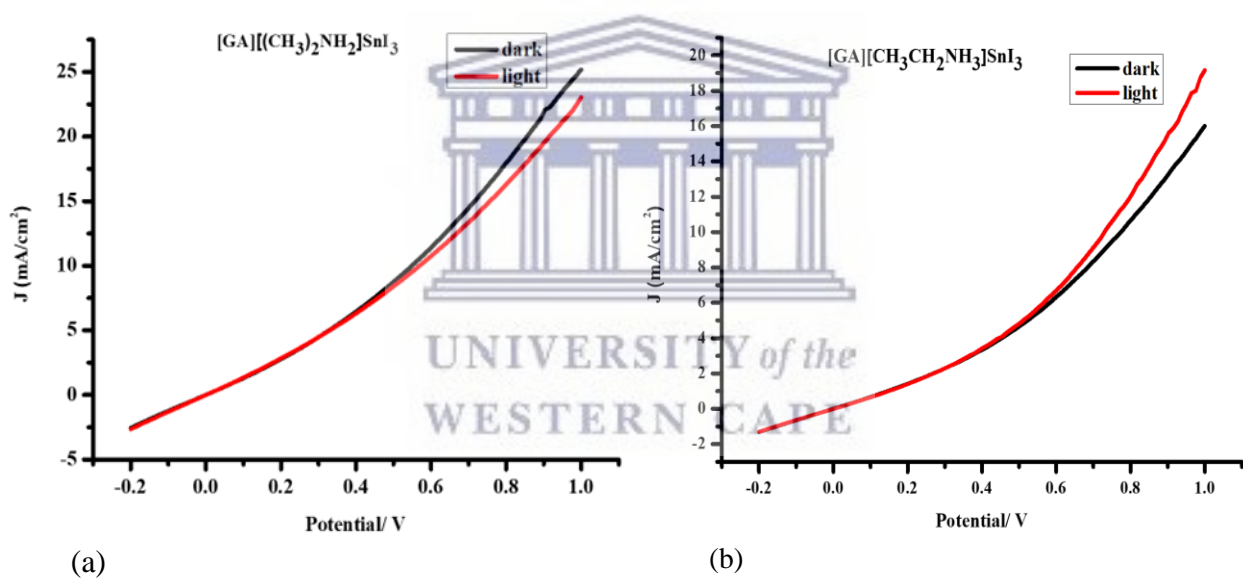


Figure 4.51: J-V curves for (a) $[GA][(CH_3)_2NH_2]SnI_3$ and (b) $[GA][CH_3CH_2NH_3]SnI_3$ photovoltaic cell devices.

Table 4.9: Device performance parameters for the MOCTPs photovoltaic cells.

Perovskite device	V _{oc} (V)	J _{sc} (mA/cm ²)	FF (%)	PCE (%)
[GA][(CH ₃) ₂ NH ₂]SnI ₃	0.0755	0.0722	5.12	2.79
[GA][CH ₃ CH ₂ NH ₃]SnI ₃	0.00604	0.105	19.00	1.20

The [GA][(CH₃)₂NH₂]SnI₃ PVC shows a greater open circuit voltage (0.0755) and short circuit current density (0.0722 mA/cm²). This is attributed to the bigger grain sizes and increased light harvesting ability of the perovskite layer [117-119], hence a good power conversion efficiency (2.79%) has been achieved. [GA][CH₃CH₂NH₃]SnI₃ MOCTP based PVC recorded PCE of 1.20% which is better than any of the devices based on SOCTPs. However, good devices should have V_{oc} value of close to 1.0 V, higher J_{sc} and lower FF (measure of the squareness of the curve) [74, 75].



Xiao *et al.* made same observation, in which mixing organic cations led to improved device performance. They synthesis hybrid perovskites from single cations and mixture of methylammonium and formamidinium organic cations. Perovskites synthesized from mixture of exhibited increased short-circuit current, outperforming the cells prepared with pure methylammonium, and PCE of 10.55% [120]. In comparison, table 4.10 shows data values of device performance of MAPbI₃ perovskite solar cells with different polystyrene concentrations reported by Kim *et al.*, which follows same device architecture with devices produced in this research [121].

Table 4.10: MAPbI₃ Device performance parameters with different polystyrene concentrations [121].

Polystyrene concentration (wt%)	J_{sc} (mA/cm²)	V_{oc} (V)	FF (%)	PCE (%)
0	17.2	0.96	69.4	11.7
1.5	19.0	0.95	70.7	13.0
3.0	19.2	0.95	71.8	13.3
4.5	15.0	0.97	73.5	10.8

Essentially, a more stable PVC gives off better PCE [122, 123]. Stability of PVC comes from hierarchy of 3 major sources which include: (a) component material and interfaces (light absorber, contacts and electrodes), (b) Cell operating conditions and device stress and (c) Module and packaging including encapsulation [124]. Optimizations studies to get the best thickness for perovskite thin film as well as for PCBM and PEDOT:PSS may be necessary to reduce chances of short circuit on the cells and improve on the efficiency of these devices.

4.11 References

1. Sessolo, M., Bolink, H. (2016). Solar cells. Perovskite Solar Cells Join the Major League. *Science*, 350, article number 917.
2. Du, Z., Zhao, Y., He, C., Wang, B., Xue, W., Zhou, H., Bai, J., Huang, B., Zhang, W., Chen, X. (2014). Syntheses and Structures of Four d^{10} Metal-Organic Frameworks Assembled with Aromatic Polycarboxylate and bix [bix = 1,4-Bis(imidazol-1-ylmethyl)benzene]. *Crystal Growth and Design*, 14, 3903-3909.
3. Du, Z., Xu, T., Huang, B., Su, Y., Xue, W., He, C., Zhang, W., Chen, X. (2015). Multiple Phase and Dielectric Transitions on a Novel Multi-Sensitive [TPrA][M(dca)₃] (M: Fe²⁺, Co²⁺ and Ni²⁺) Hybrid Inorganic-Organic Perovskite Family. *Angew Chem Int Ed*, 127, 928-932.
4. Li, G., Ching, K., Ho, J., Wong, M., Kwok, H. (2015). Identifying the Optimum Morphology in High-Performance Perovskite Solar Cells. *Advanced Energy Materials*, 5, article number 1401775.
5. Zhang, H., Wang, D., Wang, S., Zhang, T. (2018). Highly Efficient and Stable MAPbI₃ Perovskite Solar Cell Induced by Regulated Nucleation and Ostwald Recrystallization. *Materials*, 11, 1-12.
6. Grätzel, M., Grancini, G., Audinot, J., Jeanbourquin, X., Mosconi, E., Zimmermann, I., Dowsett, D., Lee, Y., Grätzel, M., De Angelis, F., Sivula, K., Wirtz, T., Nazeeruddin, M. (2016). Intrinsic Halide Segregation at Nanometer Scale Determines the High

- Efficiency of Mixed Cation/Mixed Halide Perovskite Solar Cells. *Journal of The American Chemical Society*, 138, 15821-15824.
7. Brennan, M., Draguta, S., Kamat, P., Kuno, M. (2018). Light-Induced Anion Phase Segregation in Mixed Halide Perovskites. *ACS Energy Letters*, 3, 204-213.
 8. Philippe, B., Saliba, M., Correa-Baena, J., Cappel, U., Turren-Cruz, S., Grätzel, M., Hagfeldt, A., Rensmo, H. (2017). Chemical Distribution of Multiple Cation (Rb⁺, Cs⁺, MA⁺, and FA⁺) Perovskite Materials by Photoelectron Spectroscopy. *Chemistry of Materials*, 29, 3589-3596.
 9. Abdi-Jalebi, M., Andaji-Garmaroudi, Z., Cacovich, S., Stavarakas, C., Philippe B., Richter, J., Alsari, M., Booker, E., Hutter, E., Pearson, A., Lilliu, S., Savenije, T., Rensmo H., Divitini, G., Ducati, C., Friend, R., Stranks, S. (2018). Maximizing and Stabilizing Luminescence from Halide Perovskites with Potassium Passivation. *Nature*, 555, 497-501.
 10. Bush, K. A., Rolston, N., Gold-Parker, A., Manzoor, S., Hausele, J., Yu, Z., Raiford, J., Cheacharoen, R., Holman, Z., Toney, M., Dauskardt, R., and McGehee, M. (2018). Controlling Thin-Film Stress and Wrinkling During Perovskite Film Formation. *ACS Energy Letters*, 3, 1225-1232.
 11. Zheng, X., Wu, C., Jha, S., Li, Z., Zhu, K., Priya, S. (2016) . Improved Phase Stability of Formamidinium Lead Triiodide Perovskite by Strain Relaxation. *ACS Energy Letters*, 1, 1014-1020.
 12. Prasanna, R., Gold-Parker, A., Leijtens, T., Conings, B., Babayigit, A., Boyen, H., Toney, M., McGehee, M. (2017). Band Gap Tuning Via Lattice Contraction and Octahedral Tilting in Perovskite Materials for Photovoltaics. *Journal of The American Chemical Society*, 139, 11117-11124.

13. Murali, B., Yenge, E., Peng, W., Chen, Z., Alias, M., Alarousu, E., Ooi, B., Burlakov, V., Goriely, A., Eddaoudi, M., Bakr, O., Mohammed, O. (2017). Temperature-Induced Lattice Relaxation of Perovskite Crystal Enhances Optoelectronic Properties and Solar Cell Performance. *Journal of Physical Chemistry Letters*, 8, 137-143.
14. McMeekin, D., Wang, Z., Rechman, W., Pulvirenti, F., Patel, J., Noel, N., Johnston, M., Hertz, L., Snaith, H. (2017). Crystallization Kinetics and Morphology Control of Formamidinium-Cesium Mixed-Cation Lead Mixed-Halide Perovskite Via Tunability of the Colloidal Precursor Solution. *Advanced Materials*, 29, article number 1607039.
15. Zhao, J., Deng, Y., Wei, H., Zheng, X., Yu, Z., Shao, Y., Shield, J., Huang, J. (2017). Strained Hybrid Perovskite Thin Films and Their Impact on the Intrinsic Stability of Perovskite Solar Cells. *Science Advances*, 3, 5616-5624.
16. Ono, L., Qi, Y. (2016). Surface and Interface Aspects of Organometal Halide Perovskite Materials and Solar Cells. *The Journal of Physical Chemistry Letters*, 7, 4764-4794.
17. Al Mamun, A., Ava, T., Byun, H., Jeong, H., Jeong, M., Nguyen, L., Gausin, C., Namkoong, G. (2017). Unveiling the Irreversible Performance Degradation of Organometal Halide Perovskite Films and Solar Cells During Heating and Cooling Processes. *Physical Chemistry Chemical Physics*, 19, 19487-19495.
18. Yakunin, S., Sytnyk, M., Kriegner, D., Shrestha, S., Richter, M., Matt, G., Azimi, H., Brabec, C., Stangl, J., Kovalenko, M., Heiss, W. (2015). Detection of X-ray Photons by Solution-Processed Lead Halide Perovskites. *Nature Photonics*, 9, 444-449.
19. Darriet, J., Subramanian, M. (1995). Structural Relationships Between Compounds Based on the Stacking of Mixed Layers Related to Hexagonal Perovskite-type Structures. *Journal of Materials Chemistry*, 5, 543-552.

20. Fan, Z., Xiao, H., Wang, Y., Zhao, Z., Lin, Z., Cheng, H., Lee, S., Wang, G., Feng, Z., Goddard, W. (2017). Layer-By-Layer Degradation of Methylammonium Lead Tri-iodide Perovskite Microplates. *Joule*, 1, 548-562.
21. Arnold, A., Gesing, T., Martynczuk, J., Feldhoff, A. (2008). Correlation of the Formation and the Decomposition Process of the BSCF Perovskite at Intermediate Temperatures. *Chemistry of Materials*, 20, 5851-5858.
22. Ava, T., Al Mamun, A., Marsillac, S., Namkoong, G. (2019). A Review: Thermal Stability of Methylammonium Lead Halide Based Perovskite Solar Cells. *Applied Science*, 9, 188-213.
23. Singh, H. (2013). The SAXS guide. Getting Acquainted with the Principles, 3rd Edition. Anton Paar GmbH, 1-24.
24. Schlipf, J., Docampo, P., Schaffer, C., Körstgens, V., Bießmann, L., Hanusch, F., Giesbrecht, N., Bernstorff, S., Bein, T., Müller-Buschbaum, P. (2015). A Closer Look into Two-Step Perovskite Conversion with X-ray Scattering. *The Journal of Physical Chemistry Letters*, 6, 1265-1269.
25. Egger, D., Edri, E., Cahen, D., Hodes, G. (2015). Perovskite Solar Cells: Do We Know What We Do Not Know? *Journal of Physical Chemistry Letters*, 6, 279-282.
26. Müller-Buschbaum, P. (2014). The Active Layer Morphology of Organic Solar Cells Probed with Grazing Incidence Scattering Techniques. *Advanced Materials*, 26, 7692-7709.

27. Seo, H., Kim, H., Lee, J., Park, M., Jeong, S., Kim, Y., Kwon, S., Han, T., Yoo, S., Lee, T. (2017). Efficient Flexible Organic/Inorganic Hybrid Perovskite Light-Emitting Diodes Based on Graphene Anode. *Advanced Materials*, 29, article number 1605587.
28. Demchyshyn, S., Roemer, J., Groß, H., Heilbrunner, H., Ulbricht, C., Apaydin, D., Böhm, A., Rütt, U., Bertram, F., Hesser, G., Scharber, M., Sariciftci, N., Nickel, B., Bauer, S., Głowacki, E., Kaltenbrunner, M. (2017). Confining Metal-Halide Perovskites in Nanoporous Thin Films. *Science Advances*, 3, article number 1700738.
29. Grancini, G., Marras, S., Prato, M., Giannini, C., Quarti, C., Angelis, F., Bastiani, M., Eperon, G., Snaith, H., Manna, L., Petrozza, A. (2014). The Impact of the Crystallization Processes on the Structural and Optical Properties of Hybrid Perovskite Films for Photovoltaics. *Journal of Physical Chemistry Letters*, 5, 3836-3842.
30. Moore, D., Sai, H., Wee Tan, K., Estroff, L., Wiesner, U. (2014). Impact of the Organic Halide Salt on Final Perovskite Composition for Photovoltaic Applications. *APL Materials*, 2, article number 081802.
31. Guggilla, P., Chilvery, A., Bhat, K., Bernardez, E. (2016). Thin Films to Single Crystals: Organometal Halide Perovskite. *Materials for Advanced Optoelectronics*, 2, 25-31.
32. Fu, Y., Meng, F., Rowley, M., Thompson, B., Shearer, M., Ma, D., Hamers, R., Wright, J., Jin, S. (2015). Solution Growth of Single Crystal Methylammonium Lead Halide Perovskite Nanostructures for Optoelectronic and Photovoltaic Applications. *Journal of the American Chemical Society*, 137, 5810-5818.
33. Xiao, Y., Han, G., Li, Y., Li, M., Wu, J. (2014). Electrospun Lead-doped Titanium dioxide Nanofibers and the In-situ Preparation of Perovskite-sensitized Photoanodes for Use in High Performance Perovskite Solar Cells. *Journal of Material Chemistry A*, 2, 3452-3460.

34. Ungar, T., Gubicza, J., Ribarik, G., Borbely, A. (2001). Crystallite Size Distribution and Dislocation Structure Determined by Diffraction Profile Analysis: Principles and Practical Application to Cubic and Hexagonal Crystals. *Journal of Applied Crystallography*, 34, 298-310.
35. Sadhanala, A., Deschler, F., Thomas, T., Dutton, S., Goedel, K., Hanusch, F., Lai, M., Steiner, U., Bein, T., Docampo, P., Cahen, D., Friend, R. (2014). Preparation of Single-Phase Films of $\text{CH}_3\text{NH}_3\text{Pb}(\text{I}_{1-x}\text{Br}_x)_3$ with Sharp Optical Band Edges. *Journal of Physical Chemistry Letters*, 5, 2501-2505.
36. Tsai, H., Nie, W., Blancon, J., Stoumpos, C., Asadpour, R., Harutyunyan, B., Neukirch, A., Verduzco, R., Crochet, J., Tretiak, S., Pedesseau, L., Even, J., Alam, M., Gupta, G., Lou, J., Ajayan, P., Bedzyk, M., Kanatzidis, M. (2016). High-Efficiency Two-Dimensional Ruddlesden-Popper Perovskite Solar Cells. *Nature*, 536, 312-316 .
37. Stoumpos, C., Cao, D., Clark, D., Young, J., Rondinelli, J., Jang, J., Hupp, J., Kanatzidis, M. (2016). Ruddlesden-Popper Hybrid Lead Iodide Perovskite 2D Homologous Semiconductors. *Chemistry Materials*, 28, 2852-2867.
38. Lee, S., Park, J., Nam, Y., Lee, B., Zhao, B., Di Nuzzo, D., Jung, E., Jeon, H., Kim, J., Jeong, H., Friend, R., Song, M. (2018). Growth of Nanosized Single Crystals for Efficient Perovskite Light Emitting Diodes. *ACS Nano*, 12, 3417-3423.
39. Quintero-Bermudez, R., Gold-Parker, A., Proppe, A., Munir, R., Yang, Z., Kelley, S., Amassian, A., Toney, M., Sargent, E. (2018). Compositional and Orientational Control in Metal Halide Perovskites of Reduced Dimensionality. *Nature Materials*, 17, 900-907.

40. Chen, Shiu, M., Ma, J., Alpert, M., Zhang, D., Foley, B., Smilgies, D., Lee, Choi, J. (2018). Origin of Vertical Orientation in Two-Dimensional Metal Halide Perovskites and its Effect on Photovoltaic Performance. *Nature Communications*, 9, 1336-1343.
41. Soe, C., Nie, W., Stoumpos, C., Tsai, H., Blancon, J., Liu, F., Even, J., Marks, T., Mohite, A., Kanatzidis, M. (2018). Understanding Film Formation Morphology and Orientation in High Member 2D Ruddlesden-Popper Perovskites for High Efficiency Solar Cells. *Advanced Energy Materials*, 8, article number 1700979.
42. Williams, O., Guo, Z., Hu, J., Yan, L., You, W., Moran, A. (2018). Energy Transfer Mechanisms in Layered 2D Perovskites. *Journal of Chemical Physics*, 148, article number 134706.
43. Yan, L., Hu, J., Guo, Z., Chen, H., Toney, M., Moran, A., You, W. (2010). General Post-Annealing Method Enables High-Efficiency Two-Dimensional Perovskite Solar Cells. *ACS Applied Materials and Interfaces*, 10, 33187-33197.
44. Lin, Y., Fang, Y., Zhao, J., Shao, Y., Stuard, S., Nahid, M., Ade, H., Wang, Q., Shield, J., Zhou, N., Moran, A., Huang, J. (2019). Unveiling the Operation Mechanism of Layered Perovskite Solar Cells. *Nature Communications*, 10, article number 1008.
45. Zhang, X., Ren, X., Liu, B., Munir, R., Zhu, X., Yang, D., Li, J., Liu, Y., Smilgies, D., Li, R., Yang, Z., Niu, T., Wang, X., Amassian, A., Zhao, K., Liu, S. (2017). Stable High Efficiency Two-Dimensional Perovskite Solar Cells Via Cesium Doping. *Energy Environmental Science*, 10, 2095-2102.
46. Liu, J., Leng, J., Wu, K., Zhang, J., Jin, S. (2017). Observation of Internal Photoinduced Electron and Hole Separation in Hybrid Two-Dimensional Perovskite Films. *Journal of The American Chemical Society*, 139, 1432-1435.

47. Erb, T., Zhokhavets, U., Gobsch, G., Raleva, S., Stühn, B., Schilinsky, P., Waldauf, C., Brabec, C. (2005). Correlation Between Structural and Optical Properties of Composite Polymer/Fullerene Films for Organic Solar Cells. *Advanced Functional Materials*, 15, 1193-1196.
48. Schulz, G., Ludwigs, S. (2017). Controlled Crystallization of Conjugated Polymer Films from Solution and Solvent Vapor for Polymer Electronics. *Advanced Functional Materials*, 27, article number 1603083.
49. Oku, T. (2015). Crystal Structures of $\text{CH}_3\text{NH}_3\text{PbI}_3$ and Related Perovskite Compounds Used for Solar Cells. *ISBN. InTech*, 78-953.
50. Senanayak, S., Yang, B., Thomas, T., Giesbrecht, N., Huang, W., Gann, E., Nair, B., Goedel, K., Guha, S., Moya, X., McNeill, C., Docampo, P., Sadhanala, A., Friend, R., Sringhaus, H. (2017). Understanding Charge Transport in Lead Iodide Perovskite Thin-Film Field-Effect Transistors. *Science Advances*, 3, article number 1601935.
51. Roghabadia, F., Ahmadib, N., Ahmadi, V., Di Carloc, A., Aghmiunib, K., Tehrania, A., Ghoreishib, F., Payandeha, M., Fumanid, N. (2018). Bulk Heterojunction Polymer Solar Cell and Perovskite Solar Cell: Concepts, Materials, Current Status, and Opto-Electronic Properties. *Solar Energy*, 173, 407-424.
52. Li, B., Fei, C., Zheng, K., Qu, X., Pullerits, T., Cao, G., Tian, J. (2016). Constructing Water-Resistant $\text{CH}_3\text{NH}_3\text{PbI}_3$ Perovskite Films via Coordination Interaction. *Journal of Materials Chemistry A*, 4, article number 17018.
53. Guo, X., Mcleese, C., Kolodziej, C., Samia, A., Zhao, Y., Burda, C. (2013). Identification and Characterization of the Intermediate Phase in Hybrid Organic-inorganic MAPbI_3 Perovskite. *Dalton Transactions*, 45, 3806-3813.

54. Misra, R., Ciammaruchi, L., Aharon, S., Mogilyansky, D., Etgar, L., Visoly-Fisher, I., Katz, E. (2015). Effect of Halide Composition on the Photochemical Stability of Perovskite Photovoltaic Materials. *Chemistry and Sustainability*, 9, 2572-2577.
55. Jeon, N., Noh, J., Kim, Y., Yang, W., Ryu, S., Seok, S. (2014). Solvent Engineering for High-performance Inorganic-Organic Hybrid Perovskite Solar Cells. *Nature Materials*, 13, 897-903.
56. Petrosyan, V. (1977). NMR Spectra and Structures of Organotin Compounds. *Progress in Nuclear Magnetic Resonance Spectroscopy*, 11, 115-148.
57. Glaser, T., Müller, C., Sendner, M., Krekeler, C., Semonin, O., Hull, T., Yaffe, O., Owen, J., Kowalsky, W., Pucci, A., Lovrinčić, R. (2015). Infrared Spectroscopic Study of Vibrational Modes in Methylammonium Lead Halide Perovskites. *Journal of Physical Chemistry Letters*, 6, 2913-2918.
58. Lim, A., Kim, S. (2019). Preparation, Thermal, and Physical Properties of Perovskite-Type $(\text{C}_3\text{H}_7\text{NH}_3)_2\text{CdCl}_4$ Crystals. *Crystals*, 9, 108-118.
59. Elseman A., Shalan, A., Sajid, S., Rashad, M., Hassan, A., Li, M. (2018). Copper-Substituted Lead Perovskite Materials Constructed with Different Halides for Working $(\text{CH}_3\text{NH}_3)_2\text{CuX}_4$ -Based Perovskite Solar Cells from Experimental and Theoretical View. *ACS Applied Materials and Interfaces*, 10, 11699-11707.
60. Rosales, B., Hanrahan, M., Boote, B., Rossini, A., Smith, E., Vela, J. (2017). Lead Halide Perovskites: Challenges and Opportunities in Advanced Synthesis and Spectroscopy. *ACS Energy Letters*, 2, 906-914.
61. Roiland, C., Trippe-Allard, G., Jemli, K., Alonso, B., Ameline, J., Gautier, R., Bataille, T., Le Polles, L., Deleporte, E., Even, J., Katan, C. (2016). Multinuclear NMR as a tool for

- studying local order and dynamics in $\text{CH}_3\text{NH}_3\text{PbX}_3$ ($\text{X} = \text{Cl}, \text{Br}, \text{I}$) hybrid perovskites. *Physical Chemistry Chemical Physics*, 18, 27133-27142.
62. Boschloo, G., Hagfeldt, A. (2009). Characteristics of the Iodine/Triiodide redox mediator in Dye-sensitized Solar Cells. *Accounts of Chemical Research*, 42, 1819-1826.
63. Wrackmeyer, B. (1981). Carbon-tin and Carbon-lead Indirect Nuclear Spin-spin Coupling Constants in Alkynyl Tin (IV) and Alkynyl Lead (IV) Compounds. *Journal of Magnetic Resonance*, 42, 287-297.
64. Kieslich, G., Forse, A., Sun, S., Butler, K., Kumagai, S., Wu, Y., Warren, M., Walsh, A., Grey, C., Cheetham, A. (2016). Role of Amine-Cavity Interactions in Determining the Structure and Mechanical Properties of the Ferroelectric Hybrid Perovskite $[\text{NH}_3\text{NH}_2]\text{Zn}(\text{HCOO})_3$. *Chemistry of Materials*, 28, 312-317.
65. Quarti, C., Mosconi, E., Ball, J., D'Innocenzo, V., Tao, C., Pathak, S., Snaith, H., Petrozza, A., De Angelis, F. (2016). Structural and Optical Properties of Methylammonium Lead Iodide Across the Tetragonal to Cubic Phase Transition: Implications for Perovskite Solar Cells. *Energy and Environmental Science*, 9, 155-163.
66. Etienne, T., Mosconi, E., Angelis, F. (2016). Dynamical Origin of the Rashba Effect in Organohalide Lead Perovskites: A key to Suppressed Carrier Recombination on Perovskite Solar Cells. *Journal of Physical Chemistry Letters*, 7, 1638-1645.
67. Wang, T., Daiber, B., Frost, J., Mann, S., Garnett, E., Walsh, A., Ehrler, B. (2017). Indirect to Direct Band Gap Transition in Methylammonium Lead Halide Perovskite. *Energy and Environmental Science*, 10, 509-515.

68. Gao, W., Gao, X., Abtew, T., Sun, Y., Zhang, S., Zhang, P. (2016). Quasiparticle Band Gap of Organic-Inorganic Hybrid Perovskites: Crystal Structure, Spin-Orbit Coupling, and Self-Energy Effects. *Physical Reviews, B* 93, article number 085202.
69. Kubicki, D., Prochowicz, D., Hofstetter, A., Zakeeruddin, S., Graetzel, M., Emsley, L. (2017). Phase Segregation in Cs-, Rb- and K-Doped Mixed-Cation (MA)_x(FA)_{1-x}PbI₃ Hybrid Perovskites from Solid-State NMR. *Journal of The American Chemical Society*, 139, 14173-14180.
70. Dong, Q., Song, J., Fang, Y., Shao, Y., Ducharme, S., Huang, J. (2016). Lateral-Structure Single-Crystal Hybrid Perovskite Solar Cells via Piezoelectric Poling. *Advanced Materials*, 28, 2816-2821.
71. Senocrate, A., Moudrakovski, I., Kim, G., Yang, T., Gregori, G., Gratzel, M., Maier, J. (2017). The Nature of Ion Conduction in Methylammonium Lead Iodide: A Multimethod Approach. *Journal of Angewandte Chemie (International ed. in English)*, 56, 7755-7759.
72. Kieslich, G., Forse, A., Sun, S., Butler, K., Kumagai, S., Wu, Y., Warren, M., Walsh, A., Grey, C., Cheetham, A. (2016). Role of Amine-Cavity Interactions in Determining the Structure and Mechanical Properties of the Ferroelectric Hybrid Perovskite [NH₃NH₂]Zn(HCOO)₃. *Chemistry of Materials*, 28, 312-317.
73. Besara, T., Jain, P., Dalal, N., Kuhns, P., Reyes, A., Kroto, H., Cheetham, A. (2011). Mechanism of the Order-Disorder Phase Transition and Glassy Behavior in the Metal-Organic Framework [(CH₃)₂NH₂]Zn(HCOO)₃. *Proceedings of the National Academy of Sciences of the United States of America*, 108, 6828-6832.

74. Aramburu, J., Garcia-Fernandez, P., Mathiesen, N., Garcia-Lastra, J., Moreno, M. (2018). Changing the Usual Interpretation of the Structure and Ground State of Cu^{2+} Layered Perovskite. *Journal of Physical Chemistry C*, 122, 5071-5082.
75. Varghese, A., Khadar, A. (2006). Highly Selective Derivative Spectrophotometric Determination of Tin (II) in Alloy Samples in the Presence of Cetylpyridinium Chloride. *Acta Chimica Slovenica*, 53, 374-380.
76. Ha, S., Liu, X., Zhang, Q., Giovanni, D., Sum, T., Xiong, Q. (2014). Synthesis of Organic-Inorganic Lead Halide Perovskite Nanoplatelets: Towards High-Performance Perovskite Solar Cells and Optoelectronic Devices. *Advanced Optical Materials*, 2, 838-844.
77. Jung, H., Park, N. (2015). Perovskite Solar Cells: From Materials to Devices. *Small*, 11, 10-25.
78. Kunkely, H., Vogler, A. (2001). Photooxidation of N, N'-bis (3, 5-di-tert-butylsalicylidene)-1, 2-diamino hexane-manganese (III) chloride (Jacobsen catalyst) in chloroform. *Inorganic Chemistry Communications*, 4, 692-694.
79. Huheey, J., Keiter, E., Keiter, R. (1993). Coordination Chemistry: Bonding, Spectra, and Magnetism. Inorganic Chemistry: Principles of Structure and Reactivity, NY: Harper Collins College.
80. Tian, Y., I. Scheblykin, G. (2015). Artifacts in Absorption Measurements of Organometal Halide Perovskite Materials: What Are the Real Spectra? *Journal of Physical Chemistry C*, 6, 3466-3470.
81. Stoumpos, S., Cao, D., Clark, D., Young, J., Rondinelli, J., Jang, J., Hupp, J., Kanatzidis, M. (2016). Ruddlesden-Popper Hybrid Lead Iodide Perovskite 2D Homologous Semiconductors. *Chemistry of Materials*, 28, 2852-2867.

82. Effenberger, A. (1961). Reactions of Iodine and Iodide Ions in the Presence and Absence of Polysaccharides. *Retrospective Theses and Dissertations*. 2431.
83. J. Bisquert and A. Compte, *J. Electroanalytical Chem.*, 2001, 499, 112
84. Bentley, C., Bond, A., Hollenkamp, A., Mahon, P., Zhang, J. (2016). Electrochemistry of Iodide, Iodine, and Iodine Monochloride in Chloride Containing Non-halo-aluminate Ionic Liquids. *Analytical Chemistry*, 88, 1915-1921.
85. Bard, A., Lund, H. (1973). *Encyclopedia of Electrochemistry of the Elements*, Marcel Dekker.
86. Bard, A., Faulkner, L. (2001). *Electrochemical Methods Fundamentals and Applications*. 2nd Edition. John Wiley & sons.
87. Elgrishi, N., McCarthy, B., Rountree, E., Dempsey, J. (2016). Reaction Pathways of Hydrogen-Evolving Electrocatalysts: Electrochemical and Spectroscopic Studies of Proton-Coupled Electron Transfer Processes. *ACS Catalysis*, 6, 3644-3659.
88. Lee, K., Elgrishi, N., Kandemir, B., Dempsey, J. (2017). Electrochemical and Spectroscopic Methods for Evaluating Molecular Electrocatalysts. *Nature Reviews Chemistry*, 1, article number 1038.
89. Elgrishi, M., Rountree, K., McCarthy, B., Rountree, E., Eisenhart, T., Dempsey, J. (2018). A Practical Beginners' Guide to Cyclic Voltammetry. *Journal of Chemical Education*, 95, 197-206.
90. Sampson, M., Nguyen, A., Grice, K., Moore, C., Rheingold, A., Kubiak, C. (2014). Manganese Catalysts with Bulky Bipyridine Ligands for the Electrocatalytic Reduction of Carbon Dioxide: Eliminating Dimerization and Altering Catalysis. *Journal of The American Chemical Society*, 136, 5460-5471.

91. Ventura, K., Smith, M., Prat, J., Echegoyen, L., Villagra[´]n, D. (2017). Introducing Students to Inner Sphere Electron Transfer Concepts through Electrochemistry Studies in Diferrocene Mixed-Valence Systems. *Journal of Chemical Education*, 94, 526-529.
92. Elgrishi, N., Kurtz, D., Dempsey, J. (2017). Reaction Parameters Influencing Cobalt Hydride Formation Kinetics: Implications for Benchmarking H₂-Evolution Catalysts. *Journal of The American Chemical Society*, 139, 239-244.
93. Schulz, P., Edri, E., Kirmayer, S., Hodes, G., Cahen, D., Kahn, A. (2014). Interface Energetics in Organometal Halide Perovskite-Based Photovoltaic Cells. *Energy Environmental Science*, 7, 1377-1381.
94. Akkerman, Q., Gandini, M., Di Stasio, F., Rastogi, P., Palazon, F., Bertoni, G., Ball, J., Prato, M., Petrazza, A., Manna, L. (2016). Strongly Emissive Perovskite Nanocrystal Inks for High-Voltage Solar Cells. *Nature Energy*, 2, article number 16194.
95. Samu, G., Scheidt, R., Kamat, P., Janaky, C. (2018). Electrochemistry and Spectro-Electrochemistry of Lead Halide Perovskite Films: Materials Science Aspects and Boundary Conditions. *Chemistry of Materials*, 30, 561-569.
96. Hendel, S., Young, E. (2016). Introduction to Electrochemistry and the Use of Electrochemistry to Synthesize and Evaluate Catalysts for Water Oxidation and Reduction. *Journal of Chemical Education*, 93, 1951-1956.
97. Zhao, Z., Gu, F., Li, Y., Sun, W., Ye, S., Rao, H., Liu, Z., Bian, Z., Huang, C. (2017). Mixed-Organic-Cation Tin Iodide for Lead-Free Perovskite Solar Cells with an Efficiency of 8.12%. *Advanced Science*, 2017, article number 1700204.
98. Lasia, A. (1999). Electrochemical Impedance Spectroscopy and its Applications, in Electrochemical Impedance Spectroscopy and its Applications. Modern Aspects of

Electrochemistry. Département de chimie, Université de Sherbrooke, Sherbrooke Québec, J1K 2R1.143.

99. Macdonald, D. (1990). Review of Mechanistic Analysis by Electrochemical Impedance Spectroscopy. *Electrochimica Acta*, 35, 1509-1525.
100. Loveday, D., Peterson, P., Rodgers, B. (2004). Application of EIS to Coatings. Evaluation of Organic Coatings with Electrochemical Impedance Spectroscopy Part 2. *Journal of Coatings Technology and Research*, 88, 88-93.
101. Li, Z., Mercado, C., Yang, M., Palay, E., Zhu, K. (2017). Electrochemical Impedance Analysis of Perovskite-electrolyte Interfaces. *The Royal Society of Chemistry*, 53, 2467-2470.
102. Zhao, Y., Zhu, K. (2016). Organic-Inorganic Hybrid Lead Halide Perovskites for Optoelectronic and Electronic Applications. *Chemical Society Reviews*, 45, 655-689.
103. Hsu, H., Ji, L., Ahn, H., Zhao, J., Yu, E., Bard, A. (2015). A Liquid Junction Photoelectrochemical Solar Cell Based on p-Type MeNH₃ PbI₃ Perovskite with 1.05 V Open-circuit Photovoltage. *Journal of American Chemical Society*, 137, 14758-14764.
104. Shi, D., Adinolfi, V., Comin, R., Yuan, M., Alarousu, E., Buin, A., Chen, Y., Hoogland, S., Rothenberger, A., Katsiev, K., Losovyj, Y., Zhang, X., Dowben, P., Mohammed, O., Sargent, E., Bakr, O. (2015). Solar cells. Low Trap-State Density and Long Carrier Diffusion in Organolead Trihalide Perovskite Single Crystals. *Science*, 347, 519-522.
105. Harrington, S., Devine, T. (2008). A Critical Assessment of the Mott-Schottky Analysis for the Characterisation of Passive Film-Electrolyte Junctions. *Journal of Electrochemical Society*, 155, C381.

106. Li, Z., Boix, P., Xing, G., Fu, K., Kulkarni, S., Batabyal, S., Xu, W., Cao, A., Sum, T., Mathews, N., Wong, L. (2016). Carbon Nanotubes as an Efficient Hole Collector for High Voltage Methylammonium Lead Bromide Perovskite Solar Cells. *Nanoscale*, 8, 6352-63560.
107. Wu, C., Chiang, C., Chang, S. (2016). A Perovskite Cell with a Record-High- V_{oc} of 1.61 V Based on Solvent Annealed $CH_3NH_3PbBr_3/ICBA$ Active Layer. *Nanoscale*, 8, 477-488.
108. Li, Z., Boix, P., Xing, G., Fu, K., Kulkarni, S., Batabyal, S., Xu, W., Cao, A., Sum, T., Mathews, N., Wong, L. (2016). Carbon Nanotubes as an Efficient Hole Collector for High Voltage Methylammonium Lead Bromide Perovskite Solar Cells. *Nanoscale*, 8, 6352-6360.
109. Xiao, Y., Lin, J., Tai, S., Chou, S., Yue, G., Wu, J. (2012). Pulse Electrodeposition of CoS on MWCNT/Ti as a High-performance Counter Electrode for a Pt-free Dye-sensitized Solar Cell. *Journal of Material Chemistry A*, 22, 19919-19925.
110. Xiao, Y., Han, G., Li, Y., Li, M., Wu, J. (2014). Electrospun Lead-doped Titanium dioxide Nanofibers and the In-situ Preparation of Perovskite-sensitized Photoanodes for Use in High Performance Perovskite Solar Cells. *Journal of Material Chemistry A*, 2, 16856-16862.
111. Ono, L., Wang, S., Kato, Y., Raga, S., Qi, Y. (2014). Fabrication of Semi-transparent Perovskite Films with Centimeter-Scale Superior Uniformity by the Hybrid Deposition Method. *Energy and Environmental Science*, 7, 3989-3993.

112. Chen, C., Bae, S., Chang, W., Hong, Z., Li, G., Chen, Q., Zhou, H., Yang, Y. (2015). Perovskite/Polymer Monolithic Hybrid Tandem Solar Cells Utilizing a Low-temperature, Full Solution Process. *The Royal Society of Chemistry*, 2, 203-211.
113. T. Shi, J. Chen, J. Zheng, X. Li, B. Zhou, H. Cao and Y. Wang. (2016). Ti/Au Cathode for Electronic Transport Material-Free Organic-Inorganic Hybrid Perovskite Solar Cells. *Scientific Reports*, 6, article number 39132 .
114. Huang, J., Yuan, Y., Shao, Y., Yan, Y. (2017). Understanding the Physical Properties of Hybrid Perovskites for Photovoltaic Applications. *Nature Review Materials*, 2, article number 17042.
115. Lu, J., Lin, Y., Jiang, B., Yeh, C., Kao, J., Chen, C. (2018). Organic Solar Cells: Microcavity Structure Provides High-Performance (>8.1%) Semitransparent and Colorful Organic Photovoltaics. *Advanced Functional Materials*, 28, article number 1870042.
116. Pockett, A., Eperon, G., Peltola, T., Snaith, H., Walker, A., Peter, L., Cameron, P. (2015). Characterization of Planar Lead Halide Perovskite Solar Cells by Impedance Spectroscopy, Open-circuit Photovoltage Decay, and Intensity-modulated Photovoltage/Photocurrent Spectroscopy. *The Journal of Physical Chemistry C*, 119, 3456-3465.
117. Qi, J., Yao, X., Xu, W., Jiang, X., Gong, X., Cao, Y. (2018). Efficient Perovskite Solar Cells with Reduced Photocurrent Hysteresis through Tuned Crystallinity of Hybrid Perovskite Thin Films. *American Chemical Society omega*, 3, 7069-7077.
118. Arora, N., Dar, M., Hinderhofer, A., Pellet, N., Schreiber, F., Zakeeruddin, S., Grätzel, M. (2017). Perovskite Solar Cells with CuSCN Hole Extraction Layers Yield Stabilized Efficiencies Greater than 20%. *Science*, 358, 768-771.

119. Habisreutinger, S., Mcmeekin, D., Snaith, H., Nicholas, R. (2016). Research Update: Strategies for Improving the Stability of Perovskite Solar Cells. *APL Materials*, 4, article number 091503.
120. Xiao, M., Zhao, L., Wei, S., Li, Y., Dong, B., Xu, Z., Wan, L., Wang, S. (2018). Application of Mixed-Organic-Cation for High Performance Hole-Conductor-Free Perovskite Solar Cells. *Journal of Colloid and Interface Science*, 510, 118-126.
121. Kim, H., Yusoff, A., Jang, J. (2019). Polystyrene Enhanced Crystallization of Perovskites Towards High Performance Solar Cells. *Nanoscale Advances*, 1, 76-85.
122. Yang, W., Park, B., Jung, E., Jeon, N., et al. (2017). Iodide Management in Formamidinium-Lead-Halide-Based Perovskite Layers for Efficient Solar Cells. *Science*, 356, 1376-1379.
123. Song, Z., McElvany, C., Phillips, A., Celik, I., Krantz, P., Wathage, S., Liyanage, G., Apul, D., Heben, M. (2017). Technoeconomic Analysis of Perovskite Solar Module Manufacturing with Low-Cost Materials and Techniques. *Energy Environmental Science*, 10, 1297-1305.
124. Christians, J., Habisreutinger, S., Berry, J., Luther, J. (2018). Stability in Perovskite Photovoltaics: A Paradigm for Newfangled Technologies. *ACS Energy Letters*, 3, 2136-2143.

CHAPTER 5

CONCLUSIONS AND RECOMMENDATIONS

5.1 Conclusions

Mixed-organic-cations tin halide perovskites (MOCTPs) and single-organic-cation tin perovskites (SOCTPs) were successfully synthesized by sol-gel method. Microscopic characterizations by HR SEM and HR TEM showed the hexagonal and tetragonal cubical shape typical of nano-sized perovskite materials. XRD also confirmed the characteristic tetragonal perovskite structure for these materials. SAXS results complimented HR TEM by giving more information on particle shape, particle size distribution and volume of the particle sizes in the sample. All the perovskites except dimethylammonium tin iodide were core shell hollow spheres with more than one particle size distribution at different particle size volumes in the samples. FTIR results showed all IR bands expected from the various perovskite chemical structures which include N-H stretch, C-H sp^3 , C-H stretch aldehyde, N-H bend, C-N sp^3 band and N-H wag, which confirm successful formation of the characteristic perovskite bonds during synthesis steps. Spectra of (^{13}C) NMR confirmed a shift upfield of the carbon atom in precursors as it bonded to Sn metal in the perovskite chemical structure, e.g. the carbon atom of guanidinium iodide precursor shifts from 110.57 ppm to 38.49 ppm in the $GASnI_3$ SOCTP. The same observation was seen in the MOCTPs, e.g. C-2 and C-3 atoms of ethylammonium iodide precursor shifted upfield from 37.03 ppm to 15.69 ppm as well as from 16.06 ppm to 14.39 ppm respectively in $[GA][CH_3CH_2NH_3]SnI_3$. Both FTIR and ^{13}C NMR spectra revealed that the organic cations do not bond with each other when they are mixed but bond with Sn, giving the expected chemical structures of these compounds. In addition to external

and internal morphology studies, UV-Vis was used to study the optical properties of the various perovskites.

It was established from UV-Vis studies that the MOCTPs exhibited improved optical properties compared to their counterparts (SOCTPs). A red-shift in absorption was observed from the MOCTPs relative to the SOCTPs resulting in a narrow energy band gap (E_g) for MOCTPs compared to the SOCTPs, e.g. guanidinium ethylammonium tin iodide perovskite had a band gap of 1.44 eV while ethylammonium tin iodide perovskite had a band gap of 2.89 eV. The narrowed energy band gap makes the MOCTP novel perovskites have ability to harvest more solar energy, hence better suited for photovoltaic application. CV and EIS were used to study the electrochemical properties of the MOCTPs and SOCTPs. From CV studies, it was found that the peak currents for MOCTPs is higher than those of SOCTPs, which makes MOCTPs to generate more electricity compared to SOCTPs. And from EIS studies MOCTPs showed reduced log impedance, improved phase angle, and reduced charge transfer resistance compared to SOCTPs which indicates that the conductive properties of MOCTPs were enhanced relative to SOCTPs. The SOCTPs and MOCTPs were successfully used as light absorbers in photovoltaic cells and subsequently their power conversion efficiency (PCE) were tested.

The PCE was calculated from the plot of current density-voltage (J-V). It was found that the novel MOCTPs have improved photovoltaic properties compared to the SOCTPs, e.g. 310 % increase from GASnI_3 perovskite to $[\text{GA}][(\text{CH}_3)_2\text{NH}_2]\text{SnI}_3$. This increase in PCE for MOCTPs is because of steric hindrance resulting from the surface structural modification of the mixed-organic-cations,

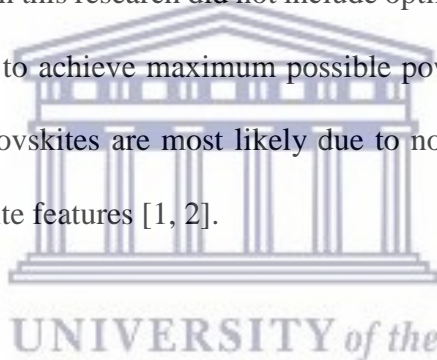
which leads to improved perovskite film formation. In addition, mixing these organic-cations promoted passivation of perovskite surface defect sites, which helped hinder charge recombination and improved charge transfer efficiency. Table 5.1 summarizes the enhancements in MOCTPs properties achieved in this research, using GASnI_3 as SOCTP and $[\text{GA}][(\text{CH}_3)_2\text{NH}_2]\text{SnI}_3$ as MOCTP.

Table 5.1. Characteristic parameters and their percentage change effected by mixing organic cations.

Parameter	SOCTP	MOCTP	% change
Optical band gap (eV)	1.46	1.45	0.68 decrease
Electrochemical band gap (eV)	1.26	1.20	4.76 decrease
Current (μA)	28.78	51.26	78.1 increase
D_{ox} (cm^2/s)	1.01×10^{-3}	1.26×10^{-3}	1.37 increase
R_{ct} (Ω)	18201	13357	26.61 decrease
log impedance	4.56	4.27	6.36 decrease
Phase angle ($^\circ$)	51.2	52.1	2.54 increase
PCE (%)	0.68	2.79	310 increase

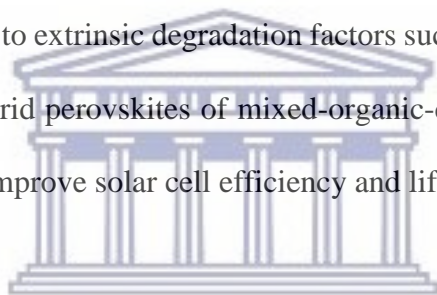
5.2 Recommendations

The approach of using multiple organic-cations as A-site in the perovskite structure yielded improved perovskite film morphology as well as improved power conversion efficiency in the solar cells fabricated from these new materials. It is recommended that further studies are done on mixed-organic cation tin halides to increase PCE to levels higher than 2.79% which was obtained in this research. Optimization studies of MOCTPs ($[\text{GA}][\text{CH}_3\text{CH}_2\text{NH}_3]\text{SnI}_3$ and $[\text{GA}][(\text{CH}_3)_2\text{NH}_2]\text{SnI}_3$) is recommended for preparation of photovoltaic cells with an improved PCE. The reported efficiencies in this research did not include optimization studies of the different layers of the photovoltaic cells to achieve maximum possible power conversion efficiency. The short circuit in synthesized perovskites are most likely due to non-optimal conditions and non-optimal morphological perovskite features [1, 2].



It is also recommended to use 100% glove box conditions to study tin halide perovskites since tin oxidizes easily from Sn^{2+} to Sn^{4+} [3-6]. This oxidation causes hole doping of the material and formation of tin oxides that promote degradation. Working under non-glove box conditions compromises the quality of the perovskite thin films. Since the adopted cell structure (planar architecture) suffers high charge mobility and versatility by the limit in the photovoltage due to the presence of sub-gap states and low intrinsic doping densities [7], it may be necessary to design a combination of both planar and mesoscopic device architectures.

More research still needs to be done to improve stability of photovoltaic cells. This problem is also observed in section 4.10 of this research whereby the fabricated devices showed some instability shortcomings. Increase in polymer molecular weight of the compounds needs to be done since increase in polymer molecular weight results in decrease in the density of the material's radical effects, hence improves the stability and PCE [8] of the device. Recently, devices that last thousands of hours under constant illumination have been reported [9-11] hence employing their strategies on mixed-organic tin halide perovskites would need to be investigated. PVCs that can withstand UV illumination have also been reported [12] which could have applicable procedures to help improve stability of the synthesized perovskites in this research. Furthermore, information on PVCs that are more resistant to extrinsic degradation factors such as oxygen and water [13, 14] could be explored amongst hybrid perovskites of mixed-organic-cations. Successfully designing more stable solar cells, would improve solar cell efficiency and lifetime.



UNIVERSITY of the
WESTERN CAPE

Moisture-induced degradation of organic-inorganic lead halide perovskites is evident from the disappearance of the XRD peaks related to the initial perovskite structure while new peaks corresponding to the degradation of PbI_2 and I_2 emergence [15, 16]. Moreover, the formation of I_2 is triggered only when both moisture and light are present. XRD peaks corresponding to SnI_2 degradation product were observed in section 4. 4. This shows that the perovskite degrades quicker hence it is recommended that stringent PVC encapsulation is developed to ensure extended outdoor lifetime.

5.3 References

1. Takahashi, Y., Obara, R., Lin, Z., Takahashi, Y., Naito, T., Inabe, T., Ishibashi, S., Terakura, K. (2011). Charge-Transport in Tin-Iodide Perovskite $\text{CH}_3\text{NH}_3\text{SnI}_3$: Origin of High Conductivity. *Dalton Trans*, 40, 5563-5568.
2. Zuo, F., Williams, S., Liang, P., Chueh, C., Liao, C., Jen, A. (2014). Binary-Metal Perovskites Toward High-Performance Planar-Heterojunction Hybrid Solar Cells. *Advanced Materials*, 26, 6454.
3. Noel, N., Stranks, S., Abate, A., Wehrenfennig, C., Guarnera, S., Haghighirad, A., Sadhanala, A., Eperon, G., Pathak, S., Johnston, M., Petrozza, A., Herz, L., Snaith, H. (2014). Lead-Free Organic-Inorganic Tin Halide Perovskites for Photovoltaic Applications. *Energy Environmental Science*, 7, 3061-3068.
4. Roghabadia, F., Ahmadib, N., Ahmadi, V., Di Carloc, A., Aghmiunib, K., Tehrania, A., Ghoreishib, F., Payandeha, M., Fumanid, N. (2018). Bulk Heterojunction Polymer Solar Cell and Perovskite Solar Cell: Concepts, Materials, Current Status, and Opto-Electronic Properties. *Solar Energy*, 173, 407-424.
5. Ogomi, Y., Morita, A., Tsukamoto, S., Saitho, T., Fujikawa, N., Shen, Q., Toyoda, T., Yoshino, K., Pandey, S., Ma, T., Hayaye, S. (2014). $\text{CH}_3\text{NH}_3\text{Sn}_x\text{Pb}_{(1-x)}\text{I}_3$ Perovskite Solar Cells Covering up to 1060 nm. *Journal of Physical Chemistry Letters*, 5, 1004-1011.
6. Kumar, M., Dharani, S., Leong, W., Boix, P., Prabhakar, R., Baikie, T., Shi, C., Ding, H., Ramesh, R., Asta, M., Graetzel, M., Mhaisalkar, S., Matthews, N. (2014) *Advanced Materials*, 26, 7122-7127.

7. Leijtens, T., Stranks, S., Eperon, G., Lindblad, R., Johansson, E., McPherson, I., Rensmo, H., Ball, J., Lee, M., Snaith, H. (2014) . Electronic Properties of Meso-Superstructured and Planar Organometal Halide Perovskite Films: Charge Trapping, Photodoping, and Carrier Mobility. *ACS Nano*, 8, 7147-7155.
8. Ding, Z., Kettle, J., Horie, M., Chang, S., Smith, G., Shames, A., Katz, E. (2016). Efficient Solar Cells are More Stable: The Impact of Polymer Molecular Weight on Performance of Organic Photovoltaics. *Journal of Materials Chemistry A*, 4, 7274-7280.
9. Christians, J., Schulz, P., Tinkham, J., Schloemer, T., Harvey, S., Tremolet de Villers, B., Sellinger, A., Berry, J., Luther, J. (2018). Tailored Interfaces of Unencapsulated Perovskite Solar Cells for > 1,000 h Operational Stability. *Nature Energy*, 3, 68-74.
10. Arora, N., Dar, M., Hinderhofer, A., Pellet, N., Schreiber, F., Zakeeruddin, S., Graetzel, M. (2017). Perovskite Solar Cells with CuSCN Hole Extraction Layers Yield Stabilized Efficiencies Greater than 20%. *Science*, 358, 768-771.
11. Tan, H., Jain, A., Voznyy, O., Lan, X., García de Arquer, F., Fan, J., Quintero-Bermudez, R., Yuan, M., Zhang, B., Zhao, Y. (2017). Efficient and Stable Solution-Processed Planar Perovskite Solar Cells via Contact Passivation. *Science*, 355, 722-726.
12. Roose, B., Baena, J., Gödel, K., Graetzel, M., Hagfeldt, A., Steiner, U., Abate, A. (2016). Mesoporous SnO₂ Electron Selective Contact Enables UV-Stable Perovskite Solar Cells. *Nano Energy*, 30, 517-522.
13. Wang, Z., Lin, Q., Chmiel, F., Sakai, N., Herz, L., Snaith, H. (2017). Efficient Ambient-Air-Stable Solar Cells with 2D-3D Heterostructured Butylammonium-Caesium-Formamidinium Lead Halide Perovskites. *Nature Energy*, 2, article number 17135.

14. Bush, K., Palmstrom, A., Yu, Z., Boccard, M., Cheacharoen, R., Mailoa, J., McMeekin, D., Hoyer, R., Bailie, C., Leijtens, T. (2017). 23.6%-Efficient Monolithic Perovskite/Silicon Tandem Solar Cells with Improved Stability. *Nature Energy*, 2, article number 17009.
15. Habisreutinger, S., Leijtens, T., Eperon, G., Stranks, S., Nicholas, R., Snaith, H. (2014). Carbon Nanotube/Polymer Composites as a Highly Stable Hole Collection Layer in Perovskite Solar Cells. *Nano Letters*, 14, 5561-5568.
16. Niu, G., Li, W., Meng, F., Wang, L., Dong, H., Qiu, Y. (2014). Study on the Stability of CH₃NH₃PbI₃ Films and the Effect of Post-Modification by Aluminum Oxide in All-Solid-State Hybrid Solar Cells. *Journal of Materials Chemistry A*, 2, 705-710.



UNIVERSITY of the
WESTERN CAPE